



HAL
open science

**Spectroscopie atomique avec un confinement
nanométrique ou tridimensionnel Recherche d'un effet
de température dans l'interaction Casimir-Polder en
champ proche**

Isabelle Maurin

► **To cite this version:**

Isabelle Maurin. Spectroscopie atomique avec un confinement nanométrique ou tridimensionnel Recherche d'un effet de température dans l'interaction Casimir-Polder en champ proche . Physique Atomique [physics.atom-ph]. Université Paris 13 - Sorbonne Paris Cité, 2016. tel-01449159

HAL Id: tel-01449159

<https://hal.science/tel-01449159>

Submitted on 30 Jan 2017

HAL is a multi-disciplinary open access archive for the deposit and dissemination of scientific research documents, whether they are published or not. The documents may come from teaching and research institutions in France or abroad, or from public or private research centers.

L'archive ouverte pluridisciplinaire **HAL**, est destinée au dépôt et à la diffusion de documents scientifiques de niveau recherche, publiés ou non, émanant des établissements d'enseignement et de recherche français ou étrangers, des laboratoires publics ou privés.

**UNIVERSITÉ PARIS 13
INSTITUT GALILÉE**

LABORATOIRE DE PHYSIQUE DES LASERS

Habilitation à diriger des recherches

Spécialité : Sciences

présentée par

Isabelle Maurin

Sujet de la thèse d'habilitation :

**Spectroscopie atomique avec confinement
nanométrique ou tridimensionnel.**

**Recherche d'un effet de température dans
l'interaction Casimir-Polder en champ
proche**

Soutenue le vendredi 16 décembre 2016 devant le jury composé de :

Mme	Anne Amy-Klein	Présidente du jury
Mme	Agnès Maître	Rapporteur
M.	Serge Reynaud	Rapporteur
M.	José Wellington Rocha Tabosa	Rapporteur
M.	Robin Kaiser	Examineur
M.	Daniel Bloch	Examineur

A François,
Thomas,
Arthur
mes rayons de soleil.

Table des matières

Curriculum vitae	9
Expériences professionnelles et scientifiques	9
Formation	10
Activités d'enseignements	10
Responsabilités	11
Pédagogiques	11
Scientifiques	11
Activités de diffusion de la science	12
Encadrement	13
Doctorants	13
Stagiaires	14
Activités de recherche	14
Collaborations	14
Publications	16
Articles parus dans des revues à comité de lecture	16
Publications dans des revues sans comité - Vulgarisation	17
Communications avec actes	17
Conférences invitées	18
Communications sans actes	20
1 Parcours Personnel	29
2 Étude des propriétés optiques linéaires et non linéaires des lasers à cascade quantique	33
2.1 Introduction	33
2.2 Les lasers à cascade quantique bicolores	35
2.3 Étude des propriétés optiques non linéaires des lasers à cascade quantique	35
2.4 Article en relation avec ce chapitre	36

3	Nanolaser à boîte quantique unique en microcavité	39
3.1	Introduction	39
3.2	Réalisation de nanolasers sans inversion de population	40
3.3	Réalisation de nanolasers à une seule boîte quantique	41
4	Spectroscopie atomique dans une nanocellule	45
4.1	Introduction générale	45
4.2	Mesure de l'interaction vW atome-surface résolue spatialement	48
4.2.1	Cellule nanométrique	48
4.2.2	Description de l'expérience	50
4.2.3	Modélisation	51
4.2.4	Résultats pour la raie à 917 nm	52
4.2.5	Résultats obtenus pour la raie D_1 (894 nm) pour des distances encore plus courtes	55
4.2.6	Cas où il y a un couplage résonant entre l'émission atomique et l'absorption de la surface	56
4.3	Spectroscopie à deux photons dans une nanocellule - Généralisation du rétrécissement Dicke [1]	58
4.4	Conclusion et perspectives	60
4.5	Articles en relation avec ce chapitre	61
5	Effet en température de l'interaction van der Waals	63
5.1	Introduction	63
5.2	Dépendance en température des propriétés optiques de surface et évaluation du coefficient de van der Waals [2,3]	65
5.2.1	Modélisation de la dépendance en température du coefficient C_3	65
5.2.2	Dépendance en température des propriétés optiques de surface	67
5.2.3	Évaluation du coefficient de van der Waals en fonction de la température	67
5.3	Étude de l'interaction atome-surface entre un atome excité et une surface thermiquement émissive en CaF_2	71
5.3.1	Cellule en CaF_2	71
5.3.2	La réflexion sélective	73
5.3.3	Expériences préliminaires pour valider notre cellule [4]	75
5.3.4	Dépendance en température des spectres de réflexion sélective pour les transitions $6S_{1/2} \rightarrow 8P_{3/2}$ et $8P_{1/2}$ [5]	76
5.3.5	Observation de résonances sub-Doppler supplémentaires autour des transitions d'absorption saturée de Cs sur la transition 6S-8P [6]	77
5.4	Étude de l'interaction atome-surface entre un atome excité et une surface thermiquement émissive en saphir - Cas faiblement résonant [7]	79
5.4.1	Présentation de la cellule	79
5.4.2	Prédictions théoriques	81
5.4.3	Expérience	81
5.5	Conclusion	83
5.6	Articles en relation avec ce chapitre	84

6	Spectroscopie atomique avec confinement 3D	85
6.1	Introduction	85
6.1.1	Motivations	85
6.1.2	Etat de l'art	86
6.2	Réalisation et caractérisation d'un film de nanosphères [8]	87
6.3	Cellule contenant une tranche d'opale	91
6.4	Caractérisation optique d'une opale Langmuir-Blodgett	93
6.4.1	Modélisation optique d'une opale fine déposée sur un substrat [9]	94
6.4.2	Modélisation optique d'une ou deux couches de billes déposées sur un substrat [10]	99
6.5	Infiltration résonante d'une opale Langmuir - Blodgett	100
6.5.1	Résultats expérimentaux [10, 11]	100
6.5.2	Modélisation de la réponse optique d'une opale infiltrée par un milieu résonant [12]	104
6.5.3	Expériences sur des opales composées de quelques couches de billes	108
6.6	Conclusion	109
6.7	Articles en relation avec ce chapitre	111
7	Perspectives	113
7.1	Étude de l'interaction atome-surface entre un atome excité et une surface thermiquement émissive en saphir superpoli - Couplage résonant	113
7.2	Mesures de l'interaction Casimir-Polder avec des molécules	116
7.3	Confinement 3D	118
	Bibliographie	119
	Articles principaux de mon HDR	129

Remerciements

Je tiens tout d'abord à remercier Agnès Maître, José Wellington Rocha Tabosa et Serge Reynaud d'avoir accepté de relire ce mémoire et d'en être rapporteurs. Je remercie également tous les autres membres du jury : Anne Amy-Klein, Robin Kaiser et Daniel Bloch d'avoir accepté d'assister à la présentation de ce travail. La version finale de ce mémoire a bénéficié de la lecture particulièrement attentive et des remarques précieuses de Anne Amy-Klein, Jean-Philippe Karr et Martial Ducloy. Je les en remercie de tout coeur.

Je voudrais remercier tous les membres de mon équipe sans qui ce travail n'aurait pas été possible : Daniel Bloch (Merci de m'avoir soutenue et guidée depuis mon arrivée au laboratoire), Martial Ducloy, Athanasios Laliotis (c'est un grand plaisir de travailler avec toi au jour le jour et de partager des conversations qui sont scientifiques ou non), Marie-Pascale Gorza, Michèle Fichet. Je remercie également les nombreux thésards, ATER, post-doctorants de l'équipe à qui je souhaite bonne chance dans leurs activités présentes et futures : Petko Todorov, Ismahène Hamdi, Thierry Passerat de Silans, Pedro Chaves de Souza Segundo, Solomn Saltiel, Marco Romanelli, Philippe Ballin, Elias Moufarej, João de Aquino Carvalho et Junior Lukusa Mudiayi. Ce travail est aussi le leur.

Les travaux présentés ici ont souvent été réalisés en collaboration avec d'autres collègues. Les résultats obtenus n'auraient été possibles sans eux : Sean Tokunaga et Benoît Darquié (étude de l'interaction molécules/surface), David Sarkisyan et Florence Thibout (pour la fabrication de nos cellules), Domingos de Sousa Meneses et Patrick Echegut (pour la caractérisation de nos surfaces), Illya zabkov et Vasily Klimov (pour la modélisation optique d'un film de nanosphère) et Chia-Hua Chuan, Agnès Maître et Serge Ravaine (pour nous avoir donné des opales ou nanobilles). Un grand merci pour leur aide.

Je remercie tous les membres de mon laboratoire (un merci particuliers à Paolo pour m'avoir conseillé pendant les répétitions de l'oral de mon HDR), et plus particulièrement les ateliers et les membres de l'administration du laboratoire (merci à Marc et Stéphane

de m'avoir aidé avec Lucile Lapierre pour la visioconférence de mon HDR) ainsi que mes collègues de l'IUT de Saint-Denis du département Mesures physiques avec qui il est si plaisant de travailler.

Je remercie également mes amis : Sylvain (merci d'avoir été le déclic qui m'a lancé à écrire mon HDR), Caroline, Franck, Richard, Nathalie, Antoine, David, Nadia et Eric ... mes parents, mon frère Gilles, Marine et surtout François, Thomas et Arthur pour leur soutien sans faille au jour le jour et leur confiance.

Curriculum vitae

Isabelle Maurin

Tél : 01 49 40 33 80 ou 33 64

née le 08 Juillet 1976

Fax : 01 49 40 32 00

isabelle.maurin@univ-paris13.fr

Expériences professionnelles et scientifiques

- 2004-...** : Maître de conférences à l'IUT de Saint-Denis au département Mesures Physiques (30^e section), recherche effectuée au Laboratoire de Physique des lasers (Institut Galilée, Villetaneuse) dans le groupe Spectroscopie aux interfaces anciennement appelé Optique Cohérente à résonance.
- 2003-2004** : Stage post-doctoral au Laboratoire de Photonique et de Nanostructures du CNRS sous la direction d'Izo Abram : *Étude du déclenchement de l'émission stimulée dans un laser à microcavité semi-conducteur*
- 2002-2003** : ATER à l'Université Denis Diderot (Paris VII), recherche effectuée au laboratoire Thales Research and Technology (pôle Matériaux et Phénomènes Quantiques) sous la direction de Carlo Sirtori : *Étude des propriétés optiques linéaires et non linéaires des lasers à cascade quantique - Génération d'ondes TéraHertz.*
- 1999-2002** : Doctorat au Laboratoire Kastler-Brossel (Paris VI) sous la direction d'Elisabeth Giacobino : *Étude du bruit quantique dans les lasers à semi-conducteur.*
- 1998-1999** : Stagiaire de DEA au CEA à Saclay (Groupe composants organiques) sous la direction de Céline Fiorini. Réalisation et caractérisation de microcavités en milieu polymère utilisées pour l'élaboration de microlasers.

Formation

1999-2002 : Thèse (bourse ministérielle) obtenue au Laboratoire Kastler-Brossel (Paris) sous la direction d'Élisabeth Giacobino avec la mention très honorable : «Étude du bruit quantique dans les lasers à semi-conducteurs (VCSELs et diodes lasers) ».

1998-1999 : DEA optique et photonique (Université Pierre et Marie Curie).

1996-1998 : Licence et maîtrise de physique fondamentale (Université Pierre et Marie Curie).

Activités d'enseignements

De 1999 à 2002, j'ai été chargée d'enseignement à l'université D'Évry Val d'Essonne à l'IUP génie des matériaux première année (total 256 h) :

- Travaux dirigés et pratiques d'ondes et propagation (optique, électronique, mécanique),

De 2002 à 2003, j'ai été Attachée Temporaire d'Enseignement et de Recherche à l'université Denis Diderot (total 96 h) :

- Travaux pratiques de physique (optique, mécanique, hydrostatique) en DEUG MIAS 1^{ère} année,
- Colles de mécanique et travaux dirigés d'optique en « Mécanique et optique » DEUG MIAS 1^{ère} année,
- Intervention dans le cours «Physique des matériaux et dispositifs quantiques » en maîtrise de physique.

Depuis septembre 2004, j'ai effectué la majeure partie de mon service à l'IUT de Saint-Denis au département Mesures Physiques :

- TP capteurs,
- CM/TD/TP Optique ondulatoire et optronique,
- CM/TD/TP Systèmes optiques (optique géométrique, photométrie, sources),
- CM/TD Mécanique vibratoire (corde vibrante et membranes),
- CM/TD Techniques du vide.

Je suis également intervenue en Licence Professionnelle Métiers de la Mesure, de l'Instrumentation et du contrôle (MMIC) de 2005 à 2013.

- CM/TD Techniques d'éclairage.

Enfin, j'ai aussi enseigné au DIU « Appareillage utilisés en médecine, en imagerie médicale et biologie » de 2006 à 2009.

- CM/TD Physique de base.

Responsabilités

Responsabilités pédagogiques

- Responsable pédagogique de la 2^e année du DUT Mesures Physiques à l'IUT de Saint-Denis depuis septembre 2008 (gestion des étudiants, intermédiaire enseignants-étudiants, responsable des projets, responsable des poursuites d'études, organisation d'une journée de présentation des poursuites d'études possibles après le DUT MP tous les ans depuis 2008, organisation de la journée des anciens (Janvier 2016), participation aux entretiens de recrutements des futurs étudiants de première année),
- Membre élu du conseil de département (2010-2011, 2014-2015, 2015-2016).

Responsabilités scientifiques

- Membre du réseau européen «Vista » (coopération entre une dizaine de laboratoires européens pour étudier sous tous les angles les lasers à semi-conducteurs à cavité verticale : VCSELs) de 2001 à 2002,
- Organisation d'une semaine de congrès à Paris pour les différents laboratoires du réseau européen «Vista » pendant ma thèse du 11-13 Juin 2001,
- Membre nommé du conseil du laboratoire de 2004 à 2012,
- Membre du jury du concours MCF 30^e section IUT d'Orsay département Mesures Physiques (juin 2015),
- Comité des experts section 30 au LPL depuis 2004,
- Membre du jury du concours d'ingénieur de recherche 30^e section au LPL (juin 2013),
- Coordinatrice française du réseau Franco - Bulgare Rila (janvier 2007 -janvier 2009), Thématique : interactions atome - surface, et spectroscopie en cellule confinée ainsi que spectroscopie cohérente,

- Sauveteur secouriste du travail depuis juillet 2013.

Activités de diffusion de la science

- Fête de la science : animation du stand scientifique du Laboratoire de Physique des Lasers lors de la manifestation Savante Banlieue/Fête de la science à l'université Paris 13 et des journées portes ouvertes de l'université Paris 13 (depuis 2004),
- Animation d'un stand scientifique au Palais de la découverte dans le cadre « une manip un chercheur » (C'nano) : « Un monde en couleur » : 3 demi-journées (fin 2009),
- Organisation de séminaires techniques au laboratoire pendant 2 ans,
- Encadrement d'un stagiaire de 3ème pendant une semaine Julien UZZAN (décembre 2009),
- « 50 ans du laser » : participation à plusieurs manifestations pour la célébration des « 50 ans du Laser » (Salon culture et jeux mathématique, la Nuit des chercheurs, visite de Lycéens)- 2010,
- Accueil de 4 classes de collège dans le cadre du Rallye des entreprises entre 2010 et 2015 organisé par la Plaine Commune (visite du laboratoire, de l'université et de la salle de vulgarisation scientifique du laboratoire),
- Accueil d'étudiants en 1ère SVT du lycée Camille Claudel de Pontault-Combault en Seine-et-marne dans le cadre de leur TPE (travaux personnels encadrés) sur l'holographie (Février 2011),
- Vice-présidente de l'association de vulgarisation scientifique Atouts Sciences et chargée des relations avec l'IUT de Saint-Denis depuis 2014,
- Développement de l'expérience de la chute des corps dans le vide ou dans l'air par 4 étudiantes en deuxième année du DUT Mesures Physiques et avec le soutien de l'association Atouts Sciences à l'occasion de la célébration des 450 ans de la naissance de Galilée (15 Mai 2014),
- Animation dans l'école maternelle Denis Papin (Petite section et Grande section) 1 journée en janvier 2014 sur le thème des ombres et de la lumière,
- Participation à un speed-dating novembre 2014 et 2015 avec des lycéennes de première et terminale scientifiques dans le cadre de la journée « Filles et maths :

une équation lumineuse »,

- Animation du stand scientifique du Laboratoire de Physique des Lasers lors de la manifestation du Printemps à la Fac (28 Mai 2015) et aussi lors des 4ème rencontres Sciences et citoyens (22 mars 2013),
- Participation au challenge Mesures Physiques 2016 "Mesures autour de l'automobile". Conception d'un système de mesure de grandeurs physiques transportable (électronique, chimie et optique), autonome, qui est ensuite déposé sur une remorque tractée par un véhicule sur une piste (au Mans). Projet effectué par 10 étudiants en 2ème année de MP. Co-encadrement de la partie optique avec Nicolas Nieuwjaer : "Mesure de l'opacité des gaz d'échappement". Responsable de la communication sur l'événement (réalisation d'un film, organisation d'une semaine d'exposition du prototype dans le hall de l'IUT de Saint-Denis, mise à jour du site web du département),
- Accueil de 3 élèves en Terminale Sciences et Techniques de Laboratoire, spécialisée en physique chimie du lycée Paul Langevin de Suresnes à l'IUT de Saint-Denis MP pour leur projet sur l'holographie (1/2 journée en janvier 2016).

Encadrement

Doctorants

- Marco Romanelli encadrement de sa première année de thèse (2001-2002) sur la partie "Spatial distribution of intensity noise in vertical-cavity surface-emitting lasers" de sa thèse,
- Petko Todorov (soutenue en Bulgarie le 21/11/2006) "Spectroscopy in absorption and reflection in nanocells with Van der Waals interaction taken into account", 17 mois passés en France correspondant à la quasi-totalité du travail expérimental,
- Thierry Passerat De Silans (soutenance le 26 Juin 2009) Interaction atome-surface : interaction de van der Waals entre un atome excité et une surface diélectrique thermiquement émissive; oscillations de Bloch pour un atome adsorbé. Thèse en cotutelle avec le Brésil,
- Philippe Ballin (soutenue le 14 juin 2012) Confinement tridimensionnel d'une vapeur de césium dans une opale de nanobilles,
- Elias Moufarej (soutenue le 19 décembre 2014) Infiltration d'une vapeur diluée dans une opale artificielle Langmuir-Blodgett : études optiques et spectroscopiques

piques,

- Joao Carlos de Aquino Carvalho (en cours depuis le 01 septembre 2014) Atomes confinés sous la longueur d'onde optique.

Stagiaires

- Yves-Oliver Renault, Stage de l'école Polytechnique, 2004 (3 mois),
- Athanasios Laliotis, Post-doctorant, 2005/2006 (1 an),
- Pedro Chaves de Souza Segundo, Post-doctorant, 2006/2007 (1 an),
- Marco Romanelli, ATER, 2006/2007 (1 an),
- David Lin, Master 1 de physique fondamentale (P6), 2015 (2 mois),
- Ibtissem Benguetat Master 1 de physique fondamentale (P11), 2016 (2 mois),
- Junior Lukusa Master 2 nanotechnologie (P13), 2016 (6 mois).

Activités de recherche

J'ai mené mon travail de recherche depuis 2004 au sein de l'équipe OCR (Optique Cohérente à résonance) maintenant nommée SAI (Spectroscopie aux interfaces).

Collaborations

Internationales :

- Universidade federal Fluminense, Niteroi, Rio de Janeiro, Brésil (A. Z. Khoury)
- Russian Academy of sciences, Moscow, Russie (Igor E. Protsenko, Yuri Golubev)
- INFN, Dipartimento di Fisica, Università di Milano, Italie (M. Travagnin, L. A. Lugiato)
- Instituto de Física, Facultad de Ingeniería, Uruguay (H. Falaiche, A. Lezama)
- P. N. Lebedev Physical Institut, Russian Academy of Sciences (Vasily V. Klimov)
- Moscow Institute of physics and technology (state university), Dolgoprundy, Russie (I. Zabkov)
- Laboratorio de Superfies, Universidade Federal da Paraíba, Joao Pessoa, Brésil (Martine Chevrollier, Thierry Passerat De Silans, Pedro Chaves de Souza Segundo et Marco Oria)

- Universidade Federale de Pernambuco, Recife, Brésil (JRR Leite, JWR Tabosa)
- Institute for Physical Research, National Academy of Sciences of Armenia (David Sarkisyan)
- National central university, Taiwan (Chia-Hua Chan)
- Institut d'électronique de l'Académie des Sciences à Sofia en Bulgarie (Petko Todorov, Christina Andreeva, Stefka Cartaleva)
- Department of physics, University of Crete en Crète (Kominis Iannis)
- Depatment of Physics, Chuo University, Japon (S. Tojo)

Nationales :

- Institut d'optique, Orsay, groupe optique quantique (Philippe Grangier)
- PhLAM, Lille (Mikhail Kolobv)
- Institut des Nanosciences de Paris (Agnès Maitre, Catherine Schwob, Laurent Coolen)
- Centre de recherche Paul Pascal à Bordeaux (Serge Ravaine)
- Laboratoire Kasler-Brossel, Paris (Florence Thibout)
- Conditions Extrêmes et Matériaux : Haute Température et Irradiation (CEMHTI Université d'Orléans (Patrick Echegut, Domingo De Sousa Meneses)
- Laboratoire XLIM, groupe Gas-phase photonic and microwave materials, Orléans (Fetah Benabid)
- Laboratoire kastler-Brossel (A. Lambrecht)
- Laboratoire des sciences des procédés et des matériaux, Villetaneuse (Jocelyn Achard, Vianney Mille et Alexandre Tallaire)

Publications

Articles parus dans des revues à comité de lecture

1. Hermier J.-P., Maurin I., Giacobino E., Schnitzer P., Michalzik R., Ebeling K. J., Bramati A., Khoury A. Z., *Quantum noise in semiconductor microlaser*, New Journal of Physics, **2**, 26.1 (2000).
2. Hermier J.-P., Kolobov M. I., Maurin I., and E. Giacobino, *Quantum spin-flip model of vertical-cavity surface-emitting lasers*, PRA **65**, 053825 (2002).
3. Maurin I., Protsenko I., Hermier J.-P., Bramati A., Grangier Ph., and Giacobino E., *Light intensity-voltage correlations and a leakage current excess noise in a single mode semiconductor laser*, PRA, **72**, 033823 (2005).
4. Bengloan J.-Y., De Rossi A., Ortiz V., Marcadet X., Calligaro M., Maurin I., Sirtori C., *Intra-cavity sum frequency generation GaAs quantum cascade lasers*, Appl. Phys. Lett 84, **12**, 2019-2021, 12 (2004).
5. Dutier G., Todorov P., Hamdi I., Maurin I., Saltiel S., Bloch D., Ducloy M., *Dicke coherent narrowing in two-photon and Raman spectroscopy of thin vapour cells*, PRA **72**, 1(R) (2005) (Rapid Comm.).
6. Passerat De Silans T., Lalot A., Romanelli M., De Souza Segundo P.C., Maurin I., Bloch D., Ducloy M., Sarkisyan A., *Selective reflection spectroscopy of a vapour at a calcium fluoride interface*, Annales de Physique, **32**, 2-3, 191, (2007).
7. Romanelli M., Maurin I., Todorov P., Chan C.-H., Bloch D., *A 2D nanosphere array for atomic spectroscopy*, Annales de Physique, **32**, 2-3, 127-130, (2007)
8. Fichet M., Dutier G., Yarovitski A., Todorov P., Hamdi I., Maurin I., Saltiel S., Sarkisyan D., Gorza M.-P., Bloch D., Ducloy M., *Exploring the van der Waals Atom-Surface attraction in the nanometric range*, Europhysics Letters, **77**, 54001, (2007)
9. Lalot A., Maurin I., Fichet M., Bloch D., Ducloy M., Balasanyan N., Sarkisyan A., Sarkisyan D., *Selective reflection spectroscopy at the interface between a calcium fluoride windows and Cs vapour*, Applied Physics B : Lasers and Optics, **90**, 415-420, (2008)
10. Passerat De Silans T., Maurin I., De Souza Segundo P.C., Saltiel S., Gorza M.-P., Ducloy M., Bloch D., De Sousa Meneses D., Echegut P., *Temperature dependence of the dielectric permittivity of CaF_2 , BaF_2 and Al_2O_3 : application to the prediction of a temperature dependent van der Waals surface interaction exerted onto a neighbouring Cs ($8P_{3/2}$) atom*, Journal of Physics : Condensed Matter, **21**, 255902, (2009).
11. Passerat de Silans T., Maurin I., Lalot A., Chaves de Souza Segundo P., Bloch D., *Extra sub-Doppler lines in the vicinity of the third resonance $6S-8P$ of atomic Cs attributed to optically induced Cs dimers*, Phys. Rev. A **83**, 043402 (2011).
12. Ballin P., Moufarej E., Maurin I. Lalot A., Bloch D, *Three-dimensional confinement of vapor in nanostructures for sub-Doppler optical resolution*, App. Phys. Lett. **102**, 231115 (2014).

13. Passerat De Silans T., Laliotis A., Maurin I., Gorza M.-P., Segundo P., Ducloy M., Bloch D., *Experimental observations of temperature effects in the near-field regime of the Casimir-Polder interaction*, Laser Physics, **24**, 074009, (2014).
14. Laliotis A., Passerat De Silans T., Maurin I., Ducloy M., Bloch D., *Casimir-Polder interactions in the presence of thermally excited surface modes*, Nature Communications, /ncomms5364, (2014).
15. Moufarej E., Maurin I., Zabkov I., Laliotis A., Ballin P., Klimov V.V., Bloch D., *Infiltrating a thin or single layer opal with an atomic vapour : sub-doppler signals and crystal optics*, Europhysics Letters, Special Issue (Proceedings of META 14-Singapore), **108**, 17008, (2014).
16. Maurin I., Bloch D., *Resonant infiltration of an opal : reflection lineshape and contribution from in-depth regions*, Journal of Chemical Physics, **142**, 234706, (2015).
17. Maurin I., Moufarej E., Laliotis A., Bloch D., *Optics of opal modeled with a stratified effective index and the effect of the interface*, JOSAB, **32**, 8, (2015).

Publications dans des revues sans comité - Vulgarisation

1. Maurin I., Todorov P., Hamdi I., Yarovitski A., Dutier G., Saltiel S., Gorza M.-P., Fichet M., Bloch D., Ducloy M., *Probing an atom in gas confined in a nanocell*, Journal of physics : conference series **19** (2005) 20-29, conference on Atoms and molecules near surfaces.
2. Hamdi I., Todorov P., Yarovitski A., Dutier G., Maurin I., Li Y.Y., Lezama A., Varzhapetyan T., Sarkisyan D., Gorza M.-P., Fichet M., Bloch D., Ducloy M., *Laser Spectroscopy with Nanometric Gas Cells : Distance Dependence of Atom-Surface Interaction and Collisions under Confinement*, Laser Physics, **15**, 987-996, (2005).
3. Maurin I., Todorov P., Hamdi I., Yarovitski A., Dutier G., Saltiel S., Gorza M.-P., Fichet M., Bloch D., Ducloy M., *Mesure à faible distance de l'interaction atome-surface de type van der Waals dans une cellule nanométrique de vapeur de Césium*, Journal de Physique IV, **135**, 235-236, (2006).
4. Gazette de la recherche de l'institut Galilée, *La couleur du rayonnement de "corps noir" sondée par des atomes*, n°12, p6, (octobre 2015).
5. Publication de nos résultats dans le journal du CNRS (INP), *L'attraction atome-surface exaltée par la chaleur*, <http://www.cnrs.fr/inp/spip.php?article3111> (26 septembre 2014).

Communications avec actes

1. Fiorini C., Prudhomme N., De Veyrac G., Maurin I., Raimond P., Nunzi J.-M., et Ledoux-Rax I., *Molecular migration mechanism for laser induced surface relief grating formation*, Synthetic Metals, **115**, 121-125, (2000).

2. Nunzi J.-M., Fiorini C., De Veyrac G., Raimond P., Maurin I., *Evidence for photoinduced molecular migration mediated surface-relief grating formation in azo-dye polymers*, Molecular Crystals and Liquid Crystals Science and Technology. Section A. Molecular Crystals and Liquid Crystals, **335**, 1, 427-434, (2000).
3. Maurin I., Hermier J.-P., Bramati A., Ducci S., Kolobov M., Khoury A. Z. et Giacobino E., *Etude du bruit quantique dans les microlasers à semi-conducteurs à cavité verticale (VCSELs)*, Journal of Physics, (2000).
4. Laliotis A., Maurin I., Todorov P., Hamdi I., Dutier G., Saltiel S., Gorza M.-P., Fichet M., Bloch D., Ducloy M., *Measuring the atom-surface van der Waals interaction in the atome-surface de type van der Waals dans une cellule nanométrique de vapeur de Césium*, Journal de Physique IV, **135**, 235-236, (2006).
5. Ballin P., Moufarej E., Maurin I., Laliotis A., Bloch D., *Sub-Doppler optical resolution by confining a vapour in a nanostructure*, 17th International School on Quantum Electronics : Laser Physics and Applications, Nessebar, Bulgarie, (2012), Proceedings of SPIE, **8770**, 87700J, (2013).
6. Todorov P., Petrov N., Maurin I., Saltiel S., Bloch D., *Detection of slow atoms confined in a Cesium vapor cell by spatially separated pump and probe laser beams*, 17th International School on Quantum Electronics : Laser Physics and Applications, Neesebar, Bulgarie, (2012), Proceedings of 17th SPIE, **8770**, 87700P, (2013).

Conférences invitées

1. Bramati A., Marin F., Hermier J.-P., Maurin I., Giacobino E., Travagnin M., Lugiato L. A., *Semiconductor lasers with reduced noise for high sensitivity spectroscopy*, International workshop for optics and spectroscopy, Hanoï, (2000).
2. Hamdi I., Yarovitski A., Todorov P., Dutier G., Maurin I., Saltiel S., Sarkisyan D., Gorza M.-P., Fichet M., Bloch D., Ducloy M., *Confining a resonant vapour in a nanocell : results and prospects*, FRISNO'8, French-Israelian Symposium on Nonlinear Optics, Ein Bokek, Israël, (2005).
3. Hamdi I., Todorov P., Maurin I., Yarovitski A., Dutier G., Saltiel S., Gorza M.-P., Fichet M., Bloch D., Ducloy M., *Analysing the atom-surface interaction through nanocell spectroscopy*, LTL-Plovdiv'2005, IV international symposium on Laser Technologies and Lasers, Plovdiv, Bulgarie, (2005).
4. Laliotis A., Maurin I., Todorov P., Hamdi I., Dutier G., Yarovitski A., Saltiel S., Gorza M.-P., Fichet M., Ducloy M., Bloch D., *Testing the distance-dependence of the van der Waals interaction between an atom and a surface through spectroscopy in a vapour nanocell*, XIV international School on Quantum Electronics and Lasers Physics, Sunny Beach, Bulgaria, (2006).
5. Passerat de Silans T., Maurin I., Gorza M.-P., Bloch D., Rios Leite J.R., Klimov V., Ducloy M., *Nanoscale Quantum Optics : nanocavity QED, atomic spectroscopy, etc.*, CEWQO, 15th Central European Workshop on Quantum Optics 2008, Belgrade (30 mai-3juin 2008).

6. Maurin I., Laliotis A., Passerat De Silans T., Dutier G., Gorza M.-P., Bloch D., Ducloy M., Sarkisyan D., *Vapour spectroscopy close to an interface : confined optical frequency references*, RFYS2008 (Russian French Young Scientist symposium), Saint Petersburg, Russie, (2008).
7. Laliotis A., Maurin I., Gorceix O., Ballin P., Ducloy M., Bloch D., *Temperature dependence of vdW forces between an atom and a dispersive surface*, Laser-Physics-2010, Ashtarak, Arménie, (2010).
8. Bloch D., Ballin P., Maurin I., Laliotis A., Gorza M-P., Ducloy M., *Atomic spectroscopy and nano-optics*, France-Japan workhop on nanophotonics, Villetaneuse-France, (4-5 nov 2010).
9. Ballin P., Maurin I., Laliotis A., Moufarej E., Gorza M-P., Ducloy M., Bloch D., *Laser spectroscopy of atoms with a sub-wavelength confinement*, 2nd France Japan workshop on Nanophotonics, Toba, Japon, (7-9 Novembre 2011).
10. Ballin P., Moufarej E., Maurin I., Laliotis A., Bloch D., *Sub-Doppler optical resolution by confining a vapour in a nanostructure*, XVII IQSE (seventeenth international school on quantum electronics : laser physics and applications) Nessebar, Bulgarie, (24-28 septembre 2012).
11. Bloch D., Maurin I., Laliotis A., Ballin P., Moufarej E., *Transitions optiques dans des vapeurs confinées de façon mésoscopique*, J₃N Journée nationale nanosciences et nanotechnologies, Bordeaux, France, (2012).
12. Laliotis A., Passerat De Silans T., Maurin I., Gorza M.-P., Ducloy M., Bloch D., *Experimental observations of temperature effects in the near-field regime of the Casimir Polder interaction*, MPLP' 2013 6th International Symposium on Modern Problem of Laser Physics, Novosibirsk, Russie, (2013).
13. Laliotis A., Maurin I., Moufarej E., Ducloy M., Bloch D., *Optical probing of atoms with a sub-wavelength confinement*, QMAP 2013 , 3rd workshop of the Sino-French Research Network on Quantum Manipulation of Atoms and Photons (GDRI QMAP), Palaiseau, France, (2013).
14. Laliotis A., Passerat De Silans T., Maurin I., Ducloy M., Bloch D., *Casimir-Polder in the Near-Field van der Waals regime Experimental Observation of Temperature effects for Cs*/sapphire*, Casimir Physics, Les Houches, France, (2014).
15. Maurin I., Moufarej E., Ballin P., Laliotis A., Bloch D., *Infiltrating an artificial opal with an atomic vapour : observation of sub-Doppler signals in linear spectroscopy*, META14 (5th International Conference on Metamaterials, Photonic Crystals and Plasmonics), Singapour, Singapour, (2014).
16. Laliotis A., Passerat De Silans T., Maurin I., Ducloy M., Bloch D., *Casimir-Polder forces in the presence of thermally excited surface modes*, PSAS 14 (International Conference on Precision Physics of Simple Atomic Systems), Rio de Janeiro, Brésil, (2014).
17. Bloch D., Klimov V.V., Ducloy M., Chaves de Souza Segundo P., Tojo S., Leite J.R.R., *Cartographier un faisceau focalisé au delà de l'approximation paraxiale*

avec des transitions quasi-interdites : transfert du moment orbital, superchiralité, Mini-colloque "Laguerre-Gauss" dans le cadre de PAMO-JSM 2014 (colloque commun de la division PAMO "Physique Atomique, Moléculaire et Optique" de la SFP-Société Française de Physique et des JSM "Journées de Spectroscopie Moléculaire"), Reims, France, (2014).

18. Bloch D., Leite J.R.R., Klimov V.V., Ducloy M., Tabosa J.W.R., Pruvost L., Chaves De Souza Segundo P., *Transferring OAM to atomic states through forbidden transitions or also from beam to beam*, Journée thématique "Physique et applications du Moment Angulaire Orbital (OAM) d'une onde électromagnétique en radio et en optique", Rennes, France, (2014).
19. Laliotis A., Passerat De Silans T., de Aquino Carvalho J.C., Chaves de Souza Segundo P., Maurin I., Leite J.R.R., Ducloy M., Bloch D., *Effets de la température sur l'interaction Casimir-Polder en champ proche*, COLOQ / Optique-Bretagne 2015, Rennes, France, (2015).
20. Laliotis A., de Aquino Carvalho J.C., Passerat De Silans T., Chaves de Souza Segundo P., Maurin I., Ducloy M., Bloch D., *Atom in front of a hot surface : Thermal dependence of the Casimir-Polder interaction*, EGAS 47 (47 th European Group for Atomic Spectroscopy), Riga, Lettonie, (2015).
21. Laliotis A., de Aquino Carvalho J.C., Maurin I., Ducloy M., Bloch D., *Spectroscopic Measurements of the Casimir-Polder Interaction with Atoms and Molecules, Casimir and Van der Waals physics : Progress and Prospects*, Hong Kong, Chine, (2016).

Communications sans actes

1. Maurin I., Hermier J.-P., Bramati A., A. Z. Khoury , V. Josse, Giacobino E., J. P. Poizat, P. Grangier, *Quantum noise in semi-conductor lasers*, colloque du réseau européen TMR Network Microlasers and cavity QED, Ulm, Allemagne, **Présentation orale**, (1999).
2. Maurin I., Hermier J.-P., Bramati A., A. Z. Khoury , V. Josse, Giacobino E., J. P. Poizat, and P. Grangier, *Quantum noise in semi-conductor lasers*, colloque du réseau VISTA, Bruxelles, Belgique, **Présentation orale**, (2000).
3. Maurin I., Hermier J.-P., Bramati A., Giacobino E., *Pump-blocking and intensity noise in semiconductor lasers*, International Quantum Electronics Conference, Nice, France, **Présentation orale** (2000).
4. Maurin I., Hermier J.-P., Bramati A., Giacobino E., Ebeling K. J., Schnitzer P., *Intensity noise correlations in vertical-cavity surface-emitting lasers*, International Quantum Electronics Conference, Nice, France, **Présentation orale** (2000).
5. Maurin I., Hermier J.-P., Khoury A. Z., Bramati A., Giacobino E., *Quantum Spin Flip Model for vertical-cavity surface-emitting lasers*, International Quantum Electronics Conference, Nice, France, **poster** (2000).
6. Maurin I., Hermier J.-P., A. Z. Khoury, S. Ducci, and E. Giacobino, *Quantum spatial intensity noise structure for Vertical-Cavity Surface-Emitting Lasers*, Quantum Optics, san Feliu de Guixols, Espagne, **poster**, (2001).

7. Maurin I., Hermier J.-P., Bramati A., Kolobov M., Khoury A. Z., S. Ducci et Giacobino E., *Etude du bruit quantique dans les microlasers à semi-conducteurs à cavité verticale (VCSELS)*, COLOQ 7, Rennes, France, **poster**, (2001).
8. Maurin I., Hermier J.-P., A. Z. Khoury , S. Ducci, M. kolobov, A. Bramati, and Giacobino E, *Quantum noise in VCSELS*, colloque du réseau VISTA, Paris, **Présentation orale**, (2001).
9. Maurin I., Hermier J.-P, Bramati A., Protsenko I., Grangier P., and E. Giacobino, *Excess noise due to the leakage current and light-voltage correin semi-conductor lasers*, colloque du réseau VISTA, Come, Italie, **Présentation orale**, (2002).
10. Romanelli M., Maurin I., Hermier J.-P., Khoury A. Z., Bramati A., and Giacobino E., *Spatial distribution of intensity noise in vertical-cavity surface-emitting lasers* , CLEO/Europe-EQEC Conference, Munich, Allemagne, **présentation orale**, (2003).
11. Maurin I., Sirtori C., Page H., *Two colors quantum cascade lasers*, colloque du réseau européen WANTED (2003), Orsay, France, **presentation orale** (2003).
12. Maurin I., Sirtori C., Page H., Dhillon S., Bengloan J.Y., calligaro M., Ortiz V., Marcedet X., *Etude des propriétés optiques linéaires et non linéaires des lasers à cascades quantiques - Génération d'ondes TéraHertz*, Journées du pôle MPQ, Agen, France, **presentation orale** (2003).
13. Maurin I., Bengloan J-Y., Calligaro M., Ortiz V., Marcedet X., Sirtori C., *Second harmonic generation in quantum cascade lasers grown on <111> GaAs substrate*, Cleo Conferences, Baltimore, USA, **presentation orale** (2003).
14. Maurin I., Bengloan J-Y., Calligaro M., Ortiz V., Marcedet X., Sirtori C., *Second harmonic generation in quantum cascade lasers grown on <111> GaAs substrate*, ITQW, Evolène, Suisse, **presentation orale** (2003).
15. Marcedet X., Ortiz V., Bengloan J-Y., Calligaro M., Maurin I., Sirtori C., *Second harmonic generation in quantum cascade lasers grown on <111> GaAs substrate*, Novel Index surfaces, Stuttgart, Allemagne, **presentation orale** (2003).
16. Marcedet X., Ortiz V., Bengloan J-Y., Calligaro M., Maurin I., Sirtori C., *Second harmonic generation in quantum cascade lasers grown on <111> GaAs substrate*, NAMBE 2003, Colorado, USA, **poster** (2003).
17. Todorov P., Hamdi I., Maurin I., Yarovitski A., Sarkisyan D., Gorza M.-P., Fichet M., Bloch D., Ducloy M., *Nanocell : a tool for the spectroscopy of a confined vapour*, CAMS, Conference on Atoms and Molecules near Surfaces, Heidelberg, Allemagne, **presentation orale** (2005).
18. Maurin I., Hamdi I., Todorov P., Yarovitski A., Dutier G., Saltiel S., Gorza M.-P., Fichet M., Bloch D., Ducloy M., *Analysing the atom-surface interaction through nanocell spectroscopy*, CAMS, Conference on Atoms and Molecules near Surfaces, Heidelberg, Allemagne, **presentation orale** (2005).
19. Hamdi I., Todorov P., Maurin I., Yarovitski A., Sarkisyan D., Gorza M.-P., Fichet M., Bloch D., Ducloy M., *Probing collision effects in the confined environment*

- of a nanocell*, 2005 EQEC European Quantum Electronics Conference, Munich, Allemagne, **presentation orale** (2005).
20. Maurin I., Lezama A., Bloch D., Ducloy M., *Nanocell spectroscopy interpreted in the frame of the Bloch vector model*, 2005EQEC, European Quantum Electronics Conference, Munich, Allemagne, **poster** (2005).
 21. Hamdi I., Todorov P., Maurin I., Yarovitski A., Dutier G., Saltiel S., Gorza M.-P., Fichet M., Bloch D., Ducloy M., *Analysing the atom-surface interaction through nanocell spectroscopy*, 2005EQEC, European Quantum Electronics Conference, Munich, Allemagne, **presentation orale** (2005).
 22. Maurin I., Todorov P., Hamdi I., Yarovitski A., Dutier G., Saltiel S., Gorza M.-P., Fichet M., Bloch D., Ducloy M., *Mesure à faible distance de l'interaction de van der Waals atome surface dans une cellule nanométrique de vapeur de Césium*, COLOQ9, 9^{me} Colloque National sur les Lasers et l'Optique Quantique, Dijon, France, **poster**(2005).
 23. Todorov P., Hamdi I., Maurin I., Dutier G., Yarovitski A., Sarkisyan D., Saltiel S., Gorza M.-P., Fichet M., Bloch D., Ducloy M., *Collisional effects in ultrathin Cs vapour cell*, IV international symposium on Laser Technologies and Lasers (LTL-Plovdiv'2005), Plovdiv, Bulgarie, **presentation orale** (2005).
 24. Fichet M., Maurin I., Laliotis A., Dutier G., Yarovitski A., Todorov P., Hamdi I., Saltiel S., Sarkisyan D., Gorza M.-P., Bloch D., Ducloy M., *Des vapeurs confinées à l'échelle nanométrique pour étudier la dépendance en distance de l'interaction van der Waals de surface*, Journée nanophotonique et Information quantique du C'nano-Ile de France, Marcoussis, France, **poster**(2006).
 25. Maurin I., Todorov P., Hamdi I., Laliotis A., Yarovitski A., Dutier G., Saltiel S., Gorza M.-P., Fichet M., Bloch D., Ducloy M., *Measuring the atom-surface van der Waals interaction in a vapour nanocell*, 34th EGAS (conference of the European group on Atomic Systems, Ischia, Italie, **poster** (2006).
 26. Laliotis A., Maurin I., Todorov P., Hamdi I., Dutier G., Saltiel S., Yarovitski A., Gorza M.-P., Fichet M., Bloch D., Ducloy M., *Measuring the atom-surface van der Waals interaction in the nanometric range*, XX ICAP, 20th International Conference on Atomic Physics, Innsbruck, Autriche, **poster** (2006).
 27. Todorov P., Hamdi I., Maurin I., Dutier G., Yarovitski A., Sarkisyan D., Gorza M.-P., Fichet M., Saltiel S., Bloch D., Ducloy M., *Spectroscopy in absorption and reflection with extremely thin cells considering Van der Waals interaction*, Romopto, International Conference on micro-to nano-photonics, Sibiu, Roumanie, **poster** (2006).
 28. Todorov P., Hamdi I., Dutier G., Maurin I., Saltiel S., Bloch D., Ducloy M., *Dicke coherent narrowing in two-photon spectroscopy of thin vapour cells*, XIV international School on Quantum Electronics and Lasers Physics, Sunny Beach, Bulgarie, **poster** (2006).
 29. Laliotis A., Maurin I., Hamdi I., Dutier G., Gorza M.-P., Fichet M., Bloch D., Ducloy M., *Measuring the atom-surface van der Waals interaction in the na-*

- nometric range*, CAMS-jobs FASTNet meeting, Danemark, **présentation orale** (2006).
30. Passerat De Silans T., Romanelli M., Segundo P., Laliotis A., Maurin I., Gorza M.-P., Bloch D., Ducloy M., *Spectroscopie laser de vapeur atomique au voisinage d'interfaces*, JSI2007 21^{me} Journées Surfaces Interfaces, Paris, France, **poster** (2007).
 31. Laliotis A., Passerat De Silans T., Segundo P., Romanelli M., Maurin I., Fichet M., Saltiel S., Todorov P., Hamdi I., Dutier G., Yarovitski A., Sarkisyan D., Gorza M.-P., Bloch D., Ducloy M., *Van der Waals atom-surface interaction in the short distance range*, FRISNO 9, 9th French-Israelian Symposium on Nonlinear optics, Les Houches, France, **poster**, (Fév. 2007).
 32. Laliotis A., Maurin I., Todorov P., Hamdi I., Dutier G., Saltiel S., Gorza M.-P., Fichet M., Bloch D., Ducloy M., *Atom Surface van der Waals interaction in the nanometric range*, ECAMP IX, 9th European Conference on Atomic and Molecular Physics, Harklion, Grèce, **poster**, (Mai 2007).
 33. Passerat De Silans T., Romanelli M., Segundo P., Laliotis A., Maurin I., Gorza M.-P., Bloch D., Ducloy M., *Laser spectroscopy of a vapour near an interface*, TRN'07 Thermal radiation at the nanoscale, Les Houches, France, **poster**, (Mai 2007).
 34. Laliotis A., Maurin I., Todorov P., Hamdi I., Dutier G., Saltiel S., Gorza M.-P., Fichet M., Bloch D., Ducloy M., *Atom-surface van der Waals interaction in the nanometric range*, IQEC CLEO'Europe International Quantum Electronics Conference, Munich, Allemagne, **présentation orale** (Juin 2007).
 35. Romanelli M., Maurin I., Todorov P., Chan C.-H., Bloch D., *Un film bidimensionnel de nanosphères pour la spectroscopie atomique*, COLOQ10, 10^e Colloque National sur les Lasers et l'Optique Quantique, Grenoble, France, **poster**, (Juil. 2007).
 36. Laliotis A., Maurin I., Todorov P., Hamdi I., Dutier G., Saltiel S., Gorceix O., Fichet M., Bloch D., Ducloy M., *Une évaluation de l'interaction van der Waals entre atome et surface résolue spatialement dans le domaine nanométrique*, COLOQ10, 10^e Colloque National sur les Lasers et l'Optique Quantique, Grenoble, France, **poster**, (Juil. 2007).
 37. Passerat De Silans T., Laliotis A., Romanelli M., Segundo P., Maurin I., Bloch D., Ducloy M., Sarkisyan D., *Spectroscopie de réflexion sélective d'une vapeur à une interface d'une fenêtre en fluorure de calcium*, COLOQ10, 10^e Colloque National sur les Lasers et l'Optique Quantique, Grenoble, France, **poster**, (Juil. 2007).
 38. Todorov P., Maurin I., Cartaleva S., Kaseva V., Andreeva C., Slavov D., Saltiel S., Bloch D., *Absorption spectra study of Cs-vapour layer with thickness close to the wavelength of the irradiating light*, Meeting in Physics at University of Sofia, Sofia, Bulgarie, **présentation orale** (Fév. 2008)
 39. Maurin I., Laliotis A., Passerat De Silans T., Dutier G., Gorza M.-P., Bloch D., Ducloy M., Sarkisyan D., *Vapour spectroscopy close to an interface : confined*

- optical frequency references*, Russian French Young Scientist symposium), Saint Petersburg : Russie, **présentation orale** (Septembre 2008).
40. Passerat de Silans T., Maurin I., Chaves de Souza Segundo P., Saltiel S., Gorza, M.-P., Bloch D., Ducloy M., de Sousa Meneses D., Echegut P., *Towards selective heat transfer between a hot surface and an atom*, EOS 2008 Annual meeting of the European Optical Society, Villepinte France 29 Sept 2008, **présentation orale** (2 Oct 2008).
 41. Passerat De Silans T., Maurin I., Ballin P., Lalotis A., De Souza Segundo P.C., Saltiel S., Bloch D., Ducloy M., De Sousa Meneses D., Echegut P., *Towards selective heat transfer between a hot surface and an atom*, FRISNO 10 (10th French Israelian Symposium on Nonlinear Optics), Ein Gedi, Israël, **présentation orale**, (Fév. 2009).
 42. Passerat De Silans T., Maurin I., Lalotis A., Bloch D., *Sub-Doppler extra-lines in the vicinity of the 388 nm line of Cs : a signature for dimer photoassociation in a thermal vapour ?*, EQEC09 (European Quantum Electronics Conference), Munich, Allemagne, **poster**, (Juin 2009).
 43. Passerat De Silans T., Maurin I., Lalotis A., Ballin P., De Souza Segundo P.C., Saltiel S., Gorza M.P., Ducloy M., Bloch D., De Sousa Meneses D., Echegut P., *Temperature-dependent van der Waals atom-surface interaction*, EQEC09 (European Quantum Electronics Conference), Munich, Allemagne, **présentation orale**, (Juin 2009).
 44. Passerat De Silans T., Maurin I., Lalotis A., Bloch D., *Résonances sub-Doppler supplémentaires autour des transitions d'absorption saturée de Cs à 388 nm : des dimères photo-associés en vapeur thermique ?*, COLOQ11, 11^e Colloque National sur les Lasers et l'Optique Quantique, Nice Mouans Sartoux, France, **poster**, (Sep. 2009).
 45. Passerat De Silans T., Maurin I., Lalotis A., Ballin P., De Souza Segundo P.C., Saltiel S., Gorza M.-P., Ducloy M., Bloch D., De Sousa Meneses D., Echegut P., *Dépendance en température de l'interaction de van der Waals entre atome et surface* COLOQ11, 11^e Colloque National sur les Lasers et l'Optique Quantique, Nice-Mouans-Sartoux, France, **poster**, (Sep. 2009).
 46. Maurin I., Ballin P., Lalotis A., Gorza M.-P., Bloch D., *Recherche d'une signature de spectroscopie atomique dans des opales de nanobilles de silice*, COLOQ11, 11^e Colloque National sur les Lasers et l'Optique Quantique, Nice-Mouans-Sartoux, France, **poster**, (Sep. 2009).
 47. Passerat De Silans T., Maurin I., Gorza M.-P., Lalotis A., De Souza Segundo P.C., Bloch D., Ducloy M., Saltiel S., De Sousa Meneses D., Echegut P., *Interacao de van der Waals entre um atomo excitado e uma superfcie dieletrica a temperatura termicamente emissiva*, EFNNE, XXVII Encontro de Fisicos Norte e Nordeste, Belem, Brésil, **présentation orale**, (Nov. 2009).
 48. Passerat De Silans T., Maurin I., Gorza M.-P., De Souza Segundo P.C., Lalotis A., Bloch D., Ducloy M., *Observacao de ressonancias adicionais em torno da*

- transicao 6S-8P do Cs. Criacao de Cs₂ induzidos por fotons em vapor quente*, EFNNE, XXVII Encontro de Fisicos Norte e Nordeste, Belem, Brésil, **poster**, (Nov. 2009).
49. Ballin P., Maurin I., Laliotis A., Gorza M.-P. et Bloch D., *Atomic spectroscopy in an opal of glass nanospheres*, Young scientists meeting in nanophotonics, Paris : France, **poster**, (Septembre 2010)
50. Ballin P., Maurin I., Laliotis A., Failache H. et Bloch D., *Spectroscopie à haute résolution avec une vapeur atomique confinée dans une opale de nanobilles en verre*, JNOG 2010, Journées Nationales de l'Optique Guidée, Besançon, **poster** (octobre 2010).
51. Maurin I., Ballin P., Laliotis A., Bloch D., *High resolution spectroscopy of an atomic vapour confined in an opal of glass nanosphere*, EOS 2010 Annual meeting of the European Optical Society, Paris, poster (octobre 2010).
52. Laliotis A., Maurin I., Gorza M.-P., Ballin P., Ducloy M., Bloch D., *Temperature dependence of vdW forces between an atom and a dispersive surface*, Laser-Physics-2010, Ashtarak : Arménie, **présentation orale** (octobre 2010).
53. Passerat De Silans T., Laliotis A., Maurin I., Gorza M.-P., Ballin P., Ducloy M., Bloch D., *Temperature dependence of van der Waals forces between an atom and a dispersive surface*, 2nd International Workshop on Fundamentals of Light-Matter Interaction, February 13-16, **poster**, Porto de Galinhas/PE, Brazil (2011).
54. Laliotis A., Passerat De Silans T., Gorza M.-P., Maurin I., Ballin P., Ducloy M., Bloch D., *Observing a temperature dependence in fundamental atom-surface interaction*, Journées C'Nano Ile-de-France, Paris, poster (24-25 mars2011).
55. Maurin I., Ballin P., Laliotis A., Bloch D., *Vapour confined in an opal of nanospheres : observation of sub-Doppler optical resonances reminiscent of the Dicke narrowing*, Journées C'Nano Ile-de-France, Paris, **poster**, (24-25 mars2011).
56. Ballin P., Maurin I., Laliotis A., Bloch D., *Vapour confined in an opal of nanospheres : observation of sub-Doppler optical resonances reminiscent of the Dicke narrowing*, EQEC2011 (European Conference on Quantum Electronics, Munich, Allemagne, **poster** (22-26 mai 2011).
57. Laliotis A., Passerat De Silans T., Gorza M.-P., Maurin I., Ballin P., Ducloy M., Bloch D., *First observation of the temperature dependence of the van der Waals Casimir-Polder interaction in the condition of thermal equilibrium*, EQEC2011 (European Conference on Quantum Electronics, Munich, Allemagne, **présentation orale** (22-26 mai 2011).
58. Ballin P., Maurin I., Laliotis A., Bloch D., *Sub-Doppler spectroscopy with a vapour confined in an opal*, ICOLS 2011 (International Conference on Laser Spectroscopy, Hameln, Allemagne, **poster** (29 mai-3 juin 2011).
59. Laliotis A., Passerat De Silans T., Gorza M.-P., Maurin I., Ballin P., Ducloy M., Bloch D., *Observing the temperature dependence of the atom-surface interaction in the van der Waals Casimir-Polder regime*, ICOLS 2011 (International Conference on Laser Spectroscopy, Hameln, Allemagne, **poster** (29 mai-3 juin 2011).

60. Passerat De Silans T., Lalot A., Gorza M.-P., Maurin I., Ballin P., Ducloy M., Bloch D., *First observation of the temperature dependence of the van der Waals Casimir-Polder interaction in the condition of thermal equilibrium*, Encontro de Física 2011, Foz do Iguaçu, Brésil, **poster** (5-10 Juin 2011).
61. Ballin P., Maurin I., Lalot A., Moufaret E., Bloch D., *Vapeur confinée dans une opale de nanobilles de silice : observation d'un rétrécissement spectral de type Dicke*, COLOQ12-Optique 2011 (Douzième Colloque National sur les Lasers et l'Optique Quantique, Marseille, **poster** (4-7 juillet 2011).
62. Lalot A., Passerat De Silans T., Maurin I., Gorza M.-P., Ballin P., Ducloy M., Bloch D., *Effets de température sur l'interaction Casimir-Polder : observation en champ proche et à l'équilibre thermique*, COLOQ12-Optique 2011 (Douzième Colloque National sur les Lasers et l'Optique Quantique, Marseille, **poster** (4-7 juillet 2011).
63. Lalot A., Passerat De Silans T., Gorza M.-P., Maurin I., Ducloy M., Bloch D., *Thermal effects in the Casimir-Polder interaction*, ICAP 2012 (23rd International Conference on Atomic Physics), Palaiseau, France, **poster** (23-27 juillet 2012).
64. Ballin P., Moufaret E., Maurin I., Lalot A., Bloch D., *Confining a vapour in a nanostructure yields a sub-Doppler resolution in linear spectroscopy*, ICAP 2012 (23rd International Conference on Atomic Physics), Palaiseau, France, **poster** (23-27 juillet 2012).
65. Todorov P., Petrov N., Slavov D., Maurin I., Saltiel S., Bloch D., *Detection of slow atoms confined in a cesium vapor cell by spatially separated pump and probe laser beams*, XVII IQSE (seventeenth international school on quantum electronics : laser physics and applications) Nessebar, Bulgarie, **poster** (24-28 septembre 2012).
66. Lalot A., Passerat De Silans T., Maurin I., Gorza M.-P., Ducloy M., Bloch D., *Temperature dependence of the atom-surface interaction in thermal equilibrium*, IQEC, International Quantum Electronics Conference, Munich, Allemagne, **presentation orale** (2013).
67. Lalot A., Passerat De Silans T., Gorza M.-P., Maurin I., Ducloy M., Bloch D., *Atoms feel the near field of thermal radiation*, International Conference on Laser Spectroscopy, Berkely, CA, États-Unis, **presentation orale** (2013).
68. Moufaret E., Ballin P., Zabkov I., Maurin I., Lalot A., Bloch D., *Confining a vapour in nanostructures for sub-Doppler linear spectroscopy*, International Conference on Laser Spectroscopy, Berkely, CA, États-Unis, **poster** (2013).
69. Lalot A., Passerat De Silans T., Maurin I., Gorza M.-P., Ducloy M., Bloch D., *Dépendance en température de l'interaction longue distance atome-surface dans les conditions de l'équilibre thermique*, Optique Paris 2013 / Coloq13, Villetaneuse, France, **poster** (2013).
70. Moufaret E., Ballin P., Zabkov I., Maurin I., Lalot A., Bloch D., *Spectroscopie sub-Doppler d'une vapeur confinée en opale*, Optique Paris 2013 / Coloq13, Villetaneuse, France, **poster** (2013).

71. Laliotis A., Passerat De Silans T., Maurin I., Ducloy M., Bloch D., *Probing near field thermal emission with atoms*, EGAS 46 (46th Conference of European Group on atomic Spectroscopy), Lille, France, **poster** (2014).
72. Moufarej E., Ballin P., Maurin I., Laliotis A., Bloch D., *Sub-Doppler linear spectroscopy in a vapour confined in an opal*, EGAS 46 (46th Conference of the European Group for atomic Spectroscopy), Lille, France, **présentation orale** (2014).
73. Maurin I., Moufarej E., Laliotis A., Bloch D., *A 1D stratified model applied to the reflection spectra of an opal as a prototype of a photonic crystal and extension to a resonant infiltration*, EOSAM 2014 (European Optical Society, Annual meeting), Berlin, Germany, **présentation orale** (2014).
74. Moufarej E., Ballin P., Laliotis A., Maurin I., Bloch D., Villalba S., Lenci L., Barreiro S., Lezama A., Failache H., *Sub-Doppler Spectroscopy in a confined vapour : towards three-dimensional confinement*, QuantArm 2014 International Conference and Workshop, Tsaghkadzor, Arménie, **poster** (2014).
75. Laliotis A., Passerat De Silans T., Maurin I., Ducloy M., Bloch D., *Casimir-Polder in the Near-Field van der Waals regime : Experimental Observation of Temperature effects for Cs*/sapphire*, QuantArm 2014 International Conference and Workshop, Tsaghkadzor, Arménie, **présentation orale** (2014).
76. Laliotis A., Passerat De Silans T., Maurin I., de Aquino Carvalho J.C., Chaves De Souza Segundo P., Ducloy M., Bloch D., *Casimir-Polder effect in the presence of thermally excited surface polaritons*, Second Brazil-France NanoSECQO, Paris, France, **poster** (2015).
77. Moufarej E., Ballin P., Maurin I., Laliotis A., Bloch D., *Sub-Doppler linear spectroscopy in an opal infiltrated with a resonant vapour*, FRISNO 13 (13th French Israelian Symposium on Nonlinear Optics), Aussois, France, **poster** (2015).
78. Laliotis A., de Aquino Carvalho J.C., Maurin I., Passerat De Silans T., Chaves de Souza Segundo P., Ducloy M., Bloch D., *Atom as a quantum probe of near field thermal emission of a hot surface*, FRISNO 13 (13th French Israelian Symposium on Nonlinear Optics), Aussois, France, **présentation orale** (2015).
79. De Aquino Carvalho J.C., Chaves de Souza Segundo P., Laliotis A., Maurin I., Oria M., Chevrollier M., Ducloy M., Bloch D., *Casimir-Polder interaction as a highly-selective probe of the near-field thermal emission*, CLEO'Europe -EQEC, Munich, Allemagne, **présentation orale** (2015).
80. Moufarej E., Maurin I., Bloch D., Laliotis A., Villalba S., Lenci L., Lezama A., Failache H., *Spectroscopie d'atomes confinés dans des opales artificielles et dans des milieux poreux*, COLOQ / Optique-Bretagne 2015, Rennes, France, **poster** (2015).
81. Maurin I., Zabkov I., Moufarej E., Laliotis A., Klimov V.V., Bloch D., *Modélisation de la réflexion d'une opale ou d'une monocouche de billes et extension à une infiltration résonnante*, COLOQ / Optique-Bretagne 2015, Rennes, France, **poster** (2015).

82. De Aquino Carvalho J.C., Chaves de Souza Segundo P., Laliotis A., Maurin I., Oria M., Chevrollier M., Ducloy M., Bloch D., *L'interaction Casimir-Polder : une sonde tres selective de l'émission thermique en champ proche*, COLOQ / Optique-Bretagne 2015, Rennes, France, **poster** (2015).
83. Laliotis A., De Aquino Carvalho J. C., Chaves de Souza Segundo P., Passerat De Silans T., Maurin I., Ducloy M., Bloch D., Tokunaga S., Darquié B., *Spectroscopic measurements of the Casimir-Polder interaction with atoms or molecules*, International Workshop on Quantum Manipulation of Atoms and Photons,Shangai, Chine, **oral** (2015).
84. de Aquino Carvalho J.C. , Laliotis A., Chaves de Souza Segundo P., Maurin I., Ducloy M. , Bloch D., *Vers une observation de l'absorption par un atome de l'émission thermique en champ proche*, COLOQ, Optique Bordeaux 2016, Bordeaux, France, **poster** (2016).

Chapitre

1

Parcours Personnel

Ce mémoire présente les travaux que j'ai réalisés depuis l'obtention de ma thèse "Étude du bruit quantique dans les lasers à semi-conducteurs (VCSELS et diodes laser)" en Juillet 2002 au Laboratoire de Physique des Lasers sous la direction d'Élisabeth Giacobino.

Suite à ma thèse, j'ai effectué un an (sept. 2002- sept. 2003) de poste de demi-ATER (Paris 7) au Laboratoire Matériaux et Phénomènes Quantiques à Thales Research and Technology sous la direction de Carlo Sirtori sur l'Étude des propriétés optiques linéaires et non linéaires des lasers à cascade quantique. Les connaissances acquises sur les lasers pendant ma thèse m'ont aidé à participer à la réalisation d'une source laser à cascade quantique bicolore (Conception de la structure par simulation, optimisation et caractérisation après sa fabrication). Nous nous sommes ensuite intéressés au mélange de fréquences dans un tel composant. J'ai fait de la simulation, participé à la conception d'un laser à cascade quantique dans lequel on peut faire de la somme de fréquences. Un tel laser compact a été élaboré. J'ai mis en évidence expérimentalement la génération du second harmonique. Ce travail est présenté dans le chapitre 2.

De décembre 2003 à août 2004, j'ai effectué un stage post-doctoral au Laboratoire de Photonique et de Nanostructures du CNRS sous la direction d'Izo Abram sur l'Étude d'un nanolaser quantique unique en microcavité. J'ai tout d'abord travaillé à déterminer les paramètres optimaux nécessaires pour réaliser des nanolasers sans inversion de population à boîtes quantiques. J'ai conclu que malheureusement les technologies de l'époque ne nous permettaient pas de produire un tel laser. Mon post-doctorat a alors changé de direction et s'est orienté vers la réalisation de nanosources à faible densité de boîtes quantiques en cavité donnant lieu à une oscillation laser, le dispositif ultime couplant une seule boîte au mode laser. Après une étude fouillée, nous avons décidé de réaliser des cavités H_1 dans un cristal photonique sur membrane ou sur oxyde de facteur de qualité de l'ordre de 4000. J'ai commencé à modéliser et optimiser ces structures. En juin 2004, j'ai obtenu un poste de maître de conférences au Laboratoire de Physique des lasers (Univesité Paris 13), ce travail a alors été interrompu. Ce travail

est présenté dans le chapitre 3.

Depuis septembre 2004, je suis maître de conférences au Laboratoire de Physique des lasers dans le groupe Spectroscopie Atomiques aux Interfaces (SAI) et j'enseigne à l'IUT de Saint-Denis au département Mesures Physiques :

L'attraction de surface van der Waals exercée sur un atome est censée varier suivant l'inverse du cube de la distance de l'atome à la surface, pour un domaine de distance qui s'étend typiquement de 1 à 1000 nm. Quoique cette loi attractive couvre une dizaine d'ordres de grandeurs en énergie, rares ont été les expériences qui ont testées effectivement la dépendance prédite. De 2004 à 2006, nous avons développé une série d'expériences analysant l'interaction de van der Waals en fonction de la distance atome - surface et avons vérifié cette loi jusqu'à une distance de 15 nm. Ces mesures ont été réalisées par spectroscopie dans une nanocellule (confinement 1D). Une vapeur d'atomes de césium était contenue dans une cellule d'épaisseur variant localement de 40 nm à 130 nm. Ce travail est détaillé dans le chapitre 4.

Depuis 2006, l'équipe travaille sur les effets en température de l'interaction van der Waals (également appelée Casimir– Polder en champ proche). J'ai participé au développement des différences expériences et tests permettant l'étude de cette interaction dans le cas d'une surface chauffée, donc émissive, plus ou moins en résonance avec les transitions atomiques du césium. Nous avons mesuré la dépendance en température de l'interaction atome-surface par des mesures spectroscopiques, lorsque l'équilibre thermique est assuré entre la surface et le vide environnant l'atome. C'est essentiellement le couplage avec les résonances de surface, thermiquement émissive, qui explique que l'interaction atome-surface augmente ou diminue avec la température, tandis que l'atome absorbe sélectivement l'énergie thermique. L'atome est en quelque sorte une sonde quantique du champ proche émis par la surface chauffée. Nos expériences ont aussi permis de vérifier les prédictions de l'électrodynamique quantique (QED), pour des températures aussi élevées que 1000 K. Ce travail a ouvert de nouvelles perspectives pour le contrôle thermique de l'interaction van der Waals et est présenté dans le chapitre 5.

Depuis 2006, l'équipe a également développé un nouvel axe de recherche sur l'étude spectroscopique d'une vapeur de césium avec un confinement tridimensionnel. Nous sommes partis d'une idée qui remonte à Dicke [13, 14] où l'élargissement Doppler avait été éliminé grâce à un confinement à des dimensions plus petites que la longueur d'onde des atomes (domaine des radiofréquences). Nous nous sommes inspirés de cette idée et avons eu l'idée de faire des mesures spectroscopiques avec des atomes confinés dans les interstices d'une opale (confinement 3D, domaine optique). En étudiant le spectre de réflexion, nous avons observé des signaux sub-Doppler pour une large plage d'angles d'incidence. Le résultat surprenant est que des résonances sub-Doppler ont également été observées pour des opales monocouches. Pour mieux comprendre comment la lumière se propage à l'intérieur d'une opale, nous avons modélisé l'opale seule par un

calcul numérique complet quand elle ne se compose que d'une ou deux couches et par un modèle multicouches de l'indice effectif dès qu'elle se compose de plus de couches. Ces modèles sont en bon accord avec nos expériences. Le modèle multicouches de l'indice effectif a été étendu au cas d'une opale infiltrée par un milieu résonant dilué et a permis de conclure que le signal sub-Doppler provenait bien du confinement tridimensionnel dans le cas d'opale pas trop fines. L'interprétation du signal sub-Doppler dans le cas de peu de couches est plus compliquée. Le signal réfléchi est un mélange entre le signal venant des atomes infiltrés dans l'opale et ceux situés au-dessus de l'opale (la transmission n'est plus nulle quand l'opale devient peu épaisse). Une exploration plus systématique et une autre modélisation sera nécessaire pour l'interpréter. Ce travail est présenté dans le chapitre 6.

Dans le chapitre 7, les travaux en cours et les perspectives de recherche de l'équipe sont présentées.

Chapitre 2

Étude des propriétés optiques linéaires et non linéaires des lasers à cascade quantique

De septembre 2002 à septembre 2003, j'ai effectué un poste de demi-ATER (Paris 7) au Laboratoire Matériaux et Phénomènes Quantiques à Thales Research and Technology dans le groupe de Carlo Sirtori. Je vais dans ce chapitre vous présenter les résultats de mes recherches.

2.1 Introduction

En télécommunications, l'information est transmise par la modulation de l'amplitude ou de la fréquence d'ondes électromagnétiques. Les dispositifs à lasers à semi-conducteurs sont des outils indispensables à la création de telles ondes. Mais presque aucune technique n'avait été développée pour générer des ondes ayant des fréquences de l'ordre du TéraHertz (1-10 THz) en 2002 quand j'ai commencé mon ATER. En effet, le développement de telles sources dans les semi-conducteurs est difficile. Cela est dû au manque de milieux à gains suffisamment forts pour compenser les pertes optiques toujours importantes à des fréquences de l'ordre du TéraHertz. En 1994, un nouveau concept de source compacte et modulable pour générer de telles fréquences, le laser à cascade quantique en GaInAs-AlInAs, a été inventé au Laboratoire Bell [15]. Carlo Sirtori est l'un des inventeurs du laser à cascade quantique.

Dans les lasers à semi-conducteurs, la lumière est générée par la recombinaison radiative des électrons de la bande de conduction avec les trous de la bande de valence autour de la bande interdite du milieu actif. La largeur de la bande interdite, dont la valeur dépend des matériaux constituant le laser, détermine la fréquence de l'onde lumineuse émise. Pour obtenir une onde de fréquence de l'ordre du TéraHertz, il faudrait un matériau ayant une très faible largeur de bande interdite, or il n'en existe aucun.

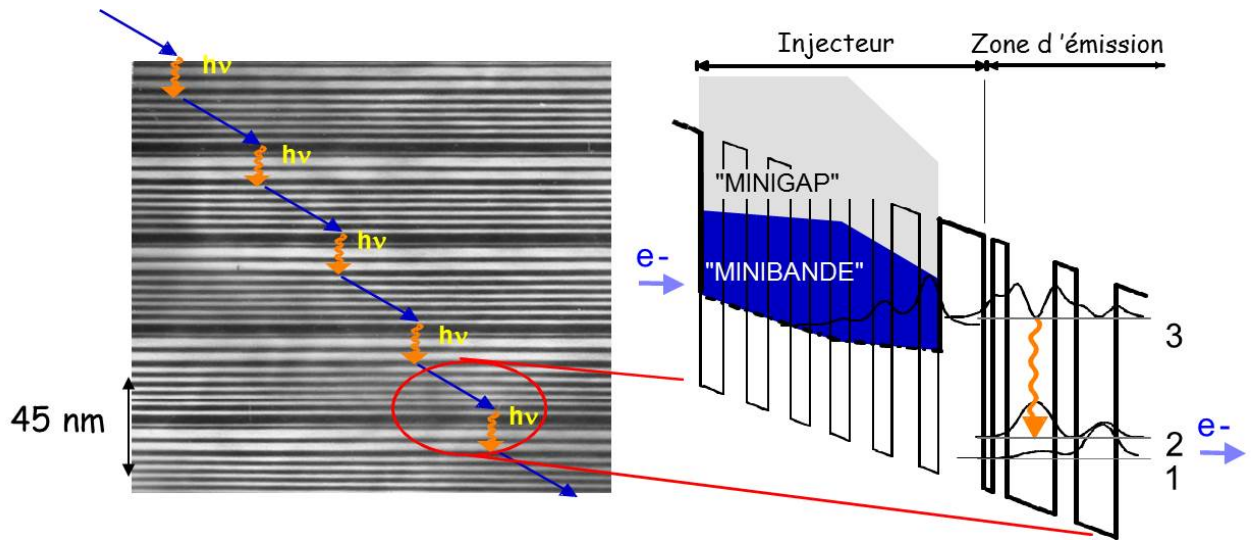


Figure 2.1 — Représentation schématique du fonctionnement d'un laser à cascade quantique.

Une solution est d'utiliser une transition lumineuse entre deux niveaux confinés dans un puits quantique (entre deux sous-niveaux d'une même bande). Alors, en changeant l'épaisseur des couches constituant le laser, on fait varier l'écart entre les niveaux intrabandes et ainsi la fréquence de l'onde émise. On peut dans ce cas réaliser des lasers pour n'importe quelle longueur d'onde sans changer de matériau, simplement en jouant sur l'épaisseur des couches constituant le laser. Cela permet d'obtenir des sources ayant un grand recouvrement spectral allant de $4.4 \mu m$ à $60 \mu m$. Un laser à cascade quantique utilise cette transition. Il est constitué par la répétition d'une série de couches (voir la figure 2.1). La région active d'un tel dispositif est divisée en deux parties : un «injecteur» et une «zone d'émission». Dans l'injecteur, les électrons sont accélérés dans un état excité (niveau 3). Dans la «zone d'émission» (le milieu actif), ils se désexcitent en émettant un photon. Ils sont alors dans l'état de plus faible énergie (niveau 2), sont collectés par l'injecteur adjacent et réinjectés dans la «zone d'émission» suivante. La structure de potentiel obtenue sous champ électrique est un escalier dans lequel les électrons descendent en cascade (d'où le nom du composant), émettant un photon à chaque marche de potentiel.

En 1998, le premier laser à cascade quantique en GaAs/AlGaAs, le matériau le plus répandu dans la fabrication des lasers à semi-conducteurs et le moins onéreux, a été développé à Thalès Research and Technology [16]. Rüdiger Kölher (Pise, Italie) et ses collègues, ont élaboré en 2002 un prototype de laser à semi-conducteurs TéraHertz : le laser à cascade quantique qui produit une onde électromagnétique de fréquence 4.4 THz, de puissance supérieure à 2 mW et a une densité de courant de seuil de l'ordre d'une centaine d'ampères par centimètre carré jusqu'à une température de 50 K [17].

Pour générer des ondes TéraHertz, on peut aussi envisager une méthode basée sur l'optique non-linéaire et le mélange de fréquences. Cet axe de recherche n'avait jamais été essayé et je l'ai exploré pendant mon poste d'ATER.

2.2 Les lasers à cascade quantique bicolores

Nous nous sommes tout d'abord intéressé à la possibilité de créer des lasers à cascade quantique bicolores. La largeur de raie des transitions intrabandes étant extrêmement étroite (en comparaison avec des lasers à semi-conducteurs interbandes), deux transitions d'énergies différentes sont optiquement découplées l'une de l'autre et ne souffrent pas de problème d'absorption mutuelle. Les transitions intrabandes sont donc idéales pour réaliser un laser émettant plusieurs longueurs d'onde dans le moyen infrarouge. Cette idée fut énoncée en premier par Gmachl et al [18] et je l'ai adaptée avec succès aux lasers à cascade quantique en GaAs/AlGaAs (figure 2.2). La meilleure structure trouvée est constituée de 30 régions actives avec une énergie de transition intrabande de $9 \mu m$, puis d'une couche tampon en GaAs et de 30 régions actives avec une énergie de transition intrabande de $11 \mu m$. Son guide d'onde a aussi été fait pour minimiser les pertes optiques et optimiser le facteur de recouvrement avec les régions actives des deux longueurs d'onde. Sur la figure 2.2 (a), on voit le spectre d'émission de ce laser bicolore. L'intensité relative de chaque longueur d'onde y reste constante quand le courant augmente. Son seuil est de l'ordre de $6.8 kA/cm^2$ et sa puissance crête au maximum de 1 W à 77K. Il fonctionne jusqu'à 195 K.

2.3 Étude des propriétés optiques non linéaires des lasers à cascade quantique

Les lasers à cascade quantique en GaAs/AlGaAs peuvent émettre deux longueurs d'onde. Ils sont, de plus, principalement composés de GaAs qui a un très fort coefficient non linéaire d'ordre 2. Nous nous sommes alors intéressé au mélange de fréquences dans un tel composant. Avant d'étudier la génération d'ondes TéraHertz par différence de fréquences pour laquelle la détection est difficile et les dispositifs sont à repenser, nous nous sommes penchés sur un cas plus simple, la génération du second harmonique d'un laser à cascade quantique dont la croissance était faite sur un substrat préparé sur le plan cristallin $\langle 111 \rangle$. En effet, dans ces conditions, le vecteur champ électrique de fréquence ω se trouve dans la bonne orientation pour exciter la polarisation non-linéaire du second ordre et générer un champ électrique de fréquence double. J'ai mis en évidence expérimentalement la génération du second harmonique (figure 2.3) [19]. Les deux courbes incrustées dans les graphes représentent les spectres à hautes résolutions de la fréquence pompe et de la seconde harmonique. La figure 2.3 (a) présente la puissance lumineuse de la seconde harmonique en fonction du courant d'alimentation. La puissance maximale émise était de l'ordre de $1 \mu W$. La pente de la courbe de puissance lumineuse a une dépendance en courant parfaitement quadratique. Cela provient du comportement linéaire de la puissance de l'émission laser ω (figure 2.3 (b)).

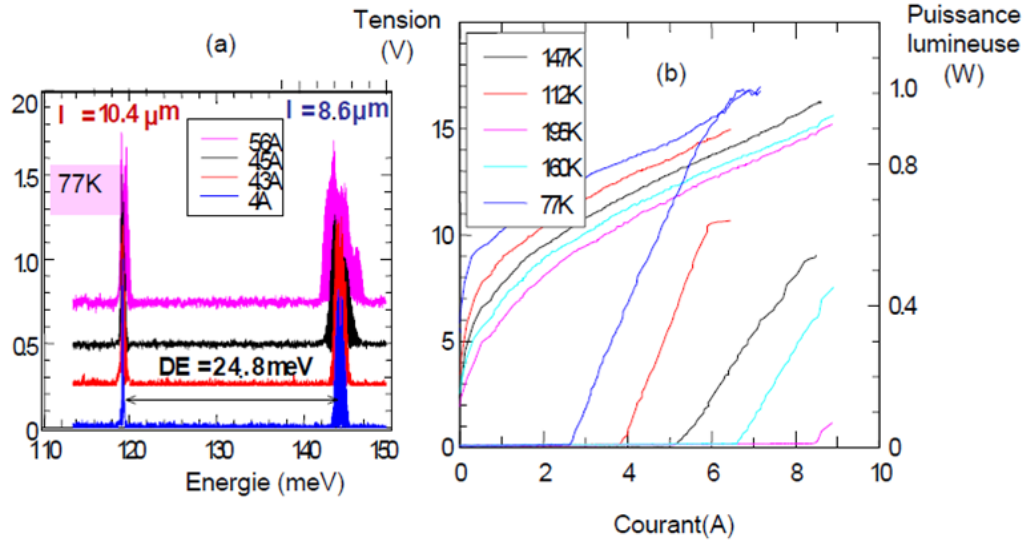


Figure 2.2 – (a) Spectre d’émission d’un laser à cascade quantique bicolor en $GaAs/Al_{0.45}Ga_{0.55}As$ à 77K. Le laser était alimenté par une alimentation pulsée. (b) Caractéristiques tension - courant et puissance - courant pour le laser à cascade quantique du (a).

J’ai également dessiné un guide d’onde asymétrique approprié pour obtenir l’accord de phase. Une attention particulière a été portée à l’optimisation du recouvrement non linéaire entre ces modes.

Ces résultats étaient encourageant pour générer des ondes TéraHertz par différence de fréquence. En 2007, l’équipe de Federico Capasso avec qui l’équipe de Carlo Sirtori travaille en étroite collaboration a réussi par différence de fréquence entre deux lasers QCLs dans le moyen infrarouge ($8.9 \mu\text{m}$ et $10.5 \mu\text{m}$) à générer une onde térahertz de quelques nanowatts à $60 \mu\text{m}$ pour une température de 150 K en utilisant un milieu actif possédant une forte non linéarité d’ordre 2 [20] ($\chi^{(2)} = 4.10^4 \text{ pm/V}$). Sa structure a été améliorée en 2008 pour fonctionner à température ambiante (300 nW à $60 \mu\text{m}$) [21].

2.4 Article en relation avec ce chapitre

L’article [19] est en relation avec ce chapitre et est reproduit à la fin de ce manuscrit.

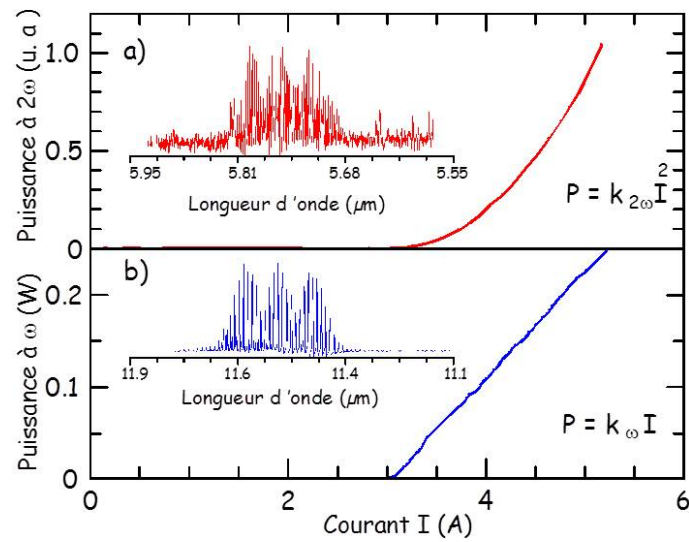


Figure 2.3 — Puissance lumineuse de la seconde harmonique 2ω (a) et de l'émission laser ω (b) en fonction du courant d'alimentation à une température de 77 K. Les deux courbes incrustées dans les graphes représentent les spectres à haute résolution de la fréquence pompe et de la seconde harmonique. [figure 2 de l'article [19]]

Chapitre 3

Nanolaser à boîte quantique unique en microcavité

Mon stage post-doctoral s'est déroulé au Laboratoire de Photonique et de Nanostructures du CNRS à Marcoussis, au sein du groupe «Photonique et électronique quantique», sous la direction d'Izo Abram et Isabelle Robert-Philip du 01 Décembre 2003 au 31 Août 2004.

3.1 Introduction

L'émission stimulée d'un laser est déclenchée à partir des premiers photons émis spontanément par le milieu actif et arrivant dans le mode « laser ». Toutefois, ce processus est en général très peu efficace, car la fraction d'émission spontanée dirigée vers le mode laser (β) est de l'ordre de 10^{-5} . Cette faible valeur de β conditionne le niveau énergétique du seuil dans le laser.

Le contrôle de l'émission de sources semi-conductrices suscite un grand intérêt, la démonstration expérimentale de cet effet ouvrant la voie à des applications innovantes en optoélectroniques (sources de photons uniques, photons jumeaux). En 2001, le groupe «Photonique et électronique quantique» au Laboratoire de Photonique et de Nanostructures (LPN) a réalisé une source de photons uniques monomodes basée sur une boîte quantique (InAs) isolée, en résonance avec le mode fondamental d'une cavité micropilier [22]. Par effet Purcell [23], la durée de vie des excitons a été diminuée d'un facteur 20 :

$$F_p = \frac{3}{4\pi^2} \frac{Q}{V} \left(\frac{\lambda}{n}\right)^3 = 20 \quad (3.1)$$

avec Q : facteur de qualité, V : volume de la zone active. Le facteur β a atteint une valeur proche de sa valeur maximale 1 ($\beta = 0.95$). En effet, en plaçant une boîte dans une cavité appropriée, l'émission spontanée est véhiculée le long d'un mode spatial préférentiel et le facteur (β) augmente considérablement.

Dans de telles microcavités possédant un facteur β proche de 1, la théorie prévoit que le seuil d'émission laser pourrait être atteint même en l'absence d'inversion de population [24]. On parle alors de laser sans inversion de population ou, abusivement, de « laser sans seuil ». L'origine de ce phénomène réside dans l'existence de deux définitions distinctes pour le seuil de l'émission laser [25] :

- dans la communauté de la physique des lasers, le seuil est atteint lorsque le gain du milieu actif est égal aux pertes,
- dans la communauté de l'optique quantique, le seuil est atteint dès qu'il existe un photon (d'origine spontanée) dans le mode laser.

Pour des cavités à faible β , ces deux définitions donnent le même résultat, alors que pour des cavités avec un β de l'ordre de 1 le seuil d'émission laser, selon la définition quantique, peut être atteint bien avant la condition d'égalité entre le gain et les pertes, autrement dit bien avant l'inversion du milieu actif. Cet attendu théorique [24, 26] n'a jamais été validé expérimentalement. Le principal verrou que comportaient ces travaux, était la fabrication d'un tel composant. Mais à la vue des résultats prometteurs obtenus au LPN ($\beta=0.95$, [22]), mon stage post-doctoral visait la réalisation de nanolasers sans inversion de population.

3.2 Réalisation de nanolasers sans inversion de population

La première partie de mon stage post-doctoral a consisté à préciser les paramètres optimaux des cavités pour la réalisation de nanolasers sans inversion de population à boîtes quantiques. J'ai appliqué le modèle développé par Rice et al [25] sur l'initiation de l'émission stimulée aux cavités que nous souhaitions fabriquer. Ce modèle d'initiation d'effet laser suggère que l'oscillation laser sans inversion de population peut être atteinte à partir d'une cavité de facteur de qualité de quelques milliers et de volume inférieur à $10 \lambda^3$ (voir Figure 3.1). Les paramètres à optimiser sont le volume de la cavité V et la densité N de dipôles émetteurs, le facteur de qualité étant imposé par la largeur homogène de la transition émissive. Au regard du savoir-faire, il semble possible d'observer des effets d'Electrodynamique Quantique en Cavité (EDQC) à température ambiante à partir de boîtes quantiques. Un renforcement de la dynamique d'émission spontanée de l'ordre de la dizaine est envisageable. Néanmoins, l'amplitude de ces effets reste largement insuffisante pour observer une oscillation laser sans inversion de population.

Pour observer un tel phénomène à température ambiante, il est nécessaire de recourir à des émetteurs de type puits quantique, offrant des densités de porteurs environ 100 fois supérieures. Mais les mécanismes efficaces de recombinaisons non-radiatives sur les flancs latéraux de la cavité masquent tout effet significatif d'EDQC dans les microcavités à puits quantiques. En revanche, ce même modèle [25] m'a indiqué que

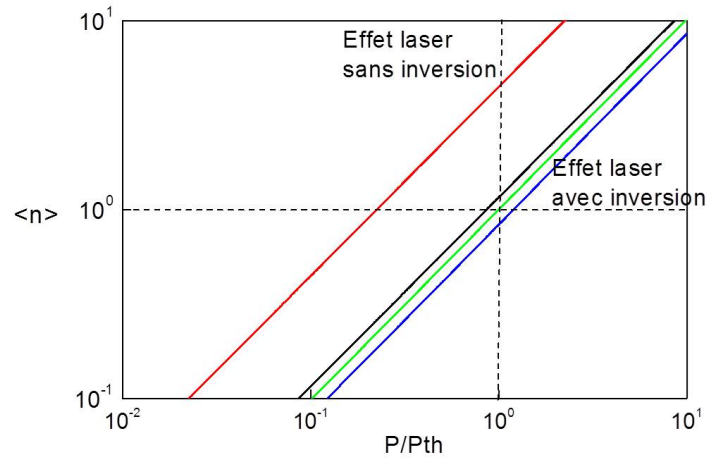


Figure 3.1 — Nombre moyen de photons dans le mode $\langle n \rangle$ en fonction de la puissance pompe normalisée à la puissance nécessaire pour atteindre l'inversion de population. En noir, cas d'une boîte couplée à mode de $Q = 8000$ et $V = 2\lambda^3$; en rouge, cas d'une boîte couplée à mode de $Q = 10^4$ et $V = 0.5\lambda^3$; en vert, 5 plans de boîtes couplées à mode de $Q = 6000$ et $V = 10\lambda^3$; en bleu, 5 plans de boîtes couplées à mode de $Q = 4000$ et $V = 10\lambda^3$.

l'effet laser peut être obtenu à partir d'une boîte unique en l'insérant dans une cavité de facteur de qualité de l'ordre de 8000 et de volume égal à $2\lambda^3$.

Mon stage post-doctoral a alors changé de direction et s'est orienté vers la réalisation de nanosources à faible densité de boîtes quantiques en cavité donnant lieu à une oscillation laser, le dispositif ultime couplant une seule boîte au mode laser.

3.3 Réalisation de nanolasers à une seule boîte quantique

Le laser à une seule boîte quantique constitue le laser à semi-conducteur ultime. Il met à profit le contrôle de l'émission spontanée en couplant un dipôle unique (la boîte quantique) à un mode de la cavité [27]. L'oscillation laser dans un tel système est obtenue lorsque la durée de vie du dipôle émetteur est plus courte que la durée de vie du photon dans la cavité. Un tel régime devrait pouvoir être atteint en réduisant la durée de vie de l'émetteur par effet Purcell et en accroissant le facteur de qualité de la cavité Q .

Après étude des caractéristiques expérimentales des microcavités existantes et du savoir-faire développé au LPN (voir figure 3.2), nous avons décidé de travailler sur des cavités de type micro-pilier avec miroirs de Bragg GaAs/AlOx de $0.5\mu\text{m}$ de diamètre

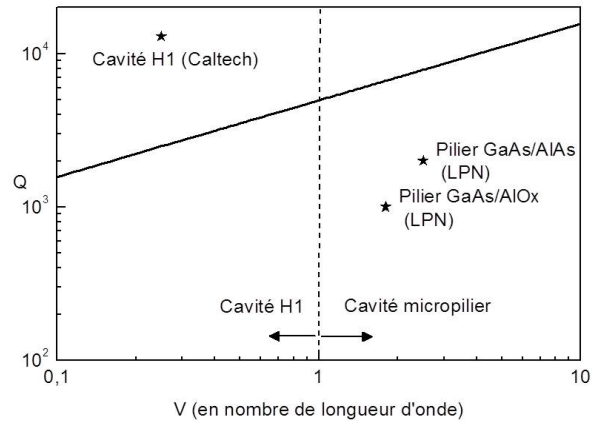


Figure 3.2 — Facteur de qualité nécessaire à l’observation de l’oscillation laser à partir d’une boîte en fonction du volume de la cavité exprimé en nombre de longueurs d’onde. Les étoiles indiquent le savoir-faire à la pointe en 2004 dans la nano-fabrication de microcavité H_1 et de micropilliers.

et de facteur de qualité de l’ordre de 5000 et avec une cavité hexagonale dans un cristal photonique sur membrane ou sur oxyde de facteur de qualité de l’ordre de 4000. J’ai travaillé à l’adaptation du modèle théorique du seuil laser présentée dans [25] aux semi-conducteurs en y incluant des effets de saturation et de réabsorption. En juin 2004, j’ai obtenu un poste de Maître de conférences au Laboratoire de Physique des lasers à Villetaneuse et ai arrêté mes activités de recherche au LPN.

Les grandes difficultés de cette recherche étaient à l’époque de trouver la structure de cavité optimale, de savoir la fabriquer en salle blanche et surtout d’être capable de positionner une boîte quantique de taille appropriée avec une précision nanométrique au centre de la cavité optique afin d’optimiser le couplage dipôle/mode de la cavité. En 2005, l’équipe du LPN a modifié l’émission spontanée de boîtes quantiques contenues dans une fibre photonique [28] ($F_p=5$) puis dans une cavité hexagonale dans un cristal photonique [29] ($F_p=28$). Pour contrôler la position de la boîte quantique, il a fallu attendre 2008 pour que le groupe de Pascale Senellart au LPN soit capable de le faire en utilisant une technique de lithographie optique [30]. Cette technique consiste à cartographier une couche contenant des boîtes quantiques éparpillées, de sélectionner la boîte quantique de taille et de spectre appropriés puis de construire autour une cavité (micropilier, cavité de cristal photonique) de telle manière que la boîte soit positionnée en son centre avec une précision nanométrique. Une fois le contrôle de la boîte quantique maîtrisé, il a alors été possible de créer des nanolasers avec une cavité contenant une seule boîte quantique. Des sources de photons uniques indiscernables à 99.56 %, environ 15 fois plus brillant que les sources usuelles, ont par exemple, aussi été créés en positionnant une boîte au centre d’un micropilier [31]. L’application d’une

tension sur la microcavité a permis de supprimer toute fluctuation électronique qui rendrait les photons émis discernables. Ces résultats ouvrent la porte vers des calculs quantiques et le développement d'ordinateurs quantiques.

Chapitre 4

Spectroscopie atomique dans une nanocellule

J'ai obtenu en septembre 2004 un poste de maître de conférences au Laboratoire de Physique des Lasers à Villetaneuse dans l'équipe Spectroscopie Atomiques aux Interfaces (SAI) co-dirigée par Martial Ducloy et Daniel Bloch. Les travaux présentés ici constituent les premiers travaux de recherche que j'ai effectué dans l'équipe SAI de 2004 à 2006.

4.1 Introduction générale

L'interaction de van der Waals est une interaction électrique de faible intensité entre des systèmes neutres polarisables (atomes, molécules, ou entre une molécule et un cristal). Johannes Diderik van der Waals fut le premier à introduire leurs effets dans les équations d'état des gaz en 1873.

L'interaction de van der Waals (vW) atome-surface représente un des prototypes les plus simples de l'interaction universelle dipôle-dipôle entre systèmes neutres. Elle a été largement étudiée théoriquement par F. London [32] et Lennard-Jones [33]. Cette interaction peut être décrite comme étant l'interaction entre le dipôle fluctuant de l'atome et son image instantanée induite dans la surface. Dans le régime électrostatique van der Waals (vW), valide typiquement pour une gamme de distances allant de $\approx 1 \text{ nm}$ (distance où les détails structuraux de la surface deviennent négligeables) jusque $\approx 1000 \text{ nm}$ (i.e. où les effets de propagation ne peuvent être négligés), l'interaction intrinsèquement attractive varie avec la distance à la paroi en C_3/z^3 où z est la distance atome-surface. Le coefficient C_3 croît d'autant plus que l'atome considéré est excité. En 1948, H.B.G Casimir et D. Polder [34] ont étudié les effets de retard de l'interaction atome-surface de longue portée et ont montré que l'interaction pour des atomes dans l'état fondamental variait dans ce cas avec la distance en C_4/z^4 .

Parallèlement, en 1948, H.B.G. Casimir a étudié l'interaction entre deux réflecteurs plans parallèles et parfaits dans un vide à température nulle et séparé par une petite distance, connu sous le nom d'effet Casimir, et a montré que ceux-ci s'attiraient mutuellement [35]. En effet, plus les plaques sont proches, moins de modes de fluctuations du vide sont permis entre les deux plaques ce qui n'est pas le cas à l'extérieur des plaques. La pression des modes à l'intérieur de la cavité est alors inférieure à celle à l'extérieur, les deux plaques s'attirent.

Notons pour mieux comprendre le lien en apparence classique de l'interaction de vW et la nature électrodynamique quantique de l'effet Casimir que l'interaction de vdW peut être aussi expliquée comme une modification du déplacement de Lamb des niveaux atomiques due au changement de la densité modale du champ électromagnétique du vide à proximité de la surface [36]. De plus en plus dans la littérature, on a tendance à ne plus distinguer l'interaction de van der Waals de l'interaction Casimir-Polder. On parle de l'interaction Casimir-Polder (CP) en champ proche (ex interaction de van der Waals) ou de l'interaction CP en champ lointain (régime retardé).

Dans l'équipe SAI, nous nous intéressons à l'interaction vW atomes-surface qui varie théoriquement avec la distance à la paroi en C_3/z^3 . Quoique cette loi attractive couvre une dizaine d'ordres de grandeurs en énergie, rares ont été jusqu'ici les expériences qui ont testé effectivement la dépendance prédite.

Dans une première approche, l'interaction de vW a été mise en évidence par l'intermédiaire de la mesure mécanique de la déviation d'un faisceau atomique (Cs, Rb, K) ou moléculaire (ClCs) dans l'état fondamental à l'approche d'une surface cylindrique métallique [37, 38]. Seuls les atomes très proches de la surface subissaient une déviation notable. Ces mesures étaient très affectées par la qualité du polissage du cylindre et n'ont pas permis de déterminer quelle était la loi de dépendance avec la distance de l'interaction de vW (z^{-3} , z^{-4} , autre ...). Dans les années 90, l'interaction de vW a été mesurée par le groupe de E. A. Hinds à Yale en mesurant la déviation d'un faisceau d'atomes de Rydberg (donc fortement polarisables) lors de la traversée d'une micro-fente métallique [39–41]. Dans ce cas, seuls les atomes au centre de la micro-fente sont transmis. En effet, ce sont les seuls pour lesquels les interactions de vW des deux plaques se compensent. La précision des mesures étaient suffisantes pour vérifier le comportement en z^{-3} de l'interaction de vW pour deux parois séparées de $3\mu\text{m}$ à 500 nm . Ces expériences menées sur des micro-fentes métalliques ont donné des résultats non reproductibles avec des surfaces diélectriques, les niveaux des atomes de Rydberg étant très fortement sensibles aux champs électriques parasites. Un montage similaire a été utilisé pour mesurer l'interaction de CP en z^{-4} [42]. A la même époque, une autre expérience a été développée par le groupe d'Aspect à Orsay. Des atomes froids dans l'état fondamental sont approchés d'un miroir diélectrique atomique. En l'absence d'onde évanescente, les atomes sont attirés par la surface (interaction attractive de vW) et viennent s'y coller. L'expérience a consisté à compenser cette attraction en ajustant la force dipolaire créée par une onde évanescente. Il a alors été possible de

mesurer l'interaction de vW et de vérifier sa dépendance en z^{-3} jusqu'à 50 nm [43].

Dans les années 2000, des expériences mesurant la dépendance de l'effet Casimir [44–46] et l'interaction Casimir-Polder en régime retardé [47,48] ont été développées. La possibilité des mesures de l'interaction Casimir a suscité un intérêt notable autant du point de vue de la physique fondamentale (tests de gravité non-newtonienne [44]) que du point de vue technologique (influence sur le fonctionnement des systèmes microélectromécaniques MEMs [49]). Des corrections par rapport au calcul théorique original [35] ont été apportées pour faire mieux concorder l'expérience et la théorie (prise en compte de la rugosité de la surface, que la surface n'est pas un conducteur parfait, corrections dues à l'émission thermique des surfaces [48]).

Le développement des nanoréseaux a aussi permis de voir la signature mécanique de l'interaction de vW en observant la figure de diffraction atomique proche d'un nanoréseau d'un faisceau de gaz rare dans l'état fondamental [50] ou dans un état métastable [51].

Simultanément, est apparu un travail fondé sur la modification du coefficient de réflexion d'atomes lents (atomes froids) de rubidium sur un miroir de cobalt magnétique [52] due à la compétition entre un potentiel répulsif contrôlé et l'attraction de la paroi. Cette étude a permis de mesurer l'interaction vW pour des distances allant de 20 à 100 nm avec une incertitude de 15%.

Historiquement, l'équipe SAI s'est orientée depuis de nombreuses années [36] vers une approche spectroscopique pour mesurer l'interaction de vW : la technique de réflexion sélective en vapeur diluée [53]. Celle-ci sonde des atomes à une épaisseur de l'ordre de $\lambda/2\pi$ (avec λ la longueur d'onde) en mesurant la modification de la réflexion lumineuse à l'interface fenêtre-vapeur lorsque la fréquence lumineuse est balayée autour de la fréquence de résonance atomique (technique détaillée et utilisée au chapitre 5 paragraphe 5.3.2). L'avantage de cette technique optique sur des techniques mécaniques est la possibilité d'étudier des niveaux à faible durée de vie donc excités et qu'elle est utilisable avec des surfaces transparentes diélectriques. Cependant la profondeur sondée par cette technique est fixée (épaisseur de l'ordre de $\lambda/2\pi$) et est donc limitée par la longueur d'onde utilisée. Dans les années 90, l'équipe SAI a montré l'intérêt des cellules de vapeur diluée de faible épaisseur sous irradiation normale [54]. Dans ces cellules, le libre parcours moyen d'un atome devient anisotrope, et est limité par la distance entre les parois de la cellule. Ceci conduit à une exaltation relative de la contribution des atomes lents, d'où une signature sub-Doppler dans la réponse spectroscopique. Dans le but d'une étude plus systématique, nous nous sommes donc orientés vers l'étude spectroscopique de l'interaction vW exercée sur des atomes excités de césium dans une nanocellule, dont l'épaisseur (nanométrique) varie localement entre 40 nm et 130 nm, permettant ainsi une étude résolue en distance de l'interaction de vW.

Je vais dans un premier temps vous présenter la cellule nanométrique que nous

avons utilisée.

4.2 Mesure de l'interaction vW atome-surface résolue spatialement

4.2.1 Cellule nanométrique

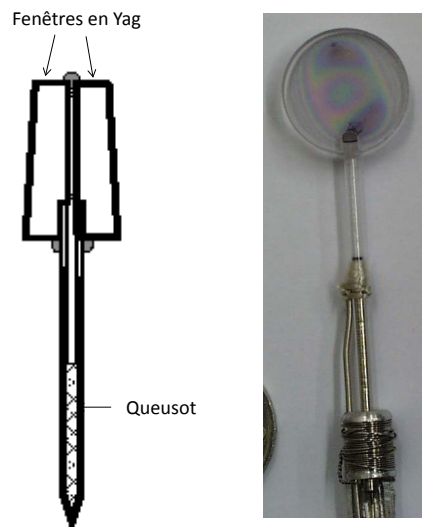


Figure 4.1 — Vue de coupe d'une nanocellule (à gauche). Photographie d'une nanocellule en Yag (à droite) allant de 30 à 1300 nm. [Fig 2.1 et 2.2 de la thèse de Gabriel Dutier [55]]

Depuis 2001, l'équipe de David Sarkisyan de l'Institut de Recherche Physique d'Ashtarak en Arménie a mis au point sur notre demande des nanocellules de vapeur d'épaisseurs variant localement et couvrant une gamme typique entre 20 et 1000 nm. Auparavant, des cellules commercialisées étaient réalisées pour des épaisseurs nominales comprises entre 10 μm et 1 mm, avec une assez grande imprécision sur l'épaisseur locale. Les cellules arméniennes sont constituées de deux fenêtres en Yag ou en saphir très bien polies maintenues espacées par un dépôt de Al_2O_3 , à environ 5 mm du bord des fenêtres, en forme d'anneaux ou en trois plots distincts [56, 57]. Ces fenêtres sont collées à haute température avec une colle minérale. La nanocellule est chauffée à 400°C pendant plusieurs heures pour évacuer les impuretés à l'origine d'un élargissement collisionnel. Lorsque la pression interne diminue, les fenêtres se rapprochent sous l'effet de la pression atmosphérique extérieure. La distance entre les fenêtres est alors très petite au centre et augmente progressivement sur les bords à cause des plots d'espacement

créant ainsi une nanocellule d'épaisseur variable. La cellule comporte un petit angle sur les fenêtres comme le montre la figure (Figure 4.1). Cet angle permet de bien séparer les faisceaux réfléchis pour les distinguer et aussi pour limiter les interférences. Les faces internes de la cellule sont fortement parallèles et proches formant ainsi un unique faisceau réfléchi.

La cellule peut être remplie de l'élément atomique souhaité (ici de césium) par l'intermédiaire d'un queusot (réservoir). Le chauffage du queusot permet de contrôler précisément la densité de vapeur de césium à l'intérieur de la nanocellule suivant la formule suivante [58] :

$$\text{Log}_{10}P = 8.211 - \frac{4006.048}{T} - 0.000601T - 0.196.\text{Log}_{10}P \quad (4.1)$$

avec P la pression en Torr et T la température du réservoir en Kelvin. La densité de la vapeur atomique n s'écrit :

$$n = \frac{P}{RT} \quad (4.2)$$

avec $R=62.363$ L.Torr/mol/K et n la densité en mol/L. La pression à température ambiante ($T = 25^\circ\text{C}$) est de 2.10^{-3} mTorr. Pour avoir un ordre de grandeur en tête, pour des températures avoisinant 150°C , la pression augmente d'un ordre de grandeur environ tous les 50°C .

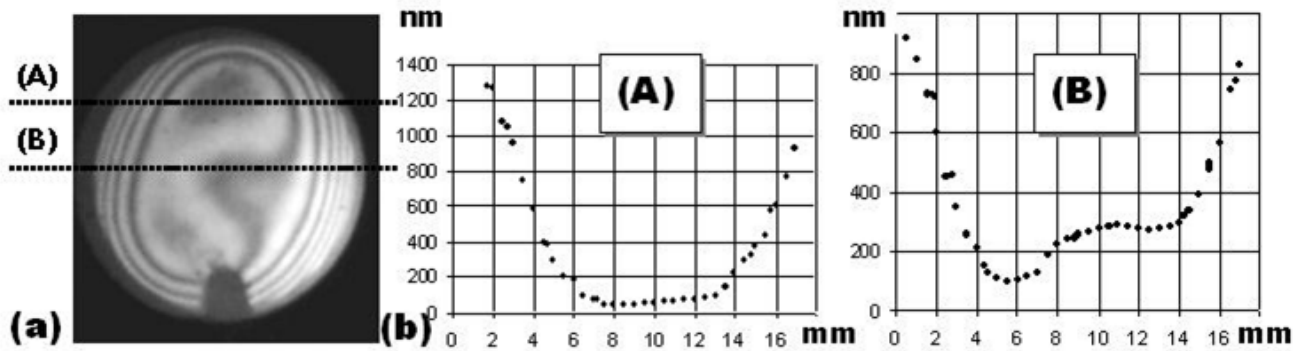


Figure 4.2 – Cartographie de l'épaisseur de la nanocellule suivant deux axes A et B. [Fig 2.10 de la thèse de Gabriel Dutier [55]]

L'épaisseur très faible des nanocellules associée à un très bon parallélisme (déviations inférieures à $1 \mu\text{m}$ sur une extension transverse de 10 mm) fait que la nanocellule se comporte comme une cavité Fabry-Perot. Les variations locales d'épaisseur apparaissent sous forme de franges d'interférences (Figure 4.2). Une étude systématique de concordance des coefficients de réflexion pour des faisceaux focalisés au même endroit mais de différentes longueurs d'onde, permet de remonter à l'épaisseur locale de

la cellule et donc de cartographier son épaisseur [56, 57]. Avec un faisceau d'environ $100 \mu\text{m}$ de diamètre, nous avons obtenu une précision entre 1 et 5 nm sur la mesure de l'épaisseur. Une fois la nanocellule caractérisée, nous l'avons utilisée pour y effectuer des mesures spectroscopiques.

4.2.2 Description de l'expérience

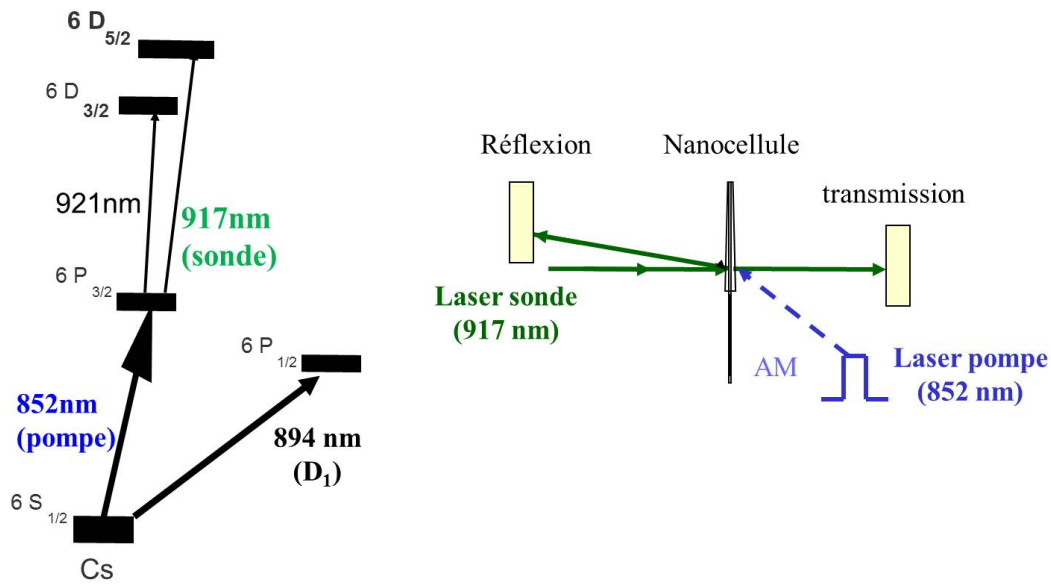


Figure 4.3 – Niveaux atomiques du césium considérés (à gauche). Schéma du montage (à droite).

La nature de type Fabry-Perot de la nanocellule a le désagréable inconvénient de mixer les signaux réfléchis et transmis. Notre étude spectroscopique s'est fondée sur une analyse détaillée des spectres expérimentaux enregistrés simultanément en transmission et réflexion (Figure 4.3), et sur une comparaison avec les formes de raies, telles que prédites par une modélisation rigoureuse et un ajustement numérique.

Notre expérience a été menée sur la transition excitée $6P_{3/2} \rightarrow 6D_{5/2}$ du césium ($\lambda = 917 \text{ nm}$) dans une nanocellule avec des fenêtres en YAG (Figure 4.3). Nous avons choisi une transition excitée pour mesurer une forte interaction principalement due au niveau $6D$. Pour atteindre cette transition excitée, une étape de pompage $6S_{1/2} \rightarrow 6P_{3/2}$ (852 nm) a été nécessaire. Pour augmenter la sensibilité de détection nous avons modulé en amplitude le faisceau pompe à 852 nm ($6S_{1/2} \rightarrow 6P_{3/2}$) et avons utilisé une détection synchrone pour la transition sonde à 917 nm ($6P_{3/2} \rightarrow 6D_{5/2}$). Pour chaque épaisseur intéressante de la nanocellule ($L = 40 \text{ nm}$, 50 nm , 65 nm , 80 nm , 100 nm et 130 nm), nous avons enregistré systématiquement la transmission et la réflexion

en fonction de la densité de césium et donc en faisant varier les effets collisionnels. Un montage auxiliaire d'absorption saturée (SA) a été joint au montage pour déterminer la position des résonances de fréquence en volume et définir l'échelle en fréquence.

Lors des premières mesures, nous avons obtenu des décalages en fréquence de nos raies (par rapport à la fréquence en volume) vers le rouge allant jusqu'à la dizaine de GHz pour de faibles épaisseurs de nanocellule (un décalage en énergie deux ordres de grandeur plus important que ceux obtenus auparavant [40, 41]). Ce décalage a été obtenu pour un élargissement Doppler de l'ordre de 250 MHz et une largeur naturelle de 5 MHz. Le décalage apparent a montré une dépendance approximative en accord avec un modèle simple (Figure 4.4). Ce dernier considère qu'à une position relative z/L où L est l'épaisseur de la nanocellule, le décalage évolue en L^{-3} . Mais le comportement de la forme globale du spectre ne peut être évalué par ce simple modèle, un modèle plus complexe a dû être développé.

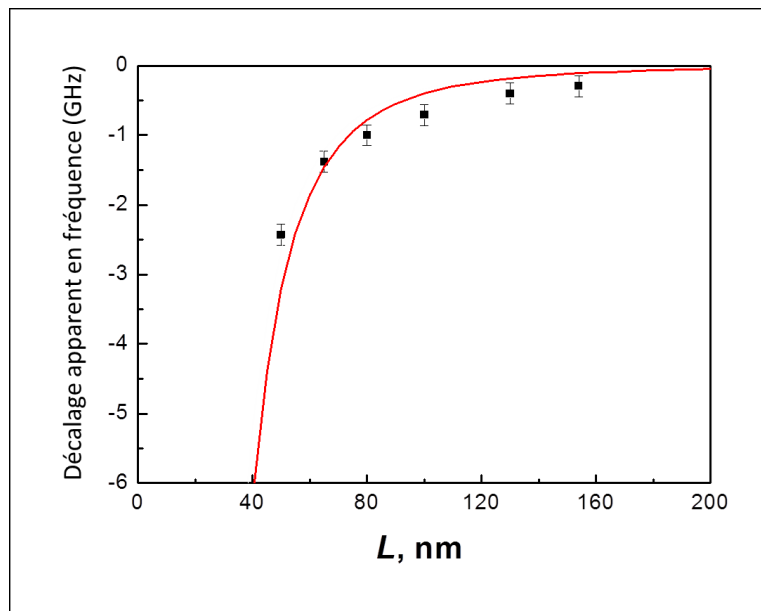


Figure 4.4 — Décalage apparent entre le pic de transmission et la transition en volume. Courbe théorique (rouge) suivant une loi en A/L^3 avec ici $A = 400 \text{ kHz} \cdot \mu\text{m}^3$. Les points noirs correspondent aux décalages expérimentaux mesurés.

4.2.3 Modélisation

Si un atome est positionné devant une surface, l'interaction de vW peut être décrite comme l'interaction entre le dipôle fluctuant de l'atome et son image instantanée induite dans la surface. Si maintenant un atome est placé entre deux surfaces ce qui correspond à la géométrie de la cellule mince, cela va créer des images multiples du dipôle atomique

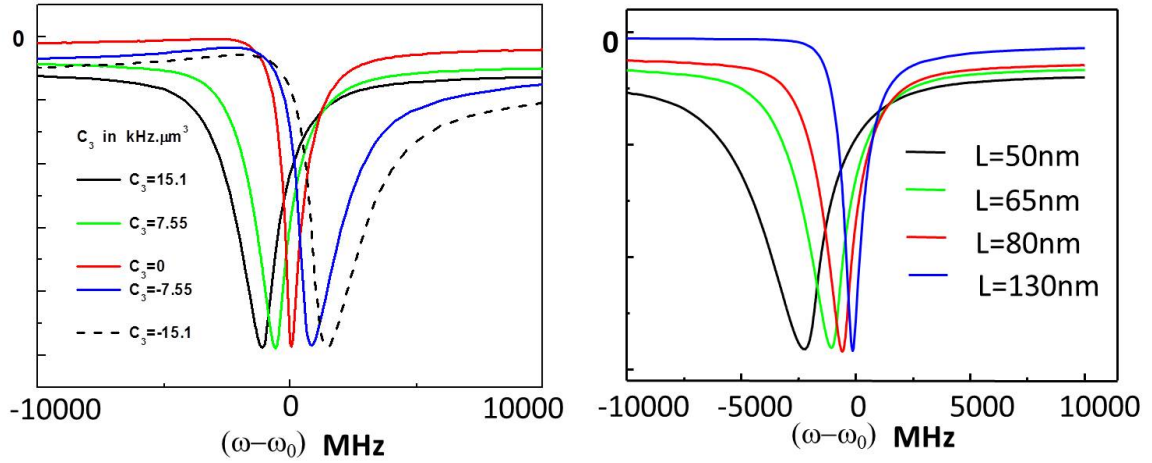


Figure 4.5 – Spectres théoriques en transmission prédits pour une nanocellule ayant des fenêtres en Yag, élargissement Doppler de l'ordre de 250 MHz . $L = 80 \text{ nm}$ (a) ; $C_3 = 7.55 \text{ kHz} \cdot \mu\text{m}^3$ (b). Pour des raisons de normalisation, les amplitudes ont été multipliées par les facteurs suivants : (a) 1 pour $C_3 = 0$; 2.55 pour $C_3 = 7.5 \text{ kHz} \cdot \mu\text{m}^3$; 3.28 pour $C_3 = 15 \text{ kHz} \cdot \mu\text{m}^3$; 2.84 pour $C_3 = -7.5 \text{ kHz} \cdot \mu\text{m}^3$ et (b) 1 pour 130 nm ; 2.96 pour 80 nm ; 4.97 pour 65 nm et 10.1 pour 50 nm . [Figure 4 de l'article [59]].

dans les parois. L'équipe a modélisé l'interaction de vW entre deux parois et a tenu compte de ces images multiples. Elle a montré qu'un potentiel ne considérant que les deux premières images est suffisant pour modéliser l'interaction vW tant que la dispersion de la surface reste négligeable [60] avec L l'épaisseur de la nanocellule :

$$V(z) = -C_3[z^{-3} + (L - z)^{-3}]. \quad (4.3)$$

Pour modéliser les spectres de réflexion et transmission, ils ont inclus dans un modèle les images multiples du dipôle atomique, le comportement de type Fabry-Perot de la nanocellule, intégré sur la position des atomes dans la nanocellule et sur la distribution des vitesses qui a été considérée comme thermique (Maxwellienne). De fortes variations de la forme des raies ont été prédites (Figure 4.5) quand l'épaisseur de la nanocellule (L) ou le coefficient d'interaction vW (C_3) changent, que cela soit pour la transmission ou la réflexion, montrant la grande sensibilité du modèle. L'étape suivante consistait à comparer l'expérience à ce modèle.

4.2.4 Résultats pour la raie à 917 nm

Comme le montre la figure 4.6, un choix unique des paramètres du modèle¹ suffit à prédire la forme de raie expérimentale en transmission et réflexion pour des épaisseurs

1. les paramètres de fit ont été optimisés pour une épaisseur de 50 nm puis utilisés pour les autres épaisseurs.

variées. Les deux signaux de transmission et de réflexion ont été traités indépendamment et ont cependant donné des résultats cohérents entre eux. La cohérence de l'évolution de la largeur avec la pression et de l'évolution linéaire du décalage des spectres avec la pression pour une épaisseur constante ont été vérifiées. Le coefficient C_3 apparaît constant pour toutes les épaisseurs à l'incertitude expérimentale près (figure 4.7) et fournit une vérification à la dépendance en z^{-3} .

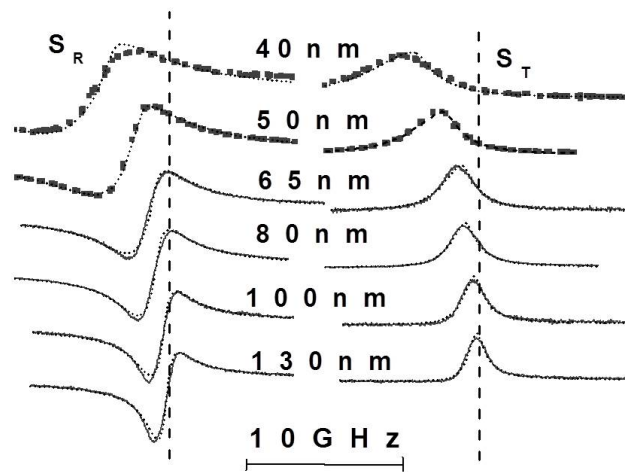


Figure 4.6 — Spectres en transmission (T) et réflexion (R) pour la transition $6P_{3/2} \rightarrow 6D_{3/2}$ du césium enregistrés à des régions d'épaisseurs variées pour une même cellule de vapeur. Les traits tiretés verticaux indiquent la position en fréquence de la transition dans l'espace libre. Les pointillés sont les courbes théoriques ajustées obtenues avec une unique valeur de $C_3 = 14 \text{ kHz} \cdot \mu\text{m}^3$ et de $\gamma = 300 \text{ MHz}$. Ces paramètres ont été ajustés pour une épaisseur de 50 nm . Un laser à long balayage discret a été utilisé pour les épaisseurs de 40 et 50 nm . Un autre laser à balayage continu moins balayable a été utilisé pour les épaisseurs plus importantes. [Figure 3 de l'article [61]]

La reproductibilité des spectres pour des zones diverses a été soigneusement testée. Pour cela, nous avons recommencé l'expérience sur d'autres zones de la cellule de même épaisseur nominale. Pour des épaisseurs supérieures à 50 nm , les spectres étaient parfaitement reproductibles (formes, décalages en fréquence...). Pour une épaisseur de 50 nm , les spectres montraient de faibles différences dans la forme suivant les zones. Plusieurs d'entre eux nous ont cependant donné exactement le même spectre, ce qui nous a permis de valider cette épaisseur. Pour des distances plus petites ($L \leq 40 \text{ nm}$), ce n'était plus du tout le cas. Cela peut s'expliquer par le fait que ce que nous mesurons

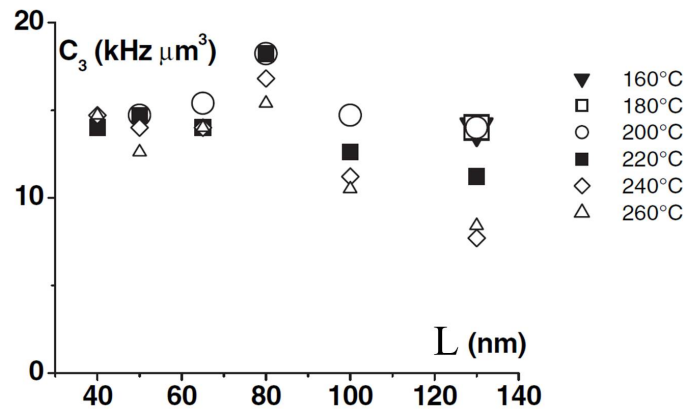


Figure 4.7 — Coefficient C_3 optimal obtenu pour différentes épaisseurs de la nanocellule L et des température de césium (donc des densités) différentes. Une augmentation de la température du césium de 20°C double approximativement la densité de césium. [Figure 4 de l'article [61]].

est une épaisseur moyenne sur la taille du spot sondé (diamètre environ $10\ \mu\text{m}$). Le moindre défaut (planéité, rugosité ...) peut permettre d'obtenir une épaisseur moyenne identique pour deux répartitions différentes localement des épaisseurs. S'il y a de fortes fluctuations de l'épaisseur localement, cela entraîne localement une forte variation de l'interaction de vW (une fluctuation entre 35 et $45\ \text{nm}$ de distance correspond à un doublement de l'interaction de vW). Nous avons estimé la rugosité de la surface de la fenêtre. Elle est de l'ordre de 1 à $2\ \text{nm}$, elle est donc faible et n'est pas en cause. Par contre les défauts de planéité (pente de $10\ \text{nm}$ pour $1\ \text{mm}$) peuvent expliquer une épaisseur moyenne identique pour deux spots différents mais des fluctuations locales de distance différentes, donc des variations fortes de l'interaction de vW, et au final un spectre d'une tout autre forme.

Des impuretés ou des charges sur les fenêtres pourraient faire que l'interaction vW ne représente qu'une fraction des perturbations subies par l'atome au voisinage d'une paroi. Une estimation d'un possible déplacement Stark résiduel a donc été faite. Pour cela, nous avons utilisé les résultats obtenus avec une interface de Yag pour la transition ($7P \rightarrow 10C$) du césium qui avait un déplacement Stark inférieur à $100\ \text{MHz}$ [62]. Nous l'avons extrapolé au cas de notre transition et estimé que le déplacement Stark ne devrait pas excéder $100\ \text{MHz}$ dans notre cas. Les déplacements spectraux observés et les distorsions ont donc bien pour origine l'interaction du Césium avec la surface de Yag elle-même. La valeur estimée de C_3 ($\approx 14 \pm 3\ \text{kHz}\cdot\mu\text{m}^3$) s'avère être en très bon accord avec la prédiction théorique la plus élémentaire ($\approx 15\ \text{kHz}\cdot\mu\text{m}^3$). Un tel accord est d'autant plus remarquable que la précision des prédictions théoriques elles-mêmes peut se ressentir : nécessité de prendre le modèle considérant toutes les images multiples, de prendre en compte l'anisotropie de l'effet de pompage vers le niveau de pompage intermédiaire, ou encore d'une distribution des vitesses des atomes

rendue non Maxwellienne par la présence des parois et l'existence du pompage vers un niveau intermédiaire, ou des corrections liées à l'émission thermique des surfaces, ou pour les courtes distances, aux contributions (non retardées) du noyau électronique aux transitions virtuelles pertinentes [63].

Pour poursuivre vers des distances très courtes, et compte tenu de ce qu'il devient de plus en plus difficile de réaliser un pompage vers un niveau excité intermédiaire sur une épaisseur très courte, nous avons entrepris des expériences sur la raie de résonance D_1 ($6S_{1/2} \rightarrow 6P_{1/2}$) du Césium qui part du niveau fondamental (Figure 4.3).

4.2.5 Résultats obtenus pour la raie D_1 (894 nm) pour des distances encore plus courtes

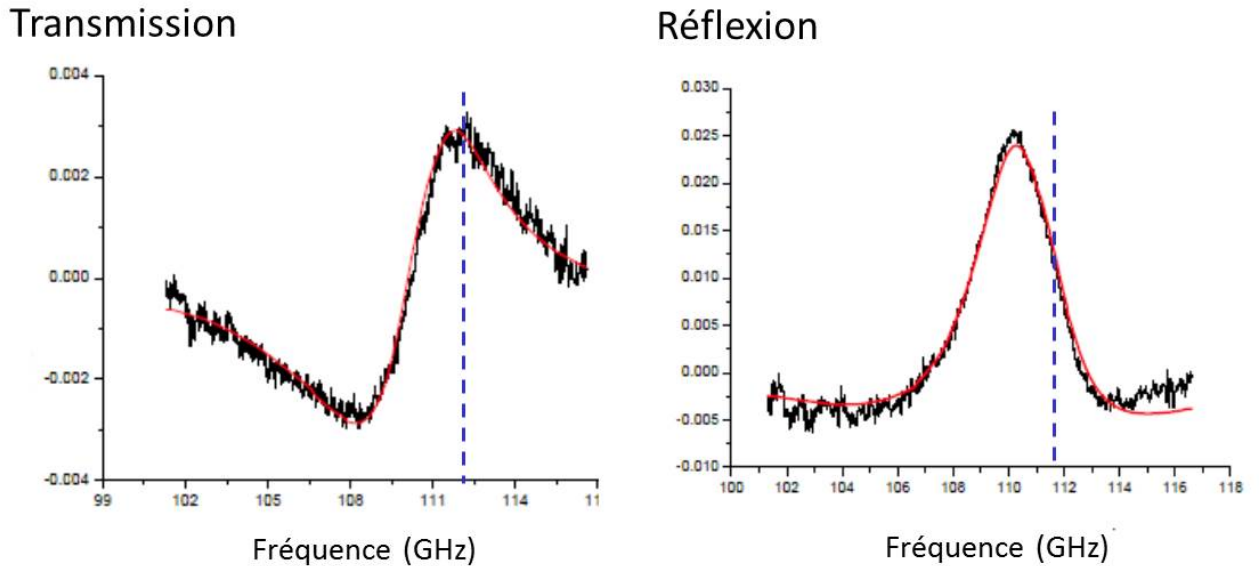


Figure 4.8 — Spectres FM obtenus en réflexion et en transmission pour une épaisseur $L=30$ nm et une température de vapeur $T=260$ °C pour la transition D_1 (894 nm). La courbe noire est la courbe expérimentale, la courbe rouge la courbe obtenue avec notre modèle avec $C_3 = 2.5$ kHz. μm^3 , le trait en pointillé montre la fréquence de transition en volume.

Si l'absence d'une raie de pompage, permettant modulation et démodulation à la détection, rend plus délicate la détection, des résultats reproductibles ont été obtenus pour des épaisseurs de cellule jusque 25 - 30 nm (figure 4.8), et les prédictions théoriques deviennent insensibles aux incertitudes entraînées par l'étape du pompage. La valeur estimée de C_3 (≈ 2.5 kHz. μm^3) reste la même jusqu'à une épaisseur de la nanocellule de 30 nm. Pourtant, les valeurs de C_3 obtenues sont plus grandes que théoriquement

prédites ($C_3(\text{théorie}) = 1 - 2 \text{ kHz} \cdot \mu\text{m}^3$) alors même que la physique atomique des niveaux impliqués pour la raie D_1 est particulièrement bien connue. Nous avons deux pistes à explorer pour expliquer ce désaccord :

- le parallélisme dans la cellule est trop bon (pour les parois extérieures de la cellule), les interférences trop fortes, ce qui modifie fortement la forme de nos spectres. Il serait bon de refaire l'expérience avec une nouvelle nanocellule présentant un petit angle qui éliminerait ces interférences.
- les collisions fortes ici à cause du fort confinement mixent peut-être l'interaction atome-atome à l'interaction atome-surface ce qui rendrait sa modélisation plus complexe et l'estimation de C_3 erronée dans notre modèle.

Les études détaillées de l'interaction vW rapportées ci-dessus pour des nanocellules ont été effectuées dans des situations où la fenêtre diélectrique à l'interface ne présente pas de couplage particulier entre les modes que peut absorber la surface et les émissions atomiques possibles. Nous nous sommes alors intéressés au cas où ce couplage atome-surface existe.

4.2.6 Cas où il y a un couplage résonant entre l'émission atomique et l'absorption de la surface

En 1999, l'équipe SAI a prouvé qu'en cas de couplage entre l'émission d'un atome et son absorption par une surface (mode de surface ou polariton de surface), il est possible d'observer : une augmentation de l'attraction voire même une répulsion [60] (surface en saphir et transition $6D_{3/2} \rightarrow 7P_{1/2}$ du césium à $12.15 \mu\text{m}$ du césium). Dans le cas du niveau $6D_{3/2}$, il existe aussi un couplage résonant entre une émission de l'atome $6D_{3/2} \rightarrow 7P_{1/2}$ à $12.15 \mu\text{m}$ et une absorption de la surface de YAG (figure 4.9). Dans le cas d'une seule surface de YAG, le coefficient C_3 prédit théoriquement est négatif, l'interaction vW est répulsive [64] ($C_3 = -32 \pm 5 \text{ kHz} \cdot \mu\text{m}^3$). Cette prédiction théorique n'a jamais été testée. Une série d'expériences (figure 4.10) sur la raie $6P_{3/2} \rightarrow 6D_{3/2}$ ($\lambda = 921 \text{ nm}$) obtenue après un pompage sur la transition $6S_{1/2} \rightarrow 6P_{3/2}$ ($\lambda = 852 \text{ nm}$) ont été effectuées de manière similaire aux mesures faites sur la transition D_2 (voir paragraphe précédent 4.2.4) avec une cellule nanométrique aux fenêtres de YAG.

On peut tout d'abord noter qu'au lieu d'observer une répulsion comme théoriquement prévu, on a un décalage des raies vers le rouge et donc une attraction. Il a été démontré par l'équipe en 2005 (voir figure 7 de [65]) qu'avec deux murs répulsifs le potentiel peut être répulsif quelle que soit la distance aux murs et induire un décalage vers le rouge donc attractif pour le centre de la nanocellule ce qui est en accord avec ce que nous avons trouvé.

La comparaison entre les spectres à 917 nm (sans couplage) et 921 nm (avec couplage) dans des conditions similaires montre que le signal obtenu à 921 nm est plus large et plus faible en amplitude. Cela est peut être la preuve d'un transfert réel d'énergie entre l'émission des atomes de césium et son absorption par les deux parois en YAG. En effet, un transfert diminuerait le temps de vie du niveau $6D_{3/2}$ et aurait pour effet d'élargir le spectre. Le rapport entre la largeur et le décalage en fréquence, qui est très caractéristique d'un spectre, ne peut être reproduit à l'aide du modèle précédemment

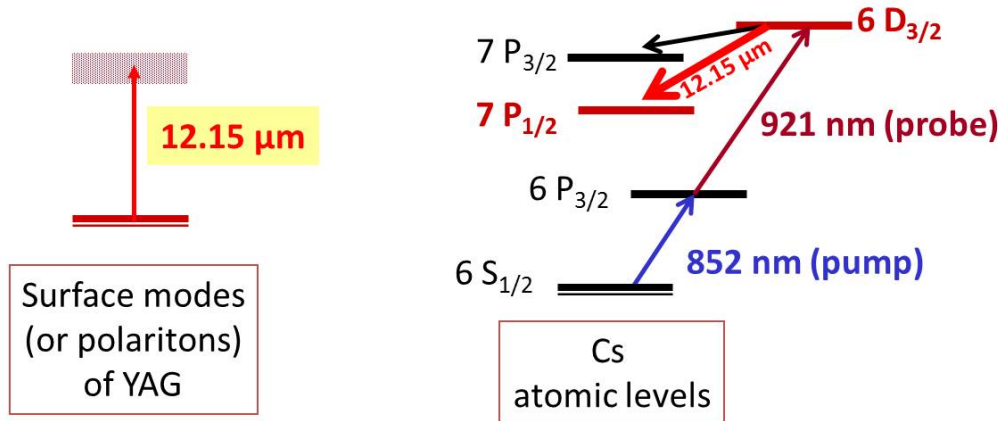


Figure 4.9 — Niveaux atomiques de l'atome de césium et son couplage avec une absorption par un mode de surface du YAG.

utilisé à 917 *nm* et nécessiterait une modélisation beaucoup plus complexe.

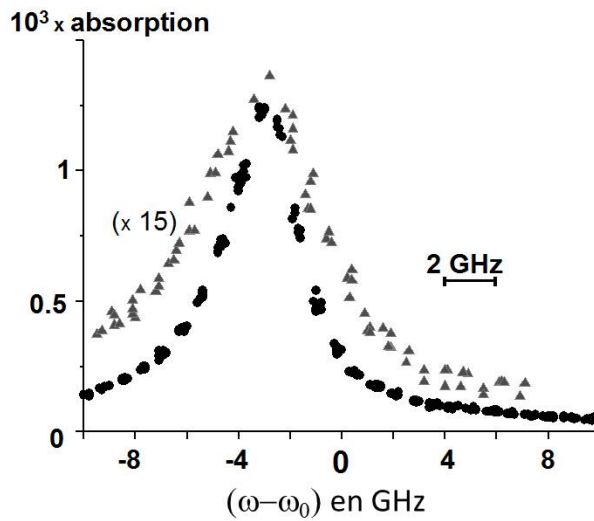


Figure 4.10 — Comparaison entre les spectres par transmission obtenus pour 917 *nm* (sans couplage - cercles) et 921 *nm* (avec couplage - triangles) pour une nanocellule en YAG d'épaisseur $L = 50 \text{ nm}$ pour une même température de vapeur de césium ($T = 240^\circ\text{C}$). [Figure 4 de l'article [65]]

Parallèlement à ces études, nous nous sommes demandés s'il était possible de faire de la spectroscopie à deux photons dans une cellule mince. Nous l'avons modélisée et avons réalisé les premiers tests expérimentaux.

4.3 Spectroscopie à deux photons dans une nanocellule - Généralisation du rétrécissement Dicke [1]

En 1953, Romer et Dicke ont prédit et observé un rétrécissement spectral sub-Doppler dans le domaine des micro-ondes [13,14]. En effet, si le mouvement des atomes est limité à moins qu'une longueur d'onde par collisions sur un gaz tampon, le signal devient sub-Doppler et est appelé rétrécissement Dicke. SAI a montré théoriquement et expérimentalement [57,66] que dans le régime d'absorption linéaire, il est également possible d'observer un rétrécissement spectral cohérent de type Romer et Dicke, pour une épaisseur de la cellule égale ou inférieure à $\lambda/2$ lorsque la lumière arrive sous incidence normale. Cet effet est dû à la contribution additive de toutes les classes de vitesse dans le régime transitoire, lorsque l'irradiation est exactement à résonance. En donnant plus de temps aux atomes pour interagir (épaisseur plus importante), ou sous une irradiation à une fréquence légèrement décalée, les interférences entre les différentes classes de vitesse cessent d'être toutes constructives. Alors que pour une épaisseur de $\lambda/2$ la forme de raie est sub-Doppler, elle ne l'est plus pour une épaisseur de λ . Elle le redevient périodiquement pour des épaisseurs de $3\lambda/2$, $5\lambda/2$ [66] ...

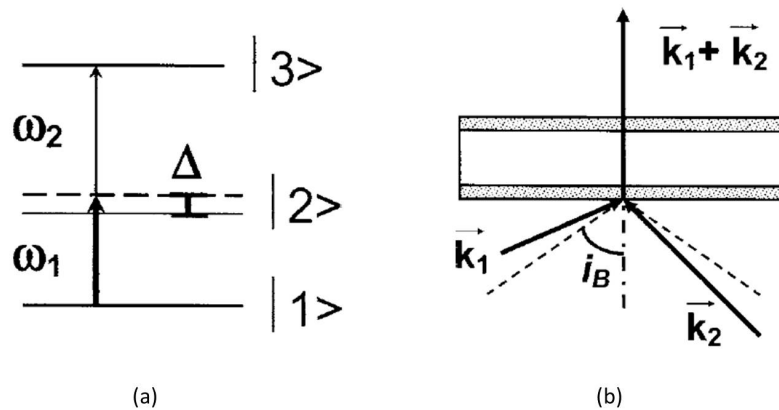


Figure 4.11 — (a) Représentation schématique d'un système atomique à trois niveaux. Δ est le désaccord entre le champ et la transition $|1\rangle \rightarrow |2\rangle$ (b) Géométrie non linéaire, proche de l'angle de Brewster permettant d'observer un rétrécissement Dicke à deux photons quand $\vec{k}_1 + \vec{k}_2$ est perpendiculaire à la nanocellule. [Figures 1 et 2 de l'article [1]]

Nous avons trouvé une géométrie permettant une généralisation du rétrécissement Dicke [1] utilisant une transition à deux photons dans une cellule mince (Figure 4.11). Pour cela, on regarde comment change la transmission d'un faisceau sonde (ω_2 , \vec{k}_2)

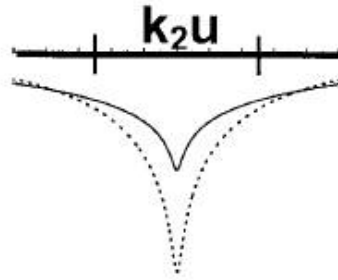


Figure 4.12 – Comparaison entre le spectre de transmission obtenu avec deux faisceaux co-propageant (trait plein) et deux faisceaux contra-propageant (traits pointillés) dans une cellule mince. [Figure 3 de l'article [1]]

lorsqu'un faisceau pompe (ω_1, \vec{k}_1) est introduit. Si la somme des deux vecteurs d'onde est perpendiculaire à la cellule (Figure (b) 4.11), un rétrécissement Dicke est possible. Cette extension au cas de transitions à deux photons permet des géométries non triviales comme d'avoir des incidences obliques pour les deux faisceaux tant que $\vec{k}_1 + \vec{k}_2$ reste perpendiculaire à la cellule. Il est ainsi possible de jouer sur l'angle d'incidence pour optimiser pour une cellule d'épaisseur donnée le rétrécissement Dicke. Si l'angle d'incidence est proche de celui de Brewster (i_B), les deux longueurs d'onde n'étant pas trop différentes, l'effet Fabry-Perrot associé à la spectroscopie dans une cellule mince peut être supprimé.

Théoriquement, dans une cellule de taille macrométrique, quand les deux faisceaux ont des fréquences proches, si les deux faisceaux sont contra-propageants le signal transmis subit un faible élargissement Doppler. Dans une configuration où les faisceaux sont co-propageants, le signal transmis subi deux fois l'élargissement Doppler alors qu'il ne l'aurait subi qu'une seule fois s'il n'y avait qu'un seul faisceau. Dans le cas d'une cellule mince, nous avons montré que c'est le régime transitoire qui caractérise la réponse optique obtenue, rendant les deux configurations comparables (Figure 4.12). La situation obtenue est alors toujours équivalente à une situation de rétrécissement Dicke. Ce rétrécissement est optimal, de manière similaire au Dicke avec un seul photon, quand l'épaisseur de la cellule (L) est telle que $L = \Lambda/2$ avec $\Lambda = 2\pi \left| \vec{k}_1 + \vec{k}_2 \right|$.

Comme test préliminaire, nous avons montré expérimentalement la possibilité d'observer un signal non négligeable provenant d'une transition à deux photons dans une cellule de 315 nm d'épaisseur remplie de césium pour deux faisceaux contra-propageants (Figure 4.13). Nous n'avons pas observé un rétrécissement Dicke mais cette expérience nous a permis de prouver la possibilité d'observer un signal et d'avoir une idée plus précise de l'amplitude des signaux.

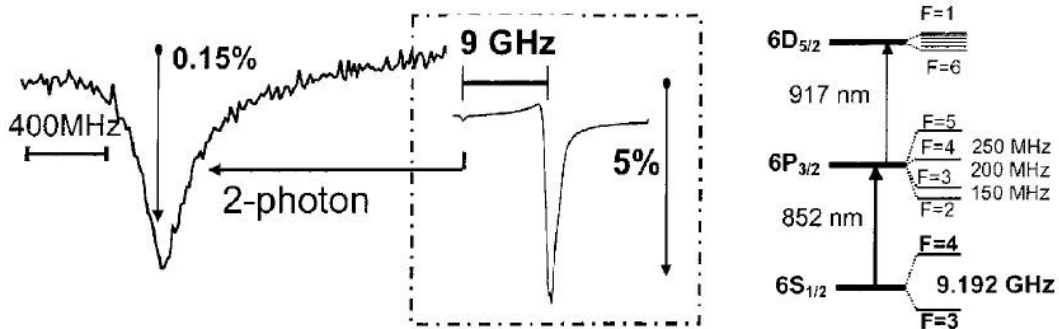


Figure 4.13 — Spectre de transmission obtenu dans une cellule de 315 nm d'épaisseur remplie d'une vapeur de Césium ($T = 220\text{ }^{\circ}\text{C}$) avec un faisceau pompe fixé sur la transition $6S_{1/2}(F = 3) - 6P_{3/2}$ et un faisceau sonde autour de la transition excitée $6P_{3/2} - 6D_{5/2}$ (917 nm). Le spectre à gauche est un zoom de la résonance à deux photons $6S_{1/2}(F = 4) - 6D_{5/2}$. [Figure 4 de l'article [1]].

4.4 Conclusion et perspectives

La loi de dépendance en z^{-3} de l'interaction de vW est donc bien vérifiée pour la transition $6P_{3/2} \rightarrow 6D_{3/2}$ (917 nm du césium) pour des distances allant de 50 nm à 130 nm. Des travaux complémentaires ont été effectués sur la raie de résonance D_1 (894 nm) du Césium. Si l'absence d'une raie de pompage, permettant modulation et démodulation à la détection, rend plus délicate la détection, des résultats reproductibles sont accessibles pour des épaisseurs de cellule jusque 25-30 nm, et les prédictions théoriques deviennent insensibles aux incertitudes entraînées par l'étape du pompage. Pourtant, les résultats indiquent pour C_3 une valeur plus grande que théoriquement prédite. Cet écart serait dû au trop fort parallélisme des fenêtres de nos nanocellules (nécessité de faire des mesures avec de nouvelles cellules avec un parallélisme plus faible) ou à des collisions fortes qui nécessiteraient une modélisation plus complexe de C_3 .

Dans le cas d'un couplage entre l'émission de l'atome de césium et son absorption par la surface de Yag, de fortes différences (forme, amplitude) ont été trouvées par rapport à un cas sans couplage. Cette différence est peut être due à un transfert réel d'énergie avec les surfaces. Une perspective de ce travail est de modifier notre modélisation pour tenir compte du couplage atome-surface et aussi des images multiples qui ne sont plus négligeables ici pour reproduire les spectres. Un autre rêve récurrent de l'équipe (voir les perspectives des articles [36, 60]) et qui a orienté la suite de nos recherches est l'étude de l'interaction de vW dans le cas d'une seule surface chauffée (donc émissive) plus ou moins en résonance avec les transitions atomiques du césium. Ce travail est longuement développé dans le chapitre suivant et a été encouragé par la modélisation théorique développée en 2006 par Marie-Pascale Gorza et Martial Ducloy de l'interaction de vW dans le cas d'un atome proche d'une surface dispersive et à température finie [2].

Parallèlement à ce travail, nous avons trouvé une géométrie permettant de généraliser le rétrécissement Dicke avec une transition à deux photons dans une cellule mince. Le premier test préliminaire que nous avons réalisé est encourageant. L'extension au cas d'une transition de type Raman, plutôt que deux photons, paraît alors prometteuse pour une détection de l'interaction de surface pour un atome dans l'état fondamental.

4.5 Articles en relation avec ce chapitre

Les trois articles [59, 61, 65] sont en relation avec ce chapitre. Ils sont reproduits à la fin de ce manuscrit.

Chapitre 5

Effet en température de l'interaction van der Waals

Cette recherche est menée dans l'équipe depuis 2006 et est toujours en cours. Elle est la suite directe du chapitre précédent et s'intéresse à l'étude de l'interaction de vW dans le cas d'une seule surface chauffée (donc émissive) plus ou moins en résonance avec les transitions atomiques du césium.

5.1 Introduction

L'attraction universelle à longue portée atome-surface de type van der Waals (Casimir-Polder en champ proche) est susceptible d'être exaltée de façon résonnante (éventuellement avec un changement de signe, la transformant en répulsion) quand l'émission virtuelle atomique se couple de façon résonnante à un processus d'absorption virtuelle par un mode de surface [60,64]. Mais que ce passe-t-il si l'on chauffe la surface ? En 1984, Hollberg, a déplacé en énergie des niveaux de Rydberg en présence d'un rayonnement du corps noir [67]. En 1998, Lai et Hinds ont montré qu'il était possible de modifier la durée de vie d'atomes de Rydberg en cavité par absorption de photons thermiques [68]. Greffet quant à lui s'est intéressé aux propriétés du rayonnement thermique en champ proche. Il a montré que l'existence d'ondes de surface conduit à des effets de cohérence inattendus. Ces effets ont été mis en évidence de façon indirecte il y a quelques années en réalisant de véritables antennes infrarouges très directionnelles [69,70].

A l'équilibre thermique, une dépendance thermique de l'interaction atome-surface a été prévue théoriquement en 1997 [71] mais n'a pas été démontrée expérimentalement. En 2007 la première mesure de la modification de l'interaction de CP effectuée dans des conditions $T \neq 0$ a été réalisée par le groupe de E. Cornell [48]. Les effets thermiques y sont notablement exaltés par un déséquilibre thermique entre la surface (600 K) et le champ du vide (300 K). L'expérience (avec un condensat d'atomes de rubidium) a été effectuée à 6-10 μm d'une surface diélectrique de silice fondue. En 2006, Marie-

Pascale Gorza et Martial Ducloy ont modélisé la dépendance thermique de l'interaction atome-surface entre un atome neutre situé dans le champ électromagnétique du vide en équilibre thermique avec une surface diélectrique dispersive à température non nulle [2]. Pour que la dépendance en température soit forte, il est nécessaire de travailler avec un matériau dont les résonances de surface $k_B T$ (k_B constante de Boltzmann et T température de la surface) émises soient proches des transitions atomiques ($\hbar c/\lambda$). Ce couplage ne peut être efficace que si le mode d'émission virtuelle est suffisamment peuplé thermiquement ($k_B T \geq \hbar c/\lambda$). Pour étudier cette dépendance en température, nous nous sommes intéressés à l'interaction entre un atome excité de Césium ($8P$) qui présente des absorptions virtuelles autour de $39 \mu m$ ($8P_{3/2} \rightarrow 7D_{1/2}$) et $29 \mu m$ ($8P_{1/2} \rightarrow 7D_{1/2}$) (voir figure 5.1) et des fenêtres en CaF_2 ou BaF_2 qui présentent, respectivement, une résonance de surface autour de $25 \mu m$ et $35 \mu m$. Pour cela, nous avons utilisé la spectroscopie de réflexion sélective (RS).

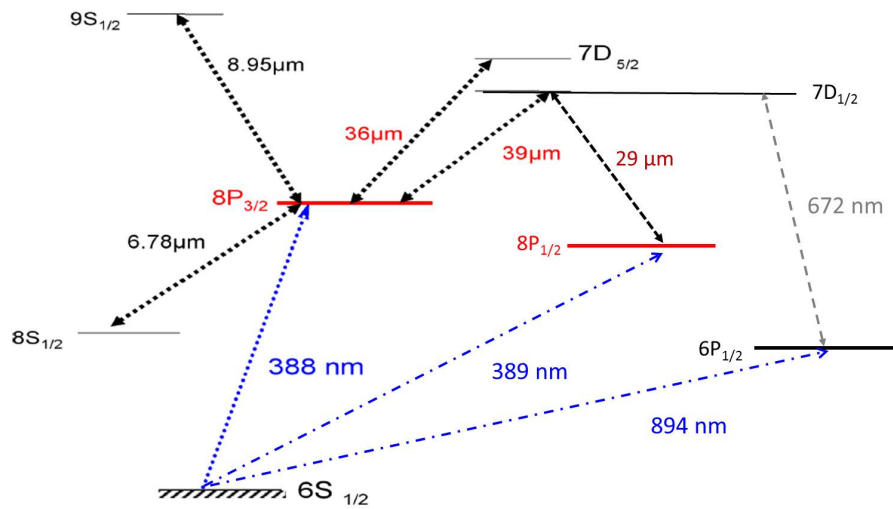


Figure 5.1 – Niveaux atomiques du Césium

Avant de présenter notre expérience, je vais expliquer comment nous avons évalué la dépendance en température des propriétés optiques de surface puis le coefficient de vW C_3 .

5.2 Dépendance en température des propriétés optiques de surface et évaluation du coefficient de van der Waals [2, 3]

5.2.1 Modélisation de la dépendance en température du coefficient C_3

Dans le régime électrostatique van der Waals (vW), l'interaction varie avec la distance à la paroi en C_3^i/z^{-3} où z est la distance atome-surface. Le coefficient C_3^i de vW dépend de la surface aussi bien que de l'atome et de son niveau d'énergie $|i\rangle$. Pour calculer C_3^i , dans le cas d'une surface parfaitement réfléchissante, on doit faire la somme des moments dipolaires électriques (D) sur toutes les transitions atomiques autorisées $|i\rangle \rightarrow |j\rangle$.

$$C_3^i = \frac{1}{12} \sum_j |\langle i | D | j \rangle|^2. \quad (5.1)$$

Dans le cas d'une surface réelle, on doit pondérer C_3^i par le coefficient de réflexion diélectrique r_{ij} qui dépend des propriétés diélectriques de la surface. Si on néglige la réponse dispersive de la surface, ce coefficient de réflexion est simplement donné par le coefficient de Fresnel et est indépendant de la température :

$$r_{ij} = \frac{\epsilon - 1}{\epsilon + 1} \quad (5.2)$$

où ϵ est la constante diélectrique en volume du matériau composant la surface. Marie-Pascale Gorza et Martial Ducloy ont développé un modèle QED complet dans lequel ils ont tenu compte de la réponse dispersive de la surface et donc d'une possible contribution résonante entre la surface (émission/absorption) et une transition atomique (absorption/émission) [2]. Ils ont considéré une situation où un atome est placé, au voisinage d'une surface, dans un rayonnement en équilibre thermique avec la surface. On a alors :

$$C_3^i(T) = \frac{1}{12} \sum_j r_{ij}(\omega_{ij}, T) |\langle i | D | j \rangle|^2 \quad (5.3)$$

avec

$$r_{ij}(\omega_{ij}, T) = r_{nonRes} + r_{Res}. \quad (5.4)$$

Le terme non résonant (r_{nonRes}) est de la forme :

$$r_{nonRes} = + \frac{4kT}{\hbar} \sum_{p=0}^{\infty} \frac{\epsilon(i\xi_p) - 1}{\epsilon(i\xi_p) + 1} \frac{\omega_{ij}}{\omega_{ij}^2 + \xi_p^2} \quad (5.5)$$

avec $\xi_p = k(2\pi kT/\hbar)$, k la constante de Boltzmann et T la température de la surface. La somme pour $p=0$ doit être multipliée par 1/2. Cette somme est une somme de Matsubara. Ce terme est toujours positif et augmente linéairement avec la température T dans la limite $kT \geq \hbar\omega_{ij}$. Il dépend de la fréquence atomique (ω_{ij}) mais aussi des

propriétés optiques du matériau sur tout le spectre en fréquence ($\epsilon(i\xi_p)$). Il tient son origine de la dépendance en distance du déplacement de Lamb dû aux fluctuations du vide et thermiques sur tout le spectre en fréquence.

Les termes en résonance (r_{Res}) tiennent compte du nombre de photons dans le mode de surface à fréquence ω_{ij} . Pour une transition atomique en absorption couplée à une émission d'un mode de surface ($\omega_{ij} > 0$) c'est-à-dire dans la cas d'une surface chauffée ($T \neq 0K$) :

$$r_{Res} = -2Re\left[\frac{\epsilon(|\omega_{ij}|) - 1}{\epsilon(|\omega_{ij}|) + 1}\right] \frac{e^{-\hbar|\omega_{ij}|/kT}}{(1 - e^{-\hbar|\omega_{ij}|/kT})} \quad (5.6)$$

Ce terme a un signe opposé par rapport au terme non résonant. Naturellement, le nombre de photons dans le mode s'annule pour $T=0$ et r_{Res} vaut alors 0. Ce terme ne donne une contribution significative que pour des température telles que $kT \geq \hbar\omega_{ij}$. Il dépend fortement des propriétés optiques du matériau sur tout le spectre en fréquence via sa réponse de surface ($S(\omega) = (\epsilon(\omega) - 1)/(\epsilon(\omega) + 1)$). La partie réelle de la réponse de surface $S(\omega) = (\epsilon(\omega) - 1)/(\epsilon(\omega) + 1)$ a une forme dispersive et présente un changement de signe (voir figure 5.3) autour de la fréquence du mode de surface. Si une transition atomique est proche d'un mode de surface, suivant que la transition atomique se trouve sur l'aile gauche, droite ou au centre du mode de surface, $Re[S]$ peut changer rapidement de valeur et surtout de signe. Si la transition atomique se trouve sur l'aile gauche, $Re[S] < 0$, $r_{Res} > 0$ alors que $r_{nonRes} > 0$, $r_{ij}(\omega_{ij}, T) = r_{nonRes} + r_{Res}$ augmente ainsi que le coefficient C_3^i . L'interaction est de plus en plus forte. Inversement, si la transition atomique se trouve sur l'aile droite, $Re[S] > 0$, $r_{Res} < 0$ et $r_{nonRes} > 0$, $r_{ij}(\omega_{ij}, T) = r_{nonRes} + r_{Res}$ diminue ainsi que le coefficient C_3^i . L'interaction est de plus en plus faible voire répulsive. Pour calculer le coefficient de l'interaction de vW entre un atome et une surface, il est donc primordiale de connaître le mieux possible la réponse de surface $S(\omega)$ sur tout le spectre et ses variations avec la température.

Il existe très peu de données dans la littérature. De plus, les quelques données trouvées sur la constante diélectrique $\epsilon(\omega)$ étaient souvent contradictoires pour plusieurs raisons :

- Utilisation de différentes techniques expérimentales,
- Différences entre les échantillons utilisés sur les propriétés optiques (impuretés, qualité du polissage de la surface, traitements chimiques ...).

Les données sur le CaF_2 sont limitées à des mesures faites à température ambiante [72–74] et à 100 K [73]. Pour le BaF_2 des mesures de réflectance ont été effectuées à 295, 373, 573 et 773 K [72, 75, 76]. Il y a de grands désaccords entre ces articles et la faible résolution des mesures réalisées nous a motivés pour réaliser de nouvelles mesures. Pour le saphir, des études systématiques ont été réalisées en fonction de la température [77–79].

Le plus souvent les différences entre ces données sont sans conséquences pour l'évaluation des résonances en volume et l'étude des propriétés optiques des matériaux. Mais, pour les résonances atome-surface, le filtrage de la réponse par une fréquence

atomique déterminée induit une grande sensibilité aux incertitudes sur la constante diélectrique [80]. Avant de réaliser nos expériences, nous avons donc décidé de mesurer la dépendance en température des propriétés optiques de nos surfaces et d'évaluer leurs coefficients de van der Waals. Une autre motivation pour la réalisation de ces mesures était la non-compatibilité avec nos prédictions théoriques de nos mesures du coefficient C_3 de l'interaction entre un atome de césium dans le niveau ($8P_{3/2}$) et une surface chauffée en CaF_2 (discutée au paragraphe 5.3.4).

5.2.2 Dépendance en température des propriétés optiques de surface

Des mesures de réflectance en température (295 - 773 K), dans la région spectrale de l'infrarouge lointain, ont été réalisées au Laboratoire CEMHTI d'Orléans par l'équipe Grandeurs radiatives et thermiques des matériaux dirigée par Patrick Echegut à l'aide d'un spectromètre à transformée de fourier dans l'infrarouge (FTIR) pour des surfaces en CaF_2 , en BaF_2 et aussi en saphir (Al_2O_3) avec son axe optique perpendiculaire à la surface pour éviter toute biréfringence. Les mesures sur le saphir ont été réalisées car c'est un matériau de référence pour nous. A partir de ces données expérimentales, j'ai modélisé et réévalué le coefficient C_3 de vW en fonction de la température pour le CaF_2 , BaF_2 et le saphir ayant un axe optique perpendiculaire à sa surface avec l'aide de Thierry Passerat De Silans (PhD) et Pedro Chaves De Souza Segundo (Post-doc).

Après avoir comparé plusieurs modèles, nous avons reproduit les courbes de réflectance expérimentale (Figure 5.2) à l'aide d'un modèle semi-quantique [81] pour la constante diélectrique. Le modèle classique pour la constante diélectrique considère que chaque mode de phonon a un taux d'amortissement constant et donc sans dépendance en fréquence. Le modèle semi-quantique prend lui en compte l'anharmonicité du potentiel. Il a l'avantage par rapport aux autres modèles d'ajuster les courbes de réflectance avec le bon nombre de phonons prévus théoriquement. Il est aussi le seul modèle permettant de reproduire les petites oscillations présentes dans la zone de Reststrahlen et qui sont attribuées à des processus de relaxation à deux phonons ou plus (Figure 5.2).¹ De telles structures n'étaient pas clairement visibles auparavant dans la littérature [72, 73] et n'étaient donc pas prises en compte.

5.2.3 Évaluation du coefficient de van der Waals en fonction de la température

Nous avons ainsi obtenu l'évolution en température de $\epsilon(\omega)$. A partir de ces données, nous avons pu reconstituer la dépendance de surface $S(\omega)$ en température (voir figure 5.3) qui est directement liée à la valeur du coefficient C_3 de vW (voir paragraphe 5.2.1). L'évolution en température du coefficient C_3 déduite est représentée sur

1. La zone de reststrahlen est caractérisée par une forte réflectivité (proche de 100 %) et une forte atténuation de l'onde électromagnétique à l'intérieur du matériau. Dans cette région, il n'y a donc plus de transmission.

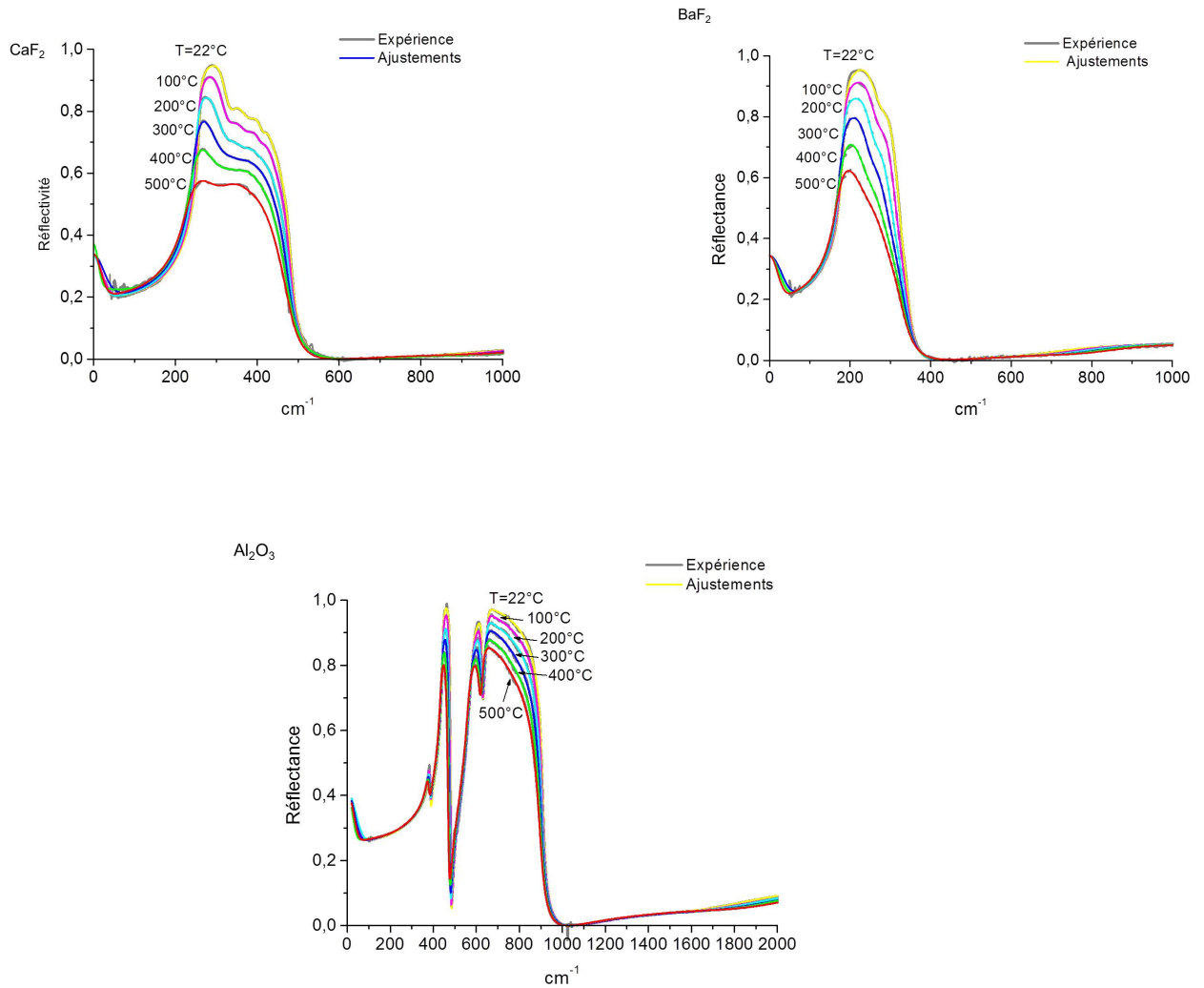


Figure 5.2 — Spectres de réflectance mesurés pour le CaF_2 (en haut à gauche), le BaF_2 (en haut à droite) et Al_2O_3 (en bas) à 295 K, 373 K, 473 K, 573 K, 673 K et 773 K avec les meilleurs ajustements obtenus en utilisant un modèle semi-quantique [81]. [Figures 1, 2 et 3 de l'article [3]].

la figure 5.4 (courbes a) pour un atome de césium dans le niveau $8P_{3/2}$ proche d'une surface en CaF_2 , BaF_2 ou saphir. Par comparaison, nous montrons aussi, sur la figure 5.4 (courbes b), l'ancienne valeur de C_3 que nous obtenions par le modèle [2] sans tenir compte d'une évolution de la constante diélectrique en température (constante diélectrique prise à température ambiante [72]). Les figures 5.4 (courbes c) et (courbes d) montrent l'évolution de C_3 si l'on considère que la constante diélectrique évolue linéairement avec la température avec comme point de départ les valeurs trouvées dans la littérature [72, 73]. La prise en compte des changements de la constante diélectrique avec la température (élargissement et déplacement de la résonance de surface) a surtout

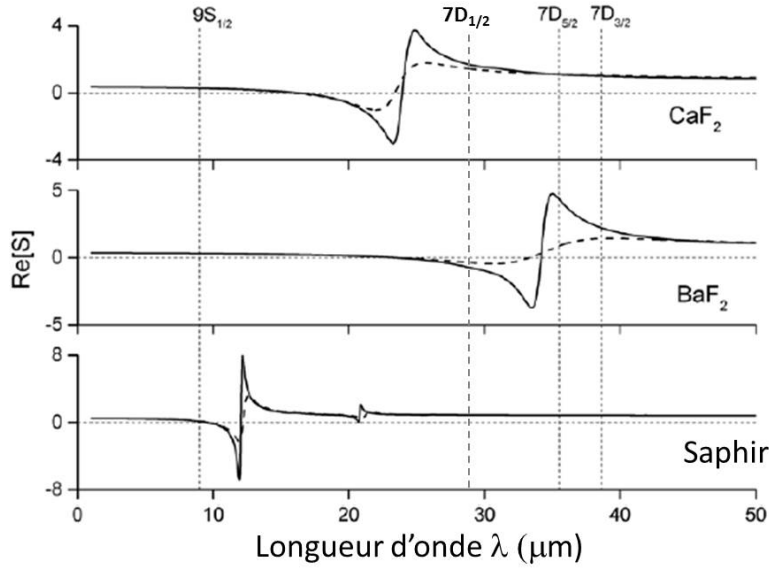


Figure 5.3 — Partie réelle de la dépendance en surface S pour le CaF_2 , BaF_2 et le saphir en fonction de la longueur d’onde. La courbe solide correspond aux mesures obtenues à température ambiante, en pointillés à 770 K. Les positions des couplages dominants avec les niveaux atomiques du Césium (voir figure 5.1) sont indiquées par des traits pointillés verticaux . La transition $8P_{3/2} \rightarrow 7D_{5/2}$ à $36.09 \mu m$ est très proche du polariton du BaF_2 à $35 \mu m$, elle se trouve sur l’aile droite du polariton du CaF_2 à $24 \mu m$ et se situe très loin de celui du saphir à $12 \mu m$. La transition $8P_{1/2} \rightarrow 7D_{1/2}$ à $29 \mu m$ se rapproche du polariton du CaF_2 tout en restant sur son aile droite , elle est passée sur l’aile gauche du polariton du BaF_2 à $35 \mu m$ par rapport à la transition $8P_{3/2}$ et elle se situe toujours très loin de celui du saphir à $12 \mu m$. [Figure 2 de l’article [5]].

modifié les prédictions pour l’interaction entre un atome $Cs(8P_{3/2})$ avec une surface en BaF_2 , car la résonance de surface de ce matériau est voisine des transitions atomiques. Elle prédit un forte dépendance en température, avec un retour à une interaction quasi - nulle; voire attractive aux hautes températures après un régime répulsif atteint en principe bien avant la température ambiante. Pour le CaF_2 , peu de changements sont observés. L’interaction diminue avec l’augmentation de la température tout en restant positive. Dans le cas du saphir, aucune des transitions atomiques importantes n’est en résonance avec les modes de surface du saphir. La contribution résonante est donc négligeable et les changements de C_3 sont supposés faibles avec la température.

Nous avons aussi évalué le coefficient de vW pour un atome de césium dans le niveau $8P_{1/2}$ proche d’une surface en CaF_2 , BaF_2 ou saphir (figure 5.5).Aucun changement visible n’est prévu pour le saphir. On note un changement plus rapide de C_3 avec la température pour le CaF_2 , par rapport à celui obtenu pour la transition $8P_{3/2}$, à cause du couplage plus fort avec la transition importante pour l’interaction de vW avec la

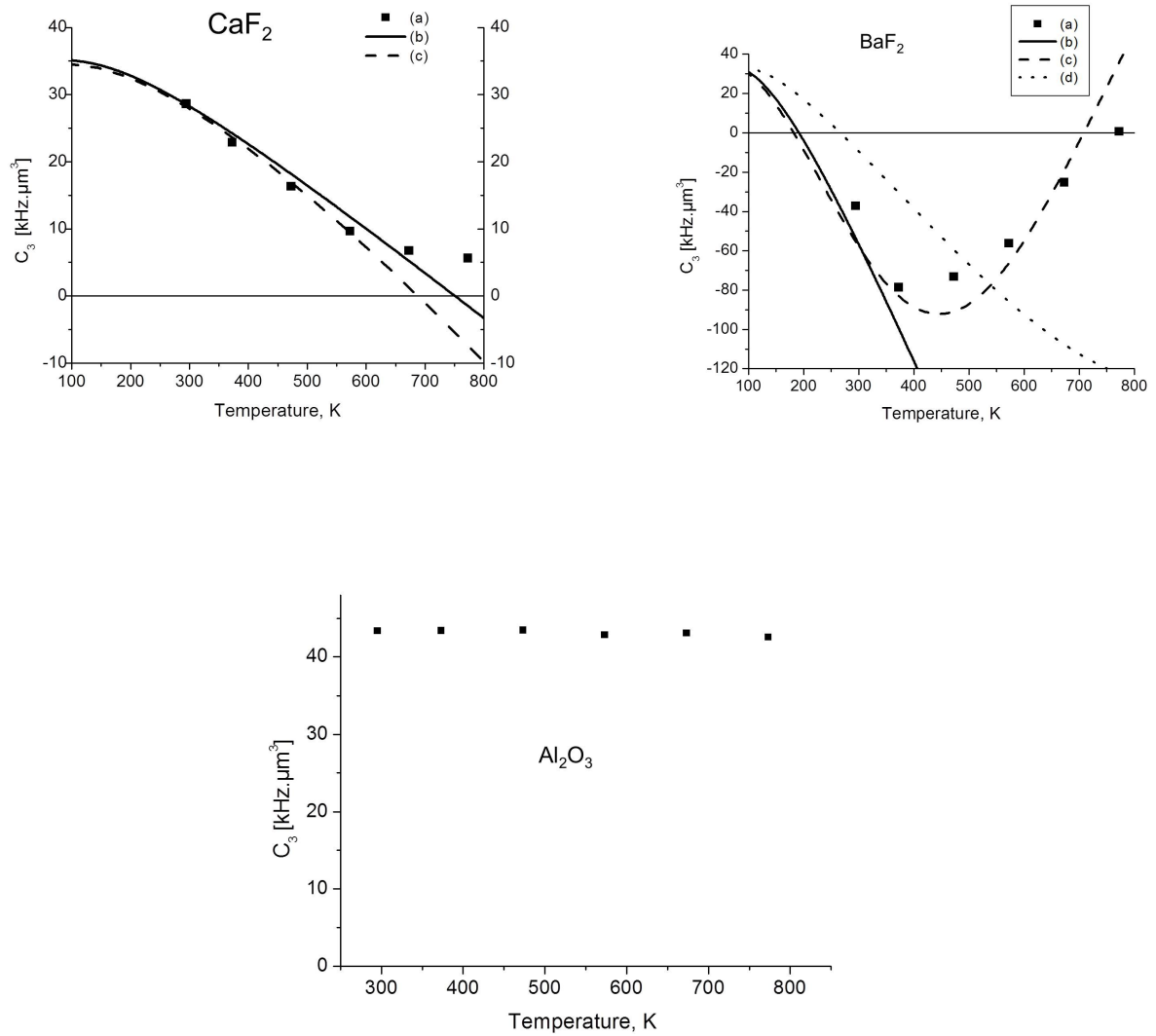


Figure 5.4 — Changement du coefficient C_3 de vW avec la température pour un atome de $Cs(8P_{3/2})$ proche d'une surface de CaF_2 , de BaF_2 et Al_2O_3 . Les points discrets (a) montrent les résultats prenant en compte la dépendance en température de la constante diélectrique. Les courbes en lignes pleines (b) montrent les résultats que nous obtenions par notre modèle théorique [2] avec une constante diélectrique prise à température ambiante [72]. Les courbes en lignes pointillées (c) tiennent compte d'une dépendance linéaire de la constante linéaire [73] avec comme point de départ une constante diélectrique mesurée à température ambiante [72]. La courbe (d), seulement pour le BaF_2 , considère un modèle pour la constante diélectrique totalement dérivé des données de [73]. [Figures 13, 14 et 15 de l'article [3]].

résonance de surface. On obtient d'ailleurs un changement de signe de C_3 autour d'une température plutôt basse de 550 K. Pour le BaF_2 , comme la transition atomique est passée sur le côté de la résonance de surface (figure 5.3) où $Re(S(\omega)) < 0$, la contribu-

tion résonante à l'interaction de vW implique une interaction toujours attractive qui augmente avec la température.

Une fois l'évolution de C_3 avec la température précisément connue dans le cas de nos surfaces, nous l'avons comparée à l'expérience correspondante.

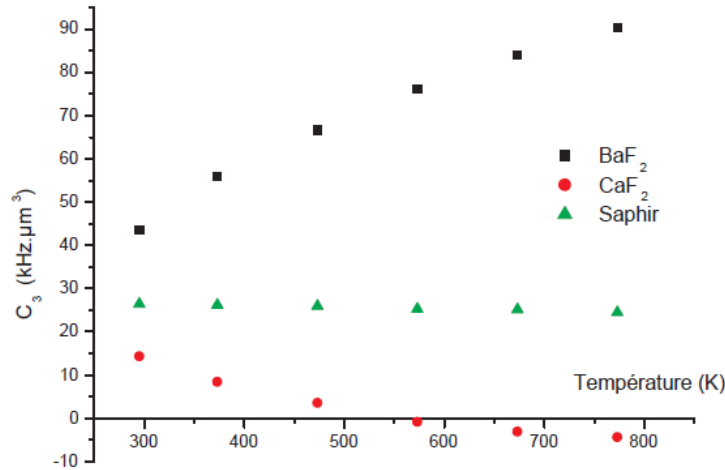


Figure 5.5 – Dépendance en température de C_3 pour l'interaction entre un atome de césium ($8P_{1/2}$) et des surfaces de CaF_2 , BaF_2 et saphir prenant en compte la dépendance en température de la constante diélectrique. [Figure 2.36 de la thèse de Thierry Passerat De Silans [82]]

5.3 Étude de l'interaction atome-surface entre un atome excité et une surface thermiquement émissive en CaF_2

5.3.1 Cellule en CaF_2

Une cellule très spéciale de vapeur scellée a été réalisée sur notre demande en Arménie par David Sarkisyan de l'Institut de Recherche Physique d'Ashtarak en Arménie, qui résiste à une vapeur de Cs chaude, et qui possède une fenêtre en fluorure CaF_2 d'un côté et une fenêtre en saphir de l'autre (Figure 5.6). Il faut souligner que le choix d'un matériau fluorure entraîne d'importants problèmes techniques. Les fluorures sont des matériaux mécaniquement fragiles, sensibles aux chocs thermiques, et dont les coefficients d'expansion thermique sont trop différents de ceux du saphir pour rendre envisageable un collage, même minéral. Ceci a amené à une conception spéciale de la cellule, où la fenêtre en fluorure est elle-même de très grande épaisseur, lui permettant

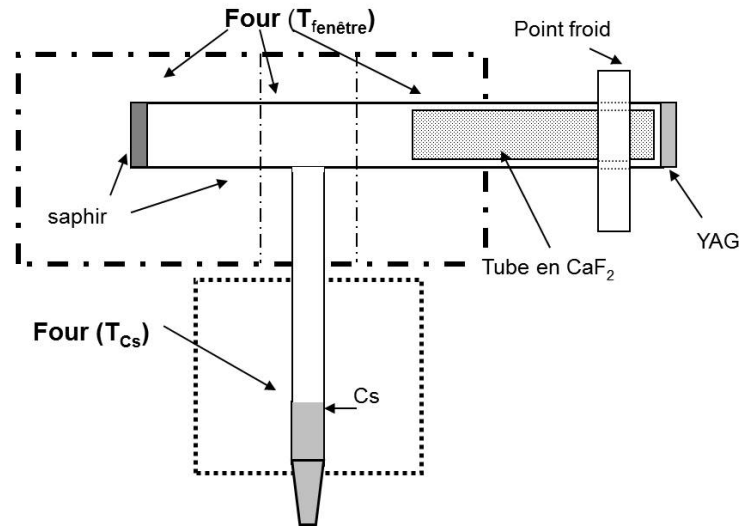


Figure 5.6 — Schéma de principe de la cellule à fenêtre fluorure, dont la grande longueur permet d'avoir une des faces en contact avec la vapeur chaude à $T_{fenetre} \succ T_{Cs}$, tandis que l'autre face reste à température ambiante, en quasi-contact avec la fenêtre YAG (à droite). La tubulure en T qui contient la vapeur de césium est elle-même en saphir. [Figure 1 de l'article [4]].

d'encaisser un gradient thermique. La partie en contact avec la fenêtre YAG (à droite de la cellule), qui ferme la tubulure de vapeur reste à température ambiante, tandis que seule une partie de la cellule est chauffée (l'interface fluorure/vapeur et la surface de saphir) et peut monter jusqu'à environ $350\text{ }^{\circ}\text{C}$. Le système de chauffage consiste en trois fours indépendants, un four pour le CaF_2 , un four pour la surface en saphir et un dernier four pour contrôler la densité de césium dans la cellule donc autour du réservoir. La fenêtre de YAG ne peut cependant pas être le point de plus basse température de la cellule, sinon la vapeur de césium arrivant dans cette région se condenserait dans l'interstice YAG/ CaF_2 ². C'est pourquoi nous avons créé un point froid (5°C) à environ 1 cm de la fenêtre de YAG pour que la vapeur soit piégée avant d'arriver dans l'interstice YAG/ CaF_2 . Les trois fours sont contrôlés par un programme de type PID, que j'ai conçu. Ce programme assure que la température des surfaces en CaF_2 et en Yag soient les mêmes, stabilise la température du queusot pour que la densité soit stable et s'assure que la température du queusot soit toujours inférieure à celle des deux autres fours pour éviter toute condensation sur les surfaces utiles.

Un point remarquable, et fort appréciable pour extraire l'information sur l'interaction de surface indépendamment des conditions expérimentales (qui sont éventuellement responsables d'un élargissement pour la transition étudiée), est qu'avec cette conception de cellule, il est possible de réaliser en simultanée une expérience de réflexion sélective (technique résumée dans le paragraphe 5.3.2) à une interface avec une fenêtre

2. épaisseur estimée à environ $100\text{ }\mu\text{m}$ à partir de l'absorption linéaire de la raie D_1 à température ambiante

en CaF_2 et avec une fenêtre saphir. En plus de la réflexion sélective (RS), le montage inclut une expérience auxiliaire de référence de fréquence par absorption saturée (AS). Le schéma du montage est montré sur la figure 5.7. Ce montage inclut un système d'acquisition et de traitement du signal que j'ai totalement informatisé et un Fabry-Perot qui contrôle le balayage du laser.

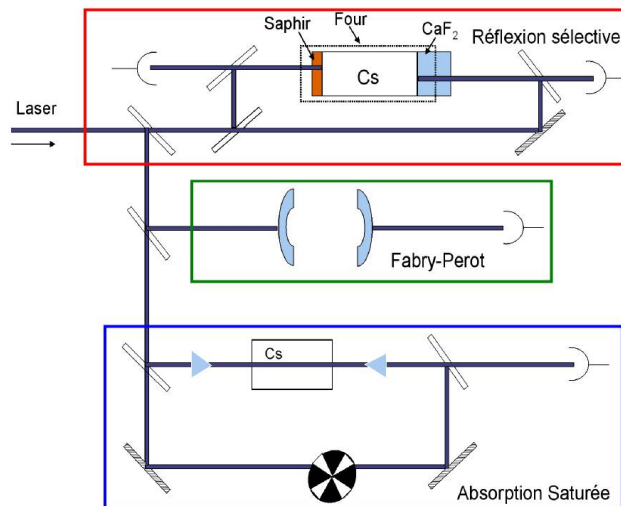


Figure 5.7 — Schéma du montage expérimental. [Figure 4.1 de la thèse de Thierry Passerat De Silans [82]]

5.3.2 La réflexion sélective

La technique de la réflexion sélective (RS) est une technique optique permettant d'étudier les effets de surface. Elle consiste à mesurer les variations du coefficient de réflexion à une interface diélectrique - vapeur atomique lorsque la fréquence d'un faisceau incident est balayé autour des fréquences de résonances de la vapeur. Cette technique a la particularité de sonder le milieu gazeux sur une faible profondeur (de l'ordre de la longueur d'onde optique), d'où son intérêt pour mesurer des effets de surface. Elle est très intéressante pour des milieux gazeux à relativement haute pression qui deviennent opaque par transmission. La différence de comportement entre les atomes qui arrivent vers la surface et qui sont en régime permanent avec le champ et ceux qui la quittent et qui sont en régime transitoire (l'excitation optique a été détruite lorsque l'atome est entré en collision avec la surface) est à l'origine de la présence dans le spectre de réflexion sélective d'une singularité sub-Doppler superposée au large signal dispersif prévu par une théorie classique de l'indice [83] (en $v_z = 0$ où v_z est la composante de la vitesse selon l'axe normal à la paroi). Si maintenant on module en fréquence le faisceau laser incident et que l'on détecte la modulation en amplitude induite sur le faisceau réfléchi, la modulation (FM) agit comme un dérivateur de la forme de raies, ce qui

favorise la forme de raie étroite. Cette réponse sans effet Doppler est essentiellement due aux atomes de vitesse "nulle" ($v_z = 0$).

En présence d'une interaction atome-surface, les résonances atomiques sont modifiées ainsi éventuellement que la largeur de leur transition. Ces modifications sont mesurables grâce à la technique de réflexion sélective. Pour mesurer l'interaction vW, il faut ensuite comparer les spectres expérimentaux de RS obtenus avec une bibliothèque de courbes théoriques développé par l'équipe [83]. Les spectres de réflexion sélective de cette bibliothèque sont caractérisés par une seule constante sans dimension $A = C_3 k^3 / (\gamma/2)$ où C_3 est le constante de vW que l'on cherche à déterminer, k le vecteur d'onde et γ la largeur de la transition optique. Chaque valeur de A conduit à un spectre de forme et symétrie différente (figure 5.8).

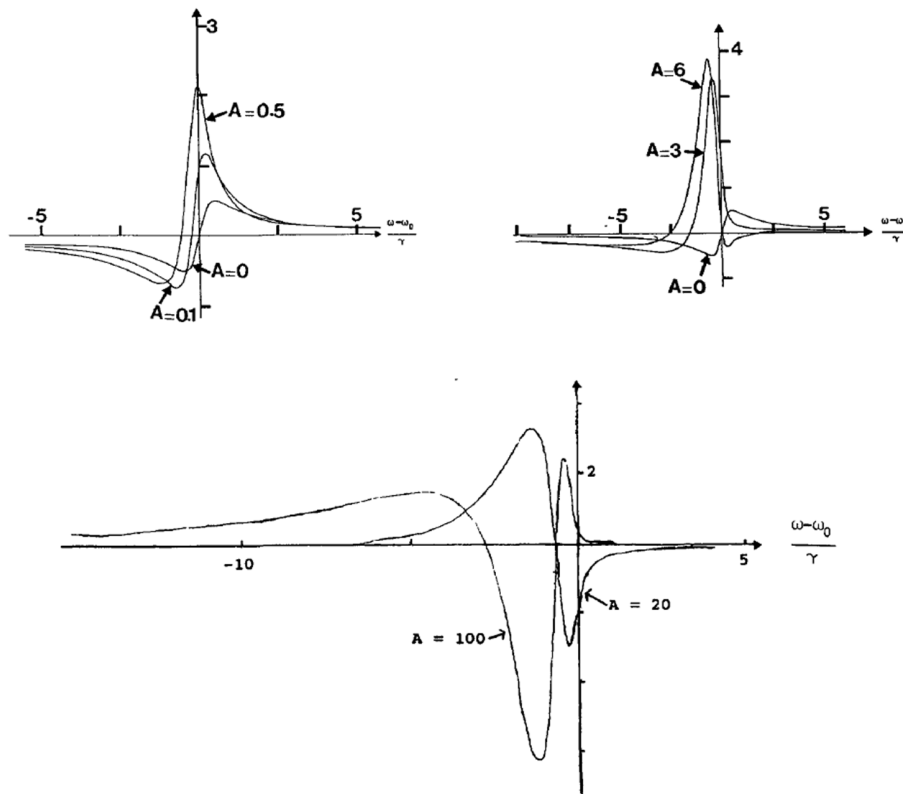


Figure 5.8 — Spectres de réflexion sélective en FM (signal dérivé) pour différentes valeurs de A [Figure 5 de l'article [83]]

5.3.3 Expériences préliminaires pour valider notre cellule [4]

La cellule a été d'abord testée dans la situation bien connue par l'équipe de la spectroscopie RS sur la raie de résonance D_1 du Césium ($6S_{1/2} \rightarrow 6P_{1/2} = 894 \text{ nm}$), qui ne présente aucun couplage particulier dans l'infrarouge lointain avec les modes de surface du CaF_2 ou du saphir (voir figure 5.1). L'expérience a été menée avec Athanasios Laliotis qui était à ce moment là en stage post-doctoral pour une année dans l'équipe.

Un tel test était particulièrement nécessaire parce que nous avons appris que des impuretés étaient présentes dans le prototype de cellule que nous avons entrepris de tester. En effet, malgré une procédure de dégazage de la cellule pendant 10h à $350 \text{ }^\circ\text{C}$ par David Sarkisyan, la cellule a été contaminée à la fabrication par des impuretés. Un excès de collisions changeant la vitesse s'avérait responsable d'un élargissement considérable et d'un déplacement des raies d'absorption saturée. Pour une détection de l'absorption saturée avec une modulation plus rapide dans cette cellule, le signal obtenu ne subissait plus cet élargissement collisionnel. Ce comportement est typique de collisions car les changements de vitesse des atomes prennent un certain temps pour avoir lieu. Un avantage de la spectroscopie RS linéaire est qu'elle est pratiquement insensible aux collisions changeant la vitesse. On observe seulement un effet résiduel des collisions, responsable d'une largeur optique (20 MHz) légèrement supérieure à la largeur naturelle (5 MHz), même aux faibles densités de Césium, et pour un déplacement de quelques MHz .

Dans ce contexte rendu délicat par ces impuretés, nous avons réussi à montrer que l'interaction vW exercée par chaque type de fenêtre (CaF_2 et saphir) reste cependant évaluable, quoique faible. En effet, même en l'absence d'élargissement collisionnel ou d'impuretés, la raie D_1 est typique d'un régime d'interaction vW faible, où l'interaction vW n'introduit qu'une perturbation par rapport au spectre RS standard et notamment un déplacement spectral qui reste très inférieur à la largeur naturelle de la transition. Dans ce but, j'ai raffiné notre technique d'ajustement numérique des spectres RS ([60,64] et refs. in), notamment par une technique d'ajustement simultané des deux formes de raie enregistrées simultanément [4]. En imposant ainsi des restrictions plus fortes sur les paramètres libres de l'ajustement, on parvient à augmenter la précision sur la détermination du coefficient vW dans ce régime de couplage vW faible. On y trouve en particulier que l'interaction vW est plus faible pour CaF_2 que pour le saphir, comme attendu d'après les valeurs de l'indice de réfraction. Ces mesures ont servi à tester la conception de la cellule qui permet de réaliser deux réflexions sélectives simultanément sur deux surfaces en même temps (CaF_2 et saphir) pour des conditions identiques (pression de vapeur atomique et température de surfaces).

Une deuxième cellule a été construite en Arménie. La cellule a été dégazée pendant 10h à $420 \text{ }^\circ\text{C}$. Elle ne présentait plus de déplacement de raie ni d'élargissement collisionnel sur nos mesures d'absorption saturée sur la raie D_1 . Nous nous sommes donc ensuite intéressés à des mesures de la réflexion sélective pour les transitions $6S_{1/2} \rightarrow 8P_{3/2}$ ($\lambda = 388 \text{ nm}$) ou $6S_{1/2} \rightarrow 8P_{1/2}$ ($\lambda = 389 \text{ nm}$), en vue de tester une dépendance résonnante

en température de l'interaction vW (voir figures 5.4 et 5.5).

5.3.4 Dépendance en température des spectres de réflexion sélective pour les transitions $6S_{1/2} \rightarrow 8P_{3/2}$ et $8P_{1/2}$ [5]

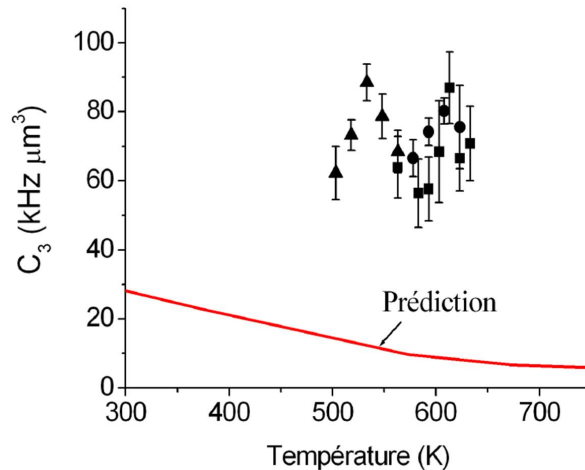


Figure 5.9 – Effets de la température sur le coefficient C_3 pour la transition $6S_{1/2} \rightarrow 8P_{3/2}$ et une surface chauffée en CaF_2 . Les points noirs représentent l'expérience et leurs incertitudes. La courbe rouge représente les prédictions théoriques [Figure 4.31 de la thèse de Thierry Passerat De Silans [82]]

Ce travail a été effectué avec Thierry Passerat De Silans (PHD), Pedro Chaves De Souza Segundo (post-doc) et Athanasios Laliotis (MCF). Comme pour l'expérience sur la raie D_1 , nous avons enregistré en simultanée les spectres de réflexion sélective sur la fenêtre saphir et sur la fenêtre CaF_2 . L'analyse de mesures systématiques de réflexion sélective sur l'interaction $Cs(8P_{3/2})$ et une surface en CaF_2 (figure 5.9) a montré un désaccord important avec les prédictions théoriques [2, 3]. Plus précisément, l'interaction atome-surface observée est tout à fait conforme à la forme attendue d'un potentiel en z^{-3} (z : distance atome-surface), mais ne montre pas de variation avec la température de surface. Les valeurs de C_3 obtenues pour le niveau $8P_{3/2}$ se situent autour de $70 \pm 20 \text{ kHz} \cdot \mu\text{m}^3$ en désaccord avec les prédictions théoriques. Des résultats similaires ont été obtenus pour le niveau $8P_{1/2}$.

Nous avons tout d'abord regardé si ce désaccord n'était pas dû à une répartition de charges sur la surface. Pour cela, le même type d'analyse avec un potentiel du type z^{-2} (interaction du dipôle atomique avec une charge distribuée sur la surface) a été réalisée. J'ai calculé les spectres correspondant correspondant à un tel potentiel et montré que nos mesures ne sont pas compatibles avec un tel potentiel. Le désaccord avec la théorie

a finalement été attribué à une dégradation de la surface, très fragile, de CaF_2 . En effet, la poursuite des expériences a montré une porosité au Cs de la fenêtre fluorure, qui laisse penser que l'état de surface de la fenêtre s'est fortement dégradé, de telle sorte que les prédictions concernant les modes de surface de la fenêtre perdent toute validité.

Au court des expériences précédemment décrites, la raie du Cs que nous avons choisi d'étudier ($6S_{1/2} - 8P_{3/2}$ à 388 nm et $6S_{1/2} - 8P_{1/2}$ à 389 nm), en raison de son couplage avec des niveaux voisins dans l'infrarouge thermique, s'est avérée présenter des résonances supplémentaires sub-Doppler d'origine inconnue apparaissant autour des transitions atomiques d'absorption saturée lorsque les faisceaux utilisés sont relativement intenses (typiquement $\geq 10mW/mm^2$), tant pour la pompe que pour la sonde (Figure 5.10). Ces expériences standard d'absorption saturée ont été obtenues avec un seul laser et un montage à faisceaux contre-propageant. Les structures hyperfines sont de signes positif (figure 5.10) ce qui indique une transmission plus forte du faisceau sonde quand le faisceau pompe est présent ce qui est typique d'une absorption saturée. Pour les résonances supplémentaires, elles ont un signe négatif ce qui indique que moins de lumière est transmise (plus de lumière est absorbée) en présence du faisceau pompe. Les résonances ont une largeur certes supérieure à celle des composantes hyperfines individuelles, mais qui s'avère inférieure à la structure hyperfine elle-même, elles ne présentent pas de structures hyperfines ce qui nous laisse penser que ces transitions ne sont pas de nature atomique. Ces structures avaient déjà été observées par l'équipe par le passé mais non étudiées à l'époque. Le désaccord entre les prédictions théoriques et les résultats expérimentaux de la réflexion sélective sur les transitions 6S-8P à l'interface du CaF_2 nous a encouragé à les étudier.

5.3.5 Observation de résonances sub-Doppler supplémentaires autour des transitions d'absorption saturée de Cs sur la transition 6S-8P [6]

Nous avons tout d'abord cherché dans la littérature si ces transitions étaient connues, les transitions des dimères de césium ayant été largement étudiées et ce n'était pas le cas. Nous avons alors exploré systématiquement ces raies supplémentaires sub-Doppler et réalisé diverses expériences. Nous avons trouvé que l'amplitude des résonances supplémentaires évolue de façon non linéaire avec l'intensité de la sonde contrairement à celle d'un pic usuel d'absorption saturée (figure 5.11). Cela nous a amené à considérer deux hypothèses à l'origine de ces structures supplémentaires : effets de propagation non-linéaires (autofocalisation de faisceau [84], émission conique [85] ...) ou formation de dimères (par collision à trois atomes [86] ou par photoassociation³ [87]).

Nous avons aussi trouvé que la position des structures supplémentaires ne change

3. La collision se fait alors entre deux atomes et un photon. Pour que le processus ait lieu, l'énergie du photon doit être égale à la différence entre les énergies des deux atomes et de celle du dimère dans un état rovibrationnel

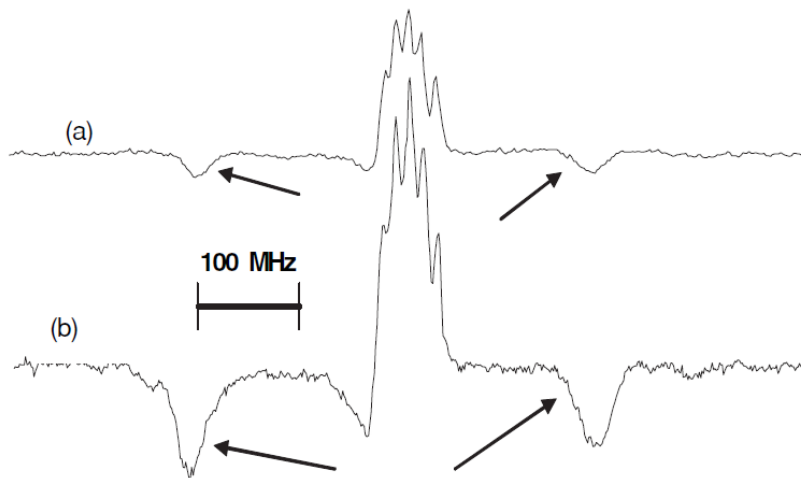


Figure 5.10 — Spectre d'absorption saturée (FM) en géométrie contre-propagante : les faisceaux pompe et sonde proviennent du même laser, accordé autour de la raie atomique $6S_{1/2}(F = 3) - 8P_{3/2}(F' = 2, 3, 4)$ de Cs. Intensité pompe : 50 mW/cm^2 , Intensité sonde : (a) 25 mW/cm^2 ; (b) 50 mW/cm^2 . Les flèches indiquent les résonances supplémentaires. $T = 80^\circ\text{C}$. [Figure 2 de l'article [6]]

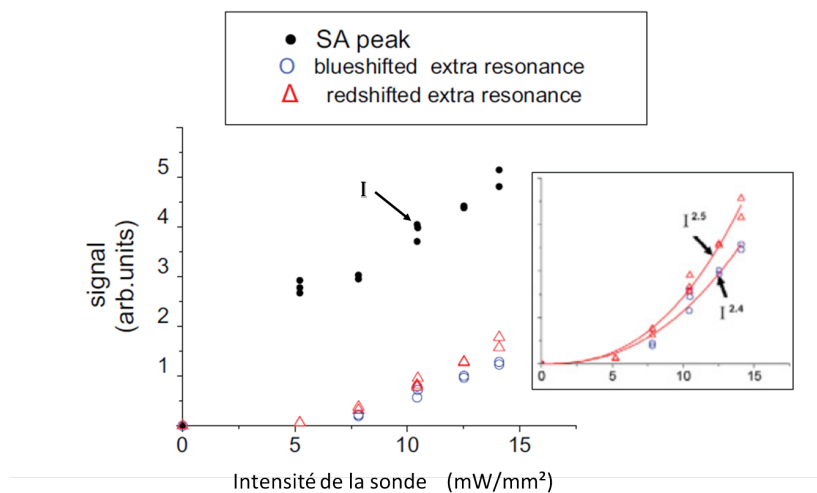


Figure 5.11 — Comparaison entre l'amplitude des pics usuels d'absorption saturée, et les résonances supplémentaires (du côté d'un désaccord bleu, ou rouge) en fonction de l'intensité sonde [Figure 3 de l'article [6]]

pas avec les conditions expérimentales. Leur position ne dépend ni de l'intensité des faisceaux, ni de la densité atomique, ni de la longueur de la cellule, ni de la cellule étudiée, ni du sens de propagation des faisceaux sonde/pompe (co-propageant ou contre-

5.4 Étude de l'interaction atome-surface entre un atome excité et une surface thermiquement émissive en saphir - Cas faiblement résonant [7] 79

propageant). Pour certaines conditions expérimentales un peu extrême (fortes densités de césium ou intensité du faisceau sonde), de nouvelles structures sont apparues. Cette invariance de position nous a permis d'éliminer l'hypothèse selon laquelle ces structures complémentaires seraient dues à des effets de propagation non-linéaire mais a confirmé l'idée qu'elles seraient dues à la formation de dimères. La particularité de notre observation est que les raies de dimères ne sont en général observables, à l'équilibre thermique, que pour des températures (ou densités) de vapeur élevées, ce qui n'est pas le cas ici. Les dimères ici formés ne le sont donc pas par collision entre trois atomes mais plutôt par un processus lumineux de photo-association. Le comportement non-linéaire des amplitudes de résonances supplémentaires avec l'intensité de la sonde (Figure 5.11) indique que le faisceau sonde participe également à la formation des dimères. Nous avons aussi analysé l'influence de la fréquence de modulation sur la formation des résonances. Nous avons trouvé que ces résonances nécessitaient un temps de formation plutôt long (quelques μs) indiquant un processus de pompage optique avant une redistribution des atomes dans les différents sous-niveaux qui éventuellement peuvent être moléculaires.

Des expériences où les faisceaux pompe et sonde sont en résonance sur des transitions indépendantes ont montré une conservation en fréquence entre les pics d'absorption saturée et les structures supplémentaires compatible avec une sélection en vitesse pour la formation des dimères. Une information spectroscopique complète nécessiterait de sonder avec un troisième laser, accordable sur une plage très large, pour repérer toutes les résonances supplémentaires induites par la présence des deux faisceaux UV engendrant les résonances supplémentaires.

Le processus ici présent permet donc d'obtenir des dimères avec des températures aussi basses que $45^\circ C$, pour une configuration expérimentale simple contrairement à celle utilisée pour la photo-association dans un nuage d'atomes froids [87].

Suite à ces expériences, nous avons décidé d'abandonner provisoirement les surfaces en fluorure trop fragiles. Une nouvelle série de mesures, avec cette fois une fenêtre de saphir plus robuste que CaF_2 et qui permet des températures bien plus élevées (≥ 1000 K) a été conduite.

5.4 Étude de l'interaction atome-surface entre un atome excité et une surface thermiquement émissive en saphir - Cas faiblement résonant [7]

5.4.1 Présentation de la cellule

Le saphir est nettement plus résistant, mécaniquement et thermiquement que les fenêtres fluorure, et insensible à une possibilité d'attaque chimique par la vapeur alcaline. Une cellule très spéciale de vapeur scellée tout en saphir a été réalisée à notre demande en Arménie par David Sarkisyan de l'Institut de Recherche Physique d'Ashta-

ak voir figure 5.12). Elle contient une fenêtre en saphir "superpoli" puis recuite à haute température⁴, avec une planéité quasiment à l'échelle atomique (rugosité $\leq 0.3nm$). Elle est reliée à un réservoir en verre contenant une goutte de césium. Elle dispose

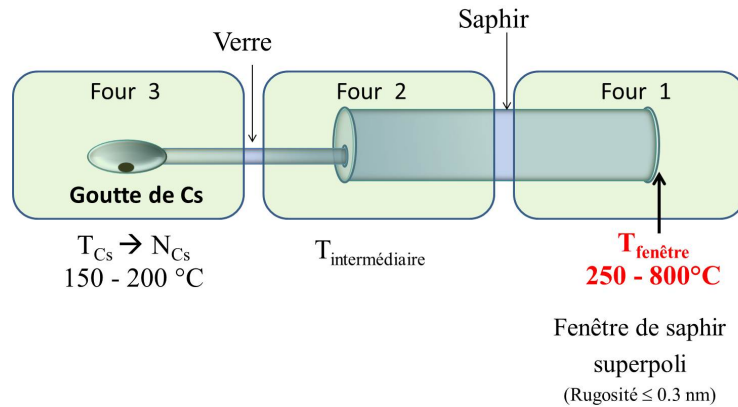


Figure 5.12 — Schéma de la cellule avec une fenêtre en saphir superpoli. [Figure 2b de l'article [7]].

de trois fours indépendants. Le four 3 permet de contrôler la densité de césium en changeant la température du réservoir en verre rempli de césium ($T_1 \approx 150 - 200^\circ C$). Un four séparé (four 1) contrôle la température de la fenêtre en saphir superpoli qui est en équilibre avec son environnement. Nous pouvons faire varier cette température jusqu'à 1200 K (température à laquelle la cellule a été dégazée de ses impuretés avant son remplissage par du césium). Le four intermédiaire 2 nous permet d'adapter le gradient entre les fours 1 et 3 et faire qu'il ne soit pas trop important, ce qui pourrait casser la cellule, et surtout éviter que la température dépasse $350^\circ C$ et que le collage verre/saphir cède. J'ai étudié la thermique de cette cellule et développé un programme pour contrôler les températures des trois fours. Une stabilité à $\pm 1^\circ C$ près a été obtenue.

La cellule a été d'abord testée dans la situation de la spectroscopie RS en modulation de fréquence (FM) sur la raie de résonance $6P_{1/2} \rightarrow 7D_{3/2}$ ($\lambda = 672$ nm) du Césium obtenue après un pompage sur le niveau $6S_{1/2} \rightarrow 6P_{1/2}$ ($\lambda = 894$ nm, D_1) (voir figure 5.13). Les traits verticaux en pointillés montrent la position de la transition $7D_{3/2} \rightarrow 5F_{5/2}$ à $10,8 \mu m$ qui est celle qui est la plus proche de la résonance de surface à $12,15 \mu m$. Elle reste cependant sur l'aile. Le couplage entre l'émission de la surface et son absorption par la vapeur est faiblement résonant.

5.4 Étude de l'interaction atome-surface entre un atome excité et une surface thermiquement émissive en saphir - Cas faiblement résonant [7] 81

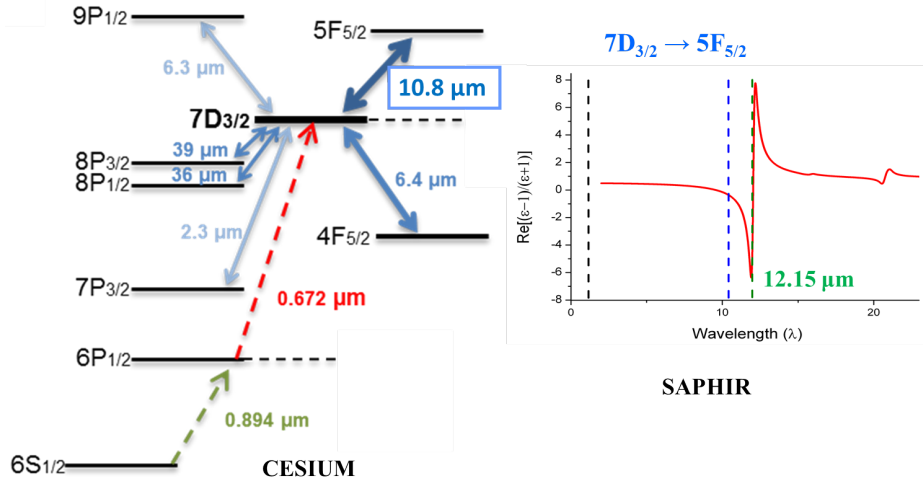


Figure 5.13 — Niveaux atomiques du césium (à gauche). Partie réelle de la réponse de surface du saphir $Re(S)$ à 1200K (à droite). Les traits verticaux en pointillés montrent la position de la transition $7D_{3/2} \rightarrow 5F_{5/2}$ à $10,8 \mu m$ qui est celle qui est la plus proche de la résonance de surface à $12,15 \mu m$. Elle reste cependant sur les ailes.

5.4.2 Prédictions théoriques

Nous avons tout d'abord prédit l'évolution de C_3 avec la température pour la transition $7D_{3/2}$ en utilisant les données expérimentales d'Orléans et un raisonnement similaire à celui présenté dans les paragraphes 5.2.2 et 5.2.3. Sur la figure 5.14, on peut voir le C_3 prédit augmente avec la température. Comment l'expliquer ? Sur la figure 5.13, on peut voir que la transition atomique $7D_{3/2} \rightarrow 5F_{5/2}$ à $10,8 \mu m$ se trouve avant le mode de surface du saphir à $12,15 \mu m$ à 1200 K et s'en approche quand la température tend vers la température ambiante, sans passer de l'autre côté. $Re(S)$ reste toujours négatif et donc comme expliqué au paragraphe 5.2.1 cela cause une augmentation de l'interaction vW et donc de C_3 avec la température (voir la figure 5.14).

Nous avons ensuite réalisé l'expérience correspondante pour tester cette prédiction.

5.4.3 Expérience

Nous avons réalisé le montage présenté sur la figure 5.15. Après pompage sur le niveau $6S_{1/2} \rightarrow 6P_{1/2}$ ($\lambda = 894 \text{ nm}$, D_1), on effectue de la spectroscopie RS en modulation de fréquence (FM) sur la raie de résonance $6P_{1/2} \rightarrow 7D_{3/2}$ ($\lambda = 672 \text{ nm}$) du Césium. Une modulation AM est appliquée sur la pompe à l'aide d'un modulateur acousto-optique pour augmenter la sensibilité de détection. La fréquence de pompe est asservie à l'aide de notre montage d'absorption saturée à 894 nm . Une attention parti-

4. pour éliminer les contraintes dues au polissage et à la découpe

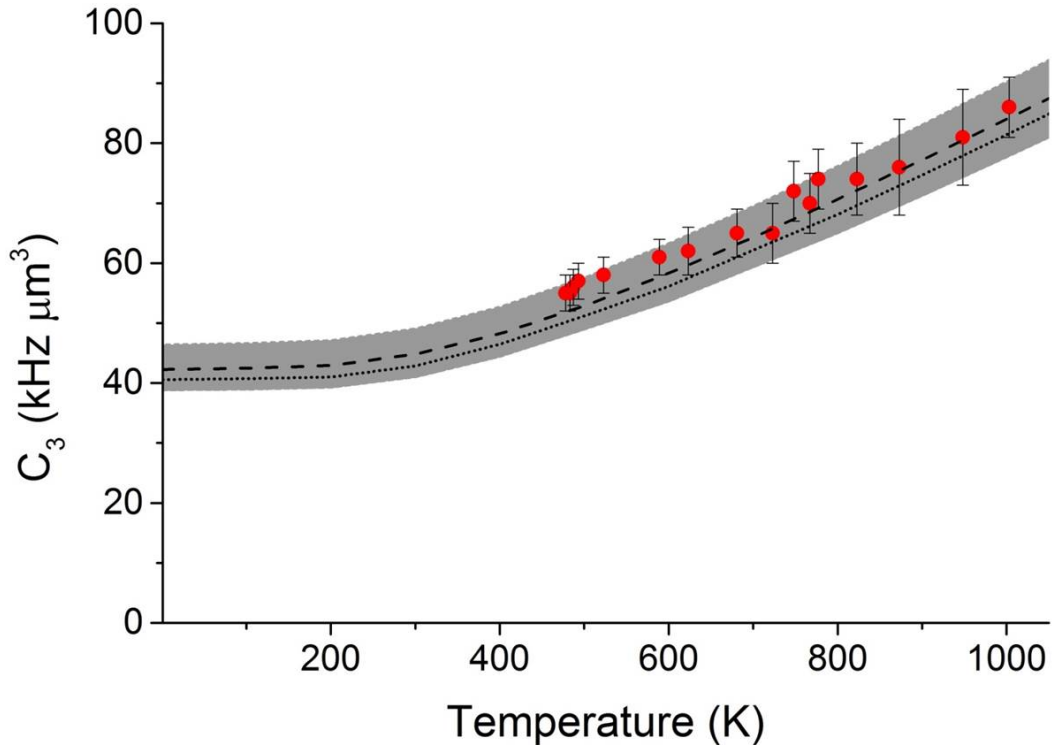


Figure 5.14 — Mesures expérimentales et prédictions théoriques pour le coefficient C_3 de l'interaction entre $Cs(7D_{3/2})$ et une surface de saphir en fonction de la température. Les points rouges représentent l'expérience. Les traits et points tirés représentent la théorie utilisant la constante diélectrique du saphir des articles [3,79]. La zone grisée de 5% autour des courbes théoriques viennent de l'incertitude sur les probabilités de transitions. [Figure 4 de l'article [7]].

culière a été portée pour éviter une sélection de vitesse lors du pompage (la transition hyperfine choisie n'était jamais en résonance avec la transition hyperfine de la sonde à 672 nm). Une seconde absorption saturée (sonde + pompe) a été installée ainsi qu'un Fabry-Perot de faible finesse pour déterminer la position des résonances de fréquence en volume et définir l'échelle en fréquence.

Nous avons effectué une étude systématique des spectres obtenus et les avons comparés à notre bibliothèque de spectres de formes de raie (selon la valeur de C_3 dans une échelle sans dimension) [61]. Nous avons estimé le coefficient $C_3(T)$ et observé une augmentation du coefficient C_3 avec la température (figure 5.14). Nous avons réalisé des tests indépendants pour valider nos résultats. Pour une température de surface constante, nous avons modifié la densité de césium et regardé si nos paramètres avaient une évolution correcte (augmentation linéaire de la largeur à mi-hauteur γ et du décalage collisionnel avec la pression de césium pour un C_3 constant). Nous avons fait le même travail sur différentes transitions hyperfines et obtenu la même évolution du coefficient $C_3(T)$. Nous avons changé la position du spot sur la fenêtre de saphir et

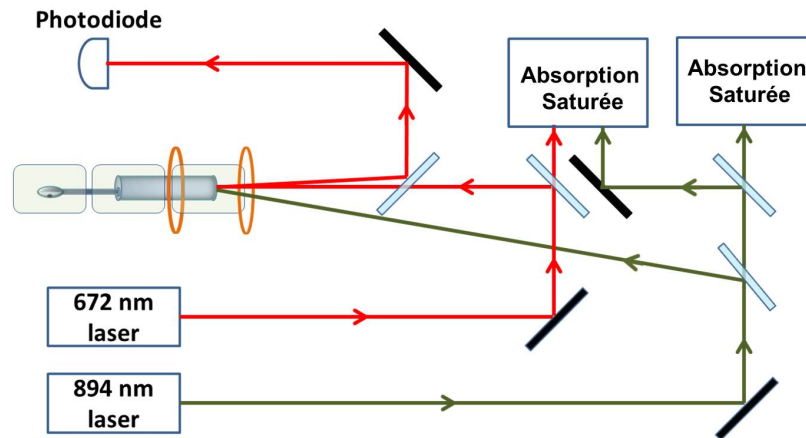


Figure 5.15 — Schéma du montage pour étudier l'interaction atome-surface entre un atome excité et une surface thermiquement émissive en saphir dans un cas faiblement résonant. [Figure 2a de l'article [7]].

n'avons obtenu aucun changement significatif. Ce résultat est crucial car les variations locales de l'épaisseur dues à la rugosité ou la présence d'impuretés (défauts ou ions) auraient pu affecter fortement l'interaction atome-surface et donc nos mesures ce qui n'est pas le cas. Contrairement au cas d'une surface en CaF_2 , le saphir est insensible à une attaque chimique par la vapeur alcaline à hautes températures. Des résultats similaires avaient été obtenus avec une cellule tout en saphir et une qualité de surface moins bonne, ce qui avait entraîné une incertitude plus importante sur l'estimation du coefficient C_3 .

Avec une surface superpolie, le coefficient C_3 est connu avec une précision de 5-10%. Il augmente de 50% lorsque la température passe de 500K à 1000K ce qui est en très bon accord avec la théorie (figure 5.14) et montre l'influence des effets thermiques sur l'interaction Casimir-Polder. L'atome apparaît ainsi comme une sonde en champ proche de l'émission thermique de corps noir. Les traits et points tiretés représentent la théorie utilisant la constante diélectrique du saphir de nos travaux précédemment décrits dans le paragraphe 5.2.1 et aussi de l'article de Barker [79]. La zone grisée de 5% autour des courbes théoriques donne l'incertitude sur le C_3 théorique et provient de l'incertitude sur les probabilités de transition qui ne sont pas toutes bien connues et aussi sur la constante diélectrique du saphir ϵ . Prendre en compte la biréfringence du saphir n'a eu que peu d'effet sur nos prédictions théoriques.

5.5 Conclusion

Pour étudier cette dépendance en température, nous nous sommes intéressés à l'interaction entre un atome excité de Césium ($8P$) qui présente des absorptions virtuelles autour de $39 \mu m$ ($8P_{3/2} \rightarrow 7D_{1/2}$) et $29 \mu m$ ($8P_{1/2} \rightarrow 7D_{1/2}$) (voir figure 5.1) et des

fenêtres en CaF_2 ou BaF_2 qui présentent, respectivement, une résonance de surface autour de $25 \mu m$ et $35 \mu m$.

Nous avons dans un premier temps étudié la dépendance en température de l'interaction atome-surface C_3 entre un atome excité de Césium ($8P$) qui présente des absorptions virtuelles autour de $39 \mu m$ ($8P_{3/2} \rightarrow 7D_{1/2}$) et $29 \mu m$ ($8P_{1/2} \rightarrow 7D_{1/2}$) et une surface en CaF_2 qui présente une résonance de surface autour de $25 \mu m$. Un désaccord entre nos résultats expérimentaux et nos prédictions théoriques, nous a amené à raffiner nos prédictions théoriques en tenant compte de l'évolution de la constante diélectrique avec la température, obtenue en réalisant des mesures de réflectance. Ce désaccord a été attribué à une dégradation de la surface, très fragile, de CaF_2 due à une attaque chimique de la surface par la vapeur de césium. Nous avons alors entrepris une nouvelle série de mesures, avec cette fois une fenêtre de saphir standard puis superpolie et un atome excité de Césium ($7D_{3/2}$). Le saphir, plus robuste que le CaF_2 , permet des températures bien plus élevées ($\leq 1200K$), mais ses résonances sont situées à $\cong 12.1 \mu m$ (soit $1200 K$). On obtient ainsi une croissance du coefficient d'attraction C_3 qui augmente de 50% de $500 K$ à $1000K$, mesurable avec la sensibilité de l'expérience et comparable aux prédictions théoriques.

Parallèlement à ce travail, nous avons observé des résonances supplémentaires sub-Doppler inconnues autour des transitions atomiques d'absorption saturée à 388 nm du césium lorsque les faisceaux utilisés, pompe comme sonde, sont relativement intenses. L'analyse systématique de ces résonances a permis de les attribuer à la formation de dimères par un processus de photo-association, bien que la vapeur, de faible densité, soit thermique.

5.6 Articles en relation avec ce chapitre

Les 5 articles [3–7] sont en relation avec ce chapitre. Les 4 principaux articles [3–5,7] sont reproduits à la fin de ce manuscrit.

Chapitre 6

Spectroscopie atomique avec confinement 3D

Cette nouvelle thématique existe dans l'équipe depuis 2006 en parallèle avec l'étude de l'évolution de l'interaction CP en champ proche avec la température.

6.1 Introduction

6.1.1 Motivations

Notre groupe a étudié en détail les propriétés spectroscopiques spécifiques des cellules minces [88] et très minces [56] contenant une vapeur atomique. Dans ces cellules, le libre parcours moyen d'un atome devient anisotrope, et est limité par la distance entre les parois de la cellule. Ceci conduit à une exaltation relative de la contribution des atomes lents, d'où une signature sub-Doppler dans la réponse spectroscopique, et la possibilité de réaliser ainsi une référence de fréquence compacte. En outre, dans le régime d'absorption linéaire, on observe un rétrécissement spectral cohérent de type Dicke [57, 66] pour une épaisseur de la cellule égale ou inférieure à $\lambda/2$; cet effet est dû à la contribution additive de toutes les classes de vitesse dans le régime transitoire, lorsque l'irradiation est exactement à résonance. Ayant observé de tels comportements spectroscopiques exotiques pour une vapeur confinée selon une direction de l'espace, il est naturel de se demander si des effets analogues peuvent survivre dans le cas d'un confinement plus fort, à deux ou trois dimensions. Il est aussi important de tester la possibilité de bénéficier de la réponse résonnante, extrêmement sélective en fréquence, des milieux gazeux dans le contexte des nanotechnologies et des nano-objets. Nous avons tout d'abord fait une étude bibliographique, puis cherché quel milieu permettant un confinement 2 ou 3 D pouvait être compatible avec une vapeur de césium.

6.1.2 Etat de l'art

Des expériences de spectroscopie de vapeur confinées 2D d'atomes ou de molécules ont été réalisées dans des fibres photoniques creuses (diamètre du coeur compris entre $10\ \mu\text{m}$ et $20\ \mu\text{m}$) dans l'équipe de Fetah Benabid [89–92]. Ce confinement a amplifié les effets non linéaires et leur a permis d'observer des rétrécissements spectraux (spectroscopie d'absorption saturée). Dans le groupe de Luigi Moi, des études de confinement 3D ont été réalisées dans des milieux poreux en verre. La taille des pores étaient de l'ordre de $7\text{-}30\ \text{nm}$. Dans ces pores de faibles tailles, les atomes alcalins sont rapidement adsorbés. Il est alors possible de les désorber en utilisant un éclairage de faible intensité dans un processus de désorption atomique induite par la lumière ("LIAD" : Light Induced Atom Desorption) [93]. Ils se sont malheureusement aperçus que les atomes qu'ils observaient par une technique spectroscopique n'étaient pas les atomes confinés dans les pores mais étaient les atomes libres autour du milieu poreux. Des mesures spectroscopiques sont possibles avec des pores plus grands. En prenant des pores de plus grande taille, il est possible de réaliser des expériences de spectroscopie. L'équipe de Svensson [94] a ainsi réalisé la spectroscopie de molécules d'oxygène confinées dans des matériaux poreux (ZrO_2 , Al_2O_3 , TiO_2) avec des pores entre 50 et $100\ \text{nm}$. La forte densité des molécules entraînait un élargissement collisionnel empêchant l'observation d'un signal sub-Doppler. L'équipe d'Horacio Failache avec qui nous travaillons en étroite collaboration a effectué des mesures spectroscopiques sur des atomes confinés dans les interstices d'un milieu poreux. Ce milieu est composé de grains de verre placés dans une cellule composée du même type de verre. La cellule est ensuite chauffée à 800°C jusqu'à ce que les grains adhèrent entre eux et à la cellule puis remplie avec une vapeur de rubidium. La spectroscopie, résolue dans le temps, de la lumière diffusée par des atomes de Rb confinés dans ce milieu poreux a été utilisée pour mesurer la taille des pores du milieu aléatoire [95]. Des rétrécissements spectraux sub-Doppler ont également été observés sur la lumière rétro-diffusée. Ces rétrécissements sont la signature d'effets non linéaires analogues à de la spectroscopie d'absorption saturée où la lumière rétro-diffusée sonde la vapeur atomique déjà saturée par la lumière incidente [96]. Des mesures type pompe-sonde ont aussi été faites [97].

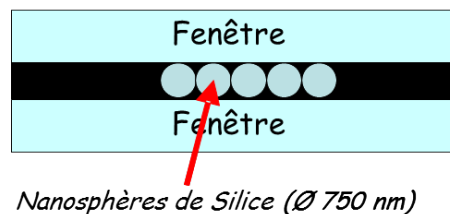


Figure 6.1 — Schéma de principe d'une cellule contenant une monocouche de sphères de silice. [Fig.1 (a) de l'article [8]]

Les opales de nanobilles de silice, qui peuvent s'empiler avec une très bonne régu-

larité si leur distribution est suffisamment mono-disperse, peuvent former des cristaux photoniques 3D. Des tentatives d'observation des modifications des bandes photoniques autour des résonances d'une vapeur de césium ont même été entreprises [98], mais qui ne visaient pas à une haute résolution en fréquence par rapport à la transition atomique. Dans un premier temps dans le groupe, nous nous sommes concentrés sur la possibilité d'un confinement tridimensionnel des atomes en utilisant une monocouche ("d'opale") de sphères diélectriques de silice (la silice étant un matériau particulièrement approprié pour des études sur des vapeurs alcalins résonnants). L'idée est d'insérer un tel film entre deux lames de verre en vue d'expériences spectroscopiques (voir figure 7.6 (a)).

6.2 Réalisation et caractérisation d'un film de nanosphères [8]

Les nanosphères de silice (SiO_2) utilisées ont été réalisées à la National Central University, Taiwan par Chia-Hua Chuan qui travaille en étroite collaboration avec l'équipe Photonique Organique et Nanostructure de notre laboratoire. Leur diamètre est de 750 nm et monodisperse (dispersion de taille inférieure à 5%). Par rapport à celles disponibles commercialement, elles ont une très faible dispersion et sont de très bonne qualité. Cette taille est bien adaptée à l'étude de transitions infrarouges tels que les raies D_1 (894 nm) et D_2 (852 nm) du Césium, notamment relativement à un possible rétrécissement Dicke cohérent lorsque le libre parcours moyen dans les espaces interstitiels entre sphères est inférieur à $\lambda/2$.

Pour obtenir un film bidimensionnel ordonné de nanosphères, avec Marco Romanelli (post-doc), nous avons testé plusieurs techniques de dépôt : l'évaporation horizontale, l'évaporation verticale contrôlée puis finalement une technique intermédiaire. Nous avons tout d'abord essayé de créer notre film par une évaporation horizontale. On dépose une goutte de mélange de solvant/nanobilles sur un substrat ayant subi un traitement hydrophobe, la goutte s'étale de tout son long sur le substrat et on attend que le solvant s'évapore. Progressivement les nanobilles se déposent sur le substrat. Nous avons essayé cette technique avec une concentration en billes très faible sans succès. Les nanobilles de silice sont très lourdes, tombent rapidement et s'entassent. Elles ne s'organisent pas du tout en monocouche mais plutôt en multicouches (figure 6.2).

Nous avons ensuite essayé la technique d'évaporation verticale contrôlée. Une lame ayant subi un traitement la rendant hydrophobe est plongée dans un mélange de solvant et de nanobilles (figure 6.3). Quand la lame monte (1), le solvant s'évapore, les nanobilles de SiO_2 attirées vers la lame par l'interaction de vW. Les forces capillaires tractent les autres nanobilles de SiO_2 vers les billes précédemment déposées sur la lame (2) où elles se déposent elles aussi peu à peu. Si on choisit bien la vitesse de translation de la lame ainsi que la concentration de nanobilles, cette méthode est connue pour donner un film 2D de très bonne qualité pour des billes en polystyrène (donc légères). Dans la cas de nos nanobilles en silice et de forts diamètres (750 nm), la gravité est

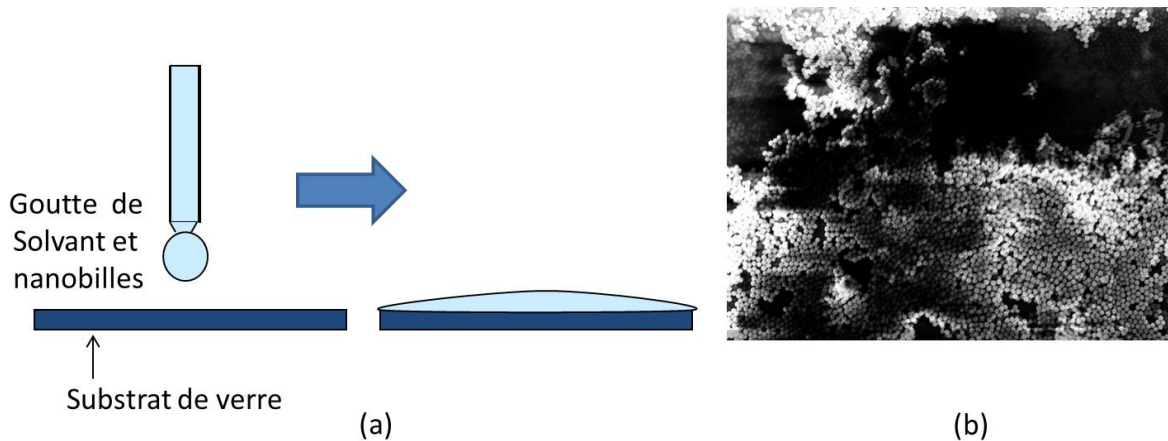


Figure 6.2 – (a) Montage expérimental utilisé pour une évaporation horizontale (b) Image du film de sphères de silice obtenu. Les images ont été prises par R. Chiron, du LPMTM, UPR 9001 du CNRS, Université Paris 13.

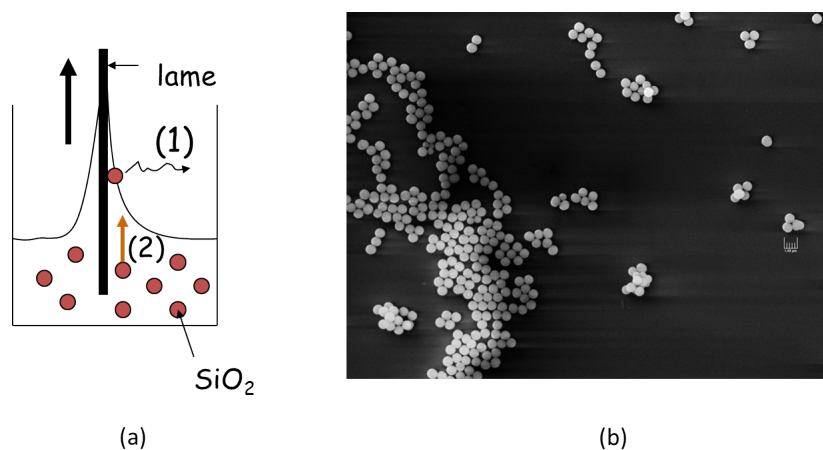


Figure 6.3 – (a) Montage expérimental utilisé pour une évaporation verticale contrôlée (b) Image du film de sphères de silice obtenu. Les images ont été prises par R. Chiron, du LPMTM, UPR 9001 du CNRS, Université Paris 13.

importante en comparaison avec les forces capillaires. Les forces capillaires ne sont pas suffisantes et nous obtenons des îlots monocouches très épars sur le substrat et donc pas du tout un film monocouche.

Nous avons finalement utilisé la technique décrite par Micheletto dans son article [99] qui est un intermédiaire entre les deux méthodes précédemment décrites (figure 6.4). Elle consiste à déposer une goutte d'une solution contenant des nanosphères sur un substrat légèrement incliné et ayant subi un nettoyage approprié pour le rendre hydrophobe. Dans les bonnes conditions, les particules s'auto-organisent en un

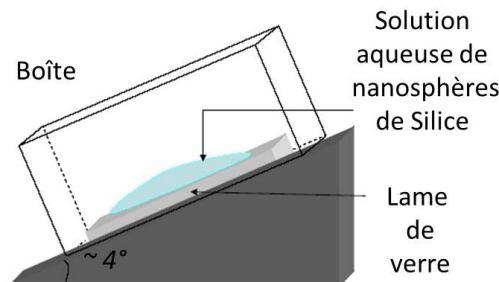


Figure 6.4 — Montage expérimental utilisé pour un dépôt intermédiaire entre une évaporation horizontale et une évaporation verticale contrôlée.

film ordonné 2-D. Dans notre cas, les paramètres expérimentaux qui se sont révélés les plus adaptés sont les suivants : inclinaison du substrat $\approx 4^\circ$, et concentration en volume des particules en solution de 0,4%. Pour réduire la vitesse d'évaporation du solvant, les échantillons étaient insérés dans une boîte de faible volume ($\approx 100 \text{ cm}^3$) pendant la formation du film. Un exemple de film obtenu est montré en figure 6.5. La taille des sphères permet d'obtenir une information suffisante en utilisant un microscope optique, plutôt qu'un microscope électronique à balayage (MEB). La méthode optique présente l'avantage de ne pas être destructive, alors que le MEB rend nécessaire la métallisation de l'échantillon et il devient inutilisable ensuite. Dans la figure 6.5, on peut distinguer un large domaine (« monocristallin ») de $60 \times 60 \mu\text{m}^2$ ce qui était un très bon résultat à l'époque au vu de l'état de l'art. On peut aussi observer quelques défauts : agrégats (rassemblement de nanosphères) et dislocations (dues à la dispersion du diamètre des nanobilles).

La réalisation de domaines auto-organisés est confirmée par la figure de diffraction produite par une diode laser UV ($\lambda = 388 \text{ nm}$) et un laser He-Ne ($\lambda = 632 \text{ nm}$) à l'incidence normale sur le film de nanosphères (voir figure 6.6 (c)). Lorsque le faisceau n'est pas focalisé, on observe un anneau de diffraction (figure 6.6 (a)), tandis que l'on observe une figure hexagonale si le faisceau est focalisé sur l'échantillon (figure 6.6 (b)). Ceci indique que lorsque le laser n'est pas focalisé, plusieurs domaines cristallins ayant des orientations différentes sont éclairés simultanément, tandis que pour un faisceau focalisé, un domaine unique de sphères organisées en un réseau hexagonal compact est à l'origine de la diffraction observée. L'étude des angles de diffraction (θ) de cette figure [8] à l'ordre (h,k) nous a permis de déterminer expérimentalement le diamètre des billes (a) ainsi que leur dispersion [8] :

$$\sin(\theta) = \frac{2\lambda}{\sqrt{3}a} \sqrt{h^2 + k^2 - hk} \quad (6.1)$$

Dans le cas de notre échantillon, nous avons trouvé : $a = 812 \pm 8 \text{ nm}$. Nous avons également montré que l'intensité relative entre les différents spots est liée à l'orientation de la structure cristalline et peut servir à connaître son orientation ou à orienter l'échantillon comme on le désire [10].

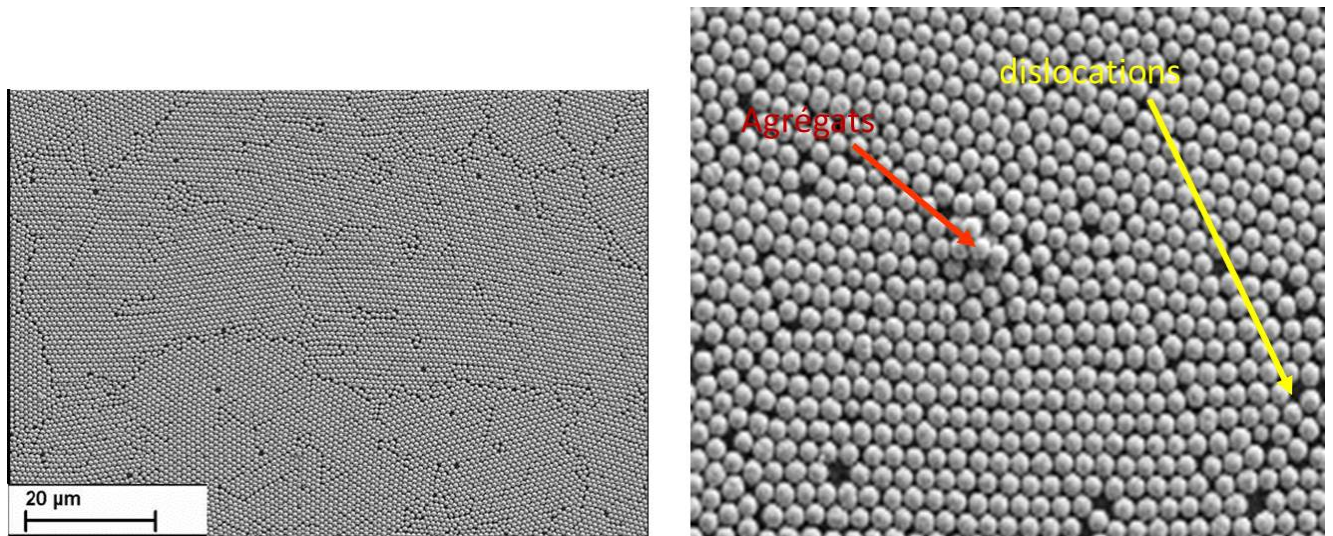


Figure 6.5 — Deux images à différentes échelles d'un film bidimensionnel de sphères de silice. Les images ont été prises par R. Chiron, du LPMTM, UPR 9001 du CNRS, Université Paris 13. [Figure 1 (b) de l'article [8]]

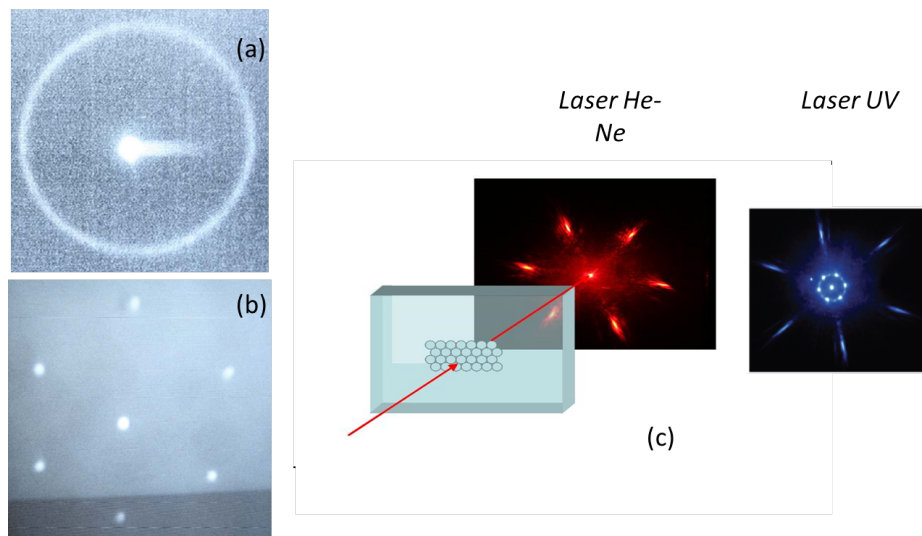


Figure 6.6 — Figure de diffraction (en transmission) d'un faisceau laser ($\lambda = 388$ nm) incident sur un film de nanoparticules : (a) le faisceau n'est pas focalisé ; (b) le faisceau est focalisé, (c) montage expérimental. [Figure 1 (c) et (d) de l'article [8]]

Nous avons obtenu des films de nanoparticules de silice de très bonne qualité à l'aide d'une méthode simple. Cela avait été rarement vu pour des billes de silice. La diffraction est facilement repérable, ce qui pourrait permettre d'étudier les effets résonnants

sur un faisceau cohérent - et directif-, plutôt que sur une lumière diffusée. Cependant, l'encapsulation de cette monocouche entre deux lames de verre est restée une tâche ardue voire impossible, d'autant plus que les zones effectivement monocouches alternent avec des zones sans billes, et d'autres porteuses de deux ou plusieurs épaisseurs, de telle sorte que la taille effective des régions libres est bien loin de correspondre à des interstices de volume étroitement monodisperses.

Cette opale monocouche a été utilisée lors l'animation d'un stand scientifique au Palais de la découverte dans le cadre « une manip un chercheur » (C'nano) : « Un monde en couleur ». Nous avons montré dans ce cadre le lien entre la figure de diffraction observée et l'information sur l'organisation nanométrique de la monocouche qui en découle.

Nous sommes ensuite partis dans une autre voie. Nous nous sommes intéressés à une tranche d'opale en volume (épaisseur $\approx 1\text{mm}$, section quelques mm^2), composée de nanobilles de silice de diamètre $d=230\text{ nm}$, et avons fait réaliser une cellule dont les deux fenêtres prenaient en sandwich cette tranche d'opale.

6.3 Cellule contenant une tranche d'opale

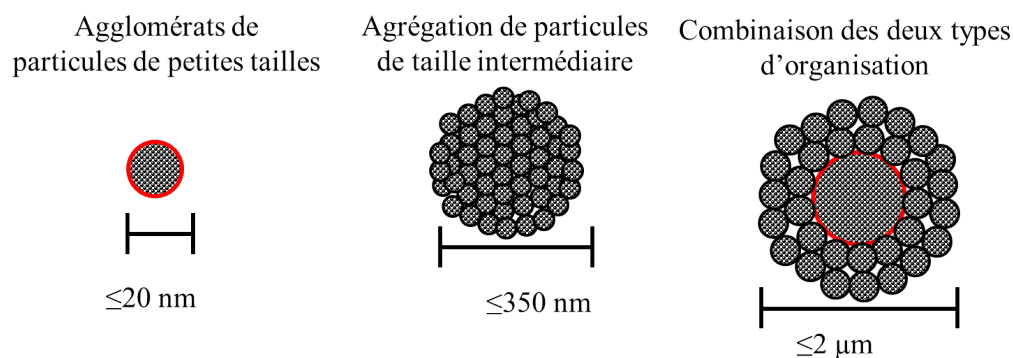


Figure 6.7 – Représentation Schématique des diverses organisations internes d'une bille de Silice fabriquée par une méthode sol-gel [100]. [fig. 2.2 de la thèse de Philippe Ballin [101]]

La tranche d'opale nous a été donnée par Agnès Maitre de l'Institut des Nanosciences de Paris. L'opale a été fabriquée par une méthode très simple mais très lente : la sédimentation. On laisse au repos un mélange solvant et nanobilles et on attend. Progressivement les nanobilles se déposent au fond du récipient, les billes les plus grosses et donc lourdes se déposent en premier. Les billes s'auto-organisent en couche par l'interaction de vW. L'opale ainsi créée possède une organisation de type cubique

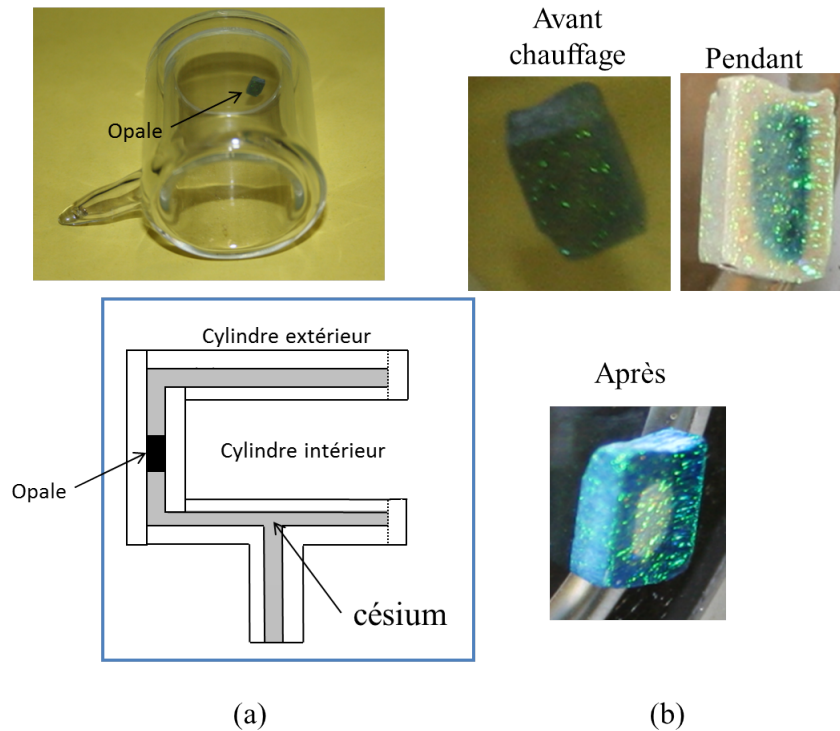


Figure 6.8 – (a) Schéma et photographie de la cellule fabriquée avec une opale prise en sandwich entre deux cylindres de verre. (b) Photographie de l’opale avant, pendant et après chauffage à $T = 280^{\circ}\text{C}$ pendant une journée. [Figure 1 de l’article [10]].

face centrée (cfc), en revanche le nombre de couches constituant l’opale ne peut être maîtrisé.

Une tranche de 1 mm d’épaisseur pour des billes de diamètre $d = 230\text{ nm}$ a été coupée dans cette opale. Cette tranche a été polie par Thierry Billeton du LPL pour rendre les deux faces de la tranche de l’opale les plus parallèles possibles. En faisant une étude bibliographique sur l’opale, nous avons découvert qu’en plus des interstices entre les nanobilles, les nanobilles étaient elles-mêmes composées d’une agrégation de particules de silice [100]. Les billes peuvent être composées d’un agglomérat de particules de très petites tailles ($\approx 10 - 20\text{ nm}$), d’agrégation de particules de tailles intermédiaires ($\approx 100\text{ nm}$), elles-mêmes constituées de petites particules, ou encore une combinaison des deux types précédents, c’est-à-dire un coeur volumineux autour duquel s’agrègent d’autres agrégats (figure 6.7). Quelle que soit leur organisation interne, les billes ne sont pas des objets uniques, elles possèdent donc une porosité propre. Nous avons donc effectué un recuit de l’opale à 900°C (en suivant l’étude de l’article [102]) pour souder entre eux les interstices composant les nanobilles et ainsi éviter que lorsque nous met-

trions l'opale en présence d'un gaz de césium, il puisse pénétrer dans ses interstices et y être confiné ou piégé. La tranche d'opale recuite a ensuite été prise en sandwich et comprimée entre deux cylindres de verre (figure 6.8(a)). Nous avons poli l'opale pour que le contact entre la tranche d'opale et les cylindres soit le meilleur possible et ainsi éviter que du césium puisse s'insérer entre l'opale et les faces du cylindre. Nous voulions à l'époque faire la spectroscopie de la lumière diffusée par des atomes de Césium confinés dans une opale. La qualité de l'interface nous importait peu en comparaison du signal provenant de la lumière diffusée à l'intérieur de l'opale. Nous verrons que l'idée de polir une opale était une très mauvaise idée surtout vue l'importance de l'interface d'entrée entre le verre et l'opale (voir paragraphe 6.4.1) indépendamment de la structure interne de l'opale pour la lumière.

La cellule a été fabriquée et remplie de césium par Florence Thibout du Laboratoire Kastler-Brossel à Paris. Avec Philippe Ballin (PHD), nous avons observé que l'opale, initialement blanche comme un matériau diffusant et non absorbant, est rapidement devenue noire, quelques heures après remplissage (voir figure 6.8 (b)). Des cycles de chauffage permettent cependant de voir apparaître des zones blanches sur l'opale, tandis que sur les fenêtres, autour de l'opale, apparaissent des zones métallisées clairement liées à un dépôt de césium. Si un quasi-blanchiment de la cellule apparaît en certains points, les régions périphériques prennent une coloration verte, attribuable à la formation d'agrégats de césium. Ces processus sont réversibles et une opale blanche peut être ré-obtenue après un chauffage fort ($\approx 280\text{ }^{\circ}\text{C}$) du corps de cellule au bout d'une journée, cependant le réservoir de césium doit être maintenu tout à fait à froid ($0\text{ }^{\circ}\text{C}$). Quelques heures après le retour à la température ambiante, la coloration verdâtre, puis métallisée, de l'opale réapparaît rapidement, signe que l'opale piège les atomes bien plus qu'attendu pour un équilibre dans un véritable volume tridimensionnel. Notons que pour cette opale, le diamètre des billes ($\approx 230\text{ nm}$) et donc la taille des zones interstitielles est très faible ce qui favorise l'apparition d'agrégats. Cela explique aussi la longueur du temps nécessaire pour rendre l'opale blanche en la chauffant. Nous avons rencontré un autre problème : l'opale a glissé au bout d'un certain temps d'utilisation dans la cellule et n'était plus prise en sandwich entre les deux fenêtres de verre.

Face à ces résultats, nous nous sommes orientés vers des opales moins épaisses composées de nanobilles de diamètres plus importants et aussi vers un autre type de cellule.

6.4 Caractérisation optique d'une opale Langmuir-Blodgett

Le groupe de Serge Ravaine du CRPP à Bordeaux nous a fourni des opales réalisées par la technique de Langmuir-Blodgett. Cette méthode décrite en détail dans la thèse de P. Massé [103] permet contrairement à la sédimentation de choisir le nombre de couches déposées sur un substrat de verre et de faire ce dépôt rapidement. Ce dépôt

s'effectue couche après couche et peut être effectué sur un substrat de grande taille ($\approx cm^2$). Le seul défaut est que l'organisation cristalline en volume est un mélange aléatoire de cfc et hexagonal compact (hc). Avant de faire de la spectroscopie dans une opale (opale avec une vapeur de césium), nous avons modélisé la réponse optique de l'opale seule (spectres de transmission et réflexion).

6.4.1 Modélisation optique d'une opale fine déposée sur un substrat [9]

Présentation du modèle

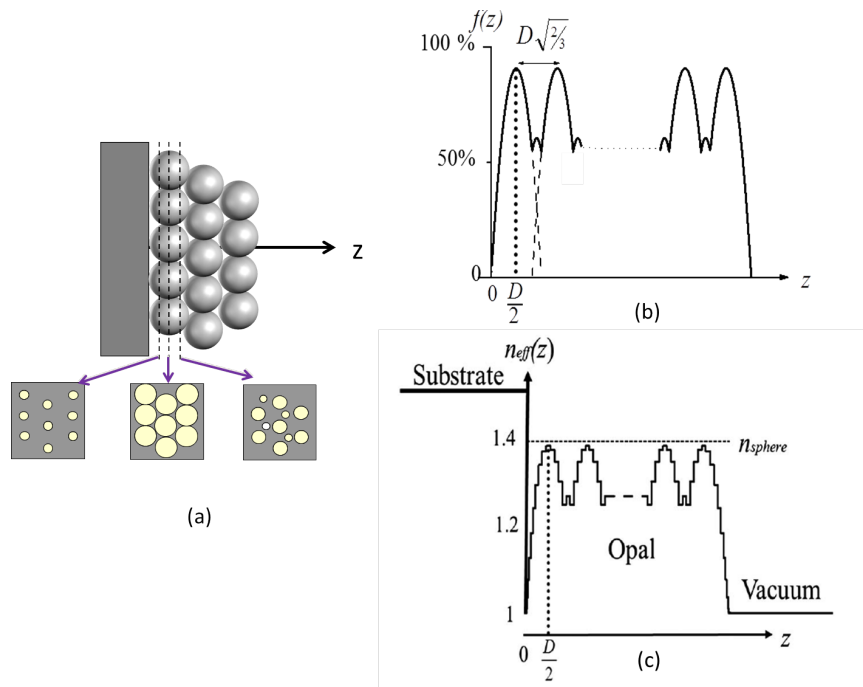


Figure 6.9 — (a) Opale faite de N couches avec un empilement de type compact. Représentation de trois plans de coupe de l'opale : coupe très près de la fenêtre de verre, coupe au niveau du centre de la première couche de billes, coupe à l'arrivée de la seconde couche. (b) Taux de remplissage de l'opale en volume. (c) Indice effectif $n_{eff}(z)$ pour une opale faite de N couches. L'opale est orientée pour que la lumière soit incidente du côté du substrat ($n_{sphere}=1.4$) montré ici dans une version stratifiée (nombre fini de couches). [Figure 1 de l'article [12]].

Une opale est un arrangement compact de sphères transparentes et un prototype simple de cristal photonique à trois dimensions. Cette empilement peut être cubique face centrée (cfc), hexagonal compact (hc) ou un mélange entre les deux selon la technique utilisée pour sa fabrication. Pour en comprendre les propriétés optiques, les modèles fondés sur des calculs numériques (par exemple la méthode des éléments finis) ou

sur le calcul des structures de bandes [104, 105] sont couramment utilisés dans la littérature. Elles peuvent prédire la réflexion, transmission, diffusion, inclure le speckle et des diffractions multiples et cohérentes. L'inconvénient de ces méthodes est la lourdeur des calculs et la difficulté d'y inclure facilement des défauts de périodicité. Des méthodes plus simples existent (Scalar wave approximation (SWA)) [106–109] mais elles ne considèrent pas les modifications optiques dues à un changement de la polarisation ou de l'angle d'incidence, et ne prennent pas en compte le couplage d'entrée-sortie entre lumière et opale. J'ai développé avec la collaboration de Daniel Bloch un modèle à une dimension, d'une grande flexibilité, qui permet de prédire les spectres de transmission et de réflexion d'une opale quel que soit l'angle d'incidence et la polarisation. L'opale est décrite comme un milieu stratifié avec un indice effectif, variant localement comme la densité d'opale contenue dans une fine couche plane. Le taux de remplissage des sphères $f(z)$ contenues dans une tranche d'opale permet d'évaluer l'indice effectif $n_{eff}(z)$ (voir figure 6.9) suivant la formule :

$$n_{eff}(z) = [f(z) \cdot \epsilon + (1 - f(z))]^{1/2} \quad (6.2)$$

où ϵ est la constante diélectrique du matériau composant les nanobilles (en SiO_2 dans le cas de nos opales).

J'ai utilisé la méthode des matrices de transfert pour évaluer les spectres de réflexion

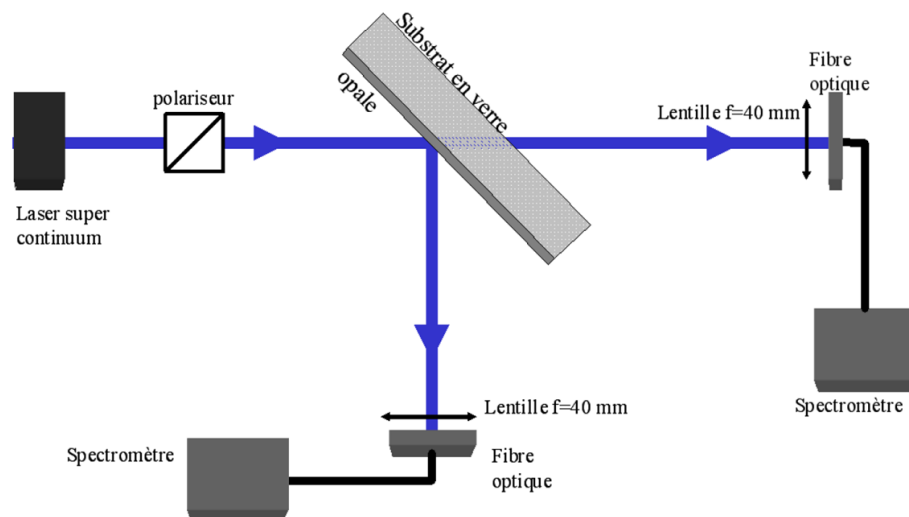


Figure 6.10 — Montage expérimental permettant de mesurer la réflexion et transmission d'une opale déposée sur un substrat de verre. [fig. 2-14 de la thèse d'Elías Moufarej [110]]

et de transmission (pour en avoir le détail voir l'appendice A de l'article [9]). Des pertes ont été ajoutées à $n_{eff}(z)$ pour tenir compte de la lumière diffusée ou diffractée avec un coefficient d'absorption de type diffusion Rayleigh en $\alpha = \beta/\lambda^4$ avec β une constante. Nos calculs permettent de retrouver les principales caractéristiques du pic de

Bragg en réflexion (position, largeur, amplitude) pour une polarisation TE ou TM, et quel que soit l'angle d'incidence. Le modèle peut être utilisé aussi bien si la lumière est incidente du côté du substrat, que du côté de l'interface vide. Le modèle montre la forte influence de l'interface avec l'opale, indépendamment de la structure interne de l'opale. Cette rupture de périodicité à l'interface, inévitable pour les cristaux photoniques, est rarement prise en compte.

Résultats et interprétations du modèle

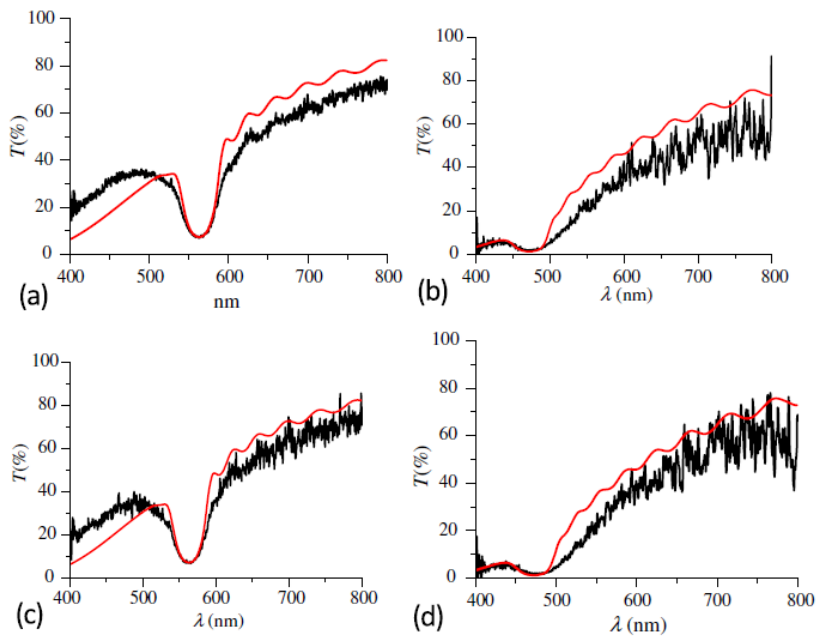


Figure 6.11 — Spectres de transmission (polarisation TE) pour une opale faite de 20 couches de billes de silice de diamètre $d = 276 \text{ nm}$. (a) et (b) sont pour une lumière incidente côté vide ; (c) et (d) côté substrat. Pour (a) et (c), $\theta = 20^\circ$. Pour (b) et (d), $\theta = 50^\circ$. Les courbes expérimentales sont en noir, les théoriques sont en rouge. Le coefficient de perte choisi est $\alpha d = 0,1$. [Figure 8 de l'article [12]].

Des expériences dédiées ont été réalisées avec la collaboration d'Elias Moufarej (PHD) pour tester la validité de notre modèle. Nous avons mesuré les spectres de transmission et de réflexion d'une opale Langmuir-Blodgett formée de 20 couches de billes de silice de diamètre $d = 276 \text{ nm} \pm 5\%$ déposées sur un substrat de verre. Pour cela, nous avons utilisé un laser impulsif super continuum (400 - 1750 nm) et enregistré la lumière réfléchie ou transmise à l'aide d'un spectromètre à fibre optique (voir montage figure 6.10). Les spectres ont été enregistrés en envoyant la lumière côté substrat ou côté vide, pour une polarisation incidente TE ou TM et pour différents angles d'incidence θ . J'ai évalué numériquement les pertes afin de reproduire les spectres de

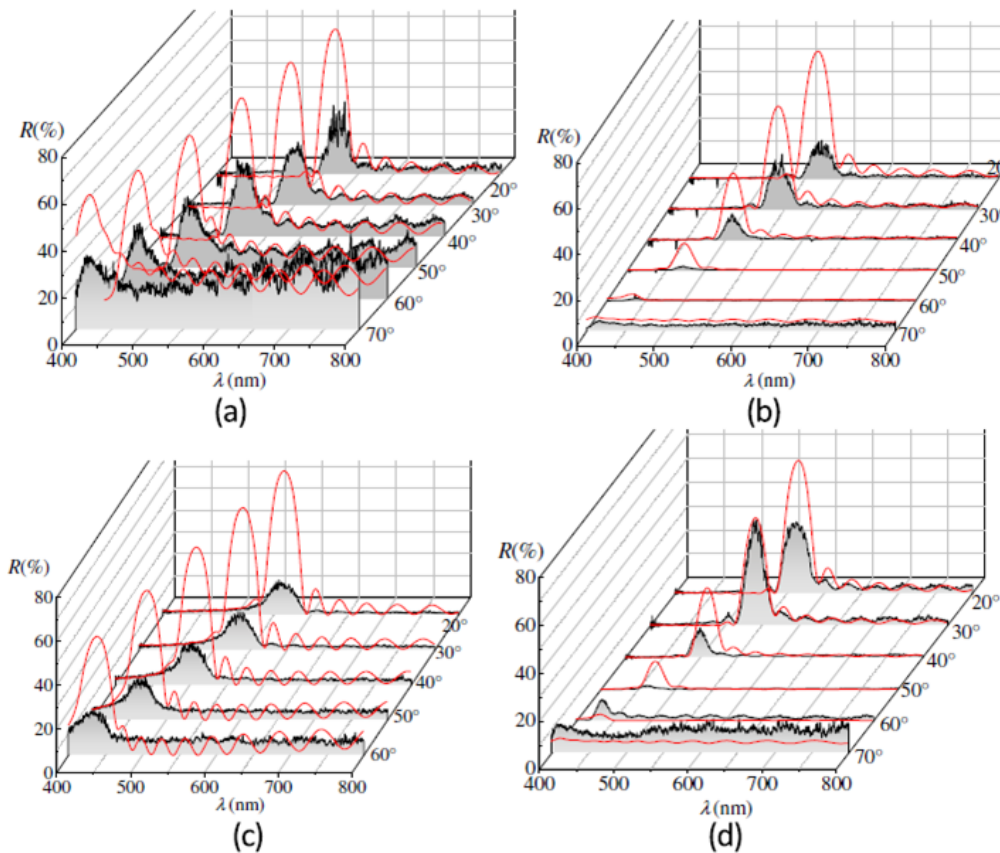


Figure 6.12 — Spectres de réflexion pour différents angles d'incidence θ pour une opale faite de 20 couches de billes de silice de diamètre $d = 276 \text{ nm}$. Les courbes expérimentales sont en noir, les théoriques sont en rouge. Le coefficient de perte choisi est $\alpha d = 0,1$. (a) et (b) sont pour un faisceau arrivant du côté vide. (c) et (d) du côté substrat. La polarisation est TE pour (a) et (c) et TM pour (b) et (d). [Figure 9 de l'article [12]].

transmission (figures 6.11) puis utilisé cette valeur pour calculer les spectres de réflexion. Un accord quantitatif satisfaisant a été obtenu (figure 6.12).

Notre modèle permet de reproduire le pic de Bragg (amplitude, largeur, position). Le pic de Bragg est dû à la périodicité à l'intérieur de la structure. Il se construit avec le nombre de couches. Au bout d'un certain nombre de couches, le spectre de réflexion ne change plus, même si le nombre de couches augmente. A cause des pertes lors de la propagation de la lumière dans l'opale, il arrive un nombre de couches à partir de laquelle une couche de plus ne change plus rien, la lumière n'atteignant plus cette couche. Notre modèle permet de voir cette construction. L'amplitude prédit est toujours plus grande que celle trouvée expérimentalement. Cela est dû au fait que l'organisation en profondeur de nos échantillons est de moins en moins compact à cause des agrégats et

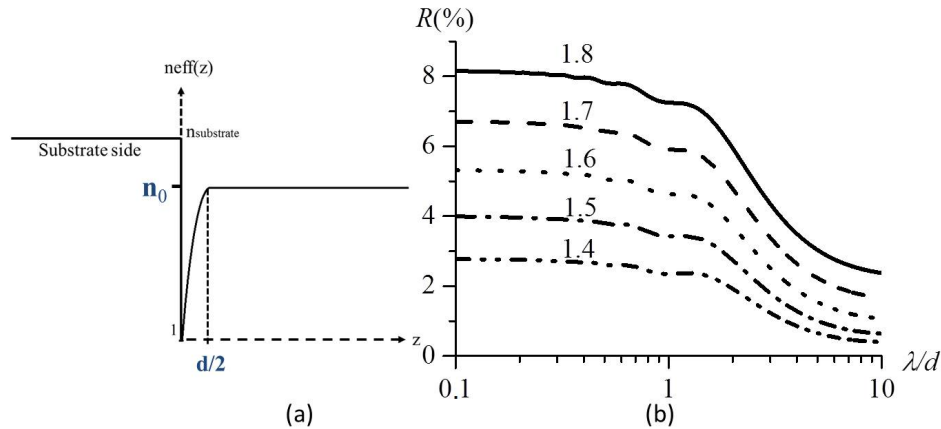


Figure 6.13 — (a) Indice effectif pour une opale "fusionnée". (b) Spectres de réflexion en fonction de λ/d en incidence normale pour une opale "fusionnée", avec une polarisation TE, du côté du substrat pour différentes valeurs de l'indice du substrat. Le coefficient de perte est $\alpha d = 0,1$. [Figure 4 de l'article [12]].

dislocations qui s'accumulent d'une couche à l'autre ce que ne considère pas notre modèle. L'amplitude change aussi avec l'angle et selon la polarisation incidente, en effet, la propagation de la lumière dans l'opale diffère suivant la polarisation. On observe un angle de "pseudo-Brewster" pour une polarisation TM. Un comportement inattendu est observé à $\theta = 60^\circ$ (figure 6.12 (d)) pour une polarisation TM proche de l'angle pseudo-Brewster. Le pic de Bragg théorique est beaucoup plus petit que celui trouvé expérimentalement. Cela peut être expliqué par une dépolarisation de la lumière réfléchie ou simplement par une polarisation imparfaite de la lumière incidente. Un mélange de polarisation TE et TM à l'intérieur de l'opale expliquerait en effet l'observation d'un pic de Bragg quand les calculs rigoureusement limités à une polarisation TM ne le prédisent pas. Les oscillations sur les ailes du pic de Bragg quant à elles sont typiques d'un effet Fabry-Perot d'une extrémité à l'autre de l'opale et dépendent donc de l'épaisseur de l'opale.

La rupture de périodicité à l'interface due à la première demi-couche (substrat/opale ou opale/vide suivant le côté par lequel on éclaire l'échantillon) est responsable de la valeur moyenne de la réflexion sur les ailes du pic de Bragg. Pour voir l'influence de cette première demi-couche, nous avons utilisé notre modèle dans le cas d'une opale "fusionnée" (voir figure 6.13(a)) c'est-à-dire pour laquelle la partie après la première demi-couche est remplacée par un indice effectif moyen. Si $\lambda < d$, la lumière est très sensible à cette rupture, le coefficient de réflexion tend vers le coefficient de Fresnel substrat/vide (figure 6.13 (b)). Si $\lambda > d$, la lumière n'est plus sensible à cette rupture, le coefficient de réflexion tend vers le coefficient de Fresnel substrat/ \bar{n}_{opale} .

Notre modèle simple 1 D permet donc de reproduire toutes les caractéristiques des spectres de transmission et réflexion pour une opale de type Langmuir-Blodgett (LB).

Notre modèle est simple et très flexible. Il peut facilement prendre en compte des défauts d'empilements, une dispersion dans l'épaisseur d'une couche ou l'introduction d'une couche de billes d'un autre matériau. Il est intrinsèquement applicable à un empilement compact de cylindres. Ce modèle ne prédit pas des pics de Bragg secondaires dûs à des plans de symétrie comme le plan (200) présent dans une structure purement cfc (organisation en volume). Ce modèle ne fonctionne plus correctement quand le nombre de couches devient trop faible et que parler de périodicité dans l'opale n'a plus vraiment de sens. Pour caractériser les opales composées d'une ou deux couches, nous avons utilisé un autre type de modélisation.

6.4.2 Modélisation optique d'une ou deux couches de billes déposées sur un substrat [10]

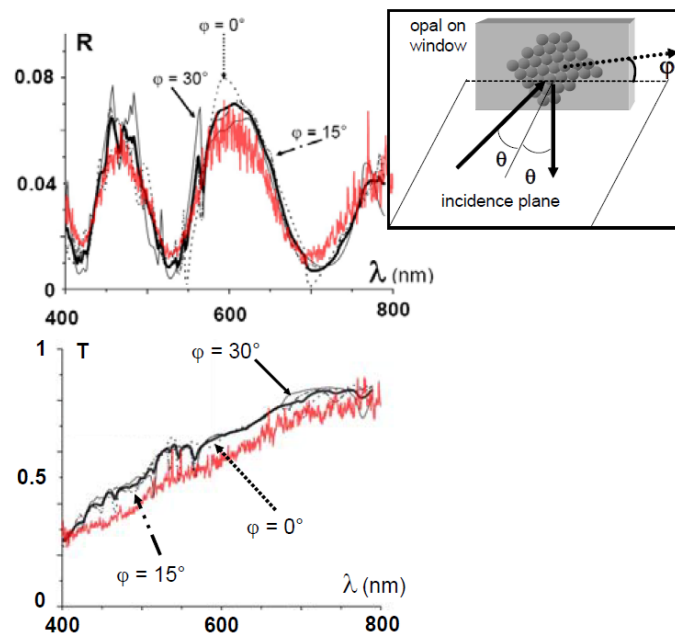


Figure 6.14 — Inset : Définition des angles d'incidence θ et d'orientation de l'opale φ . En rouge, les spectres de réflexion (R) et de transmission (T) expérimentaux pour une opale LB formée d'une monocouche de billes de silice de 276 nm de diamètre sont représentés avec $\theta = 15^\circ$ et une polarisation TM. Les spectres théoriques sont tracés en noir. Divers angles d'orientation φ sont considérés. La courbe épaisse noire représente le spectre obtenu pour une orientation aléatoire (moyennage sur toutes les angles d'orientation possibles). [Figure 6 de l'article [10]].

Pour une monocouche de billes, le modèle 1D stratifié de l'indice effectif n'est plus applicable. Un calcul numérique complet utilisant la méthode des éléments finis a été

développé par Ilya Zabkov du L.N. Lebedev Physics Institute à Moscou, avec qui nous sommes en collaboration, dans le cas d'un cristal parfait en périodicité. Ce modèle permet de calculer la réflexion, transmission et diffusion sans ajouter un paramètre de perte. L'orientation du cristal φ définie par rapport au plan d'incidence (voir la figure insérée 6.14) est alors le paramètre clé du calcul. Le modèle prédit en effet des variations rapides de la réflexion suivant l'orientation de l'opale et de la longueur d'onde incidente (figure 6.14) ce qui n'est pas le cas de la transmission. Les spectres prédits sont en très bon accord avec nos expériences obtenues pour une opale Langmuir-Blodgett monocouche avec des billes en silice de diamètre $d = 0.73 \mu m$ après un moyennage sur l'orientation. Ce moyennage est rendu nécessaire par la nature polycristalline de nos opales LB.

Quand le nombre de couches augmente, le temps de calcul et de moyennage augmente, ce qui rend vite cette modélisation inutilisable. Il est cependant possible d'imaginer d'observer les variations rapides de la réflexion suivant l'orientation de l'opale et de la longueur d'onde pour une opale LB en polystyrène où la dispersion des diamètres est beaucoup plus faible ($\approx 10^{-3}$). Après avoir caractérisé la réponse optique d'une opale LB seule, nous avons réalisé des mesures spectroscopiques en réflexion sur une opale LB infiltrée par un gaz de césium (figure 6.15). Ces cellules ont été fabriquées par Florence Thibout au LKB à Paris.

6.5 Infiltration résonante d'une opale Langmuir - Blodgett

6.5.1 Résultats expérimentaux [10, 11]

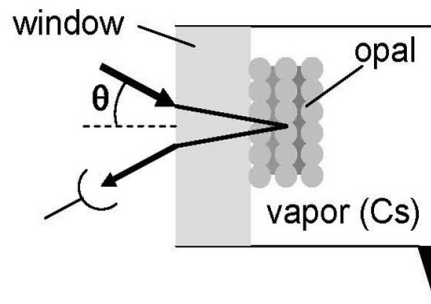


Figure 6.15 — Schéma de l'expérience pour une opale de 5 nanocouches. Pour des raisons de lisibilité l'opale a été grossie. [Figure 1 de l'article [11]].

Nos cellules de vapeur de Cs possèdent une fenêtre recouverte d'une opale de nano-

billes (10 ou 20 couches de billes de silice de $1 \mu\text{m}$ de diamètre), obtenue par dépôt de couches successives par la technique Langmuir-Blodgett (figure 6.15). Un contrôle des gradients thermiques de la cellule a permis d'éviter la formation (réversible) d'agrégats de Cs, pour des nanobilles de diamètre $d = 1 \mu\text{m}$ (mais non pour des billes de $d = 400 \text{ nm}$). Lorsque l'on envoie de la lumière sur la cellule, on observe, outre une forte diffusion et une très faible transmission, un faisceau réfléchi à l'interface opale - fenêtre de verre. Ce faisceau permet d'effectuer une spectroscopie de réflexion. De plus, une technique de modulation de fréquence (FM), qui fournit la dérivée du signal RS, exacerbe les contributions spectrales les plus étroites.

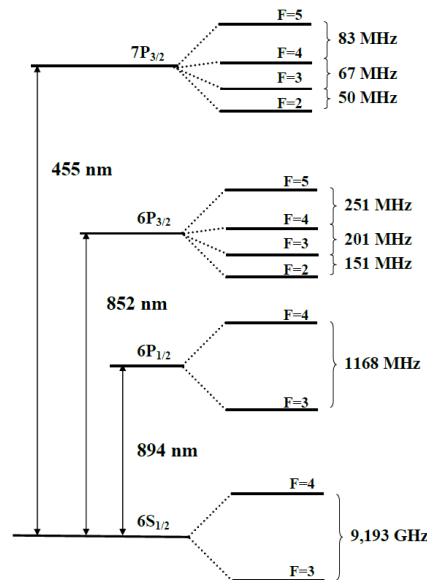


Figure 6.16 — Niveaux atomiques du césium utiles pour cette étude.

Nos premières expériences ont été effectuées sur le doublet de résonance du césium : $\lambda_1 = 894 \text{ nm}$ (D_1) et $\lambda_2 = 852 \text{ nm}$ (D_2) (figure 6.16). Les figures 6.17 et 6.18 présentent l'évolution des spectres de réflexion, que j'ai obtenue avec Philippe Ballin (PHD), sur la raie D_2 avec l'angle d'incidence, pour une opale composée de 10 couches de billes de silice de $1 \mu\text{m}$ de diamètre. Des spectres similaires ont été obtenus avec l'aide de Philippe Ballin et Elias Moufarej (PHD) avec une opale composée de 20 couches pour la raie D_1 .

Près de l'incidence normale (figure 6.17), le spectre de réflexion est plus étroit (largeur $\approx 30 \text{ MHz}$) que la largeur Doppler (demi-largeur Doppler $\approx 200 \text{ MHz}$). Quand l'angle d'incidence augmente, le signal s'élargit jusqu'à perdre son caractère sub-Doppler. Le fait que ce résultat soit le même pour un ensemble de 10 et 20 couches qui a une transmission quasi-nulle, prouve que le signal obtenu ne vient pas de la vapeur libre située au-dessus de l'opale mais bien de la vapeur confinée dans l'opale.

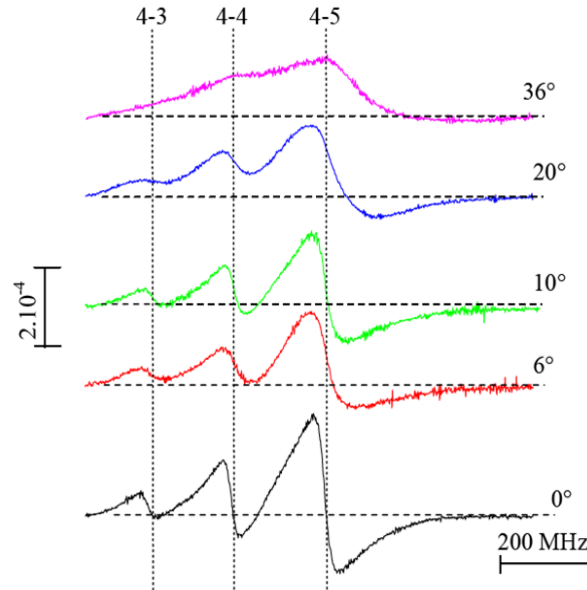


Figure 6.17 — Spectre de réflexion sur une opale (10 couches de billes de silice de $1 \mu\text{m}$ de diamètre) pour différents angles d'incidence (transition $F=4$ de la raie D_2 du césium, 12 MHz de FM, polarisation TE). [Fig.5.21 de la thèse de Philippe Ballin [101]]

Cette dépendance des spectres avec l'angle d'incidence est qualitativement le même que le comportement des signaux de réflexion sélective sur une interface plane pour une incidence non nulle [111]. Nous avons finalement attribué ce rétrécissement à une contribution exaltée, pour la région vide des interstices de la première demi-couche, des atomes en vol quasi-parallèle à la paroi (ce qui équivaut à un confinement 1-D).

Pour une gamme d'incidences assez élevées (typiquement de 40° à 60° pour l'angle externe d'incidence de la fenêtre), on observe une contribution étroite centrée sur la résonance, non élargie par effet Doppler, et qui se superpose à la structure sensible à l'élargissement Doppler (figure 6.18). La forme de cette contribution étroite qui combine absorption et dispersion, varie rapidement avec l'angle d'incidence (des variations plus lentes apparaissent sur la partie large du spectre), ainsi qu'avec la polarisation (l'incidence équivalente à un angle de Brewster exalte la contribution étroite). Cette structure étroite est plus visible quand la polarisation est TM. Aux incidences très obliques, le choix de la polarisation modifie non seulement l'amplitude des signaux (comme pour un angle de Brewster, défini sur une interface plane), mais aussi leur forme spectrale. La propagation à l'intérieur de l'opale, qui peut dépendre de la polarisation, paraît donc affecter la forme de raie alors que la réponse atomique elle-même est insensible à la polarisation. Les comportements observés, pour les composantes D_1 (894 nm) ou D_2 (852 nm) de Cs, sont globalement analogues, mais des différences marquées apparaissent, seulement pour $\theta \geq 30^\circ$, dans la combinaison entre structure étroite et l'enveloppe. Les spectres atomiques paraissent donc dépendre du rapport λ/d .

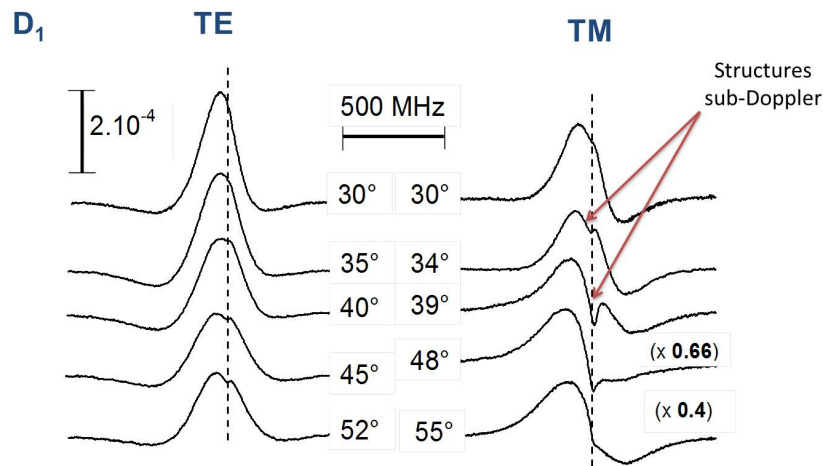


Figure 6.18 – Spectres (FM) de réflexion à différentes incidences (opale de 10 couches, billes de silice $d = 1\mu m$) pour la raie D_1 (894 nm). A gauche, pour la polarisation TE, à droite pour la polarisation TM. Les traits pointillés indiquent la position de la résonance en volume. [Figure 3 de l'article [11]].

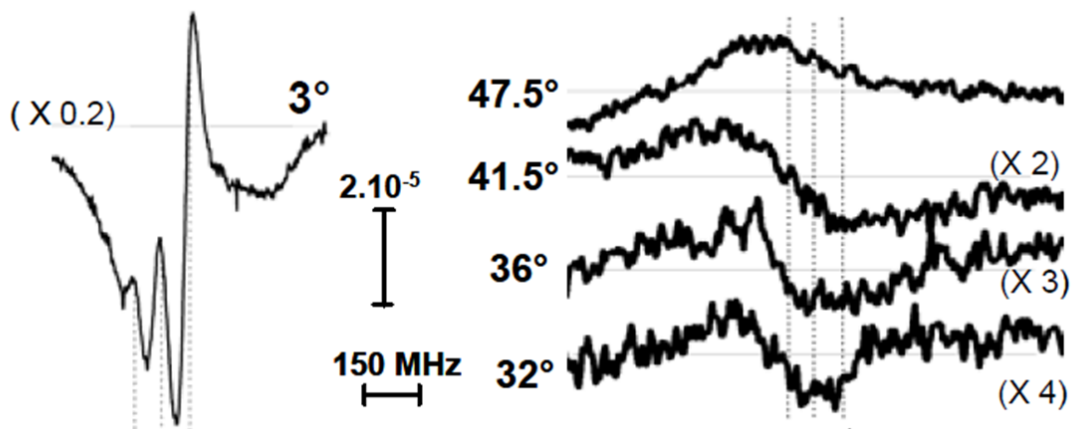


Figure 6.19 – Spectres (FM) de réflexion à différentes incidences (opale de 10 couches, billes de silice $d = 400\text{ nm}$) pour la raie 455 nm pour une polarisation TM. Les traits pointillés indiquent la position de la résonance en volume. [Figure 3a de l'article [10]].

Pour vérifier cette dépendance en λ/d , nous avons fait (thèse d'Elias Moufarej) des

mesures sur la seconde raie de résonance ($\lambda = 455 \text{ nm}$, figure 6.16) pour une opale de 10 couches de billes de silice de 400 nm de diamètre. Nous avons changé le rapport λ/d et regardé l'effet que cela avait sur nos spectres. Nous avons obtenu des résultats analogues. La forme de la contribution étroite qui combine absorption et dispersion, varie cependant plus rapidement encore avec l'angle d'incidence que pour les raies D_1 et D_2 (figure 6.19). Aux incidences obliques qui permettent d'observer la contribution étroite, des différences quantitatives notables apparaissent en changeant la longueur d'onde. Une analyse de la propagation optique à l'intérieur de l'opale, qui inclut la diffusion partielle du faisceau incident et l'émission résonante des atomes avec leurs contributions absorptive et dispersive, est donc nécessaire. J'ai travaillé avec Daniel Bloch à sa modélisation.

6.5.2 Modélisation de la réponse optique d'une opale infiltrée par un milieu résonant [12]

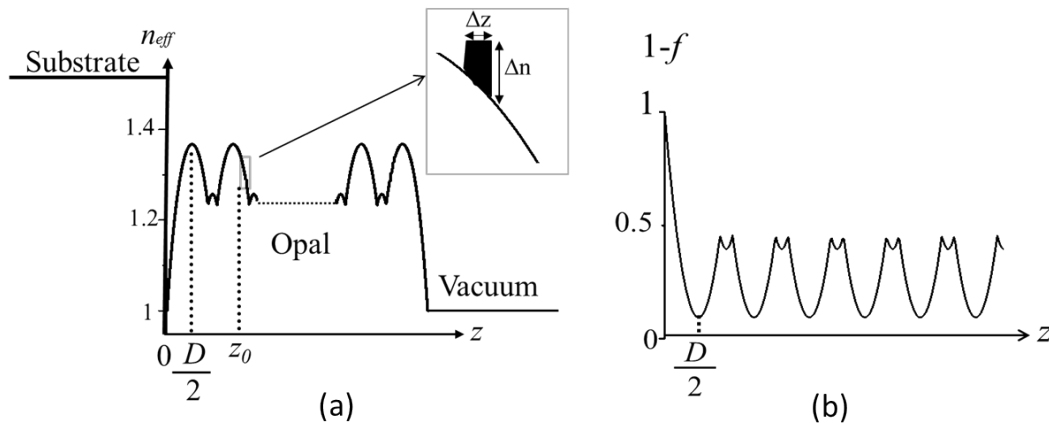


Figure 6.20 – (a) Indice effectif stratifié pour une opale incluant une couche supplémentaire perturbative $\Delta n \cdot \Delta z$ en z_0 . (b) Distribution spatiale des vides dans l'opale $1 - f(z)$ et donc du milieu résonant infiltré. [Figure 1 de l'article [9]].

Le modèle 1 D présenté dans la section 6.4 a été étendu à la situation où les interstices de l'opale (densité en $[1 - f(z)]$) qui auparavant étaient remplis de vide sont maintenant infiltrés par un milieu résonant dilué. Ce milieu est décrit par un indice complexe résonnant $\Delta n(\omega - \omega_0)$, où $(\omega - \omega_0)$ est le désaccord avec la résonance (figure 6.20). La linéarité du formalisme des matrices de transfert permet d'évaluer les variations résonnantes en réflexion par une dérivation à l'ordre 1.

Pour commencer, si on suppose une densité constante de milieu résonant infiltré, le modèle peut prédire le changement relatif de la réflexion de l'opale $\Delta R/R$ en fonction de la position z d'une tranche élémentaire de matériau infiltré (figures 6.21). Ce

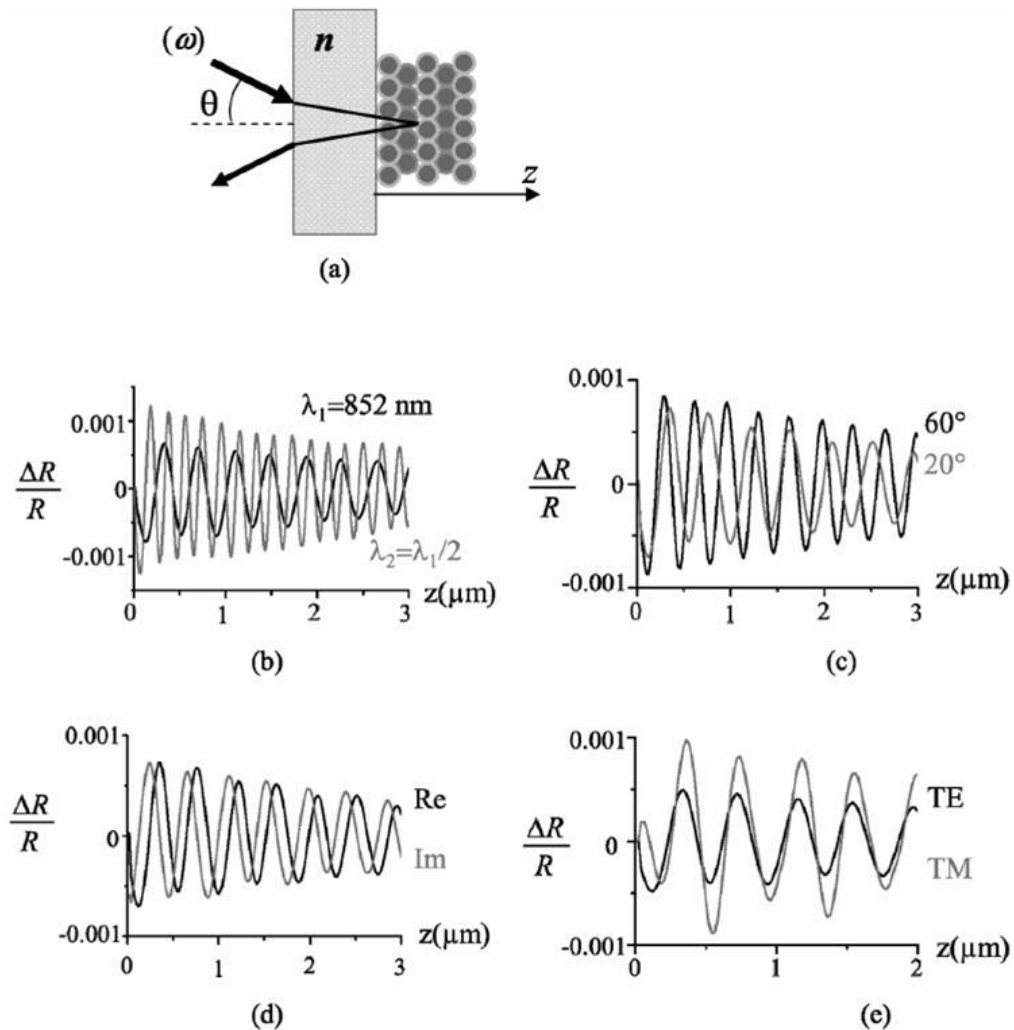


Figure 6.21 — Changement relatif de la réflexion en fonction de la position d'une tranche élémentaire additionnelle pour un angle d'incidence θ . (a) Montage expérimental (b) Comparaison entre $\lambda_1 = 852 \text{ nm}$ et $\lambda_2 = 426 \text{ nm}$ pour $\theta = 45^\circ$ et une polarisation TE. (c) Comparaison entre $\theta = 20^\circ$ et $\theta = 60^\circ$ pour $\lambda = 852 \text{ nm}$ et une polarisation TE. (d) Comparaison entre les effets d'une contribution dispersive et absorptive pour $\lambda = 852 \text{ nm}$, $\theta = 60^\circ$ et une polarisation TE. (e) Comparaison entre une polarisation TE et TM pour $\lambda = 852 \text{ nm}$ et $\theta = 45^\circ$. L'opale considérée ici est composée de 20 couches de nanobilles de silice de $1 \mu\text{m}$ de diamètre déposée sur un substrat de verre. $\alpha = 2.10^5 \text{ m}^{-1}$. $\Delta n \Delta z = 10^{-11} \text{ nm}$ pour (b), (c), (d) contribution dispersive et (e). $\Delta n \cdot \Delta z = -j \cdot 10^{-11} \text{ nm}$ pour (d) contribution absorptive. [Figure 2 de l'article [9]].

changement relatif oscille avec la position de la tranche. Sa période dépend de l'angle choisi (figure 6.21 (c)) et de la longueur d'onde incidente (figure 6.21 (b)), plus la longueur d'onde est faible plus la période est petite). Un décalage est observé quand on

passer d'une polarisation TE à TM (figure 6.21 (e)) et si l'on considère une contribution dispersive (Δn réel) ou absorptive (Δn imaginaire) pour la tranche élémentaire (figure 6.21 (d)).

Expérimentalement, la densité de matériau infiltré n'est pas constante mais suit une distribution spatiale en $1 - f(z)$ (position des interstices dans l'opale). Il est alors raisonnable de pondérer le changement relatif de la réflexion par cette distribution en $1 - f(z)$ puis d'intégrer spatialement sur toute l'opale (figure 6.22). Pour certaines incidences, il y a accord entre la périodicité optique avec laquelle l'onde se propage dans l'opale et la distribution géométrique du milieu résonant à l'intérieur de l'opale ($1 - f(z)$). Sous ces conditions d'accord de phase, la réponse résonnante fait interférer constructivement les interstices des premières couches et ceux des couches profondes. L'interférence optimale est obtenue pour des incidences différentes, selon que la réponse optique est absorptive ou dispersive. Des variations similaires sont obtenues entre une polarisation TE et TM.

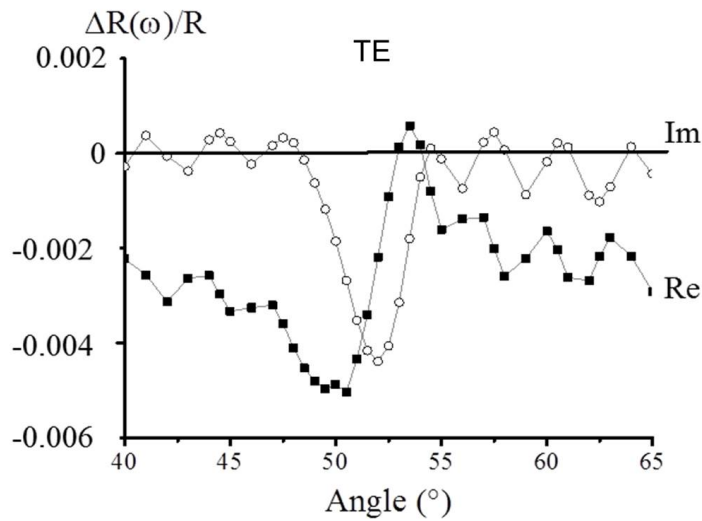


Figure 6.22 – Changement relatif de la réflexion intégrée sur toute l'opale infiltrée en fonction de l'angle d'incidence pour un milieu résonnant dispersif (noté Re, $\Delta n = 5 \cdot 10^{-4}$) ou absorptif (noté Im, $\Delta n = -j \cdot 5 \cdot 10^{-4}$). L'opale considérée est la même que précédemment dans la figure 6.21 pour une polarisation TE et $\lambda = 852 \text{ nm}$. [Figure 4 de l'article [9]].

On a considéré ensuite une réponse Lorentzienne pour le matériau infiltré :

$$\Delta n \propto (1 - f(z))[(\omega - \omega_0) - j\gamma^{-1}] \quad (6.3)$$

où ω_0 est le centre de la résonance et γ est la largeur de la Lorentzienne.

La forme de raie associée au matériau résonnant infiltré obtenue varie fortement avec l'angle d'incidence (figure 6.23). Cela ressemble à ce que nous avons observé lorsque nous avons étudié les raies D_1 (894 nm) et D_2 (852 nm) (voir figure 6.23) pour la contribution étroite sub-Doppler. La sensibilité à la polarisation prédite est analogue à ce que nous avons observé expérimentalement. Le modèle prédit des variations de forme avec l'angle d'incidence plus rapides aux longueurs d'onde petites comme expérimentalement à 455 nm (figure 6.19). Le modèle prédit de forts changements avec l'angle d'incidence et plus modestes avec la longueur d'onde. Ces résultats sont compatibles avec ce que nous avons observé pour une vapeur de césium infiltrée dans une opale Langmuir-Blodgett.

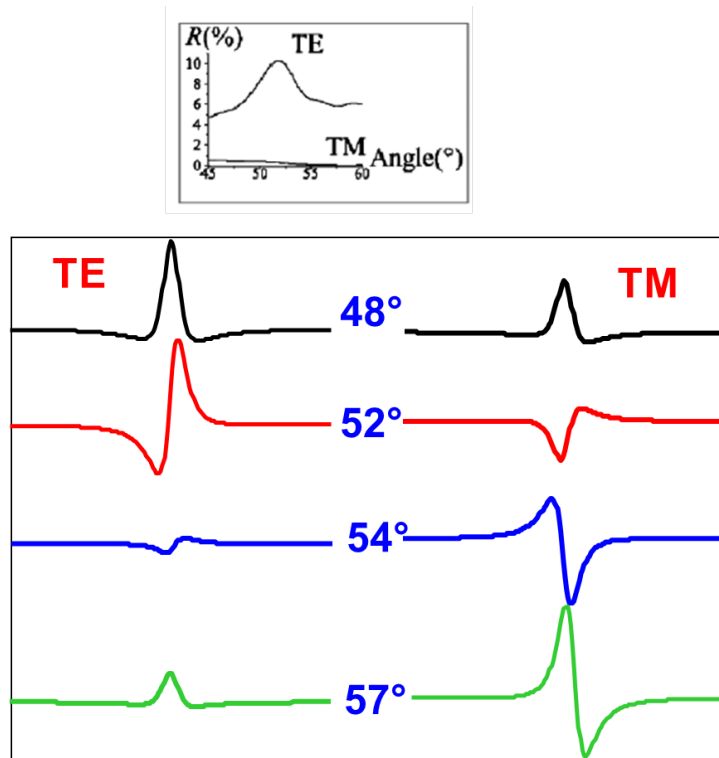


Figure 6.23 — Spectres de réflexion (FM) calculés associés à un matériau résonnant infiltré ayant une réponse Lorentzienne complexe pour différents angles d'incidence. A gauche, la polarisation est TE, à droite elle est TM. L'échelle est la même pour tous les spectres. Les valeurs de R sans infiltration résonante sont indiquées dans l'encadré. On peut y voir un pic de Bragg d'ordre deux pour la polarisation TE correspondant à un angle pseudo-Brewster pour la polarisation TM (la longueur d'onde est de 852 nm et l'opale toujours celle de la figure 6.21). [Figure 5 de l'article [9]].

Ce modèle ne permet pas de prévoir exactement la forme de nos spectres expé-

rimentaux. Il considère les atomes immobiles (sans élargissement Doppler associé au mouvement thermique atomique) ce qui n'est pas le cas d'un gaz infiltré. Ce modèle est valable uniquement à des densités d'infiltration faibles pour conserver la linéarité du formalisme des matrices de transfert. Dans nos expériences, ce critère est respecté. Dans le cas de nos opales de silice de type Langmuir-Blodgett, les défauts présents dans une couche (dislocations, agrégats ... voir figure 6.5) font que lors du dépôt couche par couche de l'opale, l'arrangement est de moins en moins compact et donc régulier. L'hypothèse suivant laquelle le gaz infiltré suit une distribution en $1 - f(z)$ devient fautive quand on va en profondeur dans l'opale. Cela réduit expérimentalement la possibilité de voir une réponse cohérente des atomes pour les couches les plus éloignées. Pour cela, il faudrait une opale mieux organisée en profondeur, tout en ayant un nombre de couches faible (pour éviter la formation d'agrégats de césium) et aussi compatible avec le matériau infiltré (pour nous le césium). Pour des opales de type LB au nombre de couches contrôlé, seules les opales avec des billes en polystyrène ont une belle organisation en profondeur (du fait de la très faible dispersion de leur diamètre $\approx 10^{-3}$). Cependant, le polystyrène étant incompatible avec une vapeur de césium, il est impossible de tester une telle cellule. Finalement, la plus importante des limitations de notre modèle est qu'il ignore la lumière diffusée considérée uniquement comme un source de perte. La lumière diffusée contribue également à l'excitation du matériau infiltré et la phase de l'excitation correspondante (pas nécessairement aléatoire) diffère habituellement de celle résultant d'une excitation par un champ qui se propage.

Bien que ce modèle ne permette pas de prévoir exactement la forme de nos spectres expérimentaux, cette analyse nous a permis de comprendre pourquoi la forme de nos spectres changeait avec l'angle d'incidence, la polarisation et la longueur d'onde. Cela nous a aussi conforté dans l'idée que les structures spectroscopiques étroites observées aux grands angles apparaissent quand il y a accord de phase entre les interférences optiques (qui dépendent de la longueur d'onde) et les contributions atomiques associées aux diverses couches d'interstices selon la géométrie de la distribution périodique propre à l'opale.

Pour explorer l'effet du nombre de couches et essayer d'en savoir plus sur l'origine du signal étroit observé, nous avons effectué des mesures sur des opales de quelques couches.

6.5.3 Expériences sur des opales composées de quelques couches de billes

Nous avons effectué avec Elias Moufarej (PHD) des expériences complémentaires sur la raie $\lambda = 894 \text{ nm}$ avec des cellules multizones contenant des opales de billes de silice de 1030 nm de diamètre avec soit 4, 3, 2, voire une couche (figure 6.24). Même avec quelques couches, la structure étroite est toujours visible sur une grande plage d'angles. Les formes de raies dépendent fortement de l'angle d'incidence et de la polarisation de la lumière. Le résultat remarquable est que des résonances étroites (sub-Doppler) sont

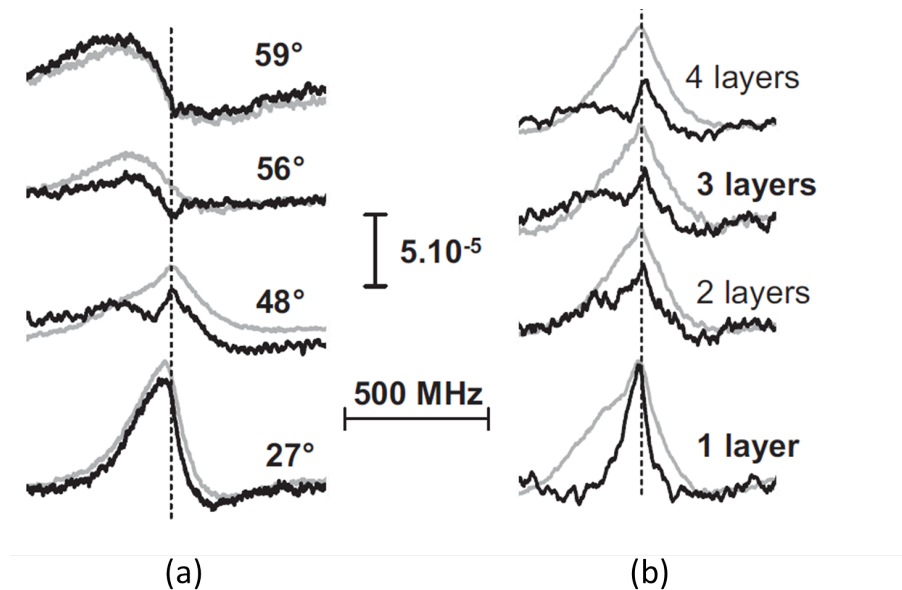


Figure 6.24 – Spectres (FM) de réflexion pour la raie 894 nm pour une opale multizone avec des billes de silice de 1030 nm de diamètre pour une polarisation TE (en gris) et TM (en noir). (a) Spectres obtenus pour une opale de 3 couches à différentes incidences. (b) Spectres obtenus à une incidence de 45° . Le nombre de couches de l’opale est indiqué sur chaque spectre. Les traits pointillés indiquent la position de la résonance en volume. [Figure 3 b de l’article [10]].

observées même avec une seule couche de nanosphères pour des incidences obliques entre $35\text{-}60^\circ$ (figure 6.24 (b)) alors que pour une seule couche nous nous attendions à ne l’observer qu’en incidence quasi-normale. Pour l’instant, nous cherchons encore une interprétation physique à l’origine de ces signaux. Cependant, ces nouvelles mesures suggèrent que des signaux sub-Doppler ne peuvent pas être attribués uniquement à un confinement tridimensionnel de la vapeur atomique dans le cas d’une seule couche. La transmission n’est plus négligeable dans le cas de quelques couches. Le signal obtenu est donc un mélange entre les atomes confinés dans les interstices de l’opale et ceux libres au-dessus de l’opale. L’interprétation et la modélisation de ces spectres se complique et nécessite encore du travail.

6.6 Conclusion

Dans un premier temps, en utilisant la technique développée par Micheletto, nous avons réussi à créer un film compact de sphères diélectriques de silice de diamètre 750 nm déposé sur un substrat de verre. Nous avons développé une méthode diffractive permettant de déterminer le diamètre des billes, l’orientation de la structure cristalline et si le film possédait ou non des domaines cristallins ayant des orientations différentes. La dispersion du diamètre des nanobilles ainsi que les agrégats présents dans nos films

nous ont empêché de prendre ce film en sandwich entre deux lames de verre et donc d'en faire une cellule.

Dans un second temps, nous nous sommes intéressés à une tranche d'opale 1 *mm* d'épaisseur, polie, composée de nanobilles de silice de 230 *nm* de diamètre que nous avons prise en sandwich entre deux fenêtres pour la mettre en cellule et mis en contact avec une vapeur de césium. L'opale épaisse et avec des interstices de faible taille (faible libre parcours moyen) s'est avérée piéger fortement la vapeur de césium comme une éponge et favoriser la formation d'agrégats. Un chauffage pendant une journée nous a permis difficilement de désorber les atomes piégés dans l'opale. De plus, au bout d'un certain temps, l'opale a glissé et n'était plus prise en sandwich entre les deux fenêtres. Face à ces résultats, il nous était donc impossible d'étudier la spectroscopie de la lumière diffusée par une telle cellule. Nous nous sommes donc orientés vers des opales beaucoup moins épaisses et avec des diamètres plus forts (augmentation du libre parcours moyen et diminution de la distance nécessaire à parcourir pour sortir de l'opale) et avons revu la structure de notre cellule.

Dans un troisième temps, nous nous sommes intéressés à des opales de type Langmuir-Blodgett déposées sur un substrat de verre pour lesquelles le nombre de couches est parfaitement maîtrisé, par contre l'empilement est un arrangement cubique face centré et hexagonal compact. J'ai développé un modèle d'indice effectif stratifié à une dimension. Ce modèle très flexible et rapide permet de prédire les spectres de transmission et de réflexion d'une opale quel que soit l'angle d'incidence et la polarisation (forme, largeur, position, amplitude ...). Le modèle peut être utilisé aussi bien lorsque la lumière est incidente du côté du substrat, que du côté de l'interface vide. Le modèle montre la forte influence de l'interface avec l'opale, indépendamment de la structure interne de l'opale. Cette rupture de périodicité à l'interface, inévitable pour les cristaux photoniques, est rarement prise en compte. Dans des expériences dédiées pour des opales LB avec des billes de silice, notre modèle montre un accord quantitatif satisfaisant en évaluant numériquement les pertes afin de reproduire les spectres de transmission. Alternativement, pour une monocouche de billes, le modèle 1D stratifié de l'indice effectif n'est plus applicable. Un calcul numérique complet utilisant la méthode des éléments finis a été développé dans le cas d'un cristal parfait en périodicité. Les spectres prédits sont en très bon accord avec les expériences après moyennage sur l'orientation (structure hexagonale) de la monocouche par rapport au plan d'incidence. Ce moyennage est rendu nécessaire par la nature polycristalline de l'opale.

Suite à cela, des opales LB ont été mises en cellule et en contact avec une vapeur de césium (10 ou 20 couches de nanobilles de 1 μm de diamètre et 10 couches de nanobilles de 400 *nm*). Quelle que soit la longueur d'onde utilisée (D_1 , D_2 ou 455 *nm*) pour nos expériences spectroscopiques, nous avons obtenu des résultats analogues. Pour une incidence quasi-normale, on observe un spectre (FM) RS franchement sub-Doppler, quoique plus large que le spectre équivalent de RS à une interface plane. Nous avons attribué ce rétrécissement à une contribution exaltée des atomes en vol quasi-parallèle

à la paroi présents dans la première demi-couche (équivalent d'un confinement 1 D). La forme de raie s'élargit notablement avec l'angle d'incidence. Pour une gamme d'incidences assez élevées (typiquement de 40° à 60° pour l'angle externe d'incidence de la fenêtre), on observe une contribution étroite centrée sur la résonance non élargie par effet Doppler, et qui se superpose à la structure sensible à l'élargissement Doppler : la forme de cette contribution étroite qui combine absorption et dispersion, varie rapidement avec l'angle d'incidence (des variations plus lentes apparaissent sur la partie large du spectre), ainsi qu'avec la polarisation (l'incidence équivalente à un angle de Brewster exalte la contribution étroite). Aux incidences obliques qui permettent d'observer la contribution étroite, des différences quantitatives notables apparaissent en changeant la longueur d'onde. Une analyse de la propagation optique à l'intérieur de l'opale, qui inclut la diffusion partielle du faisceau incident et l'émission résonante des atomes avec leur contributions absorptive et dispersive, montre que la forme de raie atomique associée à la contribution des régions internes de l'opale devraient évoluer rapidement avec les caractéristiques de la propagation (angle d'incidence, polarisation). Ces variations de forme avec l'angle d'incidence sont encore plus rapides aux longueurs d'onde les plus courtes (455 nm). Ceci est conforme à des prévisions d'un modèle que nous avons développé, qui prend en compte l'accord de phase entre les interférences optiques (qui dépendent de la longueur d'onde) et les contributions atomiques associées aux diverses couches d'interstices selon la géométrie de la distribution périodique propre à l'opale. Cette analyse nous a permis de conclure que les structures spectroscopiques étroites observées aux grands angles proviennent du confinement tridimensionnel dans l'opale.

Finalement, nous avons effectué des expériences complémentaires sur des cellules multizones de 4, 3, 2, voire une couche ($1 \mu\text{m}$ de diamètre). Nous avons observé des structures sub-Doppler, sous incidences obliques même pour une seule couche qui ne peuvent être la signature d'un confinement tridimensionnel. L'interprétation de ces formes de raies est compliquée, d'autant que la transmission dans l'opale n'étant plus nulle, le spectre obtenu est donc un mélange entre la contribution des atomes confinés dans l'opale et ceux libres au-dessus de l'opale. Ces résultats nécessitent une exploration expérimentale plus systématique et une autre modélisation. Cela introduit comme perspective de relancer la fabrication d'une opale monocouche emprisonnée entre les deux fenêtres d'une cellule.

6.7 Articles en relation avec ce chapitre

Les cinq articles [8–12] sont en relation avec ce chapitre. Les quatre principaux articles de ce chapitre [9–12] sont reproduits à la fin de ce manuscrit.

Chapitre 7

Travaux en cours et perspectives

7.1 Étude de l'interaction atome-surface entre un atome excité et une surface thermiquement émissive en saphir superpoli - Couplage résonant

Nous poursuivons actuellement des expériences analogues à celle du chapitre 5 paragraphe 5.4 pour un atome de Césium $7P_{1/2}$ et aussi $7P_{3/2}$ à l'interface avec la même fenêtre de saphir superpoli. On peut étudier ces niveaux en effectuant une réflexion sélective directement depuis le niveau fondamental par la raie de seconde résonance du Césium (459 nm et 455 nm) (voir figure 7.1). La transition atomique Cs ($7P_{3/2}$) est sur l'aile côté positif de la dispersion de la surface (contrairement au cas précédemment décrit pour le Cs($7D_{3/2}$) au paragraphe 5.4). Comme le montre la figure 7.2, l'interaction Casimir-Polder décroît alors avec la température pour Cs ($7P_{3/2}$) alors qu'elle augmentait constamment pour Cs($7D_{3/2}$). Au contraire, dans le cas de la transition ($7P_{1/2}$), elle tombe en coïncidence quasi-exacte avec le mode de surface du saphir pour Cs ($7P_{1/2}$) (couplage vers $6D_{3/2}$ à $12.15\ \mu\text{m}$). Comme le montre la figure 7.2, on attend dans ce cas un accroissement rapide de l'attraction de surface avec l'excitation thermique. Deux transitions très proches doivent donc donner deux évolutions très différentes du coefficient C_3 avec la température. Nous avons donc décidé de réaliser de manière simultanée ces deux réflexions sélectives au même endroit sur la surface superpolie et pour des conditions expérimentales identiques (même densité de vapeur de césium et température de surface). Nos premières mesures, réalisées suivant la méthode décrite au chapitre 5 paragraphe 5.3.2 utilisant un catalogue de courbes universelles dont le seul paramètre est A ($\propto C_3$ et donc $\propto \text{Re}(S)$), confirment cette différence d'évolution (figure 7.2).

En parallèle, des mesures complémentaires ont été effectuées (même méthode qu'au chapitre 5 paragraphe 5.2.2) pour déterminer la constante diélectrique pour le saphir superpoli (cette fois) suivant que l'axe optique soit orienté perpendiculairement ou pa-

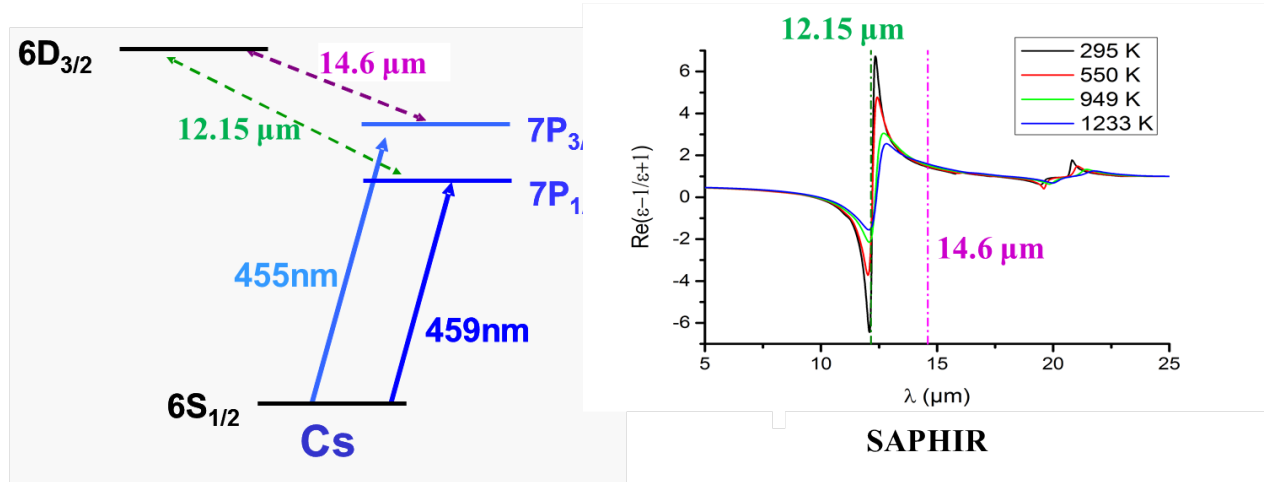


Figure 7.1 — Niveaux atomiques du césium (à gauche). Partie réelle de la réponse de surface du saphir superpoli $Re(S)$ à 295K, 550K, 949K et 1233K (à droite). Les traits horizontaux en pointillés montrent la position de la transition $7P_{3/2} \rightarrow 6D_{3/2}$ de l'aile droite de la dispersion et la transition $7P_{1/2} \rightarrow 6D_{3/2}$ au centre de la résonance.

rallèlement à la surface en saphir pour des températures allant de 295 K à 2053 K (Figures 7.1 et 7.3). Cela nous a permis de réévaluer le coefficient C_3 en fonction de la température (courbes en trait plein sur la figure 7.2). Les mesures expérimentales bien qu'en accord avec ces prédictions, sont cependant toujours légèrement au-dessus des prédictions théoriques à hautes températures. D'où peut venir cette différence ?

La théorie de la réflexion sélective utilisée ici pour reproduire nos spectres expérimentaux n'inclut pas une dispersion spatiale (en z^{-3}) pour la largeur de la transition optique, ce qui a lieu lorsque la durée de vie d'un état excité est modifiée par le transfert thermique en champ proche. Dans notre expérience, la transition $7P_{1/2}$ tombe en coïncidence quasi-exacte avec le mode de surface du saphir pour l'atome de césium dans le niveau $7P_{1/2}$. L'émission thermique de surface peut donc être absorbée et permettre un transfert résonnant réel de l'atome de césium du niveau $7P_{1/2}$ vers le niveau plus excité $6D_{3/2}$. Pour l'instant nous avons négligé cet effet. Pour en tenir compte, nous devons utiliser un nouveau "catalogue" de formes de raie modifiées incluant cet effet. Les spectres de réflexion sélective de cette nouvelle bibliothèque sont caractérisés par la constante sans dimension A ($\propto Re(S)$) mais maintenant aussi par la constante $B = k^3\Gamma$ ($\propto Im(S)$) où k est le vecteur d'onde et Γ le taux d'émission spontanée (voir figure 7.3 pour voir en même temps la forme de la partie imaginaire de la réponse de surface et la

7.1 Étude de l'interaction atome-surface entre un atome excité et une surface thermiquement émissive en saphir superpoli - Couplage résonant 15

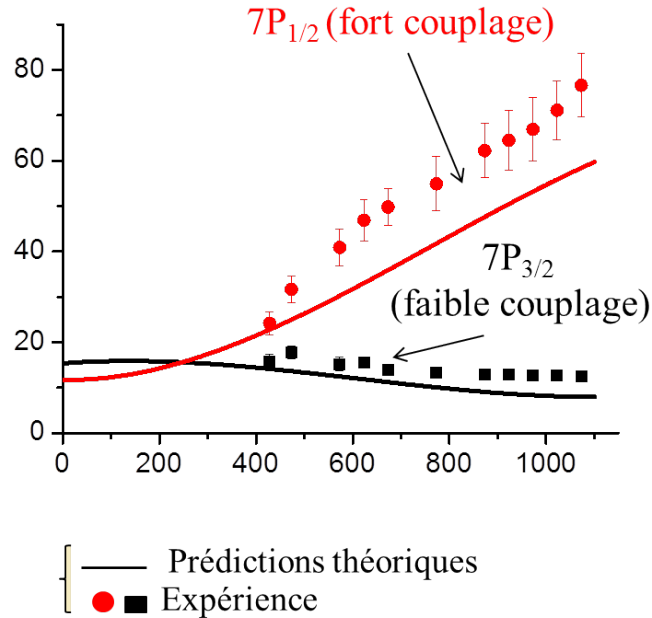


Figure 7.2 — Effets de la température sur le coefficient C_3 pour les transitions $7P_{3/2}$ et $7P_{1/2}$. Les points correspondent aux mesures expérimentales. Les courbes en traits pleins correspondent aux prédictions théoriques que nous avons obtenues avec notre modèle théorique et les mesures faites sur une surface superpolie.

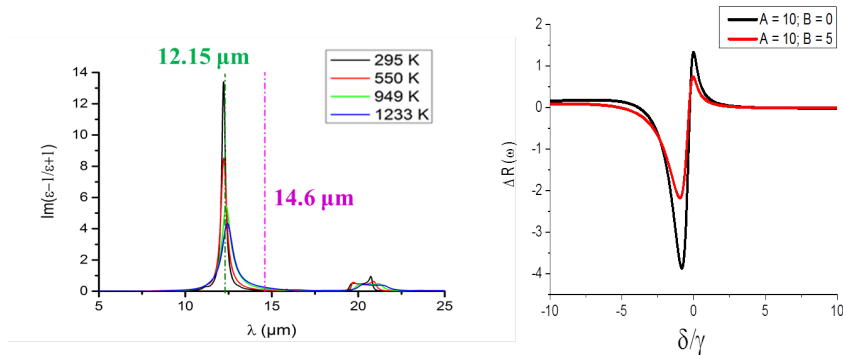


Figure 7.3 — (a) Partie imaginaire de la réponse du saphir superpoli ($\text{Im}(S)$) à 295K, 550K, 949K et 1233K. Les traits horizontaux en pointillés montrent la position de la transition $7P_{3/2} \rightarrow 6D_{3/2}$ de l'aille droite de la dispersion et la transition $7P_{1/2} \rightarrow 6D_{3/2}$ au centre de la résonance. (b) Spectres de réflexion sélective en modulation de fréquence (signal dérivé) pour différents couples (A, B) [Figure 2 de l'article [112]]

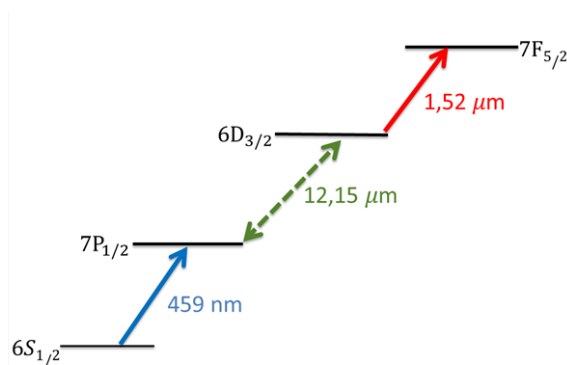


Figure 7.4 – Niveaux atomiques du césium

bibliothèque de spectres). En tenant compte alors des deux paramètres de couplage (A et B), on doit pouvoir mettre en évidence les changements de durée de vie du césium ($7P_{1/2}$) induits par l'excitation thermique de surface. L'étude simultanée sur la raie à 455 nm ($7P_{3/2}$), voire sur la raie de résonance à 894 nm (D_1) comme référence, devrait notamment introduire des contraintes sur l'ajustement suffisantes pour compenser la flexibilité accrue d'un ajustement par un catalogue à deux paramètres.

Nous voulons également étudier l'influence de la biréfringence du saphir sur la valeur du coefficient de vW peut-être à l'origine de la différence entre les mesures expérimentales et les prédictions théoriques. Nous comptons également vérifier et quantifier le transfert réel entre le niveau $7P_{1/2}$ et $6D_{3/2}$. Pour cela, nous comptons pomper la transition $6S_{1/2} \rightarrow 7P_{1/2}$ à 459 nm , puis étudier la raie de résonance $6D_{3/2} \rightarrow 7F_{5/2}$ à $1.52\mu\text{m}$ par spectroscopie RS (voir la figure 7.4).

7.2 Mesures de l'interaction Casimir-Polder avec des molécules

Notre groupe a aussi en projet de mélanger son savoir sur la réflexion sélective avec celui de l'équipe Métrologie, Molécules et Tests Fondamentaux (MMTF) sur les molécules avec l'aide de Benoît Darquié et Sean Tokunaga. Nous avons dans l'idée de faire les premières mesures de l'interaction Casimir Polder avec des molécules. Les difficultés de ces mesures est que les signaux attendus sont faibles à cause de la faible force d'oscillateur des transitions et des fonctions de répartition des molécules. Les molécules contrairement aux atomes possèdent également beaucoup plus de niveaux fondamentaux ce qui rend l'identification des raies observées plus délicates contrairement aux atomes.

Dans ce but, nous avons effectué les premiers tests pour vérifier la faisabilité de cette expérience. Nous avons réussi à obtenir un spectre de réflexion sélective des transitions ro-vibrationnelles de SF_6 (molécules bien connue et disponible chez MMTF, pression de

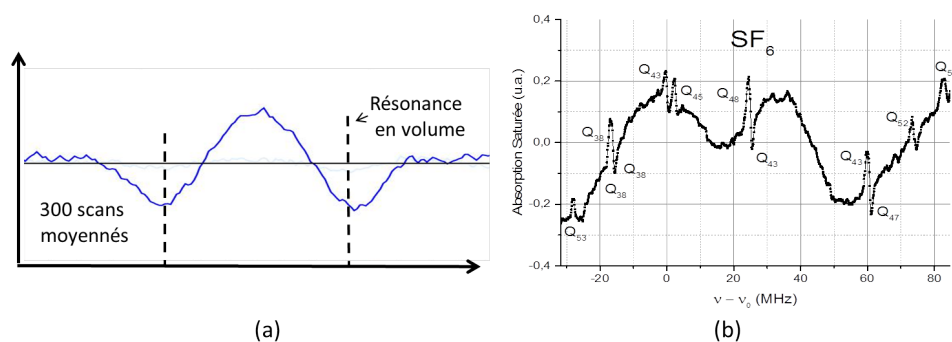


Figure 7.5 — (a) Signal de réflexion sélective obtenu avec des molécules de SF_6 , une surface en $ZnSe$ et un laser CO_2 à $10,6 \mu m$ après avoir moyenné 300 spectres. Les traits pointillés verticaux indiquent la position des résonances en volume. (b) Signal d'absorption saturée obtenu avec des molécules de SF_6 , une surface en ZnS et un laser QCL à $10,6 \mu m$. Les niveaux ro-vibrationnels du SF_6 ont été identifiés et sont indiqués sur le spectre.

400 mTorr et qui possède de fortes transitions vers $10 \mu m$) proche d'une surface en $ZnSe$ (matériau transparent vers $10 \mu m$) avec un laser CO_2 à $\lambda = 10,6 \mu m$ (disponible chez MMTF). Pour réussir à voir ce signal, il a fallu accumuler 300 spectres pendant deux heures puis les moyennés (figure 7.5 (a)). Les qualités du laser CO_2 sont sa stabilité en fréquence et sa largeur de raie ($\approx 100 Hz$), il est malheureusement très encombrant, a un balayage et modulation en fréquence limitée et un bruit d'intensité non négligeable. Pour remédier à cela, nous nous sommes orientés vers un autre type de laser : les lasers à cascades quantiques (QCL). En effet, ils sont peu encombrants, peuvent être balayés sur plusieurs GHz , peuvent être modulés en fréquence. Ils sont malheureusement moins stables (ils ont une stabilité en température de $10 mK$ alors que leur fréquence varie de $2 MHz/mK$) ce qui peut être compensé par un asservissement de la fréquence sur une absorption linéaire par exemple et les faibles signaux observés par un moyennage de nombreuses courbes. Ils ont une largeur de laser plus grande ($\approx 500 Hz$). Le bruit d'intensité est quant à lui supposé faible (en cours d'étude). Utilisant ce laser QCL, nous avons réalisé une expérience d'absorption saturée sur des molécules SF_6 avec succès (figures 7.5 (b)).

Ces expériences constituent une première étape avant de monter une expérience de réflexion sélective avec des molécules de SF_6 . Cela permettra, à plus long terme, de mettre en évidence des effets liés à la géométrie complexe des molécules (chiralité, anisotropie...) et de mieux comprendre la physisorption molécule/surface. Pour cela, d'autres molécules (NH_3 , C_2H_4 , CO_2 ou plus complexes $C_3H_6O_3$, CH_3ReO_3 ...) et surfaces seront utilisées. Ces expériences constitueront une première étape vers la spectroscopie de haute résolution de molécules confinées dans un espace micrométrique.

7.3 Confinement 3D

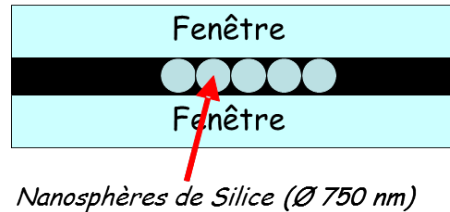


Figure 7.6 — Schéma de principe d'une cellule contenant une monocouche de sphères de silice. [Fig.1 (a) de l'article [8]]

L'obtention d'un signal sub-Doppler avec quelques couches d'opale voire une seule couche d'opale, nous encourage à faire une exploration plus systématique (changement λ , diamètre des billes, angles ...) ainsi qu'une nouvelle modélisation, le signal obtenu provenant dans ce cas de l'intérieur de l'opale mais également des atomes situés au-dessus de l'opale. Cela introduit aussi comme perspective de relancer la fabrication d'un film de nanosphère ou d'un film de cylindre emprisonné entre les deux fenêtres d'une cellule ce qui est toujours un défi technologique.

Il est également envisager d'insérer dans une telle cellule des molécules plutôt que des atomes, ces derniers étant compatibles chimiquement avec beaucoup plus de matériaux, nécessitant des structures de tailles plus grandes, ayant une largeur naturelle beaucoup plus faible qu'un atome ($1kHz$) et ne nécessitant pas de chauffer un réservoir pour changer la pression d'un gaz moléculaire. La construction d'une cellule contenant des molécules semble alors techniquement plus facilement réalisable. Est-il possible d'amplifier le signal moléculaire dans une telle cellule? D'observer un signal sub-doppler? Pour une large gamme d'angles? Il est également envisagé de détecter non plus la lumière réfléchie par un tel montage mais celle qui est diffusée.

Bibliographie

- [1] G. DUTIER, P. TODOROV, I. HAMDI, I. MAURIN, S. SALTIEL, D. BLOCH et M. DUCLOY, « Dicke coherent narrowing in two-photon and Raman spectroscopy of thin vapour cells ». *PRA (rapid comm.)* **72**, 1(R) (2005).
- [2] M.P. GORZA et M. DUCLOY, « Van der Waals interactions between atoms and dispersive surfaces at finite temperature ». *Eur. Phys. J. D* **40**, 343 (2006).
- [3] T. PASSERAT DE SILANS, I. MAURIN, P.C. DE SOUZA SEGUNDO, M.-P. SALTIEL, S. AND GORZA, M. DUCLOY, D. BLOCH, D. DE SOUSA MENESES et P. ECHEGUT, « Temperature dependence of the dielectric permittivity of CaF_2 , BaF_2 and Al_2O_3 : application to the prediction of a temperature dependent van der Waals surface interaction exerted onto a neighbouring Cs ($8P_{3/2}$) atom ». *Journal of Physics : Condensed Matter* **21**, 255 902 (2009).
- [4] A. LALLOTIS, I. MAURIN, M. FICHET, D. BLOCH, M. DUCLOY, N. BALASANYAN, A. SARKISYAN et D. SARKISYAN, « Selective reflection spectroscopy at the interface between a calcium fluoride windows and Cs vapour ». *Applied Physics B : Lasers and Optics* **90**, 415 (2008).
- [5] T. PASSERAT DE SILANS, A. LALLOTIS, I. MAURIN, M.-P. GORZA, P. SEGUNDO, M. DUCLOY et D. BLOCH, « Experimental observations of temperature effects in the near-field regime of the Casimir-Polder interaction ». *Laser Physics* **24**, 074 009 (2014).
- [6] T. PASSERAT DE SILANS, I. MAURIN, A. LALLOTIS, P. CHAVES DE SOUZA SEGUNDO et D. BLOCH, « Extra sub-Doppler lines in the vicinity of the third resonance 6S-8P of atomic Cs attributed to optically induced Cs dimers ». *PRA* **83**, 043 402 (2011).
- [7] A. LALLOTIS, T. PASSERAT DE SILANS, I. MAURIN, M. DUCLOY et D. BLOCH, « Casimir-Polder interactions in the presence of thermally excited surface modes ». *Nature comm.* **5364**, 1 (2014).
- [8] M. ROMANELLI, I. MAURIN, P. TODOROV, C.-H. CHAN et D. BLOCH, « A 2D nanosphere array for atomic spectroscopy ». *Annales de Physique*) **32**, 127 (2007).

- [9] I. MAURIN, A. MOUFAREJ, E. LALLOTIS et D. BLOCH, « Optics of opal modeled with a stratified effective index and the effect of the interface ». *JOSAB* **32**, 8 (2015).
- [10] E. MOUFAREJ, I. MAURIN, I. ZABKOV, A. LALLOTIS, P. BALLIN, V.V. KLIMOV et D. BLOCH, « Infiltrating a thin or single layer opal with an atomic vapour : sub-doppler signals and crystal optics ». *Europhysics Letters, Special Issue (Proceedings of META 14-Singapore)* **108**, 17008 (2014).
- [11] P. BALLIN, E. MOUFAREJ, I. MAURIN, A. LALLOTIS et D. BLOCH, « Three-dimensional confinement of vapor in nanostructures for sub-Doppler optical resolution ». *App. Phys. Lett.* **102**, 231115 (2014).
- [12] I. MAURIN et D. BLOCH, « Resonant infiltration of an opal : reflection line-shape and contribution from in-depth regions ». *Journal of Chemical Physics* **142**, 234706 (2015).
- [13] R. H. DICKE, « The effect of collisions upon the Doppler width of spectral lines ». *Phys. Rev.* **89**, 472 (1953).
- [14] R. H. ROMER et R. H. DICKE, « New Technique for High-Resolution Microwave Spectroscopy ». *Phys. Rev.* **99**, 532 (1955).
- [15] J. FAIST, F. CAPASSO, D. L. SIVCO, C. SIRTORI, A. L. HUTCHINSON et A. Y. CHO, « Quantum cascade laser ». *Science* **264**, 553 (1994).
- [16] C. SIRTORI, P. KNUCK, P. BARBIERI, S. COLLOT, J. NAGLE, M. BECK, J. FAIST et U. OEASTERLE, « $GaAs/Al_xGa_{1-x}$ as quantum cascade lasers ». *Appl. Phys Lett.* **73**, 3486 (1998).
- [17] R. KOLHER, A. TREDICUCCI, H.E. BELTRAM, F. ANS BEERE, E.H. LINFIELD, A. GILES DAVIES, D.A. RITCHIE, R.C. IOTTI et F. ROSSI, « Terahertz semiconductor-heterostructure laser ». *Nature* **417**, 156 (2002).
- [18] C. GMACHT, D. SIVCO, J. BAILLARGEON, F. CAPASSO et A. CHO, « Quantum cascade lasers with a heterogeneous cascade : two-wavelength operation ». *Appl. Phys Lett.* **79**, 572 (2001).
- [19] J.-Y. BENGLOAN, A. DE ROSSI, V. ORTIZ, X. MARCADET, M. CALLIGARO, I. MAURIN et C. SIRTORI, « Intra-cavity sum frequency generation GaAs quantum cascade lasers ». *Appl. Phys. Lett.* **84** (12), 2019 (2004).
- [20] M. A. BELKIN, F. CAPASSO, A. BELYANIN, D.L. SIVCO, A.Y. CHO, D.C. OAKLEY, C.J. VINEIS et G.W. TURNER, « Terahertz quantum-cascade-laser source based on intracavity difference-frequency generation ». *Nature Photonics* **1**, 288 (2007).
- [21] M. A. BELKIN, F. CAPASSO, F. XIE, A. BELYANIN, M. FISCHER, A. WITTMANN et J. FAIST, « Room temperature terahertz quantum cascade laser source based on intracavity difference-frequency generation ». *App. Phys. Lett.* **92**, 201101 (2008).
- [22] E. MOREAU, I. ROBERT, J.-M. GERARD, I. ABRAM, L. MANIN et V. THIERRY-MIEG, « Single-mode solid-state single photon source based on isolated quantum dots in pillar microcavities ». *App. Phys. Lett.* **79** (18), 2865 (2001).

- [23] E. PURCELL, « Spontaneous emission probabilities at radio frequencies ». *Phys. Rev.* **69** (11-12), 681 (1946).
- [24] G. BJORK et Y. YAMAMOTO, « Analysis of semiconductor microcavity lasers using rate equations ». *IEEE journal of quantum electronics* **27** (11), 2386 (1991).
- [25] P.R. RICE et H.J. CARMICHAEL, « Photon statistics of a cavity-QED laser : a comment on the laser-phase-transition analogy ». *Phys Rev A* **50**, 4318 (1994).
- [26] R. E. SLUSHER, U. MOHIDEEN, J. RARITY et C. WEISBUCH (éditeurs), *Microcavities ans Photonics Bandgaps*, Kluwer Academic Publishers pp 363-376 (1996).
- [27] Y. MU et C.M. SAVAGE, « One atom lasers ». *Phys Rev A* **46**, 5944 (1992).
- [28] E. VIASNOFF-SCHWOOB, C. WEISBUCH, H. BENISTY, S. OLIVIER, S. VAROUTSIS, I. ROBERT-PHILIP, R. HOUDRE et C. J. M. SMITH, « Spontaneous Emission Enhancement of Quantum Dots in a Photonic Crystal Wire ». *Phys. Rev. Lett.* **95**, 183 901 (2005).
- [29] S. LAURENT, S. VAROUTSIS, L. LE GRATIET, A. LEMAITRE, F. SAGNES, I. LAND RAINERI, A. LEVENSON, I. ROBERT-PHILIP et I. ABRAM, « Indistinguishable single photons from a single-quantum dot in a two-dimensional photonic crystal cavity ». *App. Phys. Lett.* **87**, 163 107 (2005).
- [30] A. DOUSSE, L. LANCO, J. SUFFCZYNSKI, E. SEMENOVA, A. MIARD, A. LEMAITRE, I. SAGNES, C. ROBLIN, J. BLOCH et P. SENELLART, « Controlled Light-Matter Coupling for a Single Quantum Dot Embedded in a Pillar Microcavity Using Far-Field Optical Lithography ». *Phys. Rev. L* **101**, 267 404 (2008).
- [31] N. SOMASCHI, V. GIESZ, L. DE SANTIS, J. CARLOS LOREDO, M. ALMEIDA, G. HORNECKER, S. LUCA PORTALUPI, T. GRANGE, C. ANTON, J. DEMORY, C. GOMEZ, I. SAGNES, N. DANIEL KIMURA, A. LEMAITRE, A. AUFFEVEES, A. G. WHITE, L. LANCO et P. SENELLART, « Near-optimal single-photon sources in the solid state ». *Nature Photonics* **10**, 340 (2016).
- [32] F. LONDON, « Zur Theorie und Systematik der Molekularkrafte ». *Z. fur Physik* **63**, 245 (1930).
- [33] J.E. LENARD-JONES, « Processes of adsorption and diffusion on solid surfaces ». *Trans. Faraday Soc.* **28**, 333 (1932).
- [34] H.B.G CASIMIR et D. POLDER, « The influence of retardation on London-van der Waals forces ». *Phys. Rev.* **73**, 360 (1948).
- [35] H.B.G CASIMIR, « On the attraction between two perfectly conducting plates ». *Proc. Kon. Akad. Wetenshap* **60**, 793 (1948).
- [36] D. BLOCH et M. DUCLOY, *Atom-wall interaction* (2005). Advanced in atomic, molecular and optical physics, vol 50, B. Bederson and H. Walther, Elsevier Academic press, San Diego, pp 91-156.
- [37] D. RASKIN et P. KUSCH, « Interaction between a neutral atomic or molecular beam and a conducting surface ». *Phys. Rev.* **179** (3), 179 (1969).

- [38] A. SHIH et V. A. PARSEGLAN, « Van der Waals forces between heavy alkali atoms and gold surfaces : comparison of measured and predicted values ». *Phys. Rev. A* **12** (3), 835 (1975).
- [39] A. ANDERSON, S. HAROCHE, E. A. HINDS, W. JHE et D. MESCHÉDE, « Measuring the van der Waals forces between a Rydberg atom and a metallic surface ». *Phys. Rev. A* **37** (9), 3594 (1988).
- [40] V. SANDOGHDAR, C. I. SUKENIK, E. A. HINDS et S. HAROCHE, « Direct measurement of the van der Waals interaction between an atom and its images in a micron-sized cavity ». *Phys. Rev. Lett.* **68** (23), 3432 (1992).
- [41] V. SANDOGHDAR, C. I. SUKENIK, S. HAROCHE et E. A. HINDS, « Spectroscopy of atoms confined to the single node of a standing wave in a parallel-plate cavity ». *Phys. Rev. A* **53** (3), 1919 (1996).
- [42] C. I. SUKENIK, M. G. BOSHER, D. CHO, V. SANDOGHDAR et E. A. HINDS, « Measurement of the Casimir-Polder force ». *PRL* **70**, 560 (1993).
- [43] A. LANDRAGIN, J.-Y. COURTOIS, G. LABEYRIE, N. VANSTEENKISTE, C. I. WESTBROOK et A. ASPECT, « Measurement of the van der Waals Force in an Atomic Mirror ». *PRL* **77**, 1464 (1996).
- [44] M. BORDAG, U. MOHIDEEN et V. MOSTEPANENKO, « New developments in the Casimir effect ». *Phys. Rep.* **353**, 1 (2001).
- [45] MILTON K. A., « The Casimir effect : recent controversies and progress ». *J. Phys. A* **37**, R209 (2004).
- [46] C. GENET, A. LAMBRECHT et S. REYNAUD, « Temperature dependance of the Casimir effect between metallic mirrors ». *Phys. Rev A* **62**, 012 110 (2000).
- [47] D. M. HARBER, J. M. OBRECHT, J. M. MCGUIRK et E. A. CORNELL, « Measurement of the Casimir-Polder force through center-of-mass oscillations of a Bose-Einstein condensate ». *Phys. Rev A* **72**, 033 610 (2005).
- [48] J. M. OBRECHT, R. J. WILD, M. ANTEZZA, L.P. PITAEVSKII, S. STRINGARI et E. A. CORNELL, « Measurement of the Temperature Dependence of the Casimir-Polder Force ». *Phys. Rev L* **98**, 063 201 (2007).
- [49] A. LAMBRECHT et S. REYNAUD, *Recent experiments on the Casimir effect : description and analysis* (2003). Eds. B. Duplantier et V. Rivasseau, 109.
- [50] R. E. GRISENTI, W. SCHOLLKOPF, J. P. TOENNIES, G. C. HEGERFELDT et T. KOHLER, « Determination of Atom-Surface van der Waals Potentials from Transmission-Grating Diffraction Intensities ». *PRL* **83**, 1755 (1999).
- [51] R. BRUHL, P. FOUQUET, R. E. GRISENTI, J. P. TOENNIES, G. C. HEGERFELDT, T. KOHLER, M. STOLL et C. WALTER, « The van der Waals potential between metastable atoms and solid surfaces : Novel diffraction experiments vs. theory ». *EuroPhys. Lett.* **59**, 357 (2002).
- [52] A.K. MOHAPATRA et C.S. UNNIKRISHNAN, « Measurement of the van der Waals force using reflection of cold atoms from magnetic thin-film atom mirrors ». *Europhys. Lett.* **73**, 839 (2006).

- [53] R. WOOD, « Selective reflection of monochromatic light by mercury vapour ». *Phil. Mag.* **18**, 187 (1909).
- [54] M. ORIA, M. CHEVROLLIER, D. BLOCH, M. FICHET et M. DUCLOY, « Detection of slow atoms in laser spectroscopy of a thin vapor film ». *PRA* **35** (5), 337 (1996).
- [55] G. DUTIER, *Cavite nanometrique de vapeur de Cesium : spectroscopie a haute resolution et interaction de surface de type van der Waals*. Thèse de doctorat, Laboratoire de physiques des lasers, Université Paris 13 (2003).
- [56] D. SARKISYAN, D. BLOCH, A. PAPOYAN et DUCLOY M., « Sub-Doppler spectroscopy by sub-micron thin Cs vapor layer ». *Opt. Comm.* **200**, 201 (2001).
- [57] G. DUTIER, A. YAROVITSKI, S. SALTIEL, A. PAPOYAN, D. SARKISYAN, D. BLOCH et M. DUCLOY, « Collapse and revival of a Dicke-type coherent narrowing in a sub-micron thick vapor cell transmission spectroscopy ». *Europhys Lett.* **63**, 35 (2003).
- [58] D. A. STECK, *Cesium D data line* (1997). Alkalidata, <http://steck.us/alkalidata/cesiumnumbers.1.6.pdf>.
- [59] I. MAURIN, P. TODOROV, I. HAMDI, A. YAROVITSKI, G. DUTIER, D. SARKISYAN, S. SALTIEL, M.P. GORZA, M. FICHET, D. BLOCH et M. DUCLOY, « Probing an atomic gas in a nanocell ». *Journal of physics : conferences Series* **19**, 20 (2005).
- [60] H. FAILACHE, S. SALTIEL, M. FICHET, D. BLOCH et M. DUCLOY, « Resonant van der Waals Repulsion between Excited Cs Atoms and Sapphire Surface ». *PRL* **83**, 5467 (1999).
- [61] M. FICHET, G. DUTIER, A. YAROVITSKI, P. TODOROV, I. HAMDI, I. MAURIN, S. SALTIEL, D. SARKISYAN, M.-P. GORZA, D. BLOCH et M. DUCLOY, « Exploring the van der Waals Atom-Surface attraction in the nanometric range ». *Europhysics Letters* **77**, 54001 (2007).
- [62] H. FAILACHE, S. SALTIEL, A. FISCHER, D. BLOCH et M. DUCLOY, « Resonant Quenching of Gas-Phase Cs Atoms Induced by Surface Polaritons ». *PRL* **88**, 243603 (2002).
- [63] A. O. CARIDE, G. L. KLIMCHITSKAYA, V. M. MOSTEPANENKO et S. I. ZANETTE, « Dependences of the van der Waals atom-wall interaction on atomic and material properties ». *PRA* **71**, 042901 (2005).
- [64] H. FAILACHE, S. SALTIEL, D. BLOCH et M. DUCLOY, « Resonant coupling in the van der Waals interaction between an excited alkali atom and a dielectric surface : an experimental study via stepwise selective reflection spectroscopy ». *Eur. Phys. J. D* **23**, 237 (2002).
- [65] I. HAMDI, P. TODOROV, A. YAROVITSKI, G. DUTIER, I. MAURIN, S. SALTIEL, Y. LI, A. LEZAMA, T. VARZHAPETYAN, D. SARKISYAN, M.P. GORZA, M. FICHET, D. BLOCH et M. DUCLOY, « Laser spectroscopy with nanometric gas cells : distance dependence of atom-surface interaction and collisions under confinement ». *Laser Phys.* **15**, 7 (2005).

- [66] D. SARKISYAN, T. VARZHAPETYAN, A. SARKISYAN, YU. MALAKYAN, A. PAPOYAN, A. LEZAMA, D. BLOCH et M. DUCLOY, « Spectroscopy in an extremely thin vapor cell : Comparing the cell-length dependence in fluorescence and in absorption techniques ». *PRA* **69**, 065 802 1–4 (2004).
- [67] L. HOLLBERG et J. L. HALL, « Measurement of the Shift of Rydberg Energy Levels Induced by Blackbody Radiation ». *PRL* **53**, 230 (1984).
- [68] K. S. LAI et E. A. HINDS, « Blackbody Excitation of an Atom Controlled by a Tunable Cavity ». *PRL* **81**, 2671 (1998).
- [69] JJ GREFFET, R. CARMINATI, K. JOULAIN, J.P. MULET, S. MAINGUY et Y. CHEN, « Coherent emission of light by thermal sources ». *Nature* **416**, 61 (2002).
- [70] M. LAROCHE, F. MARQUIER, C. ARNOLD, R. CARMINATI, J.J. GREFFET, S. COLLIN, N. BARDOU et J.L. PELOUARD, « Highly directional radiation generated by a tungsten thermal source ». *Opt. Lett.* **30**, 2623 (2005).
- [71] G. BARTON, « Van der Waals shifts in an atom near absorptive dielectric mirror ». *Proc. R. Soc. London* **453**, 2461 (1997).
- [72] W. KAISER, W. G. SPITZER, R. H. KAISER et L. E. HOWARTH, « Infrared Properties of CaF_2 , SrF_2 , and BaF_2 ». *Phys. Rev.* **127**, 1950 (1962).
- [73] P. DENHAM, G. R. FIELD, P.L.R. MORSE et G. R. WILKINSON, « Optical and dielectric properties and lattice dynamics of some fluorite structure ionic crystals ». *Proc. Royal Soc. London Serie A* **317**, 55 (1970).
- [74] D. F. BEZUIDENHOUT (éditeur), *Calcium fluoride (CaF_2)*, Handbook of the optical constants of solids II ed E.D. Palik (1994).
- [75] S.K. ANDERSSON, M.E. THOMAS et C. HOFFMAN, « Multiphonon contribution to the reststrahlen band of BaF_2 ». *Infrared Phys. Tech.* **39**, 47 (1998).
- [76] M. THOMAS (éditeur), *Barium fluoride (BaF_2)*, Handbook of the optical constants of solids III ed E.D. Palik (1998).
- [77] F. GERVAIS (éditeur), *High-temperature infrared reflectivity spectroscopy by scanning interferometry*, Infrared and Millimeter waves : electromagnetics Waves vol.8 (1983).
- [78] F. GERVAIS et B. PIRIOU, « Anharmonicity in several-polar-mode crystals : adjusting phonon self-energy of LO and TO modes in Al_2O_3 and TiO_2 on infrared reflectivity ». *J. Phys. C : solid state phys.* **7**, 2374 (1974).
- [79] A.S. BARKER, « Infrared Lattice Vibrations and Dielectric Dispersion in Corundum ». *Phys. Rev.* **132**, 1474 (1963).
- [80] S. SALTIEL, D. BLOCH et M. DUCLOY, « A tabulation and critical analysis of the wavelength dependent dielectric range image coefficient for the interaction exerted by a surface onto a neighbouring excited atom ». *Opt. Comm.* **265**, 220 (2006).
- [81] D. DE SOUSA MENESES, J.F. BRUN, P. ECHEGUT et P. SIMON, « Contribution of semi-quantum dielectric function models to the analysis of infrared spectra ». *Appl. Spectrosc.* **58**, 969 (2004).

- [82] T. PASSERAT DE SILANS, *Interaction Atome-Surface : Interaction de van der Waals entre un atome excité et une surface diélectrique thermiquement émissive ; oscillations de Bloch pour un atome absorbé*. Thèse de doctorat, université Paris13, Universidade federal da paraíba au Brésil (2009).
- [83] M. DUCLOY et M. FICHET, « General theory of frequency modulated selective reflection. Influence of atom surface interactions ». *J. Phys. II France* **1**, 1429 (1991).
- [84] D. GIRSHKOWSKY, « Self-focusing of light by potassium vapor ». *Phys. Rev. Lett.* **24**, 866 (1970).
- [85] J. PENDER et L. HESSELINK, « Degenerate conical emissions in atomic-sodium vapor ». *JOSAB* **7**, 1361 (1990).
- [86] T. BAN, H. SKENDEROVIC, S. TER-AVETISYAN et G. PICHLER, « Absorption measurements in dense cesium vapor using a UV violet light-emitting diode ». *Appl. Phys. B* **72**, 327 (1999).
- [87] J. WEINER, V. S. BAGNATO, S. ZILIO et P. S. JULIENNE, « Experiments and theory in cold and ultracold collisions ». *Rev. Mod. Phys.* **71**, 1 (1999).
- [88] S. BRIAUDEAU, D. BLOCH et M. DUCLOY, « Sub-Doppler spectroscopy in a thin film of resonant vapor ». *Phys Rev A* **59**, 3723 (1999).
- [89] F. BENABID, F. COUNY, J. C. KNIGHT et P. ST. J. RUSSELL, « Compact, stable and efficient all-fiber gas cells using hollowcore photonic crystal fibres ». *Nature* **69**, 434 (2005).
- [90] S. GHOSH, A. R. BHAGWAT, C. K. RENSHAW, S. GOH, A. L. GAETA et B.J. KIRBY, « Low-Light-Level Optical Interactions with Rubidium Vapor in a Photonic Band-Gap Fiber ». *PRL* **97**, 023603 (2006).
- [91] P.S. LIGHT, V. COUNY et F. BENABID, « Low optical insertion-loss and vacuum-pressure all-fiber acetylene cell based on hollow-core photonic crystal fiber ». *Opt lett* **31**, 2538 (2006).
- [92] P. S. LIGHT, F. BENABID, F. COUNY, M. MARIC et A.N. LUITEN, « Electromagnetically induced transparency in Rb-filled coated hollow-core photonic crystal fiber ». *Opt. Lett.* **32**, 1323 (2007).
- [93] A. BURCHIANTI, A. BOGI, C. MARINELLI, V. MAIBOHM, E. MARIOTTI, V. SANGUINETTI et L. MOI, « Optical characterization and manipulation of alkali metal nanoparticles in porous silica ». *Eur Phys J. D.* **49**, 201 (2008).
- [94] T. SVENSSON, E. ADOLFSSON, M. LEWANDER, S. T. XU et S. SVANBERG, « Disordered, Strongly Scattering Porous Materials as Miniature Multipass Gas Cells ». *PRL* **107**, 143901 (2011).
- [95] S. VILLALBA, H. FAILACHE, A. LALLOTIS, L. LENCI, S. BARREIRO et A. LEZAMA, « Rb resonance inside a random porous medium ». *Opt. Lett.* **38**, 193 (2013).
- [96] S. VILLALBA, A. LALLOTIS, L. LENCI, D. BLOCH, A. LEZAMA et H. FAILACHE, « sub-Doppler resonances in the backscattered light from random porous media infused with Rb vapor ». *PRA* **89**, 023422 (2014).

- [97] S. VILLALBA, H. FAILACHE, L. LENCI et V. LEZAMA, « Non-linear atomic spectroscopy inside a random porous medium ». *PRA* **90**, 052 518 (2014).
- [98] P. J. HARDING, *Photonic crystals modified by optically resonant systems*. Thèse de doctorat, University of Twente, Netherlands (2008).
- [99] R. MICHELETTO, H. FUKUDA et M. OHTSUT, « A Simple Method for the Production of a Two-Dimensional, Ordered Array of Small Latex Particles ». *Langmuir* **11**, 3333 (1995).
- [100] I. A. KARPOV, E. N. SAMAROV, V. M. MASALOV, S. I. BOZHKO et G. A. EMEL CHENKO, « The intrinsic structure of spherical particles of opal ». *Phys. of Solid State* **47**, 347 (2005).
- [101] P. BALLIN, *Confinement tridimensionnel d'une vapeur de césium dans une opale de nanobilles*. Thèse de doctorat, université Paris13 (2012).
- [102] E. N. SAMAROV, A. D. MOKRUSHIN, V. M. MASALOV, G. E. ABROSIMOVA et G. A. EMEL CHENKO, « Structural modification of synthetic opals during thermal treatment ». *Phys. of Solid State* **48**, 1280 (2005).
- [103] P. MASSE, *Cristaux photoniques colloïdaux d'architecture contrôlée*. Thèse de doctorat, Université de Bordeaux 1, Chapitre 2 (2007).
- [104] A. PENDRY, J.B.AND MACKINNON, « Calculation of photon dispersion relations, ». *Phys. Rev. Lett.* **69**, 2772 (1992).
- [105] P.M. BELLA, J.B. PENDRY, L. MARTÍN MORENOB et A.J. WARD, « A program for calculating photonic band structures and transmission coefficients of complex structures ». *Computer Physics Communications* **85**, 306 (1995).
- [106] J.F. BERTONE, PENG JIANG, K.S. HWANG et V.L. MITTLEMAN, D.M.AND COLVIN, « Thickness Dependence of the Optical Properties of Ordered Silica-Air and Air-Polymer Photonic Crystals ». *Phys. Rev. Lett.* **83**, 300 (1999).
- [107] D.M. MITTLEMAN, J.F. BERTONE, PENG JIANG, K.S. HWANG et V.L. COLVIN, « Optical properties of planar colloidal crystals : Dynamical diffraction and the scalar wave approximation ». *J. Chem. Phys.* **111**, 345 (1999).
- [108] S. SATPATHY, ZE ZHANG et M. R. SALEHPOUR, « Theory of Photon Bands in Three-Dimensional Periodic Dielectric Structures ». *Phys. Rev. Lett.* **64**, 1239 (1990).
- [109] J. WANG, L. YANG, D. LIN, Y. LUO, D. LI et Q. MENGA, « Optical studies of random disorder of colloidal photonic crystals and its evolution in evaporation induced self-assembly ». *J. Chem. Phys.* **137**, 234 111 (2012).
- [110] E. MOUFAREJ, *Infiltration d'une vapeur diluée dans une opale artificielle Langmuir-Blodgett : études optiques et spectroscopiques*. Thèse de doctorat, université Paris13 (2014).
- [111] A M AKUL'SHIN, V L VELICHANSKIÄ, A I ZHERDEV, A S ZIBROV, V I MALAKHOVA, V V NIKITIN, V A SAUTENKOV et G G KHARISOV, « Selective reflection from a glass-gas interface at high angles of incidence of light ». *Soviet J. Quantum Elect.* **19**, 416 (1989).

-
- [112] M. FICHET, F. SCHULLER, D. BLOCH et M. DUCLOY, « Interaction de van der Waals resonante entre un atome dans un etat excite et une surface dielectrique : spectres de reflexion selective ». *Ann. Phys. Fr.* **20**, 649 (1995).

Articles principaux de mon HDR

Intracavity sum-frequency generation in GaAs quantum cascade lasers

J.-Y. Bengloan, A. De Rossi, V. Ortiz, X. Marcadet, M. Calligaro, I. Maurin, and C. Sirtori

Citation: [Applied Physics Letters](#) **84**, 2019 (2004); doi: 10.1063/1.1669062

View online: <http://dx.doi.org/10.1063/1.1669062>

View Table of Contents: <http://scitation.aip.org/content/aip/journal/apl/84/12?ver=pdfcov>

Published by the [AIP Publishing](#)

Articles you may be interested in

[Terahertz sources based on intracavity frequency mixing in mid-infrared quantum cascade lasers with passive nonlinear sections](#)

Appl. Phys. Lett. **98**, 151114 (2011); 10.1063/1.3579260

[Sum-frequency generation in doubly resonant GaP photonic crystal nanocavities](#)

Appl. Phys. Lett. **97**, 043103 (2010); 10.1063/1.3469936

[Comparison of SiO₂, Si₃N₄, As₂S₃, and Ge_{0.25}Se_{0.75} dielectric layers for InP- and GaAs-based material systems for midinfrared quantum cascade laser waveguides](#)

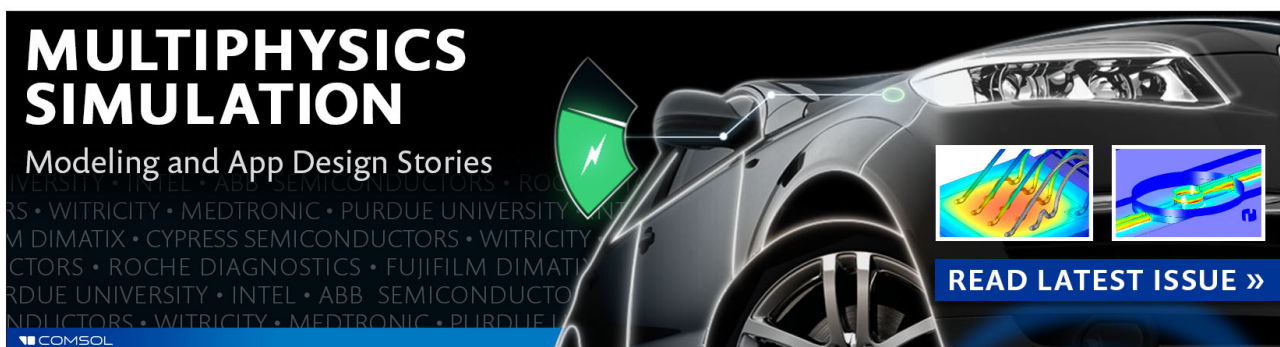
J. Appl. Phys. **106**, 053104 (2009); 10.1063/1.3197858

[Surface-emitting terahertz quantum cascade laser source based on intracavity difference-frequency generation](#)

Appl. Phys. Lett. **93**, 161110 (2008); 10.1063/1.3009198

[Molecular-beam epitaxy growth of quantum cascade lasers on \(111\)B substrates for second harmonic generation](#)

J. Vac. Sci. Technol. B **22**, 1558 (2004); 10.1116/1.1752916

The advertisement features a dark background with a sleek, modern car. On the left, the text 'MULTIPHYSICS SIMULATION' is written in large, bold, white letters, with 'Modeling and App Design Stories' below it. A green shield with a white lightning bolt icon is positioned to the right of the text. In the center, there are two small inset images: one showing a colorful thermal or stress simulation of a mechanical part, and another showing a blue and yellow simulation of a curved structure. At the bottom right, a blue button with white text says 'READ LATEST ISSUE >>'. The COMSOL logo is visible in the bottom left corner.

**MULTIPHYSICS
SIMULATION**
Modeling and App Design Stories

UNIVERSITY • INTEL • ABB SEMICONDUCTORS • ROCH
RS • WITRICITY • MEDTRONIC • PURDUE UNIVERSITY • IN
M DIMATIX • CYPRESS SEMICONDUCTORS • WITRICITY
CTORS • ROCHE DIAGNOSTICS • FUJIFILM DIMATI
RDUE UNIVERSITY • INTEL • ABB SEMICONDUCTO
NDUCTORS • WITRICITY • MEDTRONIC • PURDUE U

COMSOL

READ LATEST ISSUE >>

Intracavity sum-frequency generation in GaAs quantum cascade lasers

J.-Y. Bengloan, A. De Rossi, V. Ortiz, X. Marcadet, and M. Calligaro
Thales Research and Technology, 91404 Orsay, France

I. Maurin and C. Sirtori^{a)}
Matériaux et Phénomènes Quantiques, Université Denis Diderot-Paris 7, Paris, France

(Received 17 November 2003; accepted 16 January 2004)

Emission of coherent light at 5.75 μm wavelength has been obtained by intracavity frequency doubling of a GaAs-based quantum cascade laser. This nonlinearity originates from the second-order susceptibility of the bulk material hosting the heterostructure and can be exploited by growing the quantum cascade laser on a $\langle 111 \rangle$ substrate. © 2004 American Institute of Physics.
[DOI: 10.1063/1.1669062]

Intracavity second-harmonic generation (SHG) is a popular scheme for frequency doubling in solid state laser, for instance for the generation of very intense green light.^{1,2} On the contrary, sum frequency generation within the cavity of a diode laser is a very inefficient process because the resulting photons have energies above the gap and therefore are quickly reabsorbed by the semiconductor. This is not the case for quantum cascade (QC) lasers³ where the emitted photons are much smaller than the semiconductor gap and two or three times their energy are still in the transparency region of the material. For this reason frequency doubling in QC lasers is very attractive and can be an alternative way to access the short mid-infrared wavelength region (3–4 μm), where it is known that both diode and QC lasers have poor performance.⁴

Like most III–V and II–VI compounds, GaAs has the zincblende structure ($\bar{4}3m$) and lacks a center of symmetry within the unit cell. This gives rise to a pronounced second-order susceptibility, $\chi^{(2)}$, that can be expressed as a tensor that connects the nonlinear polarization to the pump electric fields, $E_{ij}(\omega)$. If we take, for instance, the case of SHG we can write:

$$P_i(2\omega) = \chi_{ijk}^{(2)} E_j(\omega) E_k(\omega), \quad (1)$$

where i, j, k are the Cartesian components of the fields in the system of reference of the crystal. However, there are strict polarization selection rules which set $\chi_{ijk}^{(2)}$ different from zero only for certain orientation of the electric fields. In GaAs (as for all the group $\bar{4}3m$ crystals), the $\chi_{ijk}^{(2)}$ components are equal in magnitude and nonzero only when the three indices are all different: $i \neq j \neq k$. This means that to excite the nonlinear susceptibility for a SHG process it is necessary to have the electromagnetic pump field with a nonzero projection on, at least, two of the principal crystalline axes.

QC lasers are normally grown on $\langle 100 \rangle$ substrates and, due to the intersubband selection rules, are TM polarized. This implies that the laser electric field is parallel to one of the axes and therefore the bulk $\chi_{ijk}^{(2)}$ cannot be exploited. Even so, in this configuration sum frequency generation has been demonstrated, through the engineering of the intersub-

band separation,⁵ which can give rise to giant resonant second-order nonlinear coefficients.^{6,7} However, these susceptibilities are strongly enhanced if the intersubband energy transition is also resonant with the linear absorption of the generated wave, $\alpha_{2\omega}$. This implies that the effective propagation length is limited to $1/\alpha_{2\omega}$. Moreover, the magnitudes of $\alpha_{2\omega}$ and that of the nonlinear susceptibility are both proportional to the electronic population and therefore bound to counterweight each other.

To achieve efficient nonlinear processes within the cavity of a QC laser we propose to use bulk optical nonlinearity, by realizing the growth on $\langle 111 \rangle$ substrates. In this geometry the laser electric field, always TM polarized, has the same projection (54.74°) on each of the three crystalline axes. Thus, the generated nonlinear polarization also has three equal components that make the SH electric field collinear with that of the fundamental frequency.

For the experiment we realized a GaAs/Al_{0.45}Ga_{0.55}As QC laser with an active region tuned for emission at 11 μm wavelength and a waveguide design similar to that described in Ref. 8. The structure has a 36 period active region embedded between two 4.5- μm -thick GaAs layers with an appropriate doping profile to generate a plasmon-confinement waveguide.⁹ The thickness of the whole QC laser is equal to 10.6 μm and the growth of such a long superlattice on a $\langle 111 \rangle$ substrate is not yet optimized. For this first sample, we have measured devices with larger current thresholds than those grown on $\langle 100 \rangle$ substrates and the emission wavelength is not in perfect agreement with the designed active region. However, the x-rays spectrum shows sharp satellite peaks up to the ninth order, demonstrating that good structural properties can be obtained on (111)B substrates even for such thick layers.

After growth, devices are processed into ridge lasers using ion implantation, for insulation, and chemical wet etching. The wafer is then cleaved into bars and single devices are obtained by cutting the semiconductor. Finally, lasers are In-soldered epi-side down on copper heat-sink. In order to keep low effective currents the devices are characterized at 77 K and in pulsed mode. Typical values of our current pulses are 100 ns with a repetition rate varying from 1 to 100 kHz. In Fig. 1 we report optical peak power and applied voltage as a function of the injected current for a 1.8-mm-

^{a)}Also at: Thales Research and Technology; electronic mail: carlo.sirtori@thalesgroup.com

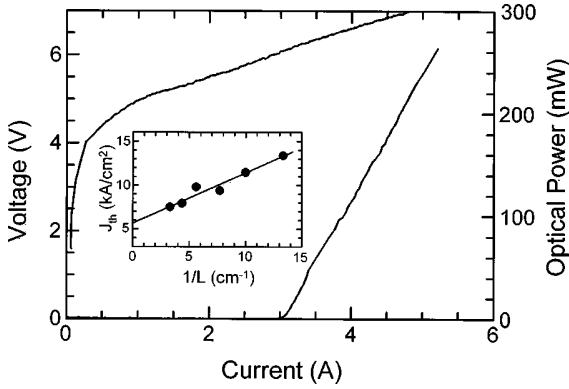


FIG. 1. Light-current ($L-I$) and corresponding voltage-current ($V-I$) characteristics, at 77 K, as recorded using a calibrated room-temperature HgCdTe detector from a single facet. The device (1.8 mm long, 18 μm wide) is driven in pulsed mode (100 ns width, 5 kHz repetition rate). In the inset, measured threshold current density vs reciprocal cavity length at 77 K. The solid line is the least-squares fit to the data. From its slope and intercept the modal gain coefficient and the waveguide loss are determined.

long and 20- μm -wide laser. The highest peak power measured is on the order of 0.5 W and the emission wavelength is $\lambda = 11.6 \mu\text{m}$ ($E_{\text{photon}} = 860 \text{ cm}^{-1}$). The threshold at 3 A corresponds to a current density of 9 kA/cm², about three times larger than on standard devices. This is in agreement also with the finding of our study (inset of Fig. 1) on the threshold current density versus reciprocal cavity length ($1/L$), a method often used in QC lasers to determine waveguide losses, α_w , and gain coefficient, g . From a linear fit of the data, we can deduce $\alpha_w = 15 \text{ cm}^{-1}$ and $g = 10 \text{ cm/kA}$. While the value of the losses agrees with our previous results,⁹ the gain coefficient is more than a factor of 3 lower than lasers grown on $\langle 100 \rangle$ substrate.

Figure 2 shows the evidence of SHG in our devices. The data at 2ω are obtained by filtering out the first-harmonic signal using a thin sapphire window that cuts off all the wavelength longer than 6.3 μm . Figure 2(a) presents light versus current ($L-I$) characteristics for the second-harmonic generation. The curve has a perfect quadratic dependence upon the injected current, as expected from the linear behav-

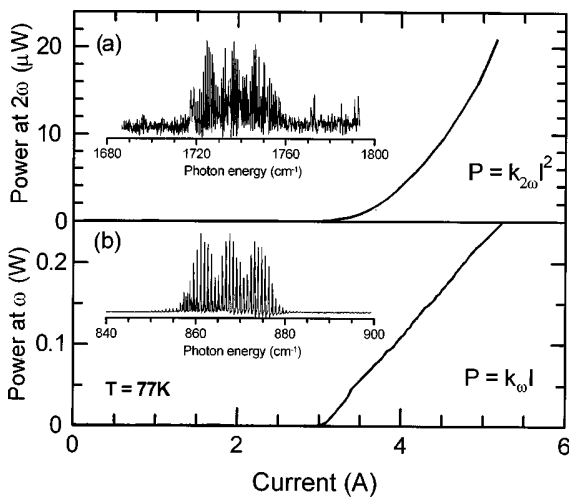


FIG. 2. Light output power vs injected current for (a) the second-harmonic generation and (b) the laser emission. The second-harmonic generation has an exact quadratic dependence on the injected current. Insets show high resolution spectra at 2ω and ω .

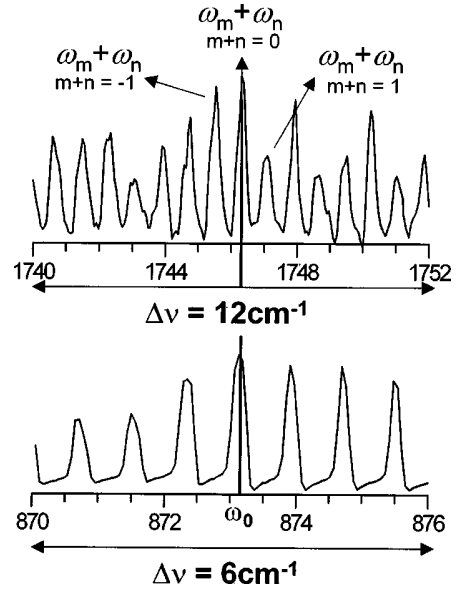


FIG. 3. Enlarged portion of the first- and second-harmonic spectra. Note that separation between longitudinal modes $\Delta\omega$ is preserved due to the non-linear interaction of different fundamental frequencies.

ior of the laser light output, shown for comparison in Fig. 2(b). The maximum SH optical power is 20 μW and is essentially determined by the value of $\Delta k = k_{2\omega} - 2k_{\omega} = 800 \text{ cm}^{-1}$, as can be seen from Eq. (2). The insets of Fig. 2 show high resolution spectra of the pump and the generated frequencies. It can be seen that the laser is not monomode, but shows a series of longitudinal modes, separated by $\Delta\omega = 0.8 \text{ cm}^{-1}$. In Fig. 3 we illustrate the fact that the different modes are all mixed by the optical nonlinearity and give rise to a sum-frequency spectra that preserve the mode separation. Note that there is a degeneracy in the generated frequencies, as each peak in the spectra can be the sum of several different pump frequencies. If we label the fundamental frequencies as $\omega_{\pm i} = \omega_0 \pm i\Delta\omega$, where ω_0 is a central frequency, it is easy to show that each generated frequency $\omega_{m+n}^{(2)} = \omega_m + \omega_n$ has the same values for all m and n provided that their sum is constant (see Fig. 3).

The Δk dependence of SHG conversion efficiency in quantum cascade lasers differs substantially from the typical situation of plane waves propagating into nonlinear crystals.¹⁰ In fact, due to the strong gain and low (25%) mirror reflectivity, the internal pump field is highly inhomogeneous. In addition, SH experiences reflections at the end-facet, and therefore cavity effects should be included. By taking these effects into account,¹¹ we can write the conversion efficiency as

$$P^{2\omega} = \eta T P_p^2 \frac{1 + R_1^{2\omega} + 2\sqrt{R_1^{2\omega}} \cos \Delta k L}{1 + R_1^{2\omega} R_2^{2\omega} + 2\sqrt{R_1^{2\omega} R_2^{2\omega}} \cos(2k_{2\omega} L)} \times \frac{|\sin((\Delta k + i(\alpha_m + 0.5\alpha_{2\omega}))L/2)|^2}{\Delta k^2 + (\alpha_m + 0.5\alpha_{2\omega})^2} \times \exp\left(-\left(\alpha_m + \frac{\alpha_{2\omega}}{2}\right)L\right), \quad (2)$$

where $P^{2\omega}$ is the emitted SH power, η is the phase-matched SHG efficiency, T is the transmission of the output facet,

P_p is the internal pump power at the output facet, connected to the emitted power through $P^\omega = T P_p \cdot R_{1,2}^{2\omega} \equiv R_{1,2} e^{-\alpha_{2\omega} L}$ is the reflectivity at 2ω of the back/output facet multiplied by the propagation loss factor and α_m are the mirror losses [$\alpha_m = (1/2L) \ln(R_1 R_2)$] at the pump frequency. In spite of its cumbersome appearance, expression (2) is fundamentally the product of three interference terms. Starting from the right end side, we can recognize the usual periodic dependence in $\Delta k L$ of the SHG modified by the presence of α_m , which renders the laser electric field nonhomogeneous in the cavity. The second term is the central denominator and corresponds to the Fabry–Perot modulation imposed by the cavity at the SH. Finally, the numerator with the $\cos(\Delta k L)$ dependence, expresses the interference of the SH wave generated in the direction toward the output facet with the one generated in the opposite direction and reflected by the back mirror. Pump field inhomogeneity implies that SHG never vanishes as $\Delta k L$ is changed.

These interferences become very important when the $\Delta k \leq \alpha_m$ and $R_{1,2}^{2\omega} \approx 1$. This is not our case, since for this first experiment no consideration of phase matching was taken into account while modeling the waveguide, and the facets of our devices were left uncoated. Moreover, the devices are driven in pulse mode and therefore considerable thermal drifts change the values of the refractive indices and tend to average out the modulations. Nevertheless, these considerations are crucial for the correct conception of phase matched devices. Indeed, in similar laser structures modal phase matching can be introduced by an appropriate design of the layer sequence and by adjusting the ridge width. According to calculations based on expression (2), for almost phase matched ($\Delta k L \approx 0$) long devices ($L = 3\text{--}5$ mm) with

backfacet coated ($\alpha_m \approx 1\text{--}2\text{ cm}^{-1}$) efficient frequency converters can be realized with conversion efficiency on the order of 1%–10%.

In conclusion, we have demonstrated the feasibility of GaAs quantum cascade lasers on (111) substrate to take advantage of bulk optical nonlinearity. For a laser at $\lambda = 11.6\ \mu\text{m}$, we have observed emission of radiation at $\lambda = 5.8\ \mu\text{m}$, signature of SHG. These devices can be considered as a new class of nonlinear materials with interplay of linear and nonlinear gain, ideal for optical parametric oscillators and amplifiers.

The authors would like to acknowledge very stimulating discussion with V. Berger and S. Dhillon.

- ¹J. A. Armstrong, N. Bloembergen, J. Ducuing, and P. S. Pershan, *Phys. Rev.* **127**, 1918 (1962).
- ²W. P. Risk, T. Gosnell, and A. V. Nurmikko, *Compact Blue Green Lasers* (Cambridge University Press, Cambridge, 2002).
- ³J. Faist, F. Capasso, D. L. Sivco, C. Sirtori, A. L. Hutchinson, and A. Y. Cho, *Science* **264**, 553 (1994).
- ⁴Feature section on mid-infrared quantum cascade lasers, *IEEE J. Quantum Electron.* **38**, 510 (2002).
- ⁵N. Owschmikow, C. Gmachl, A. Belyanin, V. Kocharovskiy, D. L. Sivco, R. Colombelli, F. Capasso, and A. Y. Cho, *Phys. Rev. Lett.* **90**, 043902 (2003).
- ⁶F. Capasso, C. Sirtori, and A. Y. Cho, *IEEE J. Quantum Electron.* **30**, 1313 (1994).
- ⁷C. Sirtori, F. Capasso, J. Faist, L. N. Pfeiffer, and K. W. West, *Appl. Phys. Lett.* **65**, 445 (1994).
- ⁸P. Kruck, H. Page, C. Sirtori, S. Barbieri, M. Stellmacher, and J. Nagle, *Appl. Phys. Lett.* **76**, 3340 (2000).
- ⁹C. Sirtori, P. Kruck, S. Barbieri, H. Page, J. Nagle, M. Beck, J. Faist, and U. Oesterle, *Appl. Phys. Lett.* **75**, 3911 (1999).
- ¹⁰A. Yariv, *Quantum Electronics* (Wiley, New York, 1988).
- ¹¹Note: a more in depth treatment of intracavity SHG will be published elsewhere, De Rossi *et al.* (unpublished).

Probing an atomic gas confined in a nanocell

I Maurin, P Todorov, I Hamdi, A Yarovitski, G Dutier, D Sarkisyan*, S Saltiel, M-P Gorza, M Fichet, D Bloch and M Ducloy**

Laboratoire de Physique des Lasers, UMR 7538 du CNRS et de l'Université Paris13,
99 Av JB Clément, F-93430 Villetaneuse, France

* Institute for Physical Research, Armenian Academy of Sciences,
Ashtarak2, Armenia

* Permanent address: Department of Physics, University of Sofia, Sofia , Bulgaria

E-mail: bloch@lpl.univ-paris13.fr

Abstract. Since the recent realization of extremely thin vapour cells (local thickness: 20-1000 nm), we investigate the optical properties of these 1-D confined vapours. Aside from their interest for Doppler-free spectroscopy, nanocells offer a new tool to evaluate collisional shift and broadening, yielding an access to the open problem of collisions under confinement. It also allows probing of the atom-surface interaction in a range of unusual short distances. The experimental exploration of the distance dependence, normally evolving according to the z^{-3} van der Waals (vW) dependence (z : the atom-surface distance), is worth doing because it could be affected by imperfections of the real surface, such as roughness, adsorbed impurities or charges. A detailed lineshape analysis is now under progress, with tight constraints imposed to the fitting by the twin information brought by simultaneous reflection and transmission spectra. Another issue is a possible resonant enhancement, susceptible to induce a repulsive vW, due to the coupling between atom excitation and a surface mode.

1. Introduction: Micro- and nano-cells of dilute vapours

For a very dilute gas, the atomic mean free path can be governed by the container geometry. A specific design, with parallel windows and a very small thickness, enables one to induce a strong anisotropy of the "mean" free path in a vapour cell, with atoms flying from wall to wall. For such thin cells, the response of the "slow" atoms (with respect to the normal velocity, *i.e.* the velocity component along the normal to the windows) to an interaction with resonant light undergoes a relative enhancement, owing to the transient build-up of the resonant interaction, which makes faster atoms less efficient (figure1).

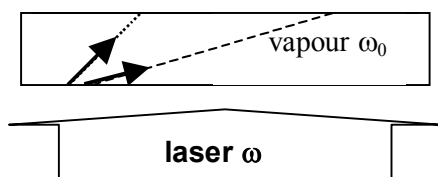


Figure 1. Atoms with nearly parallel velocity, insensitive to the Doppler shift, experience a long interaction with the optical field, and exhibit the fully developed steady-state response.

This had provided the principle of a novel method for Doppler-free spectroscopy, applicable to a variety of situations (velocity-dependent optical pumping, linear absorption, two-photon transition, *etc.*) [1] as long as the irradiation is under normal incidence. The initial demonstrations were operated with glass cells of commercial origin, filled-up with alkali-metal vapours, and whose thickness (10-1000 μm) remained much larger than the optical wavelength λ .

The recent fabrication of extremely thin cells (ETC) of vapour [2], designed with an initial sub-micrometric spacer between two carefully polished parallel windows, has revealed that under the effect of the external atmospheric pressure, the local cell thickness can become extremely small, typically spanning from 20 nm to 1 μm . This truly permits to investigate "nanocells" of vapour, and has opened a realm of novel prospects, that even extends beyond sub-Doppler spectroscopy, with the additional possibility of detecting atom-surface interaction effects in an unexplored range of distances.

Intrinsic to the extremely small thickness of ETCs is an accurate parallelism of the windows (*e.g.* deviation < 1 μm over a 10mm transverse extension) that implies a Fabry-Perot behaviour. On the one hand, this behaviour reveals very convenient to evaluate the local thickness of the nanocell [3], on the other hand, it unavoidably mixes-up the complementary information associated to reflection and transmission spectroscopies [4].

2. Spectroscopy in an ETC.

When applying transmission spectroscopy to a micro-cell, the lineshape naturally exhibits sub-Doppler features, whose exact characteristics depend on the cell thickness, type of the considered transition (*e.g.* 2-level vs. 3-level, two-photon or Raman transition), incident intensity (saturation processes), *etc.* Although most often appearing only as a small narrow contribution -peak or dip- over a broad Doppler-broadened background, these sub-Doppler features [1] can usually be singled out through a frequency-derivation of the spectrum, as made possible by FM (frequency-modulated) spectroscopy, yielding a Doppler-free signal.

With the advent of sub-micrometric thin cells, the whole spectrum easily turns to a pure Doppler-free spectrum. In fluorescence detection, the width of the excitation process decreases continuously when the ETC thickness is made shorter: this essentially corresponds to a more demanding velocity selection. This decrease can be typically observed down to the natural width, up to the regime when the interaction time is too limited, even for slow atoms, and implies finally a broadening for the smallest thickness. In contrast, the transmission spectrum, aside from the already mentioned Fabry-Perot effect (with a $\lambda/2$ periodicity), exhibits complex variations with the nanocell length. Indeed, the linear atomic response features a *coherent* spectroscopic narrowing, that extends, to the optical domain, the original observation by Romer and Dicke [5] in the microwave domain, of a *coherent* spectroscopic narrowing in a gas sample with a thickness $\sim \lambda/2$. Additionally, a periodical revival (with a λ - pseudo-periodicity) of the Dicke-narrowing [3,6] was demonstrated.

This coherent spectral narrowing [3,6,7] relies on the fact that, when an atom leaves the wall, the sudden atom excitation induced by *on-resonance* light starts to precess in phase with the electromagnetic field at the wall position, but falls out-of-phase with the local driving field under the effect of the atomic motion, with a phase mismatch finally reaching kL (L : the cell thickness, k the wave number). Such a description, relying on a time domain analysis rather than the more common frequency-domain analysis, is typical of the Dicke approach of the Doppler effect (see *e.g.* [8]) and enables one to recognize that the sub-wavelength confinement makes the Doppler effect unobservable.

A simple Bloch vector model [6] applied to ETC spectroscopy, permits to recover major predictions, and even provides hints for more complex situations. One knows that the Bloch vector $\mathbf{S}(z, v_z) = (S_x, S_y, S_z)$ characterizing the local density matrix of a two-level atom, precesses along the pseudo-magnetic field \mathbf{B} , according to $d\mathbf{S}/dt = \mathbf{S} \times \mathbf{B}$, with $\mathbf{B} = (\Omega, 0, \delta = \delta_0 - kv_z)$, where Ω is the Rabi frequency, and δ the frequency detuning between the irradiation and the resonance of the two-level system. In the Bloch vector model, the S_y component is associated to the component of the complex optical coherence needed to calculate the absorption, while S_z is the population inversion, characterizing the local amount of instantaneous fluorescence. In an ETC, the absorption, and

fluorescence, are respectively estimated from $\int_0^L S_y(z)dz$ and from $\int_0^L [1+S_z(z)]dz$ for each velocity group. Hence, on line centre ($\delta_0=0$), one has $\mathbf{B} = (\Omega, 0, -kv_z)$, and the Bloch vector, precessing around \mathbf{B} on the relevant cone, travels an angle independent of the velocity: the angular velocity dependence kv_z is indeed compensated for by an interaction time L/v_z (figure 2). Hence, the local absorption, as governed by S_y , accumulates up to a length $\lambda/2$, while the cell region between $\lambda/2$ and λ interferes destructively with the first $\lambda/2$ section of the cell, and so on, explaining the revival. For a frequency-detuned irradiation ($\delta_0 \neq 0$), the precession angle of the atomic excitation becomes velocity-dependent, leading to a smoother length dependence of the signal. This justifies for $L=\lambda/2$ the contrast between the line centre and the wings, and the apparent "Dicke narrowing" of the lineshape. This leads to the $L = (2n+1)\lambda/2$ revival of the narrow peaks. The dipole relaxation actually reduces the contrast of this lineshape periodicity. As far as the fluorescence emission is concerned, the various cell regions add incoherently, implying a continuous growth of the fluorescence with the cell length. In addition, the fluorescence is a second-order process, limited through a genuine velocity selection to those atoms slow enough to undergo a successive absorption and emission process. This makes its lineshape narrower than the transmission profile, even for the optimal $L= \lambda/2$ situation, and comparable to the one obtained in FM transmission, when the central logarithmic singularity is turned into a Doppler-free contribution.

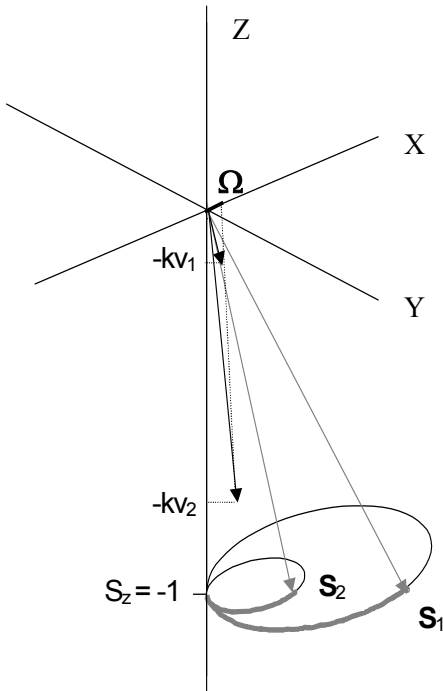


Figure 2. This representation of the motion of the Bloch vector (\mathbf{S}) shows that it rotates the same angle for small (v_1) and large (v_2) velocities when precessing around the pseudo magnetic field. The integrated S_y component increases up to an angle π , and the path described by \mathbf{S} reveals proportional to $1/v_z$ (for negligible Rabi frequency Ω): this explains the logarithmic singularity.

Saturation effects in nanocells, experimentally investigated in some works [6,9], tend to washout the main features of the Dicke coherent narrowing, although the resonances remain narrow. This washout can also be understood [10] with the Bloch vector model. Incoherent transfer through optical pumping, as occurs in an *open* two-level system, modifies the length of the Bloch vector, and tends to randomize the interferences between the various spatial and velocity contributions. For a strongly-driven *close* two-level system, the Bloch vector model shows that the optimal cell length for a given velocity group is no longer $\lambda/2$, and becomes velocity-dependent. Moreover, for a degenerate two-level system, one has to consider various time scales owing to the different Rabi frequencies involved with the Zeeman sub-states. Although saturation effects remain in the frame of a coherent excitation,

the thin cell spectroscopy intrinsically explores the dynamics of the atomic response, on a time scale that depends on the velocity distribution. This complexity of the time sequence of the nonlinear process tends to hinder any recognizable Dicke-type pseudo-periodicity.

3. Atomic collisions under confinement

Spectroscopy close to an interface, notably Selective Reflection (SR) spectroscopy [11], permits to probe strongly absorbing gases, because the probed region is made small (e.g. on the order of the wavelength in SR spectroscopy). In particular, it has been a choice technique for a long time to evaluate collisional broadening and shift in an optically dense gas. A notable advantage [12] is that the information is obtained close to the resonance line-centre and not in the far spectral wings, as it would be in a volume experiment.

There are actually few such collisions studies, even in the elementary case of the Cs resonance lines. In particular, the pressure shift had not been widely explored because it usually represents only a small fraction of the collisional broadening, while its value and sign possibly depend on the considered hyperfine components [13]. This has provided us a motivation to study collision effects in an ETC, in particular on the Cs D₁ line (894 nm), that had not been studied systematically in previous works. The possibility of a comparison with the well-known method of SR spectroscopy is also a way to check the validity of current interpretations of ETC spectroscopy. A precise comparison, with truly identical experimental conditions, is deferred to the near future, with a specially designed Cs cell including a nanometric thickness region, and a more macroscopic region suitable for SR spectroscopy.

Until now, we have conducted preliminary experiments [10] on the well-resolved Cs D₁ line, enabling a comparison of a $\lambda/2$ and $\lambda/4$ thickness. For a given spectrum obtained in an ETC, the modelling of the spectral lineshape allows one to extract both the homogeneous width (and hence the overall pressure broadening) and the shift relatively to the atomic resonance in a low-density volume experiment. This implies a simultaneous analysis of the Fabry-Perot effects, Dicke narrowing and surface interaction. The pressure dependence of the resonance broadening and shift is expected to remain linear in a large regime of density. The introduction, in the predicted lineshapes, of a van der Waals (vW) atom-surface potential known to evolve like $V(z) = -C_3 z^{-3}$ (z : the atom-surface distance) for a single wall, with a typical value $C_3 \sim 1\text{-}2 \text{ kHz}\cdot\mu\text{m}^3$ for the D₁ line, imposes a small but visible perturbation (distortion and shift) for a $\lambda/4$ thickness, that is comparable to the vW effect in SR spectroscopy. For a $\lambda/2$ thickness, the vW potential has a negligible effect. Preliminary fittings of the experimental lineshapes seem indeed slightly improved when the vW interaction is included for the $\lambda/4$ thickness [10], while no difference is observed for a $\lambda/2$ cell. Remarkably, taking into account the

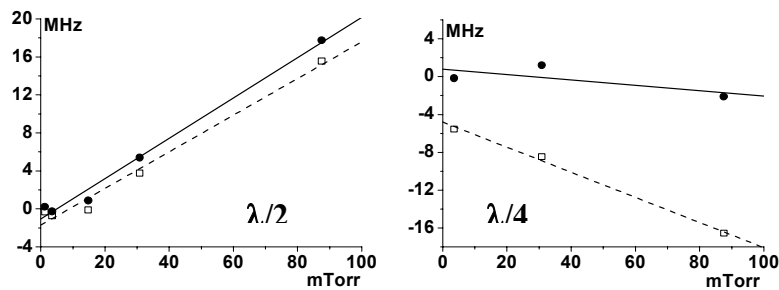


Figure 3. A comparison between the estimated resonance shifts, as appearing in a fitting of the ETC transmission lineshapes for $\lambda/2$ and $\lambda/4$ cell. The points represented by \square are obtained when neglecting the vW interaction, the points represented by \bullet take this interaction into consideration. vW shift induces not only a slight change in the estimated pressure broadening, but strong modifications of the extrapolated pressure shift, with a notable difference between the shifts estimated for a $\lambda/2$ and $\lambda/4$ thickness (see figure 3). Such a behaviour is sensitively independent of the fine

adjustment of the vW interaction coupling coefficient, enabling by the way one to cancel the residual shift at null pressure, remaining otherwise unexplained.

Because extrapolation from experimental data can be sensitive to various hindered phenomena, more systematic investigations -implying systematic variations of the cell thickness, and of the atomic density- are needed before concluding that one truly observes a thickness-dependent collisional behaviour. However, such an hypothetic possibility is worth discussing from a general point of view. An atom-atom collision, in its principle, is not very different from an atom-surface collision, especially at long distance. In particular, the atom-atom vW interaction is nothing else than the dipole-dipole coupling between the fluctuating atom-dipole and the correlated induced (and fluctuating) dipole in the atomic perturber. As long as an electromagnetic boundary lies in the vicinity of the two interacting atoms, the correlation between the fluctuations seen by the atom and its perturber can follow a variety of paths, from the direct propagation, to paths involving reflection(s) on the boundary (see e.g. [14]). Physically, these additional contributions can be understood as equivalent to a collision process where at least one of the atom is replaced by its electric image. In the principle, these contributions have to be considered when the distance to the reflecting plane remains smaller than the wavelength of the relevant (virtual) atomic transitions. Anyhow, the efficient distance in collision processes may rather be related with the square root of the collision cross-section. To our knowledge, no evaluation of this confinement effect has ever been performed in the situation of a confined vapour, with the required averaging over atomic positions and velocities. Note also that the implicit assumption that the atom dynamics -*i.e.* the velocity distribution and the population distribution among various sublevels- is independent of the cell thickness, may turn to be questionable for a very confined vapour.

4. Exploring the atom-surface van der Waals interaction at small distances

It has already been briefly recalled in section 3 that in ETC spectroscopy, the atom-surface interaction is dominated by the universal long-range vW attraction [11] between a fluctuating atom dipole and its image. The major interest of these nanocells for the probing of the vW interaction is that it extends the possibility to probe short-lived excited states, typical of optical methods such as SR spectroscopy, to an unusual range of short distances. Indeed, the z^{-3} scaling normally applies in a typical 1-1000 nm range, *i.e.* as long as retardation (Casimir) effects are negligible and before occurrence of the short-range effects depending upon the structural (atomic) details of the surface. It hence implies a validity covering a huge energy range, that is particularly worth to be tested. With ETC spectroscopy, the thickness can normally be arbitrarily chosen through the choice of the container thickness. This is in contrast with SR spectroscopy, with its probed depth $\sim \lambda/2\pi$ governed by the wavelength of observation. This interest is enhanced by the fact that the choice of methods to investigate the long-range atom-surface interaction is actually scarce [11], in spite of the ubiquity of the vW interaction. Most common methods rely on mechanical deflection, making them applicable only to ground state atoms or long-lived states. Practically, the only accurate measurements of the distance law of the interaction have been limited to the 3000-500 nm range, with Rydberg atoms that are strongly interacting and long-lived, allowing for a detection that is partly mechanical [15]. With nanocells, one envisions the possibility of probing distances at least an order of magnitude smaller, reaching a distance range where various short-range effects could limit the effectiveness of the z^{-3} scaling.

We had already reported on various evidences of the atom-surface interaction in nanocell spectroscopy. Our most recent analyses [10] show that turning from the observation [16] of the surface interaction, to a significant measurement, is now feasible. A first step was to analyze the transmission behaviour in nanocells on the Cs D_1 resonance line. When the local cell thickness turns to be very small (~ 50 -100nm), a lineshape distortion and a red-shift (up to 200MHz) are observed, that largely exceed those observed through SR spectroscopy. Moreover, the spectral lineshapes appear in good agreement with a theoretical model that assumes a known strength of the van der Waals (vW) interaction. This theory simply assumes a thermal distribution of atoms flying wall-to-wall, and integrates the transient atomic response while taking into account a vW potential. The vW potential itself is modelled according to an electrostatic description including the interaction with the multiple images induced in the two reflecting walls. These transmission experiments have been extended to

experiments in the FM mode, whose improved spectral resolution is of particular interest for large thickness (*i.e.* when the vW shift remains small), and to reflection spectra: for the smallest thicknesses, reflection spectra are indeed recorded over a low level of non resonant reflection as due to Fabry-Perot interferences, and offer a competitive possibility to observe the vW shift [16].

We are now investigating the stronger vW shift induced on high-lying excited states, such as Cs(6D), that is probed at 917 nm ($6D_{5/2}$) or 921 nm ($6D_{3/2}$) after a prior excitation on the Cs D_2 line $6S_{1/2} \rightarrow 6P_{3/2}$ at 852 nm. For these transitions, the vW interaction should be about an order of magnitude larger than for the D_1 line. Moreover, for small cell thickness, it is susceptible to provide the dominant broadening, owing to the spatial inhomogeneity of the vW shift. Thanks to a laser diode specially designed for a broad range tuneability (through step-by-step frequency changes), we could observe the broadened transmission (and reflection) spectra for various ETC thicknesses, down to 20 nm. Depending on the thickness, the observed (red) shift can be in excess of 10's of GHz -*i.e.* an energy shift 2 orders of magnitude larger than previously observed [15]-. Also, the apparent width of the largely distorted lineshape simultaneously increases for short thicknesses, remaining an approximately constant fraction of the frequency shift (*i.e.* vW induced inhomogeneous broadening). The observed shift -as measured by evaluating the frequency of the transmission peak- shows an approximate L^{-3} dependence, in agreement with a simple theoretical modelling: at a given relative position z/L , the shift is indeed predicted to evolve like L^{-3} , but the behaviour of the overall lineshape, with its weighted integration of different spatial contributions, is more difficult to evaluate.

An accurate evaluation of the surface interaction effect obviously requires more systematic experiments, because the observed lineshapes can be affected by various process, such as the pumping into the intermediate states - spatial inhomogeneities of the pumping, non thermal velocity distribution in the intermediate state -, or by the high vapour density required for these experiments, implying broadening and shift. This is why we have turned to a series of experiments for a limited number of accurately-controlled cell thickness (presently in the range 40-130 nm) with investigation of the pressure effects, and control of the effects of the pumping light: the pumping in the $6P_{3/2}$ state is expected to be nearly thermal when the pump absorption is weak, and when lineshapes are independent of the pumping power. Moreover, the careful control of a stabilized pump frequency helps to perform a reproducible selection among the various hyperfine sublevels of the resonant state. These conditions permit to extend the modelling, previously used for a resonance transition, to transitions between excited states which are sensitive to a much stronger vW interaction. On this basis, it is possible to extract an acceptable range of vW strengths from each individual spectrum, and to check if it remains constant under phenomenological spectral changes as induced by a change in the Cs density. Similarly, one can also check the consistency of the estimated widths with a pressure broadening, or even the linearity of the pressure-induced shift (actually, the vW shift and its induced inhomogeneous broadening are clearly dominant, at least for small thickness experiments, and the pressure shift can be most often neglected).

As can be seen from the various theoretical spectra shown in figure 4, in the regime of small thickness, and strong vW interaction, there is an imposed relation between the shift (e.g. as measured with the position of the peak of the transmission lineshape) and the width of the lineshape, essentially governed by the spatial inhomogeneity of the vW interaction. In other words, before any optimization of the parameters in a fitting process, one can recognize if an experimental lineshape will be acceptably fitted with the theoretical model, or if the modelling is inadequate. This obviously imposes tight constraints to the acceptable fits. Moreover, for our series of experiments, as due to a vW strength largely exceeding the Doppler broadening, the pressure broadening, although observable, modifies only marginally the predicted lineshapes.

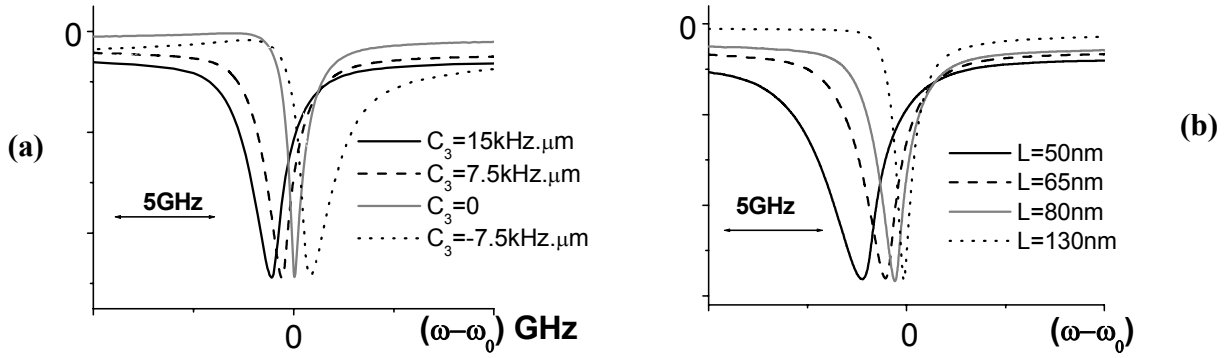


Figure 4. Theoretical transmission lineshapes through an ETC : **(a)** for a 80nm thickness and the various indicated vW strength ; **(b)** for the various indicated thicknesses, and a constant vW interaction $C_3 = 7.5 \text{ kHz} \cdot \mu\text{m}^3$. The C_3 value corresponds to the 1-wall vW strength. The lineshapes are quasi-independent of the (non resonant) reflection coefficient of the windows (here $r=0.5$). The Fabry-Perot effects included in the modelling explain the asymmetry for $C_3=0$ in (a). For normalization purposes, the amplitudes are multiplied by a respective factor: (a) 1 for $C_3 = 0$; 2.55 for $C_3 = 7.5 \text{ kHz} \cdot \mu\text{m}^3$, 3.28 for $C_3 = 15 \text{ kHz} \cdot \mu\text{m}^3$, 2.84 for $C_3 = -7.5 \text{ kHz} \cdot \mu\text{m}^3$; and: (b) 1 for 130 nm, 2.96 for 80 nm, 4.97 for 65 nm, 10.1 for 50 nm.

A specificity of ETC spectroscopy is that it allows for the simultaneous recordings of the transmission and reflection lineshapes. These lineshapes result [4] from a very different combination of absorption-related and dispersion-related lineshapes. As illustrated in figure 5, for the transition to the $6D_{5/2}$ level (917 nm line), consistent fittings for one type of signal (e.g. reflection) are actually obtained with those parameters extracted from the other signal (transmission). This provides a major evidence for the satisfactory description obtained with our modelling. Detailed tests of the numerical fittings are presently under progress to evaluate to which extent the z^{-3} dependence is verified in our range of thickness. For a 65 nm-130 nm thickness range (i.e. the vW potential varies by an order of magnitude), the estimated C_3 value seems to remain constant within a factor 2, and to be in agreement

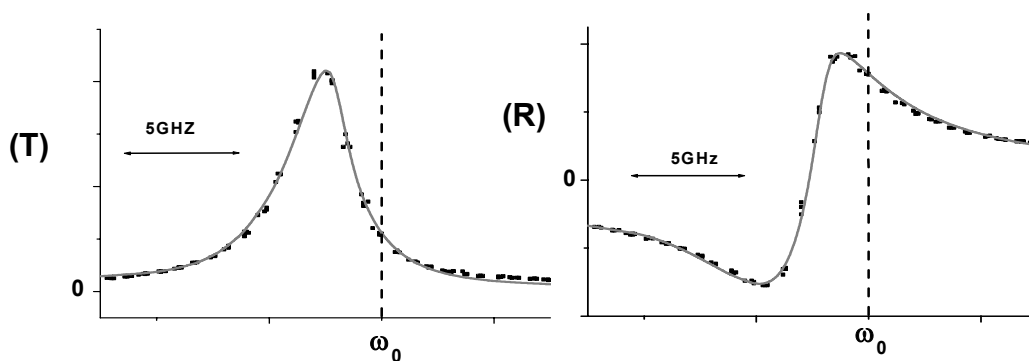


Figure 5. Experimental transmission (T) and reflection (R) spectra (black squares) as recorded on the Cs $6P_{3/2}$ - $6D_{5/2}$ line (917 nm) for a 50 nm cell thickness, and corresponding fits (grey dashed line). The nanocell temperature (220°C) is low enough to make pressure shift, and even pressure broadening, negligible. The model assumes a "thermal" pumping into Cs ($6P_{3/2}$). The fitting parameters are the same for transmission and reflection

with the theoretical expectation at an interface with YAG windows. More precise evaluations are now under progress. Note that the accuracy for the relatively large thickness is partially altered because of the hyperfine structure of the pumped $6P_{3/2}$ level, which turns to be comparable with the average shift

It should be emphasized that for extremely small thicknesses, which make our ETCs genuine 1-D "nanocells", the reproducibility of the recorded spectra becomes really an issue. For a series of experiments performed on a nanocell with YAG windows, lineshape reproducibility has been clearly verified when comparing different cell spots of equal thickness, as long as this thickness is 65 nm or more. The comparison of "50 nm" spots shows some variations in the lineshapes, although several spots appear able to provide nearly identical responses, such as the one selected as the "valid" response for 50 nm (see figure 5). For differing 40 nm spots, no effective reproducibility has been found. Rather, the apparent shift, relatively to the free-atom resonance, varies from spot to spot, by a factor that anyhow remains smaller than 2 in all cases. In spite of the accuracy of the thickness measurement, that apparently reaches in some cases 1-2 nm, the measurement intrinsically provides a thickness *averaged* on the optical spot size (typical beam diameter is 100-200 μm). Hence, the non-measured local irregularities affecting the window profiles (*i.e.* roughness, evaluated over various characteristic lengths), may induce local fluctuations in the atom-surface distance, expected to produce dramatic effects on the averaged atomic spectra, with respect to a vW potential essentially sensitive to the *inverse cube* of the distance (distance fluctuations between 35 and 45 nm correspond to a doubling of the vW shift).

5. Resonant atom-dielectric coupling in nanocells

In the modelling of ETC spectroscopy used above, the local shift of the atomic resonance induced by the surface interaction relies on an electrostatic description of the vW interaction, and includes a multiple image approach to take into account the two neighbouring interacting surfaces. Such a vW description leads to an overall spatial dependence of the vW interaction that follows a special function (the transcendental Lerch function [17]). This description is obviously more precise than the simple addition of the individual potential exerted by each of the walls, even if the overall spectral predictions are most often not very different.

Actually, this electrostatic approach applies only as long as the resonant couplings between the dielectric surface and the relevant virtual atomic transitions are not considered. Indeed, the vW atom-surface interaction is a dipole-dipole interaction, originating from the coupling between the atom dipole fluctuations (to be expanded along the virtual electric dipole transitions) and the correlated fluctuations induced in the surface. Resonances in the electromagnetic coupling between a surface polariton mode and an atom fluctuation (in virtual emission), have been shown to lead to giant and possibly repulsive interaction [18,19], along with an increased decay rate from the considered excited state [20], as governed by a surface response $(\epsilon-1)/(\epsilon+1)$, with ϵ the *complex* dielectric permittivity. In particular, the 12.15 μm virtual emission of $\text{Cs}(6D_{3/2})$ towards $(7P_{1/2})$ makes a sapphire surface strongly repulsive for a $\text{Cs}(6D_{3/2})$ level, while a YAG surface is expected to exert only a weak repulsion [18]. Simultaneously with major changes for the vW interaction induced by the *virtual* resonant coupling, a *real* energy transfer between the atomic excitation and the surface mode may occur, implying a z^{-3} lifetime shortening as due to a surface-induced quenching. Conversely, the $\text{Cs}(6D_{5/2})$ level, with its main virtual emission at 14.6 μm , is expected to remain attracted by a surface such as sapphire or YAG. This predicted difference between the two fine-structure components of the $\text{Cs}(6D)$ level had not been investigated before, as due to a lack of adequate sources.

A series of experiments on the 921 nm line $6P_{3/2} - 6D_{3/2}$ in a YAG nanocell has been performed, exploring a similar variety of situations as for the experiments on the 917 nm line (figure 6). A detailed analysis of the recorded lineshapes is still in progress. The theoretical modelling of the interaction potential reveals more delicate than in the non resonant electrostatic situation. At first sight, one anyhow notices that in spite of a predicted repulsion, no blue shift of the line is specifically observed. Actually, this does not preclude a repulsive behaviour (upward convexity of the potential),

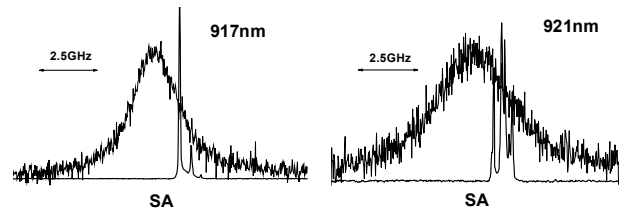


Figure 6. Comparison between the 917 nm and 921 nm spectra, recorded in a 65nm-thick cell in the same experimental conditions ($T= 220^{\circ}\text{C}$). The SA spectra are reference saturated absorption spectra (note the effect on the reference of the slight differences in the hyperfine structure of Cs ($6D_{3/2}$) and Cs ($6D_{5/2}$)). In our conditions, the shift and lineshape distortion purely originate in the surface interaction. The 921 nm linewidth is broader than the 917 nm one in spite of a smaller shift.

because with two repulsing walls, it has been shown [10] that the total potential can exhibit a repulsive behaviour at any distance while inducing a red-shift close to the nanocell center. Also, the comparison with the 917 nm transition shows that, in similar conditions, the signal has much smaller amplitude - not entirely explained by smaller transition probabilities in the free-space-, and that the signal width is nearly twice larger, in spite of an observed shift that remains comparable to, or smaller than the one observed at 917 nm. This is a possible first indication, that remains to be confirmed by a further analysis, of a surface-induced energy transfer occurring within an nanocell, when the two walls simultaneously interact with the excited atom. At least, the observed ratio between width and shift shows that the non resonant model valid for the 917 nm line is not applicable here.

6. Conclusion

In spite of the fact that nanocells permit to study atomic vapour at very unusual distances from a surface, essential techniques of high-resolution spectroscopy are proved to remain applicable with rather minor changes. The detailed analysis of the experimental spectra shows that this novel spectroscopy can effectively provide a unique tool to investigate problems not attacked previously, as the one of collision under confinement, or effective distance-dependence of the atom-surface interaction in the sub-100 nm range. Extensions of our investigations to the physics of resonant gases under strong multi-dimensional confinement, that can be approached with systems such as holey fibres or porous media [21], should offer renewed surprises, of interest for both fundamental and applied physics.

Acknowledgments

This work has been partially supported by European contract HPRN-CT-2002-00304, as part of the FASTNet programme. We also acknowledge discussion with A. Lezama in the frame of the French-Uruguayan ECOS programme (U00-E03), and with S. Cartaleva in the frame of French-Bulgarian project RILA 2005.

References

- [1] Briaudeau S, Bloch D and Ducloy M 1999 *Phys. Rev. A* **59** 3723; Briaudeau S, Saltiel S, Nienhuis G, Bloch D and Ducloy M 1998 *Phys. Rev. A* **57** R3169; Briaudeau S, Bloch D and Ducloy M 1996 *Europhys. Lett.* **35**, 337; see also Briaudeau S et al. 2000 *J. Phys. IV* **10** 145 and Briaudeau S et al. 1998 *Laser Spectroscopy XIII* (Wang YZ et al, eds. , World Scientific,) pp. 33-36
- [2] Sarkisyan D, Bloch D, Papoyan A and Ducloy M 2001 *Opt. Commun.* **200** 201

- [3] Dutier G, Yarovitski A, Saltiel S, Papoyan A, Sarkisyan D, Bloch D and Ducloy M 2003 *Europhys. Lett.* **63** 35
- [4] Dutier G, Saltiel S, Bloch D and Ducloy M 2003 *J. Opt. Soc. Am. B* **20** 793
- [5] Romer RH and Dicke RH 1955 *Phys. Rev.* **99** 532
- [6] Sarkisyan D Varzhapetyan T, Sarkisyan A, Malakyan Yu, Papoyan A, Lezama A, Bloch D and Ducloy M 2004 *Phys. Rev. A*, **69** 065802
- [7] Dutier G, Todorov P, Hamdi P, Maurin I, Saltiel S, Bloch D and Ducloy 2005 Dicke coherent narrowing in two-photon and Raman spectroscopy of thin vapour cells *Preprint* <http://fr.arxiv.org/abs/physics/0506025>.
- [8] Dicke RH 1953 *Phys. Rev.* **89** 472 and Dicke RH 1954 *Phys. Rev.* **96** 530
- [9] Varzhapetyan T, Sarkisyan D, Petrov L, Andreeva C, Slavov D, Saltiel S, Cartaleva S 2005, in SPIE Proceedings of the XIII International School on Quantum Electronics "Laser Physics and Applications", held in Burgas, Bulgaria, Sept 20-24,2004, to appear.
- [10] Hamdi I, Todorov P, Yarovitski A, Dutier G, Maurin I, Saltiel S, Li Y, Lezama A, Varzhapetyan T, Sarkisyan D, Gorza M-P, Fichet M, Bloch D and Ducloy M 2005 *Laser Phys* **15** (7)
- [11] Bloch D and Ducloy M 2005, Atom-Wall Interaction in *Adv. At. Molec. Opt. Phys.*, vol. **50**, (Bederson B and Walther H eds., Elsevier Academic Press, 2005) pp. 91-154
- [12] Akul'shin AM, Velichanskii VL, Zibrov AS, Nikitin VV, Sautenkov VV, Yurkin EK and Senkov NV 1982 *J.E.T.P. Lett.* **36** 303
- [13] Papageorgiou N, Fichet M, Sautenkov VA, Bloch D and Ducloy M 1994 *Laser Phys.* **4** 392 ; see also preliminary results for Cs D₁ line in Dutier G 2003, PhD dissertation, Université Paris 13, unpublished
- [14] Cho M and Silbey RJ 1996 *J. Chem. Phys.* **104** 8730
- [15] Sandoghdar V, Sukenik CI, Hinds EA and Haroche S 1992 *Phys. Rev. Lett.* **68** 3432; Sandoghdar V, Sukenik CI, Haroche S and Hinds EA 1996 *Phys. Rev. A* **53** 1919
- [16] Dutier G, Hamdi I, Segundo PCS, Yarovitski A, Saltiel S, Gorza M-P, Fichet M, Bloch D, Ducloy M, Sarkisyan D, Papoyan A and Varzhapetyan T 2004, in "Laser Spectroscopy. Proceedings of the XVI International Conference" (Hannaford P, Sidorov A, Bachor H and Baldwin K eds., World Scientific, Singapore) pp.277-284
- [17] Nha H and Jhe W 1996, *Phys. Rev. A* **54** 3505 (1996); and *erratum* 1999 **60** 1729
- [18] Failache H, Saltiel S, Fichet M, Bloch D and Ducloy M 1999 *Phys. Rev. Lett.* **83** 5467 and Failache H, Saltiel S, Fichet M, Bloch D and Ducloy M 2003 *Eur. Phys. J. D* **23** 237
- [19] Fichet M, Schuller F, Bloch D and Ducloy M 1995, *Phys. Rev. A* **51** 1553; Wylie M and Sipe JE 1984 *Phys. Rev. A* **30** 1185 and Wylie M and Sipe JE 1985 *Phys. Rev. A* **32**, 2030 (1985) ; Gorza M-P, Saltiel S, Failache H and Ducloy M 2001 *Euro. Phys. J. D* **15** 113-126
- [20] Failache H, Saltiel S, Fischer A, Bloch D and Ducloy M 2002, *Phys. Rev. Lett.* **88** 243603
- [21] Burchianti A, Marinelli C, Bogi A, Brewer J, Rubahn K, Rubahn H-G, Della Valle F, Mariotti E, Biancalana V, Veronesi S and Moi L 2004, *Europhys. Lett.* **67** 983

Exploring the van der Waals atom-surface attraction in the nanometric range

M. FICHET¹, G. DUTIER¹, A. YAROVITSKY^{1(a)}, P. TODOROV¹, I. HAMDI¹, I. MAURIN¹, S. SALTIEL^{1(b)},
D. SARKISYAN², M.-P. GORZA¹, D. BLOCH^{1(c)} and M. DUCLOY¹

¹ *Laboratoire de Physique des Lasers, UMR7538 du CNRS et de l'Université, Paris13 - 99, Av. J.B. Clément, F-93430 Villetaneuse, France*

² *Institute for Physical Research, National Academy of Sciences - Ashtarak 2, Armenia*

received 6 November 2006; accepted in final form 17 January 2007

published online 23 February 2007

PACS 42.50.Xa – Optical tests of quantum theory

PACS 34.50.Dy – Interactions of atoms and molecules with surfaces; photon and electron emission; neutralization of ions

PACS 32.70.Jz – Line shapes, widths, and shifts

Abstract – The van der Waals atom-surface attraction, scaling as C_3z^{-3} for z the atom-surface distance, is expected to be valid in the distance range 1–1000 nm, covering 8–10 orders of magnitudes in the interaction energy. A Cs vapour nanocell allows us to analyze the spectroscopic modifications induced by the atom-surface attraction on the $6P_{3/2} \rightarrow 6D_{5/2}$ transition. The measured C_3 value is found to be independent of the thickness in the explored range 40–130 nm, and is in agreement with an elementary theoretical prediction. We also discuss the specific interest of exploring short distances and large interaction energy.

Copyright © EPLA, 2007

The dipole-induced dipole attraction between neutral bodies is a key phenomenon in the ultimate cohesion of matter and is at the origin of covalent crystals and van der Waals molecules. This van der Waals (vW) type of attraction between fluctuating atomic dipoles is a precursor of the general Casimir interaction [1], whose paramount importance in the quantum theory of vacuum has been recognized recently, encompassing effects related to the need of a “cosmological constant” in general relativity theory, and speculations about the detection of a possible fifth force [2]. The interest for the measurement of the Casimir effect has been largely renewed with the recent upsurge of precision experiments [1,3], whose interpretation now requires to take into account various corrections such as the non-ideality of the materials, surface roughness, and non-zero temperature corrections. Simultaneously, the knowledge of the vW attraction between atomic particles, with its $-C_6r^{-6}$ potential (with r the interatomic distance), now appears as a fundamental need to predict the collisional behavior of a collection of atoms [4], ultimately connected to the possibility for cold atoms to condense according to a Bose-Einstein statistics.

Between these two related fundamental problems, an intermediate situation is provided by the atom-surface vW interaction, described by a $-C_3z^{-3}$ potential (z : the atom-surface distance). To theoretically estimate the C_3 value from the knowledge of atomic structures, an electrostatic mirror image approach is usually satisfactory in many cases. The z^{-3} dependence is expected to be valid for distances allowing to ignore the structural details of the surface (typically ≥ 1 nm), up to the micrometric range, when retardation effects impose the more complete Casimir-Polder description [2,5].

It remains fascinating to note that, although the vW z^{-3} attraction law should cover about 8–10 orders of magnitude of energy, little has been done to test this predicted dependence in an effective situation. The various developments in nanotechnologies and nanosciences should make it more important to measure effectively these remote forces, as for the Casimir force already known to be a possible limiting factor in MEMS technology [6]. In the shorter distance limit, the vW attraction is only an asymptotic “long-range” tail of the atom-surface potential, to the exact shape of which surface physics experiments are insensitive [7]. For longer distances, and after pioneering principle experiments using deflection of an atomic beam [8], precision experiments tested the

(a) Permanent address: Lebedev Physics Institute, Moscow, Russia.

(b) Also at Physics Department, Sofia University, Bulgaria.

(c) E-mail: bloch@lp1.univ-paris13.fr

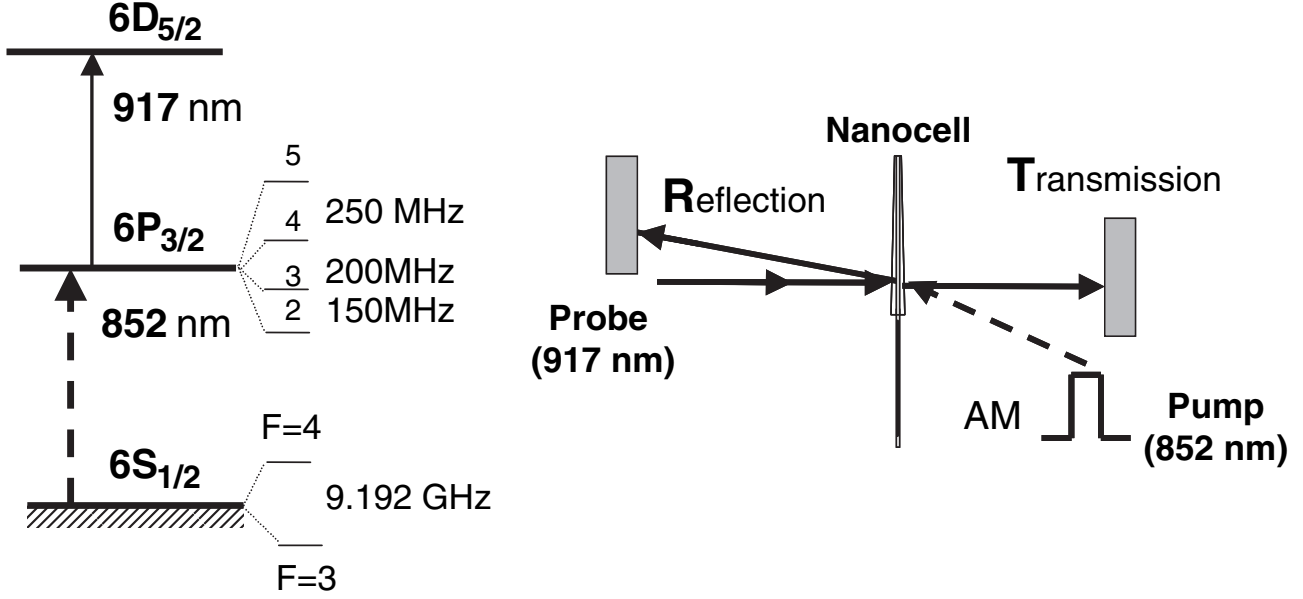


Fig. 1: Scheme of the relevant energy levels of Cs and of the experimental set-up. S_R and S_T are provided by processing the reflected and transmitted intensities through lock-in detectors.

spatial dependence on a beam of Rydberg atoms [9] channelled between two plates separated by at least 500 nm. Following the blossom of experimental measurements of vW interaction exerted on a long-lived level [10,11], the spatial dependence of vW interaction between a ground state Rb atom and a metal surface was recently investigated in the 20–100 nm range [12]. Selective Reflection (SR) spectroscopy of a vapour at an interface, in which we have been involved for a long time [13], has offered a unique capability to probe the vW interaction for short-lived excited states. It is also appropriate for analyzing the atom interaction with a (transparent) dielectric surface. Although a dielectric surface commonly exerts a weaker interaction than a metal, owing to an imperfect reflection, a specific regime of resonant coupling of the atomic excitation with the electromagnetic modes of the dielectric surface, could be demonstrated with this SR technique, leading to an exotic vW repulsion [14]. However, the depth of the region probed in the SR technique remains fixed, as governed by the (reduced) wavelength of the optical probe [13]. Here, we use an alternate technique of spectroscopy in a vapour “nanocell” [15], whose thickness d is varied in a range $d = 40\text{--}130$ nm. This allows to explore the spatial dependence of the vW interaction.

For a *beam* of atoms flying parallel to the two windows and at mid-distance (see, *e.g.*, [9]) a constant vW shift of the atomic resonance, scaling as $1/d^3$, is expected, even if multiple (dielectric) images are considered (the vW shift is here a *spectroscopic* shift, corresponding to the *difference* between the vW interaction exerted onto the final level of the transition, and the one exerted onto the initial one). However, for atoms in a *vapour*

phase, the vW shift is spatially inhomogeneous, $z = d/2$ is only the location of the minimal vW shift, and the lineshapes undergo a spatial inhomogeneous broadening leading to distortions and asymmetries. In this sense, the preliminary observation of an elementary $1/d^3$ dependence of the frequency of the minimal transmission [17] was not a sufficient evidence of the vW dependence. The principle of our estimate of the vW interaction for a given nanocell thickness d relies on a numerical comparison between the experimental spectra and a family of relevant theoretical lineshapes.

Our experiment was conducted on the $6P_{3/2}$ - $6D_{5/2}$ transition of Cs ($\lambda = 917$ nm) in a nanocell with YAG windows. The choice of a transition between excited states is to allow a strong vW shift, mainly originating in the vW interaction exerted onto the high-lying $6D$ level (fig. 1) [14]: one predicts indeed $C_3^{\text{metal}}(6D_{5/2}) = 24 \text{ kHz } \mu\text{m}^3 \gg C_3^{\text{metal}}(6P_{3/2}) = 4 \text{ kHz } \mu\text{m}^3$, and in front of a YAG window: $C_3^{\text{YAG}}(6D_{5/2}) = 17 \text{ kHz } \mu\text{m}^3$, $C_3^{\text{YAG}}(6P_{3/2}) = 2 \text{ kHz } \mu\text{m}^3$, yielding a *spectroscopic* C_3 value of $\sim 15 \text{ kHz } \mu\text{m}^3$ for YAG windows. To reach the transition of interest, a prior pumping step to Cs($6P_{3/2}$) is needed, which is performed with a 852 nm frequency-stabilized laser (see fig. 1). YAG windows were preferred to sapphire in the design of the nanocell because in the atom-dielectric surface interaction, there are no strong couplings between YAG surface resonances and virtual transitions relevant for Cs($6D_{5/2}$) [14]. The nanocell, once evacuated, is filled with an alkali-metal vapour, and consists of a system of two thick windows, that are glued and maintained separated by a nanometric spacer [15]. The external atmospheric pressure is responsible for local

variations of the nanocell thickness [15], so that translating the cell through a focused laser allows to monitor the influence of the thickness under unchanged experimental conditions. As already reported, the Fabry-Perot nature of the nanocell allows a convenient determination of the local thickness d [15]. Here, for the very small thicknesses we are interested in, a dual-wavelength measurement (633 nm and 852 nm) is sufficient: the accuracy is 1 to 5 nm, depending upon the parallelism of the windows at the considered spot, whose diameter is $\sim 100 \mu\text{m}$. Also, the Fabry-Perot nature of the nanocell allows the detection of both transmission and reflection signals (respectively S_T , and S_R) [15,16]. The spectra were simultaneously recorded, for thicknesses $d = 40 \text{ nm}$, 50 nm , 65 nm , 80 nm , 100 nm and 130 nm . The detection sensitivity is enhanced by applying a modulation to the $\lambda = 852 \text{ nm}$ pumping beam, with a subsequent synchronous detection on the $\lambda = 917 \text{ nm}$ probe. The transition in free-space is monitored by an auxiliary saturated absorption (SA) experiment on the 917 nm line in a macroscopic cell and provides the frequency reference required for interpreting the nanocell spectra. In an approach analogous to the one developed previously (*e.g.* in [14]), experiments were performed at several Cs densities —*i.e.* temperature— for each investigated spot of the nanocell. This is to minimize the influence of Cs pressure on the extracted C_3 value. Also, a variety of pumping conditions was explored to assess the spatial homogeneity of the $6P_{3/2}$ population.

In the theoretical modelling, the transmission and reflection signals S_T and S_R are derived from linearly independent integrations [16] of the local vapour response $p(z)$ as governed by the resonantly induced atomic dipole oscillation. This atomic oscillation is modelled on the basis of an instantaneous resonant Lorentzian response $\{\gamma/2 + i[\omega - \omega_0(z)]\}^{-1}$, that depends upon the detuning between the excitation frequency ω and the local vW-shifted atomic resonance $\omega_0(z)$ (γ is the optical width). It exhibits a nonlocal dependence upon the irradiating field, owing to the transient regime governing the (velocity-dependent) atomic response over the wall-to-wall trajectories. In the modelling, the unshifted transition (γ , ω) can possibly accommodate pressure broadening and shift. Hence, S_T and S_R integrate a complex interplay of natural width, Doppler broadening and velocity distribution, pressure effects, and spatial dependence of the vW potential. Our complete calculation even considers multiple electrostatic images for the vW potential, although a two-wall potential $V(z) = -C_3[z^{-3} + (d-z)^{-3}]$ agrees within 5% as long as the dispersion of the dielectric window [14] is negligible. Strong variations of the lineshapes are hence predicted when changing d , or C_3 [18]. However, when the vW interaction dominates over other causes of broadening, the spectral shift follows a $1/d^3$ dependence rather well. For parameters relevant to our problem, the modelling shows that the 40–130 nm range is sufficient to explore a factor ≥ 30 in the energy of surface interaction (see fig. 2).

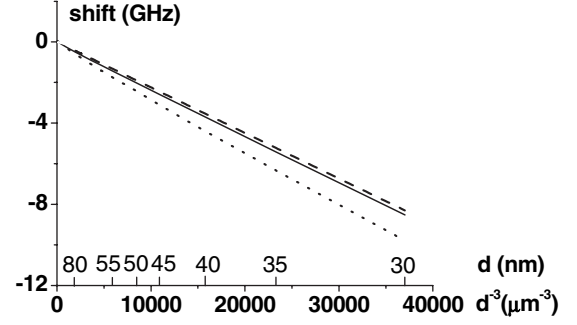


Fig. 2: vW-induced spectral shift between the dip of minimal transmission and the free-atom resonance as a function of the thickness. The calculation is performed for: $C_3 = 14 \text{ kHz } \mu\text{m}^3$, $\gamma = 300 \text{ MHz}$. The dotted line is for a gas of atoms flying wall-to-wall with a 250 MHz Doppler width. The dashed line, and the continuous line, are respectively for a beam of atoms flying at mid-distance $d/2$, and for a gas of motionless atoms.

Technically, the analysis relies on a fitting of the experimental spectra $S_T(\omega)$ and $S_R(\omega)$ with the family of C_3 curves calculated for a given thickness d . The strong constraints on the vW shift and lineshape restrict the C_3 values providing a satisfactory (least-square) fitting to a narrow-range, typically 10–20% around the central value. When the vW shift is dominant, the vW spatial broadening makes fittings nearly insensitive to the adjustment of the width of the optical transition. The main results of our systematic analysis are twofold: i) for a given experiment, a very good consistency between the shapes of S_T and S_R signals is demonstrated [18]; their relative amplitudes are also in agreement once considered the scattering losses¹; this consistency is remarkable because it appears for lineshapes that are unrelated, and with fitting parameters that are independently chosen; ii) the optimal fitting C_3 values are found to be independent of the thickness. Figure 3 illustrates synthetically this consistency: all spectra recorded in identical conditions, but for various thicknesses, are fitted with a single set of parameters. The residual discrepancies in the fitting disappear with more individual adjustments, and the individual C_3 fitting values are modified only marginally. Figure 4 is a plot of the individually optimized fitting value for C_3 for differing thicknesses, and pressure conditions. When retaining only the experiments at relatively low pressure, one gets an accurate value $C_3 \approx 14 \pm 3 \text{ kHz } \mu\text{m}^3$. For the smallest thickness (*i.e.* dominant vW contribution), the obtained C_3 values are independent of the Cs pressure, in spite of a pressure broadening visible in the lineshapes. For larger thickness ($d \geq 80 \text{ nm}$), the vW shift and broadening become partly hindered by pressure effects, and decreasing C_3 values are found when increasing the Cs density.

¹Experimentally, reflection coefficients on the windows do not accurately comply with the Fresnel formulae because of scattering. This explains variations from spot to spot in the ratios between S_T and S_R .

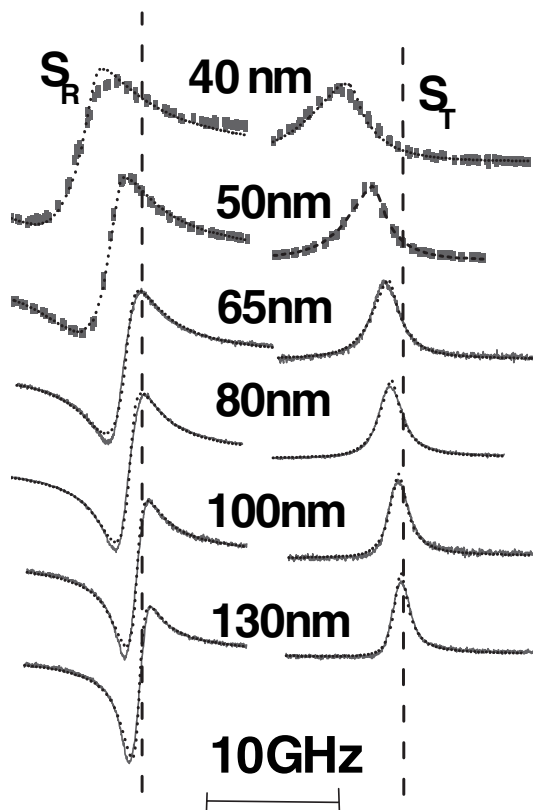


Fig. 3: Experimental lineshapes (S_R and inverted S_T) recorded on the 917 nm transition for various thicknesses. The frequency scans are continuous, or discrete (for 40 nm and 50 nm). The vertical dashed line is a marker for the SA resonance. All fittings (dotted lines) use the parameters optimized for S_T (50 nm), found to be $C_3 = 14 \text{ kHz } \mu\text{m}^3$, $\gamma = 300 \text{ MHz}$. Adjustable amplitudes are introduced to compensate for the thickness dependence of the efficiency of the $6P_{3/2}$ pumping. For 40 nm: respectively 3.3 and 4.8 for S_T and S_R ; for 65 nm: 0.25 and 0.24; for 80 nm: 0.19 and 0.15; for 100 nm: 0.11 and 0.07; for 130 nm: 0.07 and 0.04. The Cs nanocell temperature is 200°C . The pumping frequency is locked onto the $4 \rightarrow 4-5$ crossover of the D_2 line, pump power is $\sim 1 \text{ mW}$ focused on a diameter $\sim 100 \mu\text{m}$, pump absorption reaches 25% for 130 nm. The 917 nm transmission change is $\sim 5 \cdot 10^{-4}$ for 50 nm.

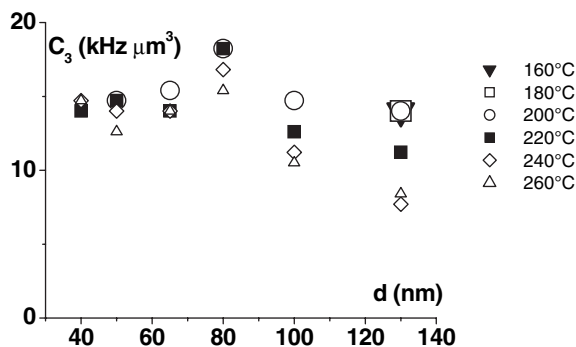


Fig. 4: Optimal fitting C_3 values found for various thickness and Cs temperatures. Increasing the Cs temperature by 20°C approximately doubles the Cs density.

And indeed, for the large thicknesses, when the vW interaction turns to be relatively small, the accuracy of the C_3 determination starts to be affected by uncertainties on the 917 nm SA reference frequency itself: an uncontrolled preferential pumping to a specific $6P_{3/2}$ hyperfine sublevel is susceptible to occur, owing to nonlinearities in the D_2 pumping.

Notwithstanding the excellent agreement between the experimental data and the theoretically modelled curves, the reproducibility issues are worth being discussed, as well as the effective nature of the interacting surface. Reproducibility in the vicinity of a dielectric interface is shown to be an issue in [2], with numerous erratic points obtained, even with well-chosen surfaces. In our experiment, the measured thickness is an average, over the laser-spot (diameter $\sim 100 \mu\text{m}$) of local wall-to-wall distance d . Because of the local surface roughness (estimated to 1–2 nm), and of the defects in planarity or parallelism (the minimal observed slope of the nanocell can be as small as $\sim 10 \text{ nm}$ for 1 mm [15]), the observed vW effect can vary for comparable spots as $\langle d \rangle^{-3} \neq \langle d^{-3} \rangle$. The surface of our nanocell largely exceeding the spot size, several experiments with a similar nominal (average) thickness can be compared. A perfect lineshape reproducibility has been found for all the various investigated spots, as long as $d \geq 65 \text{ nm}$. At $d = 50 \text{ nm}$, several spots—but not all of them—produce rigorously identical spectra: they are those here analyzed, as apparently immune to random defects of the surface that would not be compatible with the observation of similar spectra on a differing spot. For $d = 40 \text{ nm}$, sensitive variations are observed from spot to spot; however, except for a few erratic behaviours clearly out of the considered family of lineshapes, minor irreproducibilities do not prohibit a fitting as exemplified in fig. 3. Remarkably, in this regime of very strong vW interaction, minor changes in the fitting parameters suffice to interpret visible variations in the lineshapes.

The exact nature of the interacting surface can also be an issue, especially because the surface is in contact with a vapour, and because for a dielectric surface, relatively high static electric fields can induce Stark shifts. In a vapour, Cs atoms are susceptible to deposit on, or penetrate the YAG surface; however, the dielectric function characterizing the vW surface response should remain nearly unaffected by these kinds of (non-resonant) dopants [19]. The competition between the vW shift, and the Stark shift induced by a residual static field can pose a more serious problem, as recognized in [9]. Moreover, stronger residual fields can be expected for a dielectric window² than for a metal coating. In particular, for some random distributions of crystalline domains, the overall Stark shift may exhibit a z^{-2} -dependence [9], that

²Static charges and random distribution of crystalline domains have been apparently responsible for erratic signals in an experiment derived from ref. [9], but with the atomic beam of Rydberg atoms passing between dielectric walls (S. Haroche, private communication).

could be hard to distinguish from a vW shift in the spectroscopic response (conversely, a constant Stark shift would be easily detected in an analysis of our fittings). This is a severe problem for experiments on Rydberg levels, because when increasing the atomic excitation, the Stark shift grows faster than the vW shift (respectively like n^{*7} , and n^{*4} in common approximations, for n^* the effective quantum number). From our own experience with Cs* close to a YAG window, we can conclude that the influence of residual fields should remain minor: a SR experiment on the Cs($7P \rightarrow 10D$) line at $1.3 \mu\text{m}$ [20] (at a comparable YAG interface) had indeed shown the Stark shift to be negligible (*i.e.* ≤ 100 MHz). Extrapolation from Cs($10D$) ($n^* \approx 7.5$) to Cs($6D$) (with $n^* \approx 3.5$) hence implies a maximal Stark shift on the order of \sim MHz in similar conditions. Even if a possible z^{-2} -dependence is considered, the influence of the Stark shift should remain below several 100 MHz for the smaller nanocell thicknesses, and be even less for larger thicknesses. This is why we estimate that the major causes of irreproducibility are connected to uncertainties, at the level of a few nm, in the local geometry of the two planar windows, rather than to the effect of stray fields.

Our estimated value ($C_3 = 14 \text{ kHz } \mu\text{m}^3$) is in very good agreement with the $\sim 15 \text{ kHz } \mu\text{m}^3$ theoretical prediction. This agreement may be considered as remarkable in view of various pitfalls, either experimental, or theoretical. A precise evaluation of the dielectric image factor applicable to Cs($6D_{5/2}$) is delicate [21] because the situation is not purely nonresonant: the virtual *emission* coupling Cs($6D_{5/2}$) to $7D$ (in the $\sim 15 \mu\text{m}$ region) requires the accurate knowledge of the YAG spectrum and of its surface modes. Moreover, in a nanocell [22], the atom couples to a guided mode structure, and the two-wall model, or its straightforward extension to multiple electrostatic images model, may reveal too elementary. Also, the orientation of the atom has been assumed to be isotropic, implying equal contributions for the dipole fluctuating along the normal, and parallel to the interface. However, the atom could undergo a Zeeman polarization under the influence of the D_2 line pumping (the irradiation, being under near normal incidence, is polarized *parallel* to the surfaces), or through the polarized excitation of the 917 nm laser. This would restrict the summation over the virtual dipole transitions connecting the $6D_{5/2}$ level to only some directions, reducing the predicted C_3 value [22]. More generally, a recent work [23] shows that C_3 itself should exhibit a spatial dependence $C_3(z)$, because at the smaller distances, the (non retarded) contribution of the highly energetic transitions involving the electronic core becomes stronger [4]. This dependence, actually unobserved [10,12], is however expected to be smaller in our situation of a high-lying state [13], than for a ground state.

To summarize, we have investigated the z^{-3} -dependence of the vW potential for a 40–130 nm thickness range, and an energy shift spanning over a factor ~ 30 . Our technique could be extended to test the rich physics

of an atom resonantly interacting with coupled surface modes. The distances investigated here are an order of magnitude below those explored years ago for excited atoms in Rydberg levels [9], and compares favourably with those currently investigated in precision Casimir measurements [3], or with the one addressed in the recent vW interaction experiments with ground-state atoms [12]. Note that in our situation, the vW shift, whose minimal value is twice the one undergone by an atom at a distance $d/2$, is equivalent to the one of an atom located at $\sim 0.4d$ from a single wall. Also, the combined effects of the transient regime, and the steepness of the vW potential, make the central region of the nanocell spectrally dominant, as can be inferred from fig. 2: hence, the individual evaluations $C_3(d)$ turn out to be nearly free of spatial averaging. Lowering the effective atom-surface distance below 10 nm appears a realistic objective (feasibility of $d \sim 20\text{--}30$ nm is reported in [17]). This is in contrast with the vW measurements based upon the reflection of slow atoms [10,12]: the minimal distance of approach of the observed atomic trajectories is limited by the considerable force that should be applied to equilibrate the vW attraction. Similarly, the techniques of atomic force microscopy presently used for the evaluation of Casimir interaction, are hardly compatible with too high a pressure: the standard calculation predicts indeed a Casimir interaction exceeding the atmospheric pressure for $d \leq 10$ nm. Note that for these small distances, the asymptotic regime of van der Waals Casimir-related interaction remains under debate [24]. Finally, it is worth mentioning that in the small-distance regime that we explore here, we demonstrate an interaction energy (up to ~ 5 GHz, or 0.25 K) much larger than obtained in all previous investigations. This corresponds to a considerable acceleration ($\sim 8 \cdot 10^7$ g for a Cs($6D$) atom 20 nm away from one of the wall), exceeding by orders of magnitude the one obtained in laser cooling techniques. This may open a realm of exotic possibilities, such as a gradient of density for an atomic gas in the extreme vicinity with the surface.

Work partially supported by FASTNet (European contract HPRN-CT-2002-00304) and by the French-Bulgarian cooperation RILA (#09813UK).

REFERENCES

- [1] CASIMIR H. B. G., *Proc. K. Ned. Akad. Wet.*, **60** (1948) 793; for reviews, see, *e.g.*, BORDAG M., MOHIDEEN U. and MOSTEPANENKO V., *Phys. Rep.*, **353** (2001) 1; LAMBRECHT A. and REYNAUD S., in *Poincaré seminar 2002, Vacuum energy*, edited by RIVASSEAU B. V. (Birkhauser, Basel) 2003, pp. 109-126; MILTON K. A., *J. Phys. A*, **37** (2004) R209.
- [2] HARBER D. M. *et al.*, *Phys. Rev. A*, **72** (2005) 033610.

- [3] MOHIDEEN U. and ROY A., *Phys. Rev. Lett.*, **81** (1998) 4549; EDERTH T., *Phys. Rev. A*, **62** (2000) 062104; CHEN F. *et al.*, *Phys. Rev. A*, **69** (2004) 022117.
- [4] DEREVIANKO A. *et al.*, *Phys. Rev. Lett.*, **82** (1999) 3589.
- [5] CASIMIR H. B. G. and POLDER D., *Phys. Rev.*, **73** (1948) 360.
- [6] CHAN H. B. *et al.*, *Phys. Rev. Lett.*, **87** (2001) 211801; BUKS E. and ROUKES M. L., *Europhys. Lett.*, **54** (2001) 220.
- [7] GOODMAN F. O. and WACHMAN H. Y., *Dynamics of Gas-Surface Scattering* (Academic Press, New York) 1976.
- [8] RASKIN D. and KUSCH P., *Phys. Rev.*, **179** (1969) 712.
- [9] SANDOGHDAR V. *et al.*, *Phys. Rev. Lett.*, **68** (1992) 3432; *Phys. Rev. A*, **53** (1996) 1919.
- [10] LANDRAGIN A. *et al.*, *Phys. Rev. Lett.*, **77** (1996) 1464.
- [11] GRISENTI R. E. *et al.*, *Phys. Rev. Lett.*, **83** (1999) 1755; BOUSTIMI M. *et al.*, *Phys. Rev. Lett.*, **86** (2001) 2766; SHIMIZU F., *Phys. Rev. Lett.*, **86** (2001) 987.
- [12] MOHAPATRA A. K. and UNNIKRIISHNAN C. S., *Europhys. Lett.*, **73** (2006) 839.
- [13] For a review, see BLOCH D. and DUCLOY M., in *Atom-Wall Interaction*, edited by BEDERSON B. and WALTHER H., *Adv. At. Mol. Opt. Phys.*, Vol. **50** (Elsevier-Academic Press, Amsterdam) 2005, pp. 91-154.
- [14] FAILACHE H. *et al.*, *Phys. Rev. Lett.*, **83** (1999) 5467; *Eur. Phys. J. D*, **23** (2003) 237.
- [15] SARKISYAN D. *et al.*, *Opt. Commun.*, **200** (2001) 201; DUTIER G. *et al.*, *Europhys. Lett.*, **63** (2003) 35.
- [16] DUTIER G. *et al.*, *J. Opt. Soc. Am. B*, **20** (2003) 793.
- [17] DUTIER G. *et al.*, in *Laser Spectroscopy, Proceedings of the XVI International Conference*, edited by HANNAFORD P. *et al.* (World Scientific, Singapore) 2004, pp. 277-283. These measurements do not discriminate between atom-surface interaction and collision processes; see also HAMDI I. *et al.*, *Laser. Phys.*, **15** (2005) 987.
- [18] MAURIN I. *et al.*, *J. Phys. Conf. Ser.*, **19** (2005) 20. In this reference, the C_3 values given are actually $r_p C_3$, with $r_p (= 0.536)$ the dielectric image factor, because of an accidental mistake in the transcription between computer values and the meaning of the fitting parameter.
- [19] FICHET M. *et al.*, *Phys. Rev. A*, **51** (1995) 1553.
- [20] FAILACHE H. *et al.*, *Phys. Rev. Lett.*, **88** (2002) 243603.
- [21] SALTIEL S., BLOCH D. and DUCLOY M., *Opt. Commun.*, **265** (2006) 220.
- [22] GORZA M.-P., in preparation.
- [23] CARIDE A. O. *et al.*, *Phys. Rev. A*, **71** (2005) 042901.
- [24] See, *e.g.*, SCANDURRA M., arXiv:hep-th/0306076/v2 (2003); Note that for the early experiments of van der Waals interaction between two surfaces performed in the nanometric range of distances, such as in ISRAELACHVILI J. N. and TABOR D., *Proc. R. Soc. London, Ser. A*, **331** (1972) 19, the geometry actually averages on distances much larger than the minimal distance, whose estimate results from an optical measurement integrating much larger distances.

Temperature dependence of the dielectric permittivity of CaF_2 , BaF_2 and Al_2O_3 : application to the prediction of a temperature-dependent van der Waals surface interaction exerted onto a neighbouring $\text{Cs}(8P_{3/2})$ atom

This article has been downloaded from IOPscience. Please scroll down to see the full text article.

2009 J. Phys.: Condens. Matter 21 255902

(<http://iopscience.iop.org/0953-8984/21/25/255902>)

View [the table of contents for this issue](#), or go to the [journal homepage](#) for more

Download details:

IP Address: 194.254.165.167

The article was downloaded on 12/07/2010 at 08:38

Please note that [terms and conditions apply](#).

Temperature dependence of the dielectric permittivity of CaF_2 , BaF_2 and Al_2O_3 : application to the prediction of a temperature-dependent van der Waals surface interaction exerted onto a neighbouring $\text{Cs}(8\text{P}_{3/2})$ atom

Thierry Passerat de Silans¹, Isabelle Maurin¹,
Pedro Chaves de Souza Segundo¹, Solomon Saltiel^{1,2,*},
Marie-Pascale Gorza¹, Martial Ducloy¹, Daniel Bloch¹,
Domingos de Sousa Meneses^{3,4} and Patrick Echegut³

¹ Laboratoire de Physique des Lasers, UMR 7538 du CNRS et de l'Université Paris 13,
99 Avenue JB Clément, Villetaneuse, France

² Physics Department, Sofia University, 5 J Bourchier Boulevard, 1164 Sofia, Bulgaria

³ CNRS, UPR 3079 CEMHTI, 1D Avenue de la Recherche Scientifique,
F-45071 Orléans Cedex 2, France

⁴ Université d'Orléans, Polytech, Avenue du Parc Floral, BP 6749, F-45067 Orléans Cedex 2,
France

E-mail: daniel.bloch@univ-paris13.fr

Received 19 December 2008, in final form 16 April 2009

Published 27 May 2009

Online at stacks.iop.org/JPhysCM/21/255902

Abstract

The temperature behaviour in the range 22–500 °C of the dielectric permittivity in the infrared range is investigated for CaF_2 , BaF_2 and Al_2O_3 through reflectivity measurements. The dielectric permittivity is retrieved by fitting reflectivity spectra with a model taking into account multiphonon contributions. The results extrapolated from the measurements are applied to predict a temperature-dependent atom–surface van der Waals interaction. We specifically consider as the atom of interest $\text{Cs}(8\text{P}_{3/2})$, the most relevant virtual couplings of which fall in the range of thermal radiation and are located in the vicinity of the reststrahlen band of fluoride materials.

(Some figures in this article are in colour only in the electronic version)

1. Introduction

Materials that are currently used as optical windows have usually been studied in depth, notably to determine their refractive indices in their transparency regions and the shift of the edges of the transparency region with temperature. In the absorption band, optical investigations of their properties have been commonly performed to get information on their

phonon bands, not requiring the same level of accuracy as in common optical applications. However, the optical features of the surface modes, although derived from knowledge of the bulk material, require information on these optical properties within the absorption band. A sensitive tool of these surface properties—benefiting from the high accuracy of atomic physics—is provided by the spectroscopy of an atom in the close vicinity to a surface, through the van der Waals-type long-range surface interaction (see [1] and references

* now deceased.

therein). We have recently addressed [2] the problem of the accuracy of the data existing in the literature for this kind of specific experiment and, in particular, we have shown the high sensitivity of these surface responses to a minor inaccuracy in the bulk properties. This explains that to investigate properties connected to the thermal emissivity of a surface [3–6], an accurate knowledge of the temperature dependence of the optical properties of the material is needed in the thermal infrared range.

In this work, we investigate the temperature dependence of the infrared properties of fluoride crystals CaF_2 and BaF_2 . The transparency of these materials extends from UV to mid-IR ranges, and their reststrahlen band, corresponding to a strong absorption, lies in the far-infrared range. Additionally, we also perform measurements on sapphire (Al_2O_3 , perpendicular c axis), a well-known optical window material that is considered as a reference for the optical properties and for the planned experiments. To the best of our knowledge, the literature results concerning CaF_2 are limited to ambient temperature [7–9] and 100 K [8] range. For BaF_2 [7, 10, 11], reflectance data were given for the following temperatures: 295, 373, 573 and 773 K. Large discrepancies between published results and their low resolution justify the realization of new measurements.

For Al_2O_3 , systematic studies as a function of temperature had already been conducted [12, 13]. The IR behaviour is usually described with the help of several (up to four) phonon modes. However, the experimental findings vary, probably due to variations in the quality of the polishing of the sample, the degree of the impurities and the precision of the measurements.

Our aim in this work is to determine from the knowledge of reflectivity spectra the complex surface response:

$$S(\omega) = \frac{\varepsilon(\omega) - 1}{\varepsilon(\omega) + 1} \quad (1)$$

where $\varepsilon(\omega)$ represents the dielectric function. This research was triggered by an experimental search of the temperature dependence of the atom–surface interaction [4, 5], in which the fundamental effect of vacuum field temperature is susceptible to combine with the temperature dependence of the dense material. As this experiment in progress is performed on the $8P_{3/2}$ level of Cs [6, 14], for which virtual absorptive couplings to Cs ($7D_{3/2}$) and to Cs ($7D_{5/2}$) lie respectively at $\sim 256.4 \text{ cm}^{-1}$ ($\sim 39 \mu\text{m}$) and $\sim 277.8 \text{ cm}^{-1}$ ($\sim 36 \mu\text{m}$), we apply our temperature-dependent evaluations of $S(\omega)$ to the relevant predictions for this specific problem of the influence of the thermal emissivity of materials on the atom–surface interaction. Note that, in principle, extrapolation of surface properties from information from the bulk assumes that the surface is of the same nature as the bulk: let us note that here, surface changes (impurities, crystal reconstruction) occur on a thickness that is truly negligible relative to the thermal infrared wavelengths that we consider. In addition, deriving the bulk properties from a reflectivity measurement implicitly assumes this similar nature of the material in the bulk and at the interface.

This paper is presented in the following way. In section 2, we briefly describe the experimental results with reflectivity

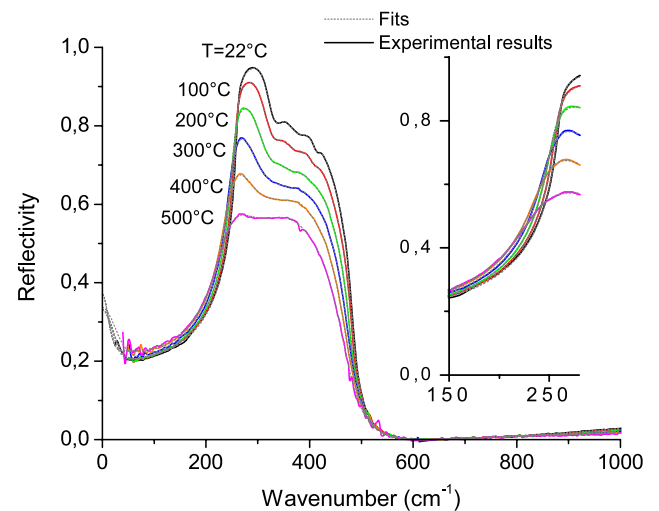


Figure 1. Experimental reflectance spectra of CaF_2 and fits obtained with semi-quantum dielectric function models for sample temperatures between 22 and 500 °C.

spectra as a function of temperature. In section 3, we present the theoretical model [15] of dielectric permittivity that we use to fit the spectra. In section 4, we discuss additional criteria to make individual fittings of a given experimental curve consistent with the expected temperature behaviour, and we provide our estimates of the dielectric permittivity spectra, and of the spectrum of the surface response as a function of temperature. In section 5, we present the results of the calculation of the van der Waals attraction coefficient for Cs($8P_{3/2}$) in front of surfaces of CaF_2 , BaF_2 and Al_2O_3 as a function of temperature. By comparing the predictions resulting from various models of permittivity, not limited to our findings, we illustrate why a sensitive knowledge of the temperature-dependent permittivity is required.

2. Experimental details

The samples were optically polished on both sides, with a diameter $\sim 8 \text{ mm}$ and a 0.8 mm thickness for CaF_2 and BaF_2 , and a 1 mm thickness for Al_2O_3 (with c axis perpendicular to the window). The reflectivity spectra of CaF_2 , BaF_2 and Al_2O_3 in the infrared range were acquired with a Bruker infrared Fourier spectrometer (IFS) 113v interferometer for various temperatures ranging between room temperature and 500 °C in steps of 100 °C. The heating was provided by heating a ceramic plate mounted in contact with the rear facet of the sample. The experimental resolution spectrum was $\sim 4 \text{ cm}^{-1}$ and the accuracy on the measured reflectivity was $\sim 2\text{--}3\%$.

To extract optical information on the bulk properties of the material, one should note that, as long as the sample is absorbing in the frequency range that is analysed, the reflected intensity only originates in the reflectivity from the input window. Conversely, when the absorption along the sample remains weak, the reflected light should include the reflection from the second window. However, the obtained reflected intensity also combines reflectivity of the sample with the thermal emission of the ceramic hotplate.

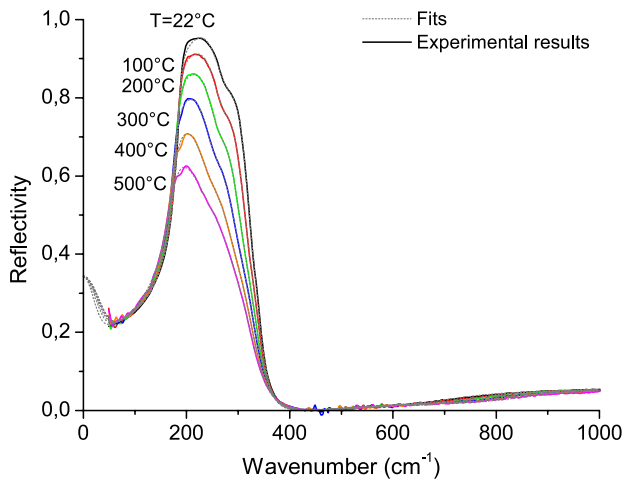


Figure 2. Experimental reflectance spectra of BaF₂ and fits obtained with semi-quantum dielectric function models for sample temperatures between 22 and 500 °C.

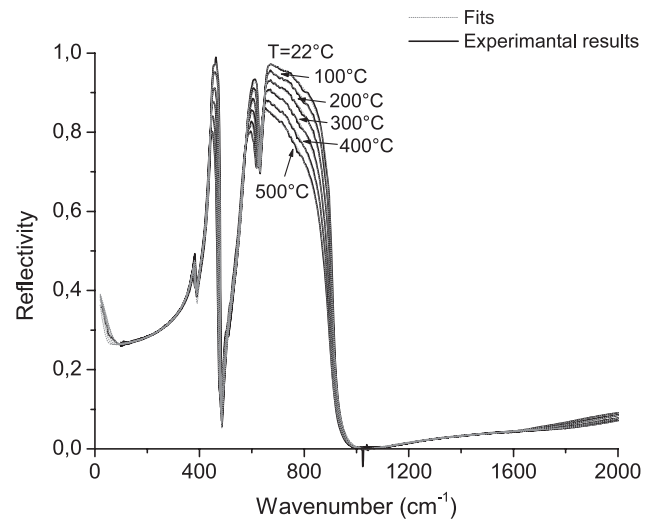


Figure 3. Experimental reflectance spectra of Al₂O₃ and fits obtained with semi-quantum dielectric function models for sample temperatures between 22 and 500 °C.

The measured reflectivity spectra are reported in figures 1–3. For CaF₂, at low temperatures, the spectra exhibit small structures inside the reststrahlen band, which disappear when the temperature increases (see figure 1). These small oscillations, although not consistently mentioned in the literature because of a lower resolution and sensitivity, do not result from interferences nor from an artefact. They were already observed in [7, 8]. Such oscillations are clearly the multiphonon process signature, as explained in [8]. For BaF₂ (see figure 2), we also observe the multiphonon contribution within the reststrahlen band. For Al₂O₃ (see figure 3), the reflectance spectra are more complex and present smaller oscillations also due to multiphonon processes in the reststrahlen region. As a general trend for all these spectra, the sharp edges of the reflectivity get smoother with increasing temperatures.

One also notes on the spectra some apparent oscillations on the wings (50–100 cm⁻¹ and 500 cm⁻¹ for CaF₂ and BaF₂ or 1000 cm⁻¹ for Al₂O₃). They must be attributed to noise: the reflectivity being weak and the detector sensibility low, the signal-to-noise ratio becomes weak.

3. Dielectric constant: theoretical background

In the frame of classical dielectric models [13, 16], the dielectric function ϵ can be described by

$$\epsilon(\omega) = \epsilon_\infty + \sum_j \frac{S_j \Omega_j^2}{\Omega_j^2 - \omega^2 - i\gamma_j \omega} \quad (2)$$

where ϵ_∞ , Ω_j , S_j and γ_j are, respectively, the high-frequency value of the dielectric constant, and the transverse optical wavenumber, the dielectric strength and the damping of the j th phonon. Such a description does not take into account the lattice anharmonicity that makes crystal vibrations interact with the phonon bath in a more complex way: in particular, the damping should not simply be a constant γ_j , but should be highly frequency-dependent, which is due to multiphonon

interactions (see [15] and references therein). The effect of this multiphonon interaction was addressed in several models [10, 15]. It can be notably taken into account in an advanced model [15] where γ_j is replaced by a self-energy function $P_j(\omega)$, consisting of a sequence of peaks that are well reproduced by ‘extended’ Gaussian functions (i.e. with Kramers–Kronig counterparts):

$$\epsilon(\omega) = \epsilon_\infty + \sum_j \frac{S_j \Omega_j^2}{\Omega_j^2 - \omega^2 - 2\Omega_j P_j(\omega)} \quad (3)$$

with $P_j(\omega) = \sum_n \tilde{g}_{n,j}(\omega)$:

$$\begin{aligned} \tilde{g}_{n,j}(\omega) = & \frac{2A_{n,j}}{\sqrt{\pi}} \left[D\left(\frac{2\sqrt{\text{Ln}(2)}(\omega + \omega_{n,j}^0)}{\gamma_{n,j}}\right) \right. \\ & - D\left(\frac{2\sqrt{\text{Ln}(2)}(\omega - \omega_{n,j}^0)}{\gamma_{n,j}}\right) \left. \right] \\ & + iA_{n,j} \exp\left(-\frac{4\text{Ln}(2)(\omega - \omega_{n,j}^0)^2}{(\gamma_{n,j})^2}\right) \\ & - iA_{n,j} \exp\left(-\frac{4\text{Ln}(2)(\omega + \omega_{n,j}^0)^2}{(\gamma_{n,j})^2}\right) \end{aligned} \quad (4)$$

and where $A_{n,j}$, $\omega_{n,j}^0$ and $\gamma_{n,j}$ are, respectively, the amplitude, the location and the damping parameters of Gaussians, and $D(x)$ is the Dawson integral which is given by

$$D(x) = \exp(-x^2) \int_0^x \exp(t^2) dt. \quad (5)$$

Within such a frame, which considerably increases the number of free parameters, a major problem is to identify the right number of parameters, allowing getting an accurate fitting of the experimental spectra, while keeping the number of parameters at a minimum [15]. The objective pursued in section 4 is to extract a unique spectrum of permittivity from the reflectivity data, while finding criteria of consistency relative to the temperature dependence.

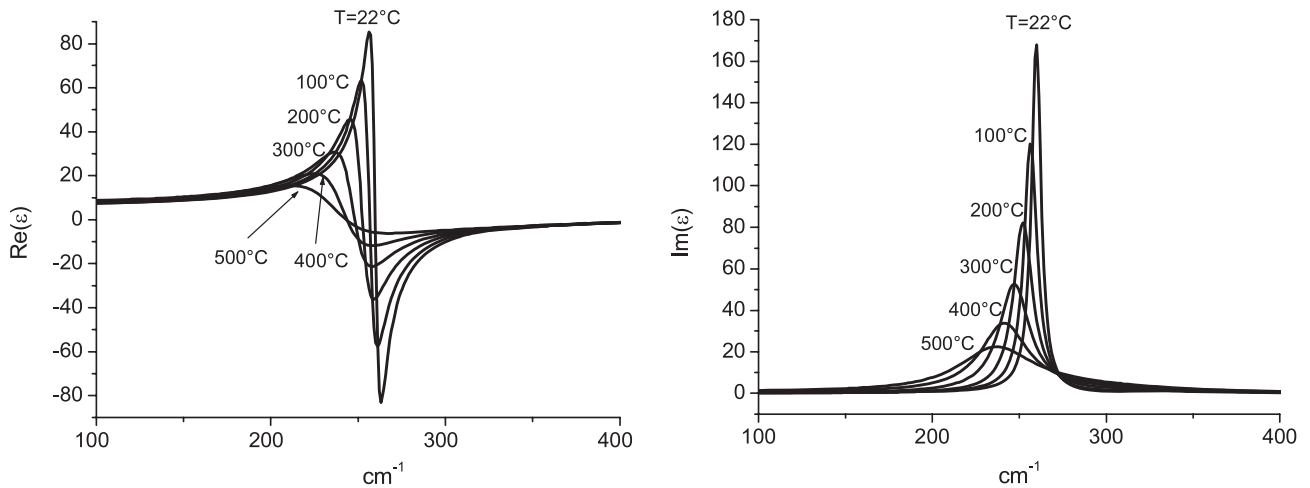


Figure 4. Dielectric constant of CaF_2 (real and imaginary parts) for sample temperatures between 22 and 500 °C.

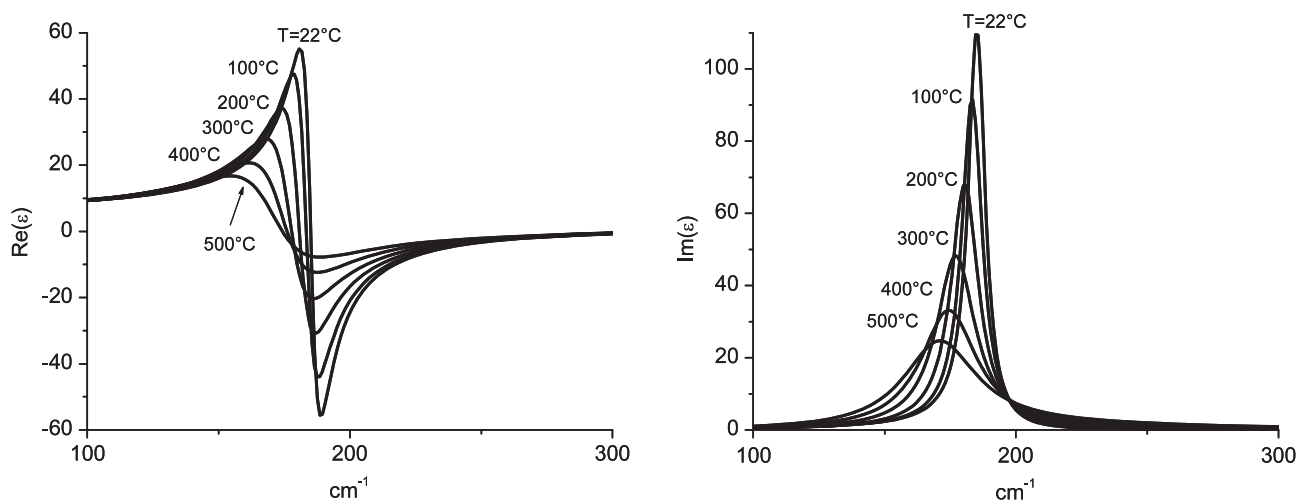


Figure 5. Dielectric constant of BaF_2 (real and imaginary parts) for sample temperatures between 22 and 500 °C.

4. Fitting results and discussion

All the numerical fitting spectra have been obtained with *Focus*, a curve fitting programme developed by one of us (DdSM) that is in free access on the web [17].

In figures 1–3, in which the experimental spectra are reproduced, we have also plotted our best fits obtained on the basis of the semi-quantum model described in section 3. The parameters used for these fits are applied to determine the spectral behaviour of the dielectric permittivity $\varepsilon(\omega)$ (figures 4–6). These parameters are reported in tables 1–3 for CaF_2 , BaF_2 and Al_2O_3 , respectively, and the complex spectra of self-energy are shown in figures 7–9.

For consistency of the fittings with other known criteria, we have selected fittings for which the extrapolation at zero frequency of the dielectric constant ε_0 is in agreement with the one known in the literature at ambient temperature (i.e. 6.63 for CaF_2 [9], 6.7–7.4 for BaF_2 [11] and 9.395 for Al_2O_3 ordinary ray [18]). We also have tried to impose as much as possible that parameters appearing in the dielectric constants and in the self-energy (see tables 1–3 and figures 4–9) evolve

linearly with temperature. Such an *a priori* behaviour can be justified (see, e.g., [19]). Note that, in the absence of such a requirement, which applies to a set of spectra recorded at various temperatures, a single reflectivity spectrum can be equivalently fitted by several systems of parameters, at the expense of the reliability of the extrapolated spectra of permittivity (figures 4–6) or of the surface responses (figures 10–12).

For CaF_2 (figure 1), and as predicted by group theory [20], infrared activity only concerns phonon modes with the T_{1u} symmetry which is triply degenerate. So to fit the infrared spectra and their temperature dependence, a dielectric function model involving a single anharmonic phonon term was used. A rather complex self-energy function was also necessary to reproduce the optical response due to the multiphonon processes, i.e. the numerous small structures appearing within the reflection band. In spite of some apparently erratic variations of the individual parameters with temperature (table 1), these parameters are needed to take care of the evolution of the multiphonon contributions observed around 400 cm^{-1} . Figure 10 shows that the temperature behaviour

Table 1. Parameters of the semi-quantum model used to fit the thermal infrared spectra of CaF₂.

	Temperature (°C)					
	22	100	200	300	400	500
Global parameters						
ε_∞	2.02	2.019	2.07	2.11	2.1	2.16
S_1	4.18	4.04	3.95	3.89	3.83	3.67
Ω_1 (cm ⁻¹)	272.74	278.17	283.63	288.71	291.76	299.23
Self-energy						
$A_{1,1}$ (cm ⁻¹)	9.83	8.63	5.01	3.82	14.55	12.12
$\omega_{1,1}^0$ (cm ⁻¹)	54.67	54.5	54.5	54.5	54.5	54.5
$\gamma_{1,1}$ (cm ⁻¹)	260.19	245.23	214.99	189.55	167.09	179.98
$A_{2,1}$ (cm ⁻¹)	8.65	10.15	4.77	7.67	10.88	9.25
$\omega_{2,1}^0$ (cm ⁻¹)	332.74	328.92	319.06	307.51	307.47	298.43
$\gamma_{2,1}$ (cm ⁻¹)	31.34	38.81	39.26	51.86	67.18	87.66
$A_{3,1}$ (cm ⁻¹)	11.145	12.598	14.44	10.27	6.66	4.07
$\omega_{3,1}^0$ (cm ⁻¹)	370.78	370.35	357.47	345.84	352.88	352.24
$\gamma_{3,1}$ (cm ⁻¹)	58.39	54.58	89.84	65.17	56.51	79.67
$A_{4,1}$ (cm ⁻¹)	2.33	3.04	0.995	6.08	3.73	1.74
ω_0^{41} (cm ⁻¹)	413.56	408.84	408.99	397.19	398.97	398.97
$\gamma_{4,1}$ (cm ⁻¹)	18.61	25.91	27.16	77.05	60.76	55.25
$A_{5,1}$ (cm ⁻¹)	12.95	8.22	5.81	0.97	0.31	0.129
$\omega_{5,1}^0$ (cm ⁻¹)	448.59	440.498	441.07	443.51	443.78	443.78
$\gamma_{5,1}$ (cm ⁻¹)	104.74	74.79	80.31	32.76	9.86	6.3
$A_{6,1}$ (cm ⁻¹)	9.94	23.14	29.56	38.64	46.1	51.45
$\omega_{6,1}^0$ (cm ⁻¹)	640.11	619.098	625.31	618.89	620.18	621.83
$\gamma_{6,1}$ (cm ⁻¹)	483.71	436.706	492.69	537.695	602.62	690.66

Table 2. Parameters of the semi-quantum model used to fit the thermal infrared spectra of BaF₂.

	Temperature (°C)					
	22	100	200	300	400	500
Global parameters						
ε_∞	2.12	2.12	2.12	2.11	2.115	2.11
S_1	4.38	4.07	3.799	3.52	3.24	2.99
Ω_1 (cm ⁻¹)	194.14	202.71	209.42	217.77	226.32	235.02
Self-energy						
$A_{1,1}$ (cm ⁻¹)	5.13	3.91	2.79	2.078	1.45	0.86
$\omega_{1,1}^0$ (cm ⁻¹)	132.23	131.107	124.61	133.28	128.533	123.53
$\gamma_{1,1}$ (cm ⁻¹)	142.04	136.54	136.08	127.26	128.34	124.56
$A_{2,1}$ (cm ⁻¹)	6.9	5.63	4.64	3.53	4.21	5.24
$\omega_{2,1}^0$ (cm ⁻¹)	278.48	270.11	260.89	251.44	244.89	243.97
$\gamma_{2,1}$ (cm ⁻¹)	48.2	40.48	35.17	33.87	46.78	72.15
$A_{3,1}$ (cm ⁻¹)	13.84	11.23	9.908	8.09	5.42	2.67
$\omega_{3,1}^0$ (cm ⁻¹)	331.79	326.13	318.63	307.496	295.39	295.89
$\gamma_{3,1}$ (cm ⁻¹)	46.69	52.66	65.34	80.05	64.18	47.398
$A_{4,1}$ (cm ⁻¹)	14.97	28.36	37.02	48.67	57.38	64.83
ω_0^{41} (cm ⁻¹)	520.53	501.32	494.65	491.41	480.38	481.53
$\gamma_{4,1}$ (cm ⁻¹)	286.4	321.43	352.42	367.86	385.52	410.35

of the overall shape of the self-energy function, is consistent with the tendency that is expected. The peak amplitude of the corresponding dielectric constant (figure 4) decreases by 82% when the temperature increases from 22 to 500 °C. Simultaneously, the resonance corresponding to the maximum of $\text{Im}[\varepsilon(\omega)]$ shifts from 260 to 240 cm⁻¹.

Table 3. Parameters of the semi-quantum model used to fit the thermal infrared spectra of Al₂O₃.

	Temperature (°C)					
	22	100	200	300	400	500
ε_∞	3.03	3.013	3.03	2.98	3.019	3.019
S_1	0.42	0.47	0.41	0.49	0.47	0.44
Ω_1 (cm ⁻¹)	373.86	371	370	359.67	351.66	350.6
$A_{1,1}$ (cm ⁻¹)	24.41	28.45	26.06	47.79	67.54	62.47
$\omega_{1,1}^0$ (cm ⁻¹)	199.33	204.6	219.02	219.02	208.88	215.22
$\gamma_{1,1}$ (cm ⁻¹)	248.99	241.5	229.88	203.74	200.32	196.77
S_2	2.73	2.74	2.63	2.53	2.45	2.41
Ω_2 (cm ⁻¹)	439.71	436.34	435.06	432.09	429.92	427.39
$A_{1,2}$ (cm ⁻¹)	5.68	7.87	7.86	8.86	9.49	10.3
$\omega_{1,2}^0$ (cm ⁻¹)	423.58	419.54	416	413.48	409.06	403.75
$\gamma_{1,2}$ (cm ⁻¹)	38.51	45.62	59.5	65.28	77.7	93.32
S_3	2.87	2.81	2.87	2.81	2.83	2.82
Ω_3 (cm ⁻¹)	580.42	582.2	582.98	578.97	581.61	582.95
$A_{1,3}$ (cm ⁻¹)	1.43	5	11.48	23.67	28.36	29.86
$\omega_{1,3}^0$ (cm ⁻¹)	371.13	371.61	307.94	354.27	362.12	347.12
$\gamma_{1,3}$ (cm ⁻¹)	190.22	200.24	237.29	192.02	198.47	206.02
$A_{2,3}$ (cm ⁻¹)	10.12	9.12	7.86	8.09	5.63	4.75
$\omega_{2,3}^0$ (cm ⁻¹)	536.83	534.45	526.44	534.32	537.77	526.56
$\gamma_{2,3}$ (cm ⁻¹)	117.73	108.42	118.29	93.84	79.03	79.42
$A_{3,3}$ (cm ⁻¹)	15.56	19.17	20.42	25.5	27.59	30
$\omega_{3,3}^0$ (cm ⁻¹)	914.59	912.06	878.14	839.97	815.08	805.6
$\gamma_{3,3}$ (cm ⁻¹)	333.25	414.24	418.35	369.58	366.08	362.4
$A_{4,3}$ (cm ⁻¹)	6.13	6.29	8.99	9.36	15.55	17.81
$\omega_{4,3}^0$ (cm ⁻¹)	1299.6	1353.68	1298.6	1333.72	1301.19	1294.23
$\gamma_{4,3}$ (cm ⁻¹)	895.54	953.88	947.96	996.79	927.75	997.607
S_4	0.15	0.15	0.138	0.15	0.17	0.175
Ω_4 (cm ⁻¹)	638.35	636.59	633.87	628.1	618.72	610.88
$A_{1,4}$ (cm ⁻¹)	6.77	6.98	7.19	8.78	15.72	22.99
$\omega_{1,4}^0$ (cm ⁻¹)	640.36	638.2	634.9	619.7	565.2	506.43
$\gamma_{1,4}$ (cm ⁻¹)	30.03	34.07	35.79	84.38	159.506	233.39

For BaF₂ (figure 2), the fits also involve a single anharmonic phonon term and a self-energy structure to take care of the multiphonon processes. The evolution of the fitting parameters is here clearly monotonic with temperature. The amplitude of the corresponding dielectric constant (figure 5) decreases by 16% when the temperature increases from 22 to 500 °C and the resonance shifts from 185 to 171 cm⁻¹.

For Al₂O₃ (see figure 3), the fit involves four phonon terms, all with their own self-energy functions, but only a single resonance (called S_3 in table 3) exhibits a complex self-energy structure. The amplitude of the corresponding dielectric constant for the main peak decreases by 4.5% when the temperature increases from 22 to 500 °C and the resonance shifts from 443 to 432 cm⁻¹ (figure 6).

5. Predictions for the $C_3(T)$ van der Waals coefficient for the interaction between Cs(8P_{1/2}) and a fluoride window

The long-range atom–surface van der Waals (vW) interaction is a dipole–dipole interaction between the quantum dipole fluctuations of an atom and its electric image induced in the

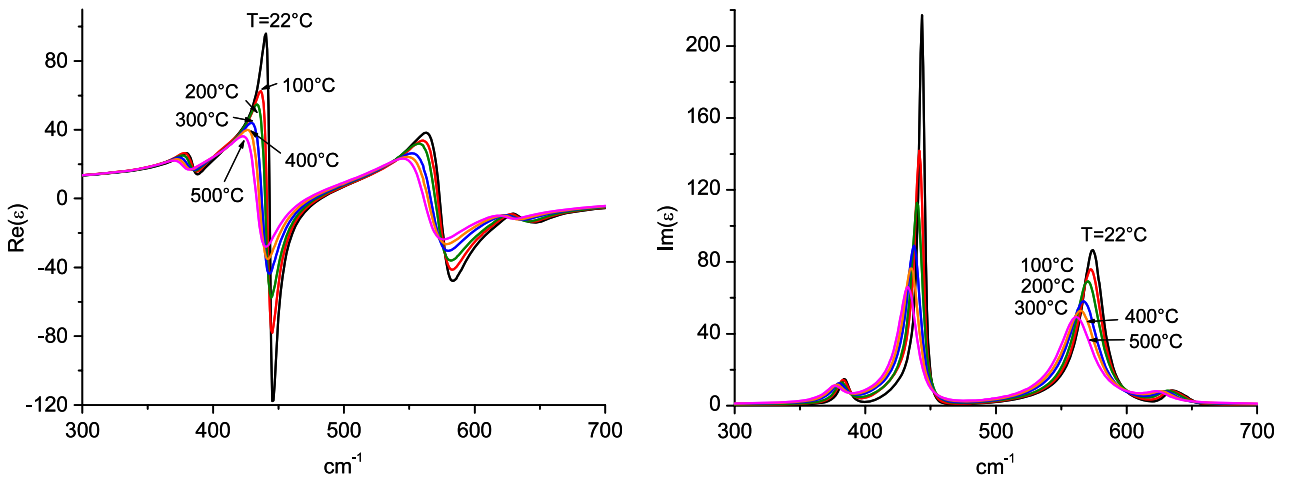


Figure 6. Dielectric constant of Al_2O_3 (real and imaginary parts) for sample temperatures between 22 and 500 °C.

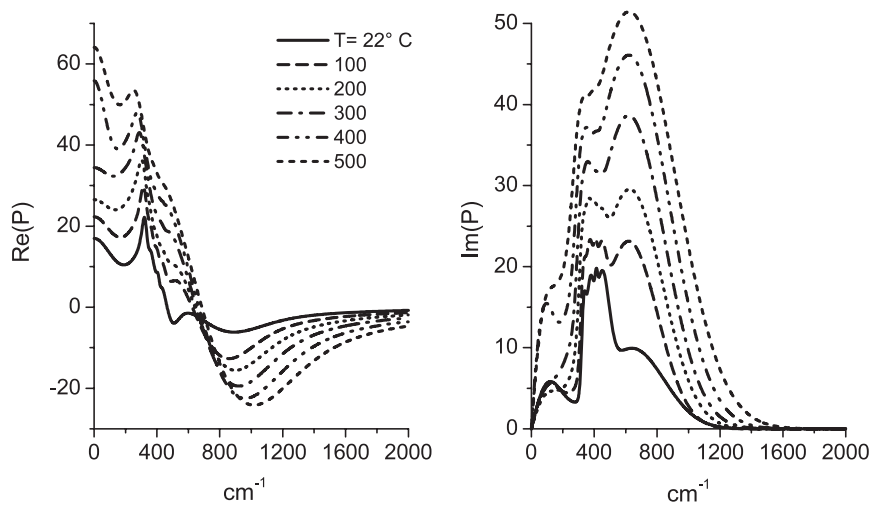


Figure 7. Self-energy $P(\omega)$ (real and imaginary parts) of CaF_2 for sample temperatures between 22 and 500 °C.

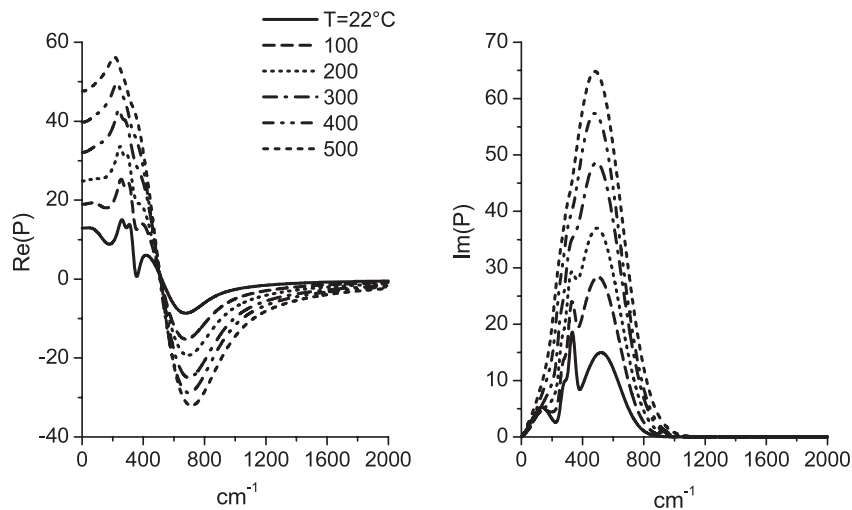


Figure 8. Self-energy $P(\omega)$ (real and imaginary parts) of BaF_2 for sample temperatures between 22 and 500 °C.

surface, so that an atom is submitted to a potential $V(z) = -C_3z^{-3}$, with z the atom–surface separation and C_3 the coefficient of the van der Waals (vW) interaction (i.e. attraction

as long as $C_3 > 0$). The C_3 coefficient is known (for a review, see [21]) to depend notably upon the virtual transitions connecting the atomic level of interest, and upon the surface

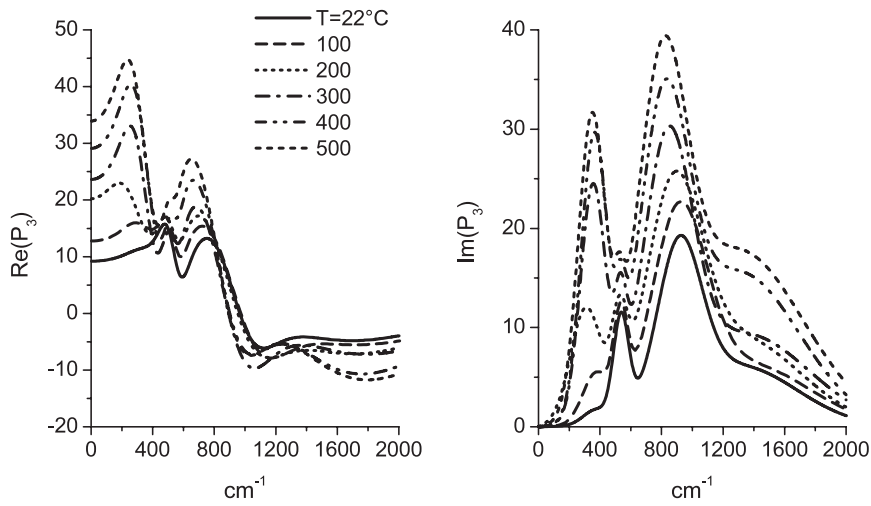


Figure 9. Self-energy $P_3(\omega)$ (real and imaginary parts) of Al_2O_3 (for S_3 resonance only, see table 3) for sample temperatures between 22 and 500 °C.

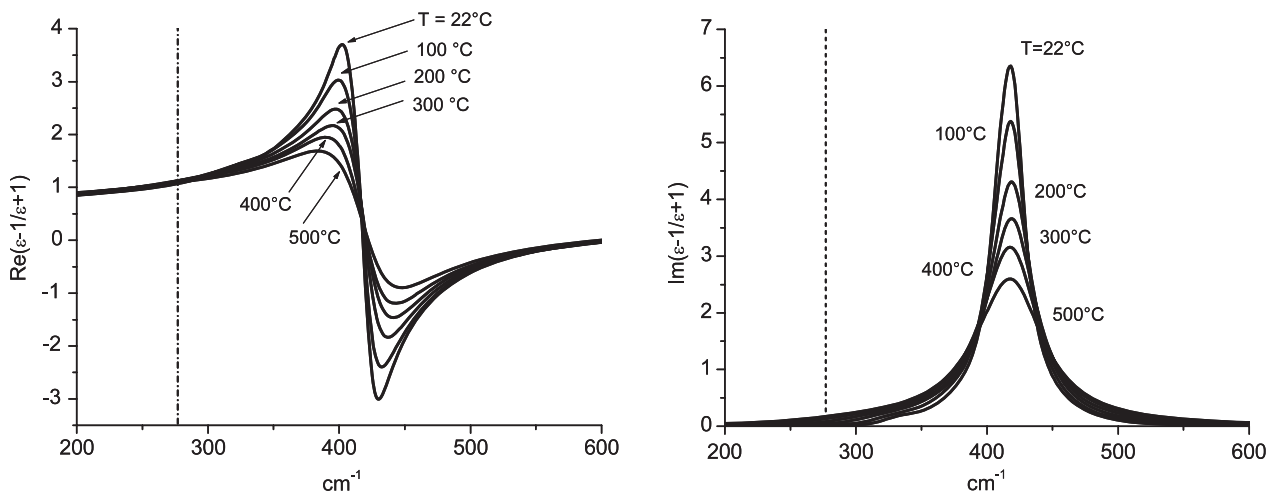


Figure 10. Surface response function $S(\omega)$ of CaF_2 (real and imaginary parts) for sample temperatures between 22 and 500 °C. The virtual atomic absorption of the Cs transition $8P_{3/2} \rightarrow 7D_{3/2}$ is indicated by a vertical dashed line at 277.8 cm^{-1} .

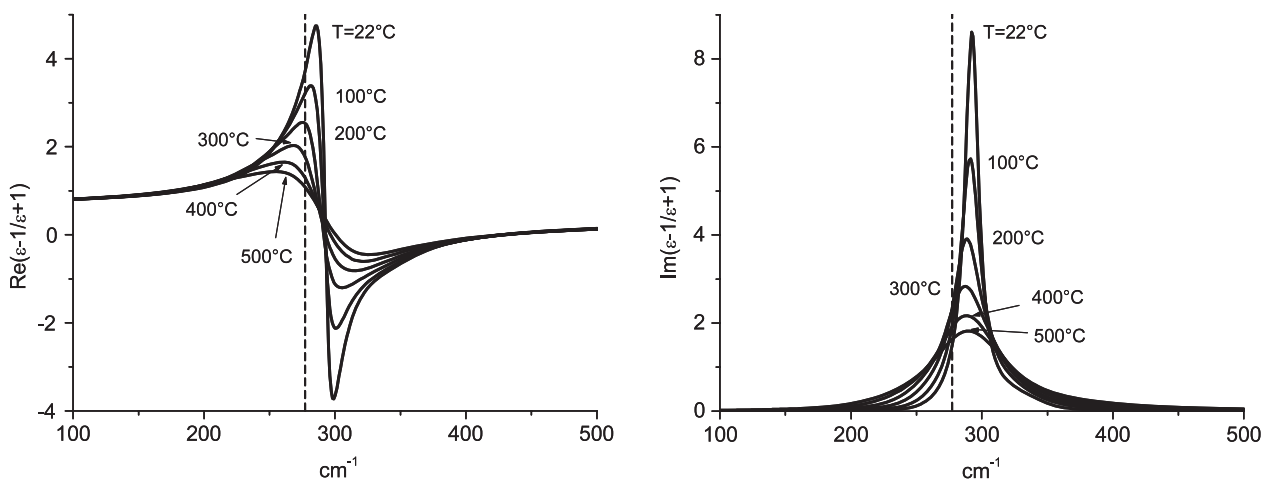


Figure 11. Surface response function $S(\omega)$ of BaF_2 (real and imaginary parts) for sample temperatures between 22 and 500 °C. The virtual atomic absorption of the Cs transition $8P_{3/2} \rightarrow 7D_{3/2}$ is indicated by a vertical dashed line at 277.8 cm^{-1} .

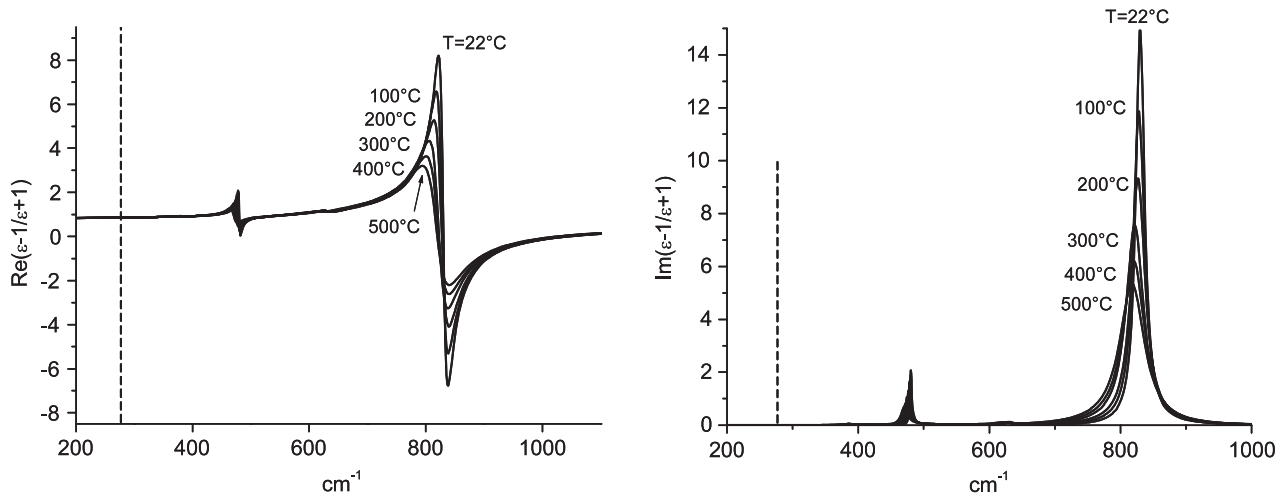


Figure 12. Surface response function $S(\omega)$ of Al_2O_3 (real and imaginary parts) for sample temperatures between 22 and 500 °C. The virtual atomic absorption of the transition $\text{Cs}8\text{P}_{3/2} \rightarrow 7\text{D}_{3/2}$ is indicated by a vertical dashed line at 277.8 cm^{-1} .

resonances, determined from the knowledge of the spectrum of the surface response $S(\omega)$:

$$C_3(|i\rangle) = \sum_j r_{ij}(T) |i\rangle \langle j|^2 \quad (6)$$

with $|i\rangle$ the considered atomic state, D the dipole operator and $r_{ij}(T)$ the dielectric image coefficient. This image coefficient, equal to unity for an ideal electrostatic reflector, depends on the surface response spectrum $S(\omega)$ and on the vacuum temperature.

The theoretical temperature dependence of $r_{ij}(T)$ and hence of $C_3(T)$ was recently analysed in [5] (see notably equations (3.10) and (3.11) of this reference), under the assumption that the temperature of the surrounding vacuum field (i.e. roughly the thermal number of photons) is in equilibrium with that of the dense material. In this approach, the spectrum of the dielectric permittivity is taken as phenomenologically granted. Clearly, to study the evolution over a limited temperature range in [5], and keeping the assumption that the temperature evolution of the vacuum field is relatively decoupled from the details of the spectral modifications of the dense material, the spectrum of dielectric permittivity to be considered should be the one at the relevant temperature.

Below, we apply the results obtained in the preceding sections in order to predict the temperature dependence in the sensitive case of $\text{Cs}(8\text{P}_{3/2})$, and to compare it with alternative predictions resulting from various modelling of the dielectric permittivity. Indeed, the $8\text{P}_{3/2}$ level of Cs, of relatively easy experimental access [6, 14], exhibits major couplings in the thermal infrared range, as recalled in table 4, reproduced from [14]. As already noticed, surface resonances of fluoride materials also fall into the thermal infrared range, so that strong variations of the C_3 coefficient are expected with temperature. In particular, the surface thermal emissivity is susceptible to resonantly couple to a virtual atomic absorption (the frequency position of the most relevant one, at 277.8 cm^{-1} ($\sim 36 \mu\text{m}$), is indicated in figures 10–12), opening up the possibility of a vW repulsion above a certain temperature.

Table 4. Contribution of each virtual transition—with transition wavelengths indicated, a minus sign being used for a virtual emission—to the C_3 coefficient for $\text{Cs}(8\text{P}_{3/2})$, assuming the surface is an ideal reflector [14]. Dominant contributions are printed in bold.

Level (i)	λ (μm)	C_3^i ($\text{kHz } \mu\text{m}^3$)
5D _{3/2}	−0.89	<0.01
5D _{5/2}	−0.89	0.01
6D _{3/2}	−3.12	0.08
6D _{5/2}	−3.16	0.71
7D_{3/2}	39.05	5.32
7D_{5/2}	36.09	37.78
8D _{3/2}	4.95	0.42
8D_{5/2}	4.92	3.70
9D _{3/2}	3.29	0.09
9D _{5/2}	3.28	0.80
10D _{3/2}	2.72	0.03
10D _{5/2}	2.72	0.31
11D _{3/2}	2.44	0.02
11D _{5/2}	2.43	0.16
12D _{3/2}	2.27	0.01
12D _{5/2}	2.27	0.09
6S _{1/2}	−0.39	0.03
7S _{1/2}	−1.38	0.31
8S_{1/2}	−6.78	12.07
9S_{1/2}	8.94	11.63
10S _{1/2}	3.99	0.38
11S _{1/2}	3.00	0.09
12S _{1/2}	2.58	0.04

$$C_3 = \sum_i C_3^i = 73.79 \text{ kHz } \mu\text{m}^3$$

In figures 13–15, we have plotted the predicted C_3 values of $\text{Cs}(8\text{P}_{3/2})$ as a function of temperature. For purposes of comparison, these values are derived from the formulae obtained in [5] (equations (3.10) and (3.11)) applied with various modellings of permittivity or the dielectric window. Note that, because in equations (3.10) and (3.11) of [5], an analytical expansion of the permittivity is required for the nonresonant term—i.e. the permittivity must be defined for an imaginary frequency—we have actually combined, for the model derived from our measurements, the actual resonant contribution and a nonresonant contribution, gently

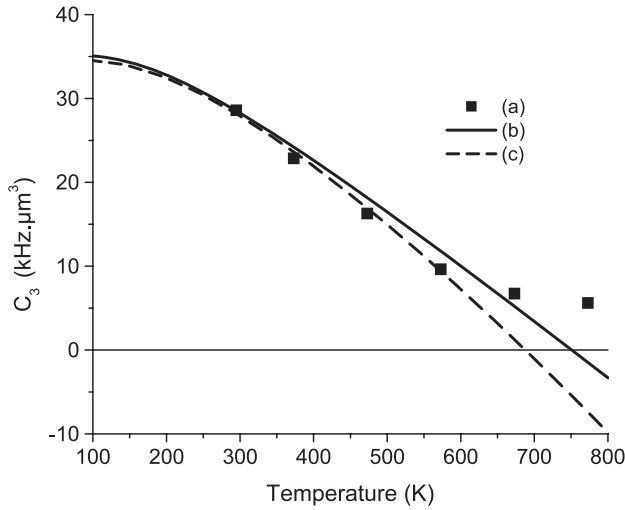


Figure 13. Predicted C_3 vW coefficient for Cs($8P_{3/2}$) in front of a CaF_2 window as a function of temperature: discrete points (a) CaF_2 permittivity according to the fitting of our temperature-dependent experimental results; curve (b) CaF_2 permittivity according to the room-temperature measurements of [7]; curve (c) CaF_2 permittivity including linear temperature corrections (extrapolated from [8]) to the room-temperature measurements of [7].

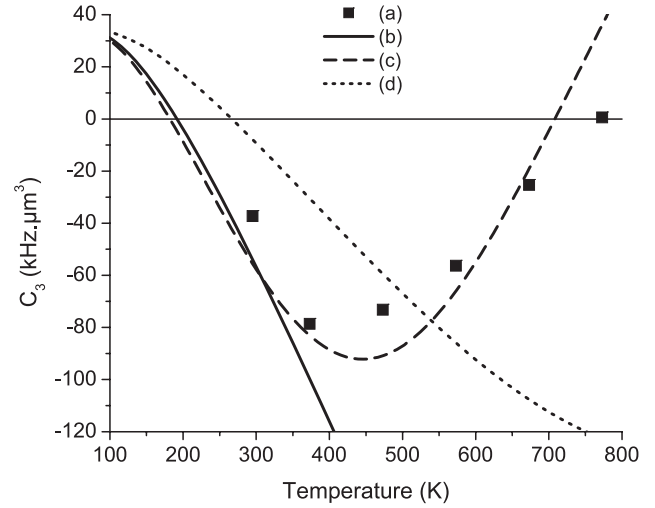


Figure 14. Predicted C_3 vW coefficient for Cs($8P_{3/2}$) in front of a BaF_2 window as a function of temperature; discrete points (a) BaF_2 permittivity according to the fitting of our temperature-dependent experimental results; curve (b) BaF_2 permittivity according to the room-temperature measurements of [7]; curve (c) BaF_2 permittivity including linear temperature corrections (extrapolated from [8]) to the room-temperature measurements of [7]; curve (d) BaF_2 permittivity including linear temperature corrections (extrapolated from [8]) to the room-temperature measurements of [8].

evolving with temperature, estimated from an elementary classical model for the material: indeed, it is only for the knowledge of the resonant term that an accurate estimate of the permittivity is needed. This comparison includes: (i) the temperature dependence solely resulting from the temperature dependence of the vacuum, the dielectric medium properties being those found (in our experiments) at room temperature; (ii) the discrete evaluations of the C_3 values resulting from our measurements of reflectivity, performed for a discrete set of temperatures and (iii) temperature-linearized models. About this last type of modelling, it is justified in current models in the literature to assume that all temperature dependence of optical parameters of a given material can be linearized [19], once the optical properties of the material were determined for two temperatures. This approach is based on an extended form of the classical oscillator model (cf equation (2)) assuming

$$\varepsilon(\omega, T) = \varepsilon_\infty + \sum_j \frac{S_j(T)\Omega_j^2(T)}{\Omega_j^2(T) - \omega^2 - i\gamma_j(T)\omega} \quad (7)$$

with the temperature dependence of the transverse optical wavenumber Ω_j , of the dielectric strengths, S_j , and of the damping of the j th phonon, linearized in the following form:

$$\begin{aligned} \Omega_j(T) &= \Omega_j(T_0) + a_j[T - T_0] \\ S_j(T) &= S_j(T_0) + b_j[T - T_0] \\ \frac{\gamma_j}{\Omega_j}(T) &= \frac{\gamma_j}{\Omega_j}(T_0) + c_j[T - T_0] \end{aligned} \quad (8)$$

with T_0 a reference temperature, and a_j, b_j and c_j being constant coefficients.

In this modelling, the high-frequency limiting value of the dielectric constant, ε_∞ , also exhibits a linear temperature

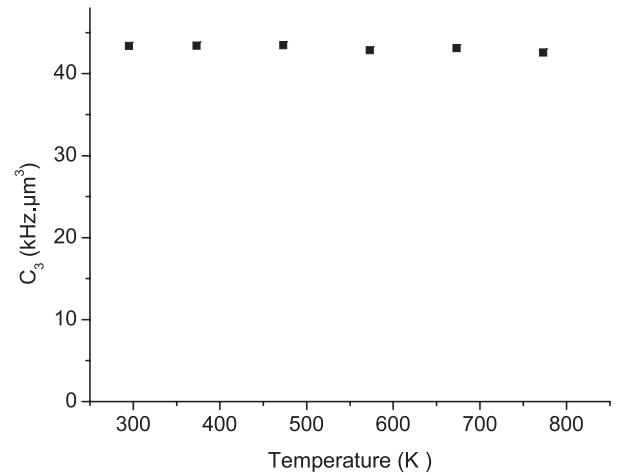


Figure 15. Predicted C_3 vW coefficient for Cs($8P_{3/2}$) in front of a Al_2O_3 window as a function of temperature: the Al_2O_3 permittivity is according to the fitting of our temperature-dependent experimental results.

dependence:

$$\varepsilon_\infty(T) = \varepsilon_\infty(T_0) + e[T - T_0] \quad (9)$$

where e is a constant coefficient.

We extrapolate coefficients for linearized temperature dependence from the results of Denham *et al* [8], who measured fluoride crystals' dielectric permittivity at two cold temperatures (100 and ~ 300 K) and we find (taking $T_0 = 300$ K)

$$\begin{aligned} \text{for } \text{CaF}_2 : \quad a_1 &= -0.03 \text{ cm}^{-1} \text{ K}^{-1}; \\ a_2 &= -0.03 \text{ cm}^{-1} \text{ K}^{-1}; \quad b_1 = 0.00063 \text{ K}^{-1}; \end{aligned}$$

$$b_2 = 0 \text{ K}^{-1}; \quad c_1 = 0.0001 \text{ K}^{-1}; \\ c_2 = 0.00025 \text{ K}^{-1}; \quad e = -0.00003 \text{ K}^{-1}.$$

and for BaF₂ :

$$a_1 = -0.02 \text{ cm}^{-1} \text{ K}^{-1}; \\ a_2 = -0.035 \text{ cm}^{-1} \text{ K}^{-1}; \quad b_1 = 0.0004 \text{ K}^{-1}; \\ b_2 = 0.00013 \text{ K}^{-1}; \quad c_1 = 0.0002 \text{ K}^{-1}; \\ c_2 = 0.0005 \text{ K}^{-1}; \quad e = -0.000045 \text{ K}^{-1}.$$

Note that in the modelling of [8]—as in [7]—two phonons are actually obtained, the second phonon with a contribution ten times smaller than the first one, because the multiphonon processes through a self-energy are not considered. Although the experimental results at room temperature in [8] slightly differ from those obtained both in [7] and in our experiments, it can be reasonably assumed that the systematic uncertainties or errors in [8] affect only marginally the extrapolated temperature dependence, so that this linearized temperature behaviour can be applied without inconsistency to the measurements of [7] or [19].

As shown in figure 10, for CaF₂, the atomic transition ($8P_{3/2}-7D_{3/2}$) on which the most sensitive temperature effects are expected is located on a wing of the complex response function. This explains that, in figure 13, the temperature behaviour of C_3 is relatively insensitive to the detailed modelling of the CaF₂ response. However, one notes that at the highest temperatures for which we have studied CaF₂, we are not able to predict whether the vW interaction turns out to be repulsive, while this would be a major practical conclusion to be derived in view of the current experiments for CaF₂.

For BaF₂, the atomic transition ($8P_{3/2}-7D_{3/2}$) falls in closer resonance with the surface response (figure 11), so that the effects with temperature on the van der Waals coefficients should be very important. Indeed, predictions for the temperature dependence of C_3 radically differ according to the modelling of the BaF₂ response (figure 14). It is clear in particular that the basic model of temperature effects for the vW interaction, although able to predict the fundamental feature of a strong temperature dependence connected to the resonant coupling between the atomic absorption and the thermal emissivity, is far from being sufficient as long as quantitative data are expected. In the refined models for which the temperature dependence of the material properties is also considered, the temperature behaviour for C_3 exhibits strong nonlinear variations: this is because the general effect of broadening of the BaF₂ surface resonance with increasing temperature is susceptible to be enhanced, or counteracted, by the shift of the resonance.

At last, for our ‘reference’ material Al₂O₃, for which the atomic transitions falling in the thermal infrared ($8P_{3/2}-7D_{3/2}$) are out of resonance of the complex response function S (figure 12), the predicted variation of the C_3 coefficient remains marginal (figure 15) in our considered temperature range. The real and imaginary parts at this atomic frequency do not change when the temperature increases.

6. Conclusion

Although fluoride materials are usually considered to be simple and well-known materials, it appears that a precise

and consistent fitting of reproducible data require an elaborate procedure. These details, often of a minor importance in most of the applications, can actually lead to dramatic effects when the sharp selectivity of Atomic Physics resonance are considered. Our precise study of temperature dependence should provide a basis for a refined comparison between the theory, and the results of an experiment in progress.

Acknowledgment

The Paris 13 team acknowledges partial support by INTAS South-Caucasus Project (grant 06-1000017-9001).

References

- [1] Failache H, Saltiel S, Fichet M, Bloch D and Ducloy M 2003 Resonant coupling in the van der Waals interaction between an excited alkali atom and a dielectric surface: an experimental study via stepwise selective reflection spectroscopy *Eur. Phys. J. D* **23** 237–55
See also Fichet M, Schuller F, Bloch D and Ducloy M 1995 van der Waals interactions between excited states and dispersive dielectric surfaces *Phys. Rev. A* **51** 1553
- [2] Saltiel S, Bloch D and Ducloy M 2006 A tabulation and critical analysis of the wavelength dependent dielectric image coefficient for the interaction exerted by the surface onto a neighbouring excited atom *Opt. Commun.* **265** 220
- [3] See e.g. and refs therein Joulain K, Mulet J-P, Marquier F, Carminati R and Greffet J-J 2005 Surface electromagnetic waves thermally excited: radiative heat transfer, coherence properties and Casimir forces revisited in the near field *Surf. Sci. Rep.* **57** 59–112
- [4] Dutier G, Hamdi I, Chaves de Souza Segundo P, Yarovitski A, Saltiel S, Sarkisyan D, Papoyan A, Varzhapetyan T, Gorza M-P, Fichet M, Bloch D and Ducloy M 2004 *Coupling of Atoms, Surfaces and Fields in Dielectric Nanocavities Proc. 16th Int. Conf. on Laser Spectroscopy* ed P Hannaford *et al* (Singapore: World Scientific) pp 277–84
- [5] Gorza M-P and Ducloy M 2006 van der Waals interactions between atoms and dispersive surfaces at finite temperature *Eur. Phys. J. D* **40** 343–56
- [6] Passerat de Silans T, Lalotias A, Romanelli M, Chaves de Souza Segundo P, Maurin I, Bloch D, Ducloy M, Sarkisyan A and Sarkisyan D 2007 Selective reflection spectroscopy of a vapour at a calcium fluoride interface *Ann. Phys. Fr.* **32** 191–4
- [7] Kaiser W, Spitzer W G, Kaiser R H and Howarth I E 1962 Infrared properties of CaF₂, SrF₂ and BaF₂ *Phys. Rev.* **127** 1950–4
- [8] Denham P, Field G R, Morse P L R and Wilkinson G R 1970 Optical and dielectric properties and lattice dynamics of some fluorite structure ionic crystals *Proc. R. Soc. A* **317** 55–77
- [9] Bezuidehout D F 1991 Calcium fluoride (CaF₂) *Handbook of Optical Constants of Solids II* ed E D Palik (San Diego, CA: Elsevier Academic) pp 815–35
- [10] Andersson S K, Thomas M E and Hoffman C 1998 Multiphonon contribution to the reststrahlen band of BaF₂ *Infrared Phys. Technol.* **39** 47–54
- [11] Thomas M 1998 Barium fluoride (BaF₂) *Handbook of Optical Constants of Solids III* ed E D Palik (San Diego, CA: Elsevier Academic) pp 683–99
- [12] Gervais F and Piriou B 1974 Anharmonicity in several-polar-mode crystals: adjusting phonon self-energy of LO and TO modes in Al₂O₃ and TiO₂ to infrared reflectivity *J. Phys. C: Solid State Phys.* **7** 2374–86

- [13] Gervais F 1983 High-temperature infrared reflectivity spectroscopy by scanning interferometry *Infrared and Millimeter Waves: Electromagnetics Waves* vol 8 (New York: Academic) pp 279–339
- [14] Chaves de Souza Segundo P, Hamdi I, Fichet M, Bloch D and Ducloy M 2007 Selective reflection spectroscopy on the UV third-resonance line of Cs: simultaneous probing of a van der Waals atom–surface interaction sensitive to far IR couplings and interatomic collisions *Laser Phys.* **17** 983–92
- [15] De Sousa Meneses D, Brun J F, Echegut P and Simon P 2004 Contribution of semi-quantum dielectric function models to the analysis of infrared spectra *Appl. Spectrosc.* **58** 969–74
- [16] Puchkov A V, Basov D N and Timusk T 1996 High T_c superconductors: an infrared study *J. Phys.: Condens. Matter* **8** 10049
- [17] Focus web site <http://crmht.cnrs-orleans.fr/pot/software/focus.html>
- [18] Tropf W J and Thomas M E 1998 Aluminium oxide (Al_2O_3) *Handbook of Optical constants of solids III* ed E D Palik (San Diego, CA: Elsevier Academic) pp 653–82
- [19] Thomas M 1991 Temperature dependence of the complex index of refraction *Handbook of Optical constants of solids II* ed E D Palik (San Diego, CA: Elsevier Academic) pp 177–201
- [20] Kroumova E, Aroyo M I, Perez-Mato J M, Kirov A, Capillas C, Ivantchev S and Wondratschek H 2003 Bilbao crystallographic server: useful databases and tools for phase-transition studies *Phase Transit.* **76** 155–70
See also Ganesan S and Burstein E 1965 Selection rules for second order infrared and Raman processes II. Fluorite structure and the interpretation of second order infrared and Raman spectra of CaF_2 *J. Physique* **6** 645–8
- [21] Bloch D and Ducloy M 2005 Atom–wall interaction *Advances in Atomic, Molecular and Optical Physics* vol 50 ed B Bederson and H Walther (San Diego, CA: Elsevier Academic) pp 91–156

A. LALLOTIS¹
I. MAURIN¹
M. FICHET¹
D. BLOCH^{1,✉}
M. DUCLOY¹
N. BALASANYAN²
A. SARKISYAN²
D. SARKISYAN²

Selective reflection spectroscopy at the interface between a calcium fluoride window and Cs vapour

¹ Laboratoire de Physique des Lasers, UMR 7538 du CNRS, Université Paris 13, 93430 Villetaneuse, France
² Institute for Physical Research, NAS of Armenia, Ashtarak 2, Armenia

Received: 16 October 2007

Published online: 8 February 2008 • © Springer-Verlag 2008

ABSTRACT A special vapour cell has been built, that allows the measurement of the atom–surface van der Waals interaction exerted by a CaF₂ window at the interface with Cs vapour. Mechanical and thermal fragility of fluoride windows make common designs of vapour cells impractical, so that we have developed an all-sapphire sealed cell with an internal CaF₂ window. Although some impurities have remained when filling up the prototype cell, leading to line broadening and a shift, the selective reflection spectrum of the Cs *D*₁ line (894 nm) makes apparent the weak van der Waals surface interaction. The uncertainties introduced by the effects of these impurities in the van der Waals measurement are nearly eliminated when comparing the selective reflection signal at the CaF₂ interface of interest and at a sapphire window of the same cell. The ratio of the interactions respectively exerted by a sapphire interface and a CaF₂ interface is found to be 0.55 ± 0.25 , in good agreement with the theoretical evaluation of ~ 0.67 .

PACS 34.35.+a; 42.62.Fi; 42.70.Km

1 Introduction

The long-range van der Waals (vW) atom–surface attraction [1] tackles various fundamental problems, and imposes various constraints in the development of nanotechnologies, like the deposition of atoms in nanolithography. With regard to its universality and to the possibilities to achieve exotic situations [2–5], the experimental investigations have remained relatively limited and, in particular, the list of materials submitted to experimental investigation has remained short. Most of the experiments have employed an optical detection, hence requiring transparency of the surface (occasionally, a thin metal film provides a sufficient transparency [1, 6]). To investigate these vW effects, we have developed for a long time selective reflection (SR) spectroscopy at a vapour interface [1–3, 7–10], a technique that typically probes the vapour at the interface on a depth $\lambda/2\pi$, with λ the optical irradiation wavelength, and more recently extended it to spectroscopy in a vapour nanocell [11]. Materials were limited to glass (fused silica), sapphire and YAG (for

nanocells, to YAG and sapphire only). Alternate measurements were performed with cold atoms, at a glass interface or at an interface of a glass piece coated with a thin layer (see e.g. [11] for references). Extending the number of materials for the measurement of the vW interaction is of interest, especially when exotic effects such as vW repulsion [2, 3] occur for specific interfaces [2–5, 12].

A particular interest of fluoride crystals is that their surface resonances are located in the thermal infrared range. This makes them good candidates to investigate how the thermal emissivity of the surface influences the vW interaction exerted onto a resonantly absorbing atom: it is indeed expected that thermally populated surface polariton modes will virtually exchange energy with the neighbouring energy levels, so that a temperature-controlled resonant enhancement of the atom–surface interaction will occur, leading to a giant attraction or a possible repulsion [4, 5, 12]. To implement the corresponding SR experiments, that require both a relatively dense (hot) vapour of alkali (Cs in our case) and hot windows of a controllable temperature, a specially designed vapour cell must be built up. Indeed, fluoride materials are mechanically fragile and exhibit a large thermal expansion coefficient, making impractical most of the standard designs for glass or sapphire cells. In the present work, a prototype Cs vapour cell with a CaF₂ window was constructed (Sect. 2). A SR experiment on the *D*₁ resonance line (894 nm) was implemented (Sect. 3), in order to test the cell via the evaluation (Sect. 4) of the vW atom–surface interaction. Impurities having remained in the evacuation/filling up of the cell make the measurement more complex, but we show that the vW interaction exerted by the CaF₂ window can be reliably compared to the one exerted by a sapphire interface when recording and fitting simultaneously the two spectra.

2 Design of a cell with a CaF₂ window

The vapour cell must obey the following requirements: it must be resistant to a high temperature (to warrant a sufficient density of Cs and for future experiments involving thermal emissivity), it must be evacuated to avoid unwanted collision broadening and shift and it has to be compatible with a CaF₂ window. We discuss below the available technologies before describing our cell.

✉ Fax: +33-1 4940 3390, E-mail: bloch@lpl.univ-paris13.fr

The current technology with glass blowing allows the convenient build up of sealed glass cells, resistant to a hot Cs vapour up to $\sim 200^\circ\text{C}$, but it cannot be extended to the sealing of special crystalline windows. Sealed cells with a metallic housing and various windows such as sapphire or even fluoride windows can be prepared with commercial systems of windows soldered to a metallic mount; however, it is advised for the metal/window region not to exceed a maximal temperature of $\sim 200^\circ\text{C}$. Alternatively, a metallic housing cell, with windows mechanically held by metal (copper) rings, is conceivable for a system under permanent evacuation but this makes it difficult to monitor the vapour pressure. Such a design, operative with materials of a sufficient mechanical resistance, is at a high risk with fragile fluoride windows.

All-sapphire cells [13] can be realized with a special mineral glue connecting a sapphire tube and sapphire windows, the cell being sealed after evacuation and introduction of the alkali metal. Such cells are resistant to very high temperature (up to $\sim 1000^\circ\text{C}$ with an appropriate cell design). Although sapphire windows can easily be replaced by non-birefringent YAG windows, such a replacement is not permitted for fluoride materials due to their mechanical fragility and to very different thermal expansion coefficients. In a similar manner, the mineral gluing technology cannot be extended to an all-fluoride cell.

This led us to design our special cell on the basis of an all-sapphire sealed cell, with a fluoride window inserted inside the tubing, mechanically maintained close to one of the windows. An issue for the observation of a SR signal at the CaF_2 interface is to make negligible the absorption in this interstitial region.

The cell (Fig. 1) has a T-shaped geometry, in order to allow for an independent control of the vapour density (through the temperature of the alkali-metal reservoir) and of the temperature of the window (controlled through the temperature of the cell body). It has two opposite windows, one of which is of YAG, and the other one of sapphire ($\perp c$ axis, to avoid birefringence). The CaF_2 window consists of a long (~ 7 cm in our prototype cell) cylindrical piece. This allows the CaF_2

tube to accommodate a temperature gradient: the YAG window is maintained at room temperature outside the oven, so that the corresponding extremity of the CaF_2 tube remains cold, while the other extremity of the CaF_2 tube reaches an adjustable temperature (up to $\sim 350^\circ\text{C}$) (Fig. 1). This makes the free space between the CaF_2 window and the YAG window non-critical: indeed, at room temperature, the very low alkali-metal vapour density yields negligible effects on the transmission (conversely, in the absence of a temperature gradient, the SR signal at the CaF_2 interface is contaminated by the transmission signal of the interstitial volume for separation distances as short as 100 nm). To reduce still further this vapour density, and to avoid Cs condensation in the interstitial region, a cooled ($\sim 5^\circ\text{C}$) metal ring is usually set around the sapphire tubing.

As shown in Fig. 1, the oven has a complex structure and is made of independent sections; each of them contains heating wires (structured in doubled coils to minimize the induced magnetic field). These wires are surrounded by thermally isolating bricks of alumina powder. Note that, as usual in the construction of a T-shaped all-sapphire cell, a convenient filling up of the cell reservoir imposes the bottom part of the reservoir to be of glass (and hence at $T < 200^\circ\text{C}$) but the Cs density is governed by the temperature of the upper free surface, i.e. the temperature of the oven T_{res} . Also, the T-shape of the cell divides the heating wires in the top part of the oven (T_{windows}) into two independent subsections. This is the reason for a temperature gradient inside the top part of the oven (the temperature of the top part is monitored through two thermal probes located close to the two respective windows), that can be suppressed if sending independent currents in the heating wires, or if specifically adjusting the lengths of the wires. In view of experiments where the surface temperature could be varied while keeping constant the Cs density (in principle governed by the temperature in the Cs reservoir), the independence of the top and bottom sections of the oven was also tested. An adjustable temperature difference of $30\text{--}120^\circ\text{C}$ is currently obtained for the bottom part at $150\text{--}200^\circ\text{C}$ (we operate at a minimal $\sim 30^\circ\text{C}$ nominal difference because of the uncertainty in the temperature measurement). With an improved isolation between the oven sections, it should not be difficult to increase this relative independence to a larger scale, and the upper limit in temperature is essentially a matter of the outgassing conditions.

Although we could not find any data on the chemical resistance of fluoride windows to hot alkali vapour, and in spite of the possibility of a migration of fluorine atoms from heated fluoride materials, no special problems have been detected when repeatedly heating the cell up to $\sim 350^\circ\text{C}$. Unfortunately, although a standard procedure was used for the cell outgassing, but maybe at a too limited temperature (350°C , 10 h), some impurities were found in the only cell prototype available for a long duration. These impurities are responsible for a major (collision) broadening of the saturated absorption (SA) signal observed on the D_1 line of Cs (894 nm), turning it into a Doppler-broadened signal instead of a Doppler-free one. The expected sub-Doppler signal, that is nevertheless tiny and appears on a broad background (Fig. 2), is recovered only with a fast modulation [14, 15], that minors the influence of velocity-changing collision processes. As shown

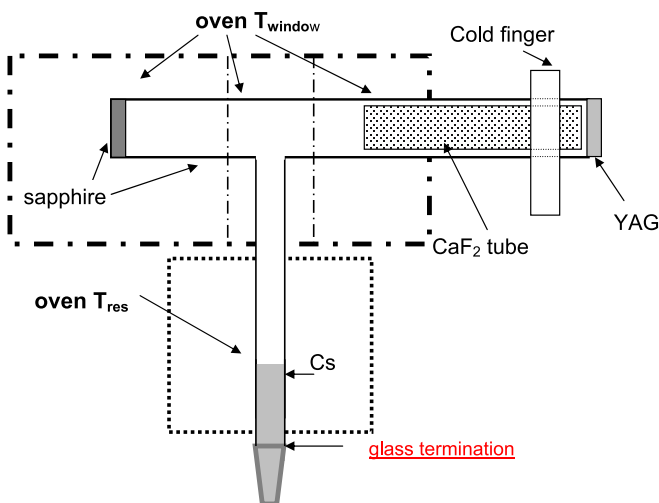


FIGURE 1 Scheme of the Cs vapour cell. In the top oven, the heating source is located in the left- and right-hand parts surrounding the connection to the Cs reservoir

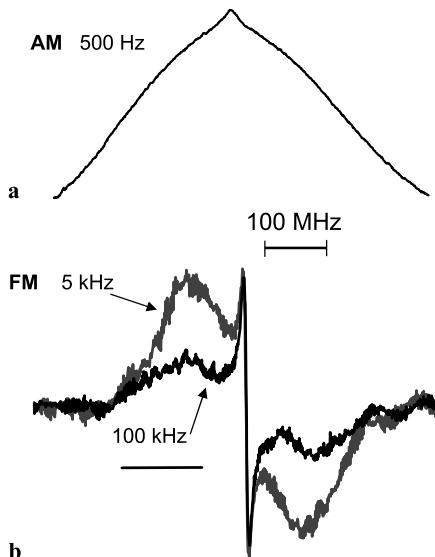


FIGURE 2 Saturated absorption (SA) spectrum recorded on the prototype cell with impurities. (a) AM (500 Hz) applied to the pump signal; (b) in FM, the sub-Doppler signal emerges more clearly from the broad background for a fast FM

below, these impurities have a less dramatic effect in SR spectroscopy.

3 Experimental set-up and main spectroscopic features

The smaller sensitivity of SR spectroscopy to impurities, as compared to the SA technique, originates in its linear nature, and its fast response time governed by the atomic dipole lifetime (on the contrary, the SA efficiency depends on the long lifetime of the induced change in population that follows a photon absorption, and impurities strongly affect this duration). However, one still clearly observes a residual broadening in our SR experiments.

Several SR spectroscopy experiments were already performed on the Cs resonance lines, allowing the vW interaction to be measured. The present one, schematized in Fig. 3, does not differ essentially from these previous experiments. Rather, a double SR set-up has been implemented in order to monitor simultaneously the SR spectrum at the CaF₂ interface and at the opposite sapphire window. The laser is here a tuneable narrow-line-width distributed Bragg reflector (DBR) laser at 894 nm, and its frequency scan linearity is monitored by analysing the transmission through a low-finesse very stable Fabry–Pérot (FP) cavity. The laser is also frequency modulated (FM), in order to obtain purely Doppler-free SR spectra [16] through demodulation of the reflected beam. A frequency marker for the atomic resonances in volume is usually required for the analysis of the vW interaction in the SR spectrum: this is why a simultaneous SA experiment is implemented in an auxiliary cell, with an amplitude modulation (AM) applied to the pump beam. Note that to compare the atomic resonances in volume, and close to the surface, the pressure conditions should be the same as in the SR cell. This is why the tiny and narrow SA signal available in the special cell when the pump undergoes a fast modulation was compared to the SA signal of the auxiliary experiment. The

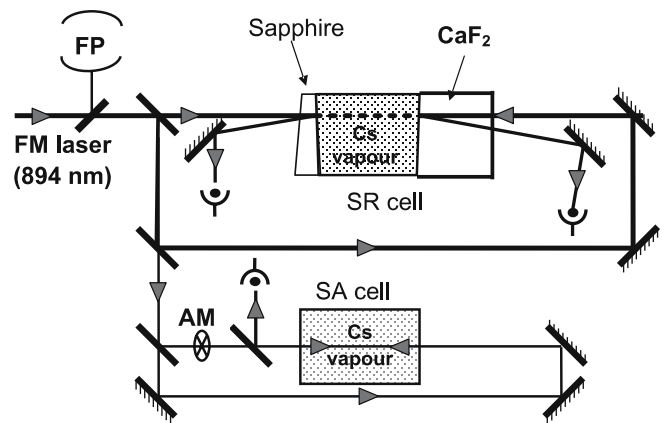


FIGURE 3 Scheme of the experimental set-up

SA signal in the special cell appears red shifted by $\sim -5.2 \pm 0.5$ MHz for all hyperfine structure (h.f.s.) components (experiments performed at room temperature, so that the pressure shift induced by Cs–Cs collisions is entirely negligible).

To evaluate the possible competitive presence of a spectroscopic signal originating in the thin interstitial region between the CaF₂ window and the YAG window, we have attempted to measure the (FM) signal reflected by the CaF₂–YAG interface. The SR signal, typically integrating the atomic response over $\lambda/2\pi$, is hence negligible relatively to the Doppler-broadened linear absorption signal resulting from the back and forth propagation through the interstitial region. Comparing this signal with the absorption through the whole cell kept at room temperature (vapour column ~ 8 cm), we extrapolate that the interstitial spacing is on the order of 50 μm (the back and forth absorption in this interstitial region is below 10^{-3} , and is observable only through a large-amplitude FM). This ensures that when recording the SR spectrum with a hot vapour, the signal of the transmission through the interstitial region remains largely negligible: the contribution of the interstitial region is still further reduced by the cooling close to the YAG window and by the FM technique that specifically enhances the narrow signals.

We have recorded the SR spectra of the Cs D_1 line $6S_{1/2}(F = 3, 4) \rightarrow 6P_{1/2}(F' = 3, 4)$ across the four (entirely resolved) h.f.s. components. The signals from the sapphire and from the CaF₂ windows were recorded simultaneously, and for various temperatures of the Cs reservoir. The irradiation intensity is kept low (≤ 0.1 mW/cm²) to ensure the linearity of the SR technique. The temperature of the top part of the cell has no significant influence over the SR signal amplitude. At low temperatures (~ 100 °C), when the Cs self-broadening is negligible, the minimal SR width is found to be on the order of 27 MHz, largely exceeding the natural width of the transition. The SR spectra exhibit a notable asymmetry, along with a red frequency shift, typical of the vW interaction (see Fig. 4). The apparent shift, relatively to the SA frequency marker, varies slightly with the Cs pressure conditions and with the considered h.f.s. components. It is actually much larger than the red shift currently found for the vW interaction, on the order of 2–3 MHz, and hence originates in the residual impurities in the cell, and possibly in a Cs-pressure shift for the higher Cs temperatures. As shown in Sect. 4, it

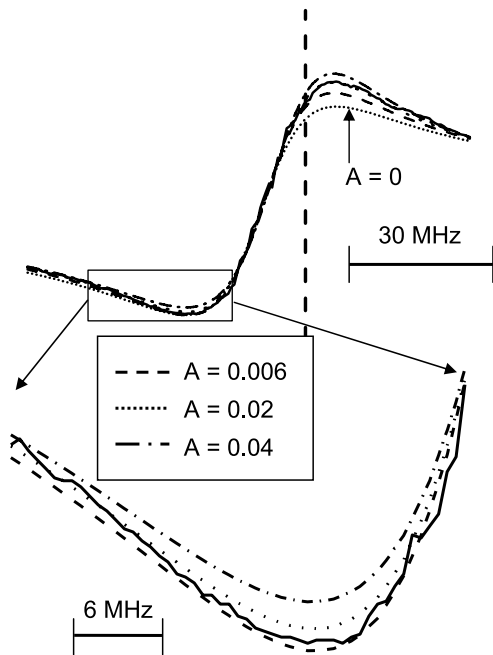


FIGURE 4 An experimental SR spectrum ($T_{Cs} = 140^\circ\text{C}$) recorded on the CaF_2 window. For $A = 0.006$, $A = 0.02$ and $A = 0.04$, the optimal fittings lead to the respective shifts -7.1 MHz, -5.1 MHz and -3.3 MHz, and widths 32.0 MHz, 32.6 MHz and 32.9 MHz. The vertical dashed line is the SA reference. The dotted line is a fit neglecting the vW interaction ($A = 0$). The zoom on the left-hand wing shows that it may not be easy to decide if $A = 0.02$ is better than $A = 0.006$

remains possible to extract an estimate of the vW interaction, although the vW effects are largely hindered by volume collisions effects.

4 Analysis of the vW interaction

The vW interaction simultaneously shifts and distorts (asymmetry) the optical transition. The vW interaction on the D_1 resonance line is known to perturb only weakly the (FM) SR spectrum, and is responsible for an approximate spectral shift not exceeding a few MHz, smaller than the minimal width of the transition (~ 5 MHz in the absence of any collisions). It had however been demonstrated that, even when collisions (buffer gas or self-broadening) impose the dominant broadening, the vW interaction, although of a weaker influence, had to be approximately taken into account to allow for a correct evaluation of the influence of collisions [9]. Here, the novelty is that we aim at evaluating as precisely as possible the vW interaction exerted by the CaF_2 window, or at least to compare it with the one exerted on the sapphire window, in spite of the large impurity broadening.

We recall here the general method for extracting the vW interaction from a (FM) SR spectrum. When the Doppler width largely exceeds the homogeneous optical width, and in the linear regime, (FM) SR experimental line shapes are amenable to dimensionless line shapes [1, 7–10], dependent on a single dimensionless parameter A characterizing the vW interaction ($A = 2C_3k^3/\gamma$, with $k = 2\pi/\lambda$, γ the optical width of the relevant transition [7] and C_3 the coefficient of the spatial dependence of the transition frequency, evolving according to $\omega(z) = \omega_\infty - C_3z^{-3}$, with z the atom–surface dis-

tance). In numerous realistic cases, the finite ratio between the Doppler width (ku , with u the most probable velocity) and the optical width (γ) imposes a slight correction to the dimensionless theoretical line shapes [1], but no additional parameter is introduced as the Doppler width is intrinsically fixed by the experimental conditions. One hence attempts to fit an experimental line shape with theoretical dimensionless line shapes for different A values. The adjustable parameters are the amplitude, width, location of the resonance (when not imposed by the free-space reference) and possibly a vertical offset. C_3 is hence determined from the limited range of A values allowing an acceptable fitting. The consistency of the fittings is usually checked by establishing that a single C_3 value is found in spite of phenomenological changes imposed to the line shapes when varying the pressure (see e.g. [1–3, 8–10]).

In the ‘weak vW regime’ ($A \ll 1$) of our experiments, the optimal fitting width $\gamma(A)$ is nearly independent of the A value, but there is a strong interplay between the location of the resonance (i.e. frequency shift as possibly resulting from collisions) and the A value (Fig. 4). This makes it very difficult to extract unambiguously the VW interaction from a single SR spectrum, notably when the spurious shift originating in the residual impurities is unknown. This is why we have attempted to benefit from the simultaneous recording of the SR signal at the two different interfaces, assuming that the Cs vapour (density and collisions) is homogeneous in the top part of the cell. Hence, only a single parameter for the width, and another one for the shift, are to be adjusted when simultaneously fitting the experiments with sapphire and with CaF_2 . The tighter constraint imposed in the fitting method brings a great help to the consistency of the fittings. In addition, the coupled fitting of two independent signals recorded simultaneously with the same laser eliminates most of the effects related to a possible tiny laser frequency drift.

In our situation, the vW coefficients for CaF_2 and sapphire are expected to differ notably, owing to an approximate $(\epsilon - 1)/(\epsilon + 1)$ dependence [1], yielding a theoretical ratio ~ 0.67 (as predicted from the respective refractive indices of CaF_2 ($n = 1.430$) and sapphire ($n = 1.758$), and $\epsilon = n^2$). Hence, in analysing the data, the objective is to find the optimal range of coefficients (A_1, A_2) characterizing the vW coupling. Figure 5 shows that high-quality fittings of the experimental curves can be obtained in spite of the restricted number of adjustable parameters. Significantly, for each experimental

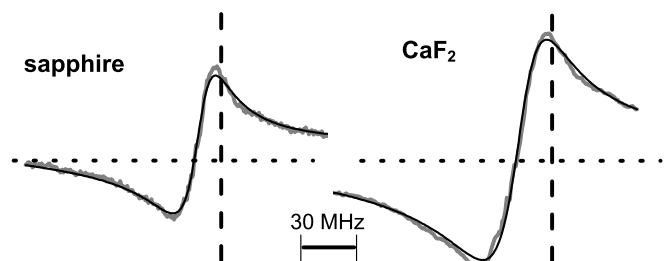


FIGURE 5 Optimal fitting (black) of two simultaneously recorded spectra (grey), under the constraint of a single parameter, for the shift (-4.5 MHz), and respectively for the width (27.8 MHz). One has $T_{Cs} = 120^\circ\text{C}$. The vertical dashed line is the SA reference. One has $A(\text{CaF}_2) = 0.024$ ($C_3 = 0.96 \text{ kHz } \mu\text{m}^3$), $A(\text{sapphire}) = 0.042$ ($C_3 = 1.68 \text{ kHz } \mu\text{m}^3$). The ratio of fitting amplitudes is 0.57 in the fitting, 0.516 in theory

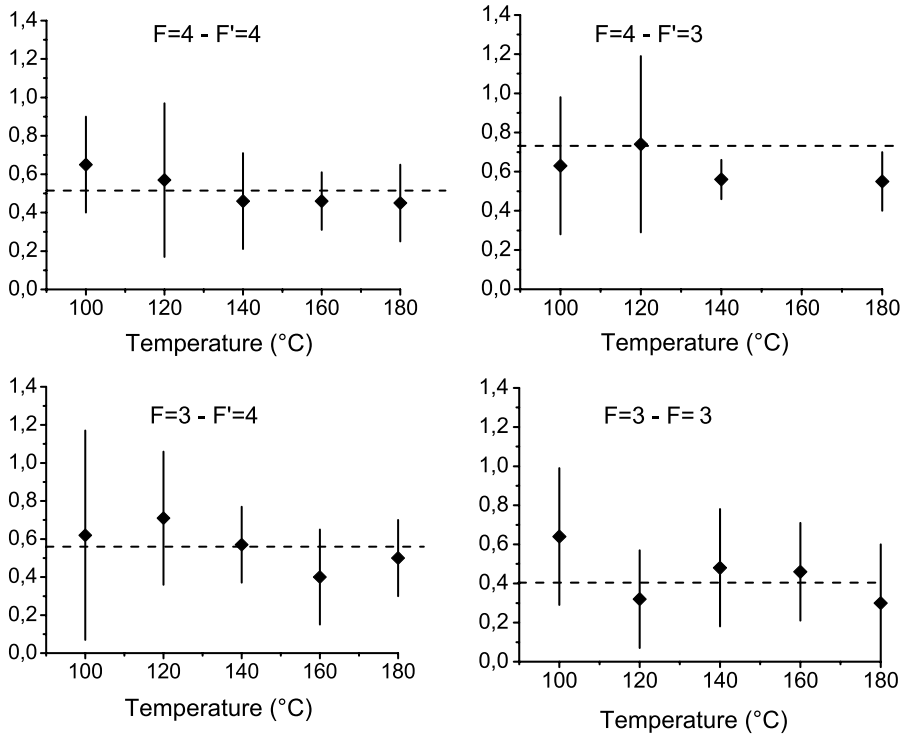


FIGURE 6 Ratio of the vW strength coupling C_3 between sapphire and CaF_2 window, as extrapolated from the fits for different Cs temperatures

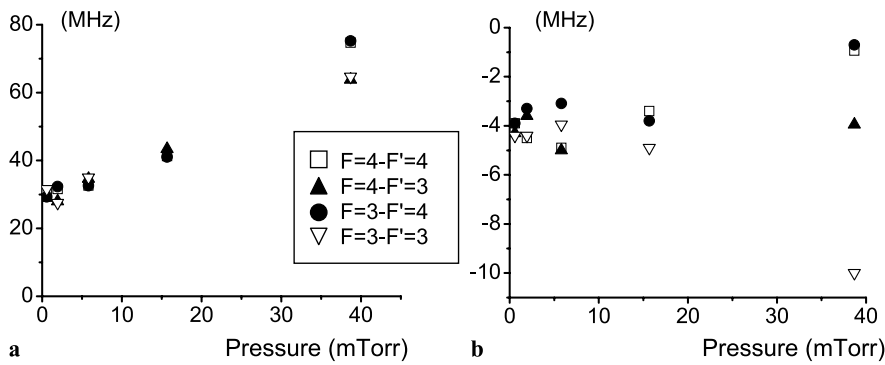


FIGURE 7 Widths (a) and shifts (b) as a function of Cs pressure for the various hyperfine transitions, as extrapolated from the fitting of SR spectra

curve to be fitted, the domain of acceptable (A_1 , A_2) values is strongly limited, and the cloud of fitting (A_1 , A_2) parameters is notably characterized by the ratio A_1/A_2 between the interactions exerted by the CaF_2 window and by the sapphire window. In addition, the assumption that the Cs vapour density is the same at the two interfaces should impose the relative amplitudes of the two SR signals. This is indeed verified, within the limits of the experimental uncertainty, mostly affecting the non-resonant reflection, which usually departs from the predicted value (i.e. Fresnel formula) owing to scattering losses at the interface. As illustrated in Fig. 6, the estimated $C_3^{\text{sapphire}}/C_3^{\text{CaF}_2}$ ratio remains constant ($\sim 0.55 \pm 0.25$) when varying the temperature conditions, in very good agreement with the theoretical value (~ 0.67). The accuracy for the individual values for C_3 is lower than for the relative interaction exerted by sapphire and CaF_2 , respectively; the obtained values $C_3^{\text{sapphire}} = 1.4 \text{ kHz } \mu\text{m}^3$, $C_3^{\text{CaF}_2} = 1.0 \text{ kHz } \mu\text{m}^3$ are in an acceptable agreement with the predicted ones (respectively $1.0 \text{ kHz } \mu\text{m}^3$ and $0.67 \text{ kHz } \mu\text{m}^3$, as deduced from a $2.0 \text{ kHz } \mu\text{m}^3$ value predicted for the D_1 line at an ideal interface, according to $C_3^{\text{ideal}}(6P_{1/2}) = 4.43 \text{ kHz } \mu\text{m}^3$ [2, 3] and

$C_3^{\text{ideal}}(6S_{1/2}) = 2.42 \text{ kHz } \mu\text{m}^3$ [8]). Lastly, an optical width and collision shift are associated with each fitting of an experimental recording, allowing us to plot the Cs pressure self-broadening and shift (Fig. 7). These variations of the pressure effects, partly dependent upon the investigated hyperfine component, are compatible with previous estimates of self-broadening [17–19] or even shift¹, although the accuracy, affected as usual by the pressure scale uncertainty ($\sim 40\%$ originating in a $\sim 5^\circ\text{C}$ temperature uncertainty), suffers here from the offset introduced by the impurity broadening. Also, the residual shift ($\sim -4 \text{ MHz}$) and broadening ($\sim 20 \text{ MHz}$) attributed to the impurities remain constant when varying the cell temperature (temperature of the body or of the Cs reservoir as well), showing that the impurities that have appeared

¹The uncertainty affecting the evaluation of a pressure shift (see [17–19]), already large because it is accompanied by a pressure broadening, becomes considerable when the vW interaction is not taken into account. This makes it sometimes difficult to evaluate the individual behaviour of each hyperfine component (see e.g. [8]) Moreover, the vW interaction induces an apparent (red) shift, that systematically increases with pressure, leading to erroneous interpretations when the vW interaction is neglected as in [20]

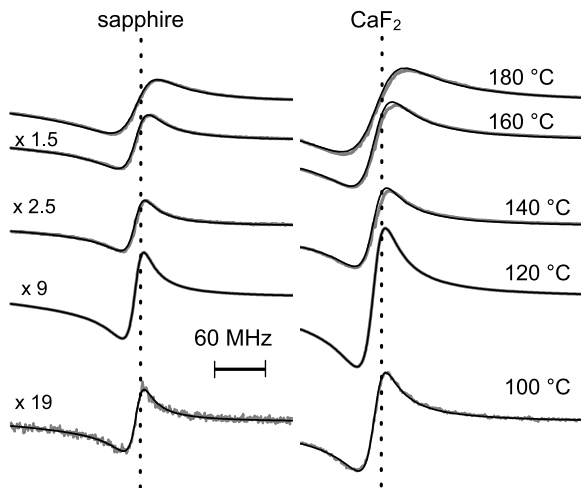


FIGURE 8 A series of experimental (grey) spectra fitted (black) with a unique C_3 value ($1.4 \text{ kHz}/\mu\text{m}^3$ for sapphire, $1 \text{ kHz}/\mu\text{m}^3$ for CaF_2) and only adjustable amplitudes; shifts and widths are also imposed as a result of the linear extrapolation of Fig. 7

when filling up the cell are of a nearly constant density, and not stored in a dense phase with a temperature-controlled gas equilibrium; moreover, the residual shift corroborates the SA experiment (Sect. 3). As further evidence of the consistency of our fittings and extrapolation from a series of spectra, Fig. 8 shows the ability to fit a series of spectra with a single C_3 value (for respectively sapphire and CaF_2), and the optical width and shift values deduced from Fig. 7.

5 Conclusion

In summary, we have designed an alkali vapour cell with a fluoride window susceptible to be heated to a high temperature. The principle of construction, allowing the contact of high-temperature vapour with the window of interest, is actually applicable to any interface made of a crystal (or material) resistant to hot alkali vapour. In spite of spurious impurities that have degraded the vacuum conditions in the prototype cell, we show that the atom–surface vW interaction can be measured at the interface with the special window, hence validating the design of the construction. Such a cell is an important step to study the specific influence of the thermal emittance of fluoride windows on suitable atomic transitions, such as the $\text{Cs } 6S_{1/2} \rightarrow 8P_{3/2}$ line [10]. In add-

ition, it appears that the coupled analysis of the vW interaction exerted on two different windows, as extracted from a simultaneous recording, is a particularly robust method to estimate reliably the strength of the C_3 coefficient of the vW interaction, notably when stray effects can hinder the specific vW contribution.

ACKNOWLEDGEMENTS This work was partially supported by FASTNet (European contract HPRN-CT-2002-00304) and by the INTAS South-Caucasus Project (grant 06-1000017-9001).

REFERENCES

- 1 For a review, see e.g. D. Bloch, M. Ducloy, Atom–wall interaction, in *Advances in Atomic, Molecular, and Optical Physics*, vol. 50, ed. by B. Bederson, H. Walther (Elsevier Academic, San Diego, CA, 2005), pp. 91–156
- 2 H. Failache, S. Saltiel, M. Fichet, D. Bloch, M. Ducloy, *Eur. Phys. J. D* **23**, 237 (2003)
- 3 H. Failache, S. Saltiel, M. Fichet, D. Bloch, M. Ducloy, *Phys. Rev. Lett.* **83**, 5467 (1999)
- 4 G. Dutier, I. Hamdi, P.C.S. Segundo, A. Yarovitski, S. Saltiel, M.-P. Gorza, M. Fichet, D. Bloch, M. Ducloy, A. Papoyan, T. Varzhapetyan, in *Laser Spectroscopy. Proceedings of the XVI International Conference*, ed. by P. Hannaford (World Scientific, Singapore, 2004), pp. 277–284
- 5 M.-P. Gorza, M. Ducloy, *Eur. Phys. J. D* **40**, 343 (2006)
- 6 V. Sandoghdar, C.I. Sukenik, E.A. Hinds, S. Haroche, *Phys. Rev. Lett.* **68**, 3432 (1992)
- 7 M. Ducloy, M. Fichet, *J. Phys. II (Paris)* **1**, 1429 (1991)
- 8 M. Chevrollier, M. Fichet, M. Oria, G. Rahmat, D. Bloch, M. Ducloy, *J. Phys. II (Paris)* **2**, 631 (1992)
- 9 N. Papageorgiou, M. Fichet, V.A. Sautenkov, D. Bloch, M. Ducloy, *Laser Phys.* **4**, 392 (1994)
- 10 P. Chaves de Souza Segundo, I. Hamdi, M. Fichet, D. Bloch, M. Ducloy, *Laser Phys.* **17**, 983 (2007)
- 11 M. Fichet, G. Dutier, A. Yarovitskiy, P. Todorov, I. Hamdi, I. Maurin, S. Saltiel, D. Sarkisyan, M.-P. Gorza, D. Bloch, M. Ducloy, *Europhys. Lett.* **77**, 54001 (2007)
- 12 S. Saltiel, D. Bloch, M. Ducloy, *Opt. Commun.* **265**, 220 (2006)
- 13 D.G. Sarkisyan, V. Krupkin, B. Glushko, *Appl. Opt.* **33**, 5518 (1994)
- 14 R.K. Raj, D. Bloch, J.J. Snyder, G. Camy, M. Ducloy, *Phys. Rev. Lett.* **44**, 1251 (1980)
- 15 see also M. Pinard, Thèse d’Etat, Université Paris 6 and ENS (1980), unpublished
- 16 A.M. Akul’shin, V.L. Velichanskii, A.S. Zibrov, V.V. Nikitin, V.V. Sautenkov, E.K. Yurkin, N.V. Senkov, *JETP Lett.* **36**, 303 (1982)
- 17 I. Hamdi, P. Todorov, A. Yarovitski, G. Dutier, I. Maurin, S. Saltiel, Y. Li, A. Lezama, T. Varzhapetyan, D. Sarkisyan, M.-P. Gorza, M. Fichet, D. Bloch, M. Ducloy, *Laser Phys.* **15**, 987 (2005)
- 18 G. Dutier, Ph.D. dissertation, Université Paris 13 (2003), unpublished
- 19 V. Vuletic, V.A. Sautenkov, C. Zimmermann, T.W. Hänsch, *Opt. Commun.* **99**, 185 (1993)
- 20 R. Müller, A. Weis, *Appl. Phys. B* **66**, 323 (1998)

Experimental observations of temperature effects in the near-field regime of the Casimir–Polder interaction

T Passerat de Silans^{1,2}, A Laliotis¹, I Maurin¹, M-P Gorza¹,
P Chaves de Souza Segundo³, M Ducloy¹ and D Bloch¹

¹ Laboratoire de Physique des Lasers, Université Paris 13- Sorbonne Paris-Cité, CNRS UMR 7538, 99, av. J B Clément F-93430 Villetaneuse, France

² Laboratório de Superfícies, Departamento da Física, Universidade Federal da Paraíba, Cx. Postal 5086, 58051-900, João Pessoa, PB, Brazil

³ Unidade Acadêmica de Educação, Centro de Educação e Saúde, Campus Cuité, Universidade Federal de Campina Grande, Cuité, PB, Brazil

Email: athanasios.laliotis@univ-paris13.fr

Received 26 October 2013

Accepted for publication 23 January 2014

Published 28 May 2014

Abstract

We investigate the temperature dependence of the Casimir–Polder interaction on the electrostatic limit. This unusual phenomenon relies on the coupling between a virtual atomic transition and a thermal excitation of surface polariton modes. We first focus on the scenario in which a Cs($8P_{3/2}$) atom is next to a CaF₂ or BaF₂ surface. Our theoretical predictions show a strong temperature dependence of the van der Waals coefficient at experimentally accessible conditions. A series of spectroscopic measurements performed in a specially designed Cs vapor cell containing a CaF₂ tube is presented. Our results illustrate the sensitivity of atom–surface interaction experiments to the quality and chemical stability of the surface material and emphasize the need for using more durable materials, such as sapphire. Finally, we discuss selective reflection experiments with Cs($7D_{3/2}$) in an all-sapphire cell that clearly demonstrate a temperature-dependent van der Waals coefficient.

Keywords: Casimir–Polder interaction, near field thermal emission, laser spectroscopy, van der Waals coefficient

(Some figures may appear in colour only in the online journal)

1. Introduction

Interactions between neutral but polarizable objects are ubiquitous and fundamental for our understanding of the physical world. A typical example is the long-range atom–surface force, most commonly known as the Casimir–Polder interaction [1]. In the near field, it is most commonly described as the interaction between the fluctuating dipole and its image, whereas in the far field it becomes easier to portray it as a distance-dependent Lamb shift because of the modification of vacuum or thermal fluctuations by the reflective boundary [2].

The temperature dependence of the Casimir–Polder interaction is an important consideration when comparing theory and experiment, and temperature corrections are fundamental for

any precision measurement involving atoms close to surfaces [3, 4]. On a more practical side, atom–surface interactions at non-zero temperatures can be of relevance for atom or molecule chips [5–9] and for miniaturized frequency references or clocks [10, 11].

Although the effects of thermal fluctuations on the Lamb shift were demonstrated in a high-precision experiment in the early 1980s [12], the Casimir–Polder interaction was observed several years later [13] and its temperature dependence was more elusive. The only measurement demonstrating such effects was made at distances of approximately 5–10 μm , when the strength of the interaction is extremely small. Critical to experimental success [14] was an enhancement attributable to an out-of-equilibrium effect [15], when

the surface is held at a higher temperature with respect to its surrounding environment.

Looking much closer at the surface, typically at approximately 100 nm, the shift of an atomic level takes the familiar form of $-C_3/z^3$, where C_3 is the van der Waals coefficient. The classical picture of an atom interacting with its image is less accommodating for thermal effects, because the reflected field of a dipole antenna does not fundamentally depend on temperature [16, 17]. This intuition is supported by quantum electrodynamics (QED) calculations for an atom or molecule in front of a perfect or dispersion-less conductor [18].

However, material dispersion and especially surface polaritons are of great importance in the near field. In this regime, thermal emission is dominated by surface excitations and becomes almost monochromatic in contrast to the well-known broadband black body spectrum [19, 20]. Similarly, the van der Waals interaction is dominated by the resonant coupling between atom dipole transitions and surface polaritons. This is usually relevant for excited-state atoms whose couplings in the mid-infrared range coincide with surface excitations of common dielectrics. It was demonstrated that the coupling between a virtual atomic emission and a surface mode excitation can lead to extraordinary effects such as atom–surface repulsion or even giant attraction [21, 22]. The inverse effect requires a thermal excitation of the polariton modes that can now be coupled to an atomic absorption and leads to a temperature-dependent van der Waals interaction [2, 21, 23, 24]. This exotic behavior is only accessible when the thermal energy is comparable with that of the atomic transition (i.e., $\hbar\omega_o = k_B T$). For room temperatures, this dictates a transition wavelength of approximately $50\mu\text{m}$.

This reasoning essentially excludes ground state atoms and, in general, places heavy constraints on the appropriate atom surface system. An extensive study of materials [25] suggests that Cs($8P_{3/2}$) dipole couplings $8P_{3/2} \rightarrow 7D_{3/2}$ and $8P_{3/2} \rightarrow 7D_{5/2}$ at $39\mu\text{m}$ and $36\mu\text{m}$, respectively (figure 1), can couple resonantly to CaF_2 and BaF_2 surface polaritons at $24\mu\text{m}$ and $35\mu\text{m}$, respectively. The dielectric properties of these materials were experimentally measured as a function of temperature [26]. We detail the theoretical predictions of the temperature dependence of the van der Waals coefficient for Cs($8P_{3/2}$) against CaF_2 , BaF_2 and sapphire surfaces. We also describe the corresponding experiments that were inconclusive because of surface quality deterioration. Finally, we briefly describe for a successful series of experiments against Cs($7D_{3/2}$) a sapphire interface that will be reported in detail elsewhere.

2. Theoretical predictions

In the near field, the atom–surface interaction induces a free energy shift that is given by $-C_3/z^3$. The van der Waals coefficient depends on the surface as well as the atom and its given energy state $|i\rangle$. To calculate C_3 , one needs to sum the contribution of all allowed dipole couplings $|i\rangle \rightarrow |j\rangle$, which for a perfect reflector is proportional to the square of the electric dipole moment matrix element $\langle i|D|j\rangle$. In the

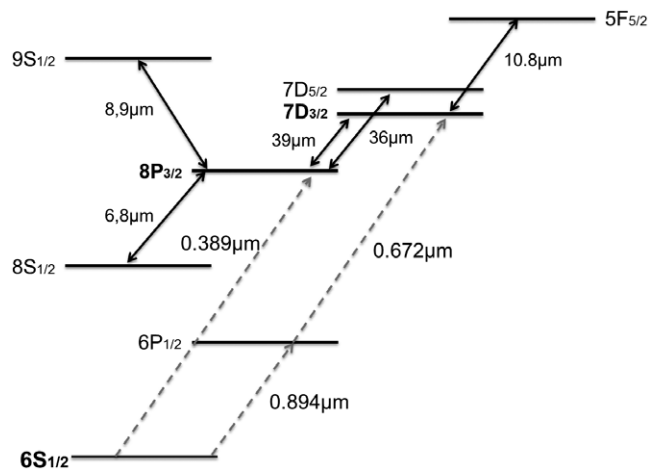


Figure 1. Schematic diagram of Cs energy levels relevant to our experiments.

case of a real surface, this has to be multiplied by an image coefficient r_{ij} , which depends on the dielectric properties of the surface. Ignoring the dispersive response of the material, the image coefficient is simply given by $r = (\epsilon - 1) / (\epsilon + 1)$, independent of ambient temperature, and is consistent with the classical picture of a dipole interacting with its own image in front of a surface with finite reflectivity. A complete QED description [16] is required to account for surface dispersion. A few theoretical studies have dealt with this problem in the past [23–25] and have shown that there are two contributions to the image coefficient. The first resembles a distance-dependent Lamb shift attributable to vacuum and thermal fluctuations covering the entire frequency spectrum. The second is reminiscent of the interaction between a classical oscillating dipole and its own reflected field [27]. For convenience, the former dispersive contribution will henceforth be referred to as non-resonant, r_{nr} , whereas the latter will be referred to as resonant, r_{res} .

For an upward coupling, $|i\rangle \rightarrow |j\rangle$ the resonant term takes the form:

$$r_{res} = -2\text{Re}[S(\omega_o)] n(\omega_o, T) \quad (1)$$

where $\omega_o = \omega_j - \omega_i > 0$ is the transition frequency and the factor $S(\omega_o) = (\epsilon(\omega_o) - 1) / (\epsilon(\omega_o) + 1)$ is the complex surface response from which the polariton modes are defined and $n(\omega_o, T) = 1 / \left(e^{\frac{\hbar\omega_o}{kT}} - 1 \right)$ is the mean occupation number of each mode by photons. The term in equation (1) owes its existence to temperature. In the case of a downward transition, $\omega_o < 0$, the resonant term has a similar temperature dependence given by $n(\omega_o, T) = n(|\omega_o|) + 1$ but survives even at zero temperatures because of spontaneous emission [23].

In reality, an atomic level $|i\rangle$ has numerous couplings and isolating the resonant term of a given transition is extremely difficult. In figure 2, we show the real part of the surface response as a function of frequency for calcium fluoride, barium fluoride and sapphire, with surface resonances at $24\mu\text{m}$, $35\mu\text{m}$ and $12\mu\text{m}$, respectively. In table 1 we show the temperature dependence of the most dominant dipole couplings, starting from the $8P_{3/2}$ level, for each of these three materials

Table 1. Contribution of each dipole coupling to the C_3 van der Waals coefficient between Cs($8P_{3/2}$) and (a) CaF₂, (b) BaF₂ and (c) sapphire at different temperatures. C_3 is measured in kHz μm^3 and the temperature is measured in Kelvin. The negative sign denotes a downward transition. The C_3 value, given by the sum of each individual contribution, is also shown at the end of each table. The contributions to C_3 were calculated using measurements of the dielectric constant at room temperature [26].

(a) CaF ₂								
Cs($8P_{3/2}$)	λ (μm)	C_3 (perfect reflector)	C_3 ($T = 0$)	C_3 ($T = 200$)	C_3 ($T = 400$)	C_3 ($T = 600$)	C_3 ($T = 800$)	C_3 ($T = 1000$)
8S _{1/2}	-6.78	12.07	2.17	1.99	1.27	0.38	-0.56	-1.52
7D _{3/2}	39.05	5.32	3.11	2.92	1.93	0.69	-0.63	-1.99
7D _{5/2}	36.09	37.79	21.8	19.98	11.19	0.19	-11.5	-23.48
9S _{1/2}	8.94	11.63	5.19	5.44	6.41	7.61	8.88	10.19
8D _{5/2}	4.92	3.7	1.51	1.55	1.71	1.9	2.09	2.3
Total		73.71	34.94	33.04	23.73	12.05	-0.37	-13.09
(b) BaF ₂								
Cs($8P_{3/2}$)	λ (μm)	C_3 (perfect reflector)	C_3 ($T = 0$)	C_3 ($T = 200$)	C_3 ($T = 400$)	C_3 ($T = 600$)	C_3 ($T = 800$)	C_3 ($T = 1000$)
8S _{1/2}	-6.78	12.07	3.14	2.86	2.09	1.23	0.34	-0.56
7D _{3/2}	39.05	5.32	3.01	0.71	-5.84	-13.19	-20.77	-28.43
7D _{5/2}	36.09	37.79	21.07	-11.44	-105.46	-211.34	-320.54	-431.09
9S _{1/2}	8.94	11.63	5.13	5.49	6.49	7.62	8.79	9.97
8D _{5/2}	4.92	3.7	1.52	1.58	1.75	1.94	2.13	2.33
Total		73.71	35.06	0.42	-99.69	-212.4	-328.64	-446.33
(c) Sapphire								
Cs($8P_{3/2}$)	λ (μm)	C_3 (Perfect reflector)	C_3 ($T = 0$)	C_3 ($T = 200$)	C_3 ($T = 400$)	C_3 ($T = 600$)	C_3 ($T = 800$)	C_3 ($T = 1000$)
8S _{1/2}	-6.78	12.07	1.55	1.52	1.19	0.54	-0.26	-1.13
7D _{3/2}	39.05	5.32	3.9	3.92	3.87	3.75	3.6	3.44
7D _{5/2}	36.09	37.79	27.57	27.65	27.2	26.24	25.03	23.71
9S _{1/2}	8.94	11.63	7.32	7.37	7.98	9.21	10.73	12.4
8D _{5/2}	4.92	3.7	2.17	2.18	2.24	2.36	2.51	2.67
Total		73.71	44.14	44.27	44.13	43.78	43.32	42.84

as calculated using the QED theory described in [23] and data for the dielectric constants given in [26]. As can be verified in table 1, the temperature dependence of the C_3 coefficient is predominantly attributable to dipole couplings that are close to the respective polariton resonances. In the case of BaF₂ and CaF₂, these are the $8P_{3/2} \rightarrow 7D_{5/2}$ and $8P_{3/2} \rightarrow 7D_{3/2}$ couplings. In the case of sapphire, these couplings clearly are out of the range of the surface polariton and their temperature dependence is modest. It is worth noticing that the $8P_{3/2} \rightarrow 9S_{1/2}$ coupling at $8.9\mu\text{m}$, which is closer to the sapphire surface resonance, practically cancels any temperature dependence induced by the dominant coupling at $36\mu\text{m}$. A close examination of table 1 is very instructive. It reveals the complexity of the C_3 dependence on temperature and illustrates the importance of Casimir–Polder-type experiments for our understanding of the electromagnetic properties of materials and surfaces. It is also worth mentioning that the temperature dependence of the dielectric constant itself [26] has been here neglected when calculating the values in table 1. In figure 2, the dotted lines show the surface response when the surface is at $T = 770\text{K}$. The effects are dramatic for the polariton resonances but not for the rest of the spectrum. Our predictions for C_3 are almost unaffected in the case of sapphire and CaF₂, but they need to be revised for BaF₂ [26].

3. Selective reflection experiments on the $6S \rightarrow 8P$ line

Frequency modulated (FM) selective reflection at the interface between a window and vapor is one of the few linear spectroscopic methods providing a signal with sub-Doppler resolution [10, 28–30]. Extensive theoretical and experimental studies have shown that, in its simplest form, it is sensitive to atoms typically within a distance of $\lambda/2\pi$ from the surface of the window. This unique characteristic makes it ideal to probe atom–surface interactions in the near-field regime [30–32]. The van der Waals coefficient is measured by comparing the experimentally obtained spectra to a library of theoretical curves [22]. Using a fitting process, we extracted C_3 , the transition line width Γ and the collisional shift δ . This well-established method has been repeatedly used in the past to measure the van der Waals coefficient [30–37]. Note that in most cases the shift of a given transition is governed solely by the van der Waals interaction of the high-lying state.

The experiments that are reported here were performed on the third resonance line of Cs at 388nm [37, 38]. Initially, we used an extended cavity laser system with a diode emitting at the ultraviolet (UV) spectral range. Unfortunately, the power output was limited to 1 to 2 mW and the beam quality

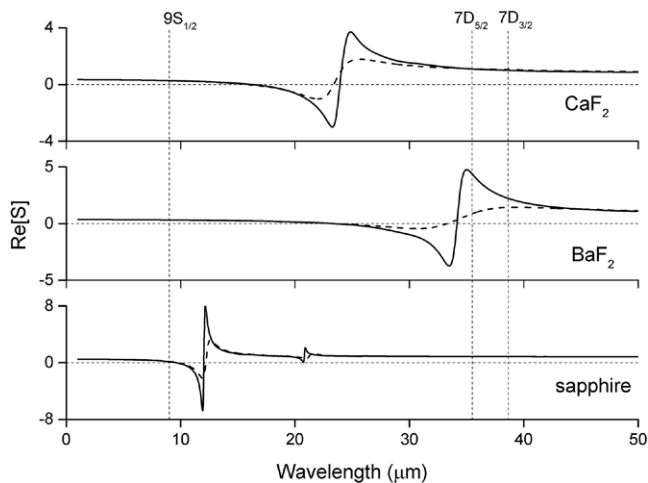


Figure 2. The real part of the image coefficient for CaF_2 , BaF_2 and sapphire as a function of wavelength [26]. The solid curve represents measurements at room temperature, whereas the dashed curve represents measurements made at $T = 770$ K. The position of the dominant dipole couplings is shown as a vertical dashed line. The dominant coupling $8P_{3/2} \rightarrow 7D_{5/2}$ at $36.09 \mu\text{m}$ is very close to the BaF_2 polariton at $35 \mu\text{m}$, on the wings of the CaF_2 polariton at $24 \mu\text{m}$, and very far away from the sapphire polariton at $12 \mu\text{m}$.

was low. Eventually, this source was replaced by an amplified, frequency-doubled 780 nm laser diode with a final output power of approximately 100 mW at UV wavelengths. This frequency source had the additional advantage of allowing us to scan both the $6S_{1/2} \rightarrow 8P_{1/2}$ line at 387.6 nm and the $6S_{1/2} \rightarrow 8P_{3/2}$ line at 388.8 nm. The source with the UV diode was frequency modulated by applying a voltage on the piezoelectric element attached to the grating of the extended cavity laser. The frequency-doubled source was modulated by double-passing the beam through an acousto-optic modulator. A saturated absorption was performed in a slightly heated ($\sim 80^\circ\text{C}$) sapphire vapor cell. Additionally, we used a stable Fabry–Perot cavity with a free spectral range of 83 MHz as a frequency marker. These auxiliary experiments allowed us to determine the absolute frequency of the laser throughout our scans with an accuracy of a few MHz.

In figure 3, we show the vapor cell in which selective reflection measurements were performed. The design was identical to the one described in a previous publication [35], but this time no impurities were present. The fabrication of a vapor cell with CaF_2 windows was technically challenging because of the different thermal expansion coefficients between the window and the main body of the cell, which is made out of sapphire. The cell has a T-shape, with one window made of sapphire and the other one made of YAG. A hole is drilled in the main body of the cell, onto which the sidearm is attached. A CaF_2 tube is inserted inside the cell, almost in contact with the YAG window. The small gap between the tube and the window is approximately $100 \mu\text{m}$. This part of the cell is kept at low temperatures to ensure that Cs density within the gap stays negligible and does not affect the selective reflection that is performed on the CaF_2 interface. The temperature of the cell is controlled by independent ovens. The first and second ovens control the temperature of the sapphire window and the CaF_2

tube, respectively. The third controls the sidearm (reservoir) temperature and, therefore, the Cs density inside the cell. To avoid Cs condensation on the tube or the window, the upper part of the cell is always kept at slightly higher temperatures than the sidearm. Repeated attempts to fabricate a similar cell with a BaF_2 tube were unsuccessful because of the fragility and chemical instability of the material at high temperatures [39].

Typically, we record selective reflection spectra on the CaF_2 tube and the sapphire window simultaneously. Our well-established experimental protocol is as follows. First, for a given window temperature we vary the Cs vapor pressure, therefore changing the transition line width because of pressure broadening and the collisional shift. The same process is repeated for both the $F = 3 \rightarrow F' = 2, 3, 4$ and the $F = 4 \rightarrow F' = 3, 4, 5$ manifolds of the $6S_{1/2} \rightarrow 8P_{3/2}$ transition, whose spectra are fundamentally different because of the different relative weight of the hyperfine transitions. Unfortunately, it soon became evident that the quality of the CaF_2 tube started to deteriorate after use at high temperatures in the presence of chemically aggressive Cs vapor. The most striking effect was the fact that the material became porous and Cs in the gas phase infiltrated the tube. This meant that a parasitic Doppler shaped absorption induced by Cs atoms inside the tube was always superimposed on the selective reflection spectrum.

We nonetheless finished an extensive series of measurements. In figure 4, we show two simultaneously recorded selective reflection spectra on the CaF_2 and sapphire interfaces. Initially, we attempted to fit the spectra by imposing the same parameters for the vapor line width Γ (including pressure broadening) and for the collisional shift δ , as compared with the saturated absorption reference, which should remain a fraction of Γ . This is a reasonable restriction under the assumption that the vapor pressure within the cell is only controlled by the Cs reservoir in the sidearm of the cell. However, in our case the porous CaF_2 tube also acts as an independent reservoir, making it impossible to assign a uniform value to Γ and δ throughout the cell. We therefore fitted each spectrum independently and this gave satisfactory results, as can be verified in figure 4. Given the state of the CaF_2 tube, it was rather surprising that all of the measurements and fits allowed us to consistently extract the values for the C_3 coefficient that are shown in figure 5 as a function of the window temperature. The experimental results are at odds with theoretical predictions, which are also shown in the same figure.

Finally, we attempted to fit our experimental spectra using a potential of the form $-C_2/z^2$ to describe the interaction between the atom and the surface. This potential could result if the surface is electrically charged or somehow contaminated with Cs adsorbents [4, 40, 41]. For this purpose, a new library of curves was produced and the fitting process was repeated using C_2 , Γ (line width) and δ (collisional shift) as independent parameters. The quality of the fits was satisfactory; however, the values of Γ and δ required to produce those fits were unreasonable and inconsistent with previous spectroscopic measurements on the $6S_{1/2} \rightarrow 8P_{3/2}$ line [37]. In figure 6, we can see the collisional shift, as extracted from the fits of experimental spectra using both $-C_3/z^3$ (solid points) and $-C_2/z^2$ (open points). Data are

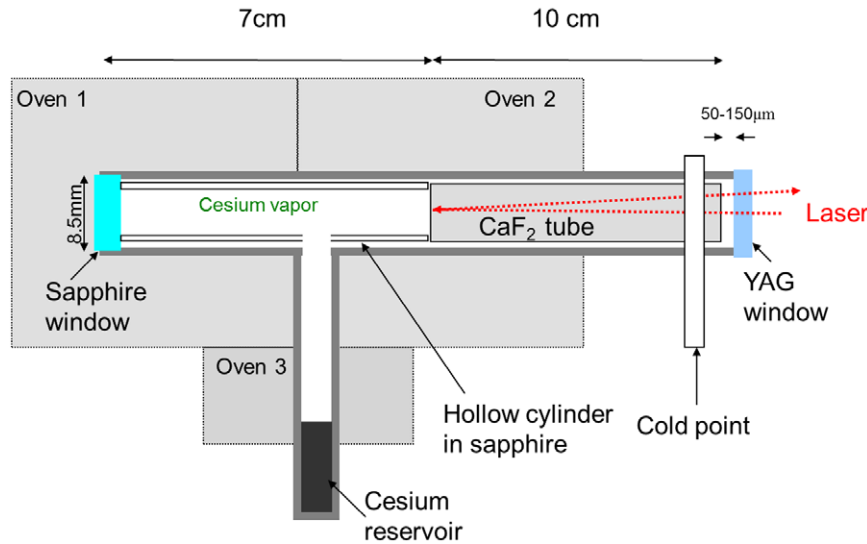


Figure 3. Schematic diagram of the Cs vapor cell containing a CaF_2 tube, which was used for these experiments [36]. The cell is heated by three independent ovens. Ovens 1 and 2 control the temperature of the upper part of the cell, whereas oven 3 controls the temperature of the Cs reservoir and, therefore, the Cs vapor pressure within the cell. Selective reflection is performed on the inner side of the tube, whereas the other side, close to the YAG window, is kept at low temperatures to avoid the presence of Cs vapor in the gap between the tube and the window.

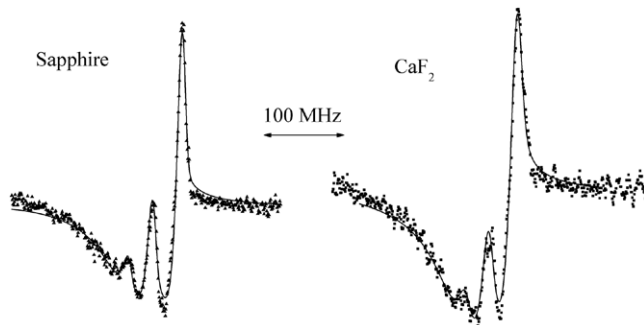


Figure 4. Selective reflection measurements performed on both sapphire and CaF_2 interfaces. The points represent experimentally measured spectra, whereas the solid lines show the fits obtained using the theoretical model. In the case of sapphire, we obtained the following values: $C_3 = 59 \text{ kHz } \mu\text{m}^3$, $\Gamma = 15.6 \text{ MHz}$, and $\delta = -6.3 \text{ MHz}$. For CaF_2 , we obtained the following values: $C_3 = 66 \text{ kHz } \mu\text{m}^3$, $\Gamma = 23.5 \text{ MHz}$, and $\delta = -5.4 \text{ MHz}$.

presented for both sapphire (circles) and CaF_2 (squares) windows. It is clear that, even at low pressures, one needs to impose a large positive collisional shift when fitting with a $-C_2/z^2$ potential, something that is artificial in normal conditions. Moreover, the previously reported collisional shift was approximately $-60 \text{ MHz Torr}^{-1}$ [37], a measurement that is only supported when fitting with $-C_3/z^3$ potential.

These arguments lead to the conclusion that our measurements cannot be explained with a $-C_2/z^2$ potential, and that we can have relative confidence in the values extracted for the van der Waals coefficient. However, it seems that the chemical nature of the surface was significantly altered and this dramatically modifies the polariton resonances relative to what we have supposed for our theoretical calculations. Note, in particular, that an ideal roughness is assumed when converting the bulk properties of the material from measured values of the dielectric constant into surface polariton modes.

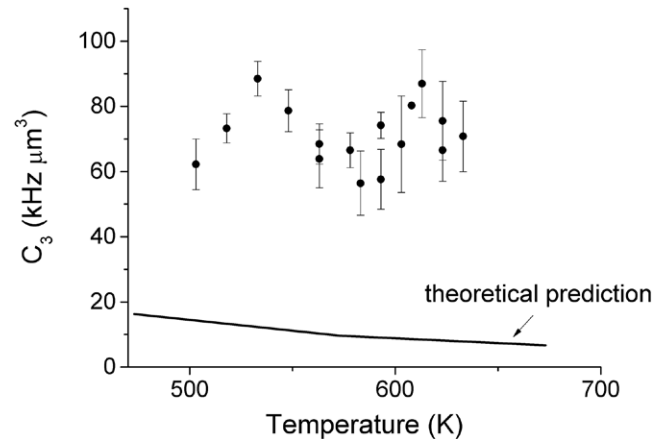


Figure 5. C_3 as a function of the CaF_2 window temperature.

4. Selective reflection experiments on the $6P \rightarrow 7D$ line

The fragility of CaF_2 has forced us to turn our attention to different materials such as sapphire, which has been used for this purpose in the past and has been remarkably stable in the presence of alkali vapors [42, 43]. Moreover, technology allows the fabrication of all-sapphire vapor cells that can withstand very high temperatures. For our selective reflection experiments that are naturally sensitive to the quality of the windows, we have acquired specially designed all-sapphire vapor cell with a sidearm that can be heated to almost $1000 \text{ }^\circ\text{C}$, made by the group of Sarkisyan [43]. The main window was super-polished, with an average surface roughness of approximately 0.3 nm . This cell replaced a similar but much older one with windows of unknown quality that was initially used for our measurements.

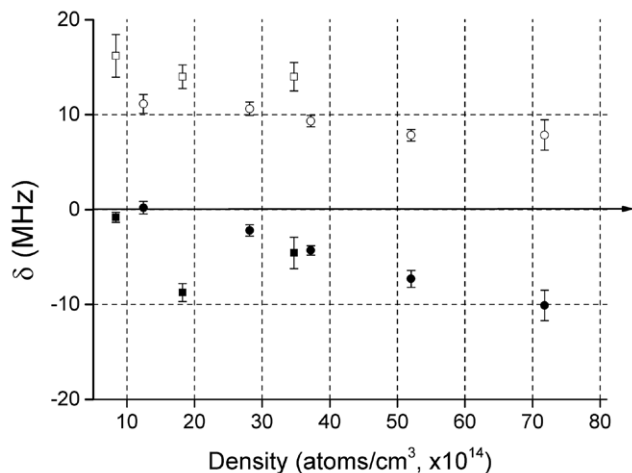


Figure 6. Values of the collisional shift as extracted from the fits of our experimental measurements. The solid circles (sapphire window) and squares (CaF₂ window) represent the collisional shift obtained when fitting with a $-C_3/z^3$ potential. The open circles and squares represent the results obtained for $-C_2/z^2$ potential.

As can be verified in table 1, the van der Waals coefficient for Cs(8P) near sapphire displays no temperature dependence [26]. Therefore, we needed to find another atomic level for which a dominant dipole coupling is closer to the sapphire polariton at $12\ \mu\text{m}$. An obvious candidate is Cs(7P_{1/2}), whose coupling with 6D_{3/2} is at $12.15\ \mu\text{m}$ [21]. Probing the weak 6S_{1/2} → 7P_{1/2} transition at $459\ \text{nm}$ is, however, difficult because of the lack of low-noise laser sources at this wavelength [34]. Moreover, this coupling is so close to the sapphire polariton that it becomes sensitive to the surface quality and therefore it is challenging to ascertain a theoretical prediction.

Instead, we chose Cs(7D_{3/2}) as our first candidate. This level has an upward coupling, 7D_{3/2} → 5F_{5/2}, at $10.8\ \mu\text{m}$ (figure 1), whereas the couplings at $36\ \mu\text{m}$ and $39\ \mu\text{m}$ are far from the sapphire resonance (figure 2). The relatively small transition wavelength suggests that temperature needs to be substantially increased before a change of the van der Waals coefficient can be observed. For our experiments, the atoms are first pumped with a high-power laser to the Cs(6P_{1/2}) level, and from there selective reflection is performed with a red laser on the 6P_{1/2} → 7D_{3/2} transition at $672\ \text{nm}$. This time we performed measurements for window temperatures as high as $1000\ \text{K}$, with a significant increase of C_3 from $\sim 50\ \text{kHz}\ \mu\text{m}^3$ at $500\ \text{K}$ to $\sim 80\ \text{kHz}\ \mu\text{m}^3$ at $1000\ \text{K}$. The results of our experiments in both all-sapphire cells verify our theoretical predictions. A typical spectrum obtained for the $F = 4 \rightarrow F' = 3, 4, 5$ manifold of the 6P_{1/2} → 7D_{3/2} transition is shown in figure 7. The quality of the fit is impressive and allowed us to measure the van der Waals coefficient with an uncertainty of less than 15% from a single spectrum. More details on these experiments will be provided in an upcoming publication [44].

5. Conclusions

We have provided an overview of selective reflection experiments aimed at measuring the temperature dependence of the

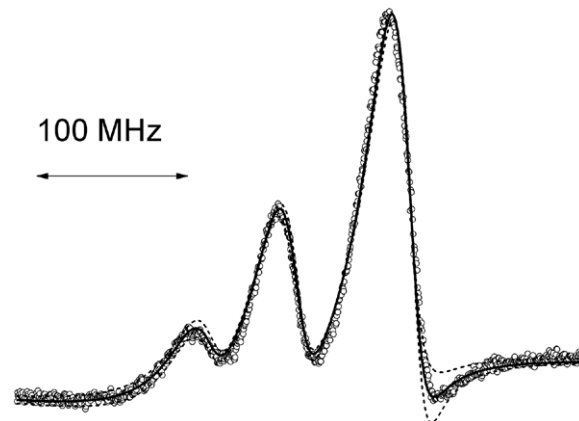


Figure 7. Selective reflection spectrum of the $F = 4 \rightarrow F' = 3, 4, 5$ manifold of the 6P_{1/2} → 7D_{3/2} transition. The experimental spectrum is shown with open dots. The sapphire window temperature was $T = 500\ \text{K}$. The best fit (solid line) was obtained for $C_3 = 59\ \text{kHz}\ \mu\text{m}^3$, $\Gamma = 17\ \text{MHz}$ and $\delta = 0$. The dashed curves represent fits for which we imposed a C_3 value different by $\pm 15\%$.

Casimir–Polder interaction between an atom and a surface in the near-field regime. Initial measurements were performed in a specially designed cell containing a CaF₂ tube on the 6S_{1/2} → 8P_{3/2} transition of Cs. Even though theoretical estimates predicted a strong variation of C_3 with temperature, this was not observed. The reason for this surprising fact is the deterioration of the CaF₂ tube, which makes it impossible to predict the polariton modes on which the temperature dependence of the van der Waals coefficient critically relies. For this reason, we did not further pursue the fabrication of a BaF₂ cell even though the predicted thermal effects are huge. Instead, we focused on an all-sapphire cell. Our measurements on the 6P_{1/2} → 7D_{3/2} line of Cs show a C_3 temperature dependence that agrees with our QED calculations. It is clear from our theoretical predictions that the temperature dependence of the van der Waals interaction is specific to the atom–surface system in question. In the future, one could take advantage of this phenomenon to tune or even eliminate atom–surface interactions at a specific temperature.

Acknowledgments

We acknowledge financial support from CAPES-COFECUB (Ph 740-12) and useful discussions with J R Rios Leite, H Failache and M Chevrollier. It has also been a pleasure to collaborate with D Sarkisyan, who fabricated both the CaF₂ and the all-sapphire cell for our experiments. We also thank G Pichler for kindly offering us his all-sapphire cell in which initial experiments on Cs(7D_{3/2}) were performed.

References

- [1] Casimir H B G and Polder D 1948 The influence of retardation on the London–van der Waals forces *Phys. Rev.* **73** 360–72
- [2] Barton G 1997 Van der Waals shifts in an atom near absorptive dielectric mirrors *Proc. R. Soc. Lond. A* **453** 2461

- [3] Wolf P, Lemonde P, Lambrecht A, Bize S, Landragin A and Clairon A 2007 From optical lattice clocks to the measurement of forces in the Casimir regime *Phys. Rev. A* **75** 063608
- [4] Harber D M, Obrecht J M, McGuirk J M and Cornell E A 2005 Measurement of the Casimir–Polder force through center-of-mass oscillations of a Bose–Einstein condensate *Phys. Rev. A* **72** 033610
- [5] Reichel J 2001 Microchip traps and Bose–Einstein condensation *Appl. Phys. B* **74** 469–87
- [6] Kohnen, M, Sukko, M, Petrov, P G., Nyman R A, Trupke, M and Hinds E A 2011 An array of integrated atom–photon junctions *Nature Photon.* **5** 35–8
- [7] Pollock S, Cotter J P, Laloties A, Ramirez-Martinez F and Hinds E A 2011 Characteristics of integrated magneto-optical traps for atom chips *New J. Phys.* **13** 043029
- [8] Meek S A, Conrad H and Meijer G 2009 Trapping molecules on a chip *Science* **324** 1699–702
- [9] Buhmann S Y, Tarbutt M R, Scheel S and Hinds E A 2008 Surface-induced heating of cold polar molecules *Phys. Rev. A* **78** 052901
- [10] Ballin P, Moufaret E, Maurin I, Laloties A and Bloch D 2013 Three-dimensional confinement of vapor in nanostructures for sub-Doppler optical resolution *Appl. Phys. Lett.* **102** 231115
- [11] Villalba S, Failache H, Laloties A, Lenci L, Barreiro S and Lezama A 2013 Rb optical resonance inside a random porous medium *Opt. Lett.* **38** 193–6
- [12] Hollberg L and Hall J L 1984 Measurement of the shift of Rydberg energy levels induced by black body radiation *Phys. Rev. Lett.* **53** 230–3
- [13] Sukenik C I, Boshier M G, Cho D, Sandoghdar V and Hinds E A 1993 Measurement of the Casimir–Polder force *Phys. Rev. Lett.* **70** 560–3
- [14] Obrecht, J M, Wild R J, Antezza M, Pitaevskii L P, Stringari S and Cornell E A 2007 Measurement of the temperature dependence of the Casimir–Polder force *Phys. Rev. Lett.* **98** 063201
- [15] Antezza M, Pitaevskii L P and Stringari S 2005 New asymptotic behavior of the surface–atom force out of thermal equilibrium *Phys. Rev. Lett.* **95** 113202
- [16] Wylie J M and Sipe J E 1984 Quantum electrodynamics near an interface *Phys. Rev. A* **30** 1185–93
Wylie J M and Sipe J E 1985 Quantum electrodynamics near an interface II *Phys. Rev. A* **32** 2030–43
- [17] Fichet M, Schuller F, Bloch D and Ducloy M 1995 Van der Waals interactions between excited atoms and dispersive surfaces *Phys. Rev. A* **51** 1553–64
- [18] Ellingsen S, Buhmann S Y and Scheel S 2010 Temperature-independent Casimir–Polder forces despite large thermal photon numbers *Phys. Rev. Lett.* **104** 223003
- [19] Shchegrov A V, Joulain K, Carminati R and Greffet J J 2000 Near-field spectral effects due to electromagnetic surface excitations *Phys. Rev. Lett.* **85** 1548–51
- [20] Greffet J J, Carminati R, Joulain K, Mulet J P, Mainguy S and Chen Y 2002 Coherent emission of light by thermal sources *Nature* **416** 61–4
- [21] Failache H, Saltiel S, Fichet M, Bloch D and Ducloy M 1999 Resonant van der Waals repulsion between excited Cs atoms and sapphire surface *Phys. Rev. Lett.* **83** 5467–70
- [22] Failache H, Saltiel S, Fichet M, Bloch D and Ducloy M 2003 Resonant coupling in the van der Waals interaction between an excited alkali atom and a dielectric surface: an experimental study via stepwise selective reflection spectroscopy *Eur. Phys. J. D* **23** 237–55
- [23] Gorza M P and Ducloy M 2006 Van der Waals interactions between atoms and dispersive surfaces at finite temperature *Eur. Phys. J. D* **40** 343–56
- [24] Hinds E A, Lai K S and Schnell M 1997 Atoms in micron sized metallic and dielectric waveguides *Phil. Trans. R. Soc. Lond. A* **355** 2353–65
- [25] Saltiel S, Bloch D and Ducloy M 2006 Tabulation and critical analysis of the wavelength dependent dielectric image coefficient by a surface onto a neighbouring excited atom *Opt. Commun.* **265** 220–33
- [26] Passerat de Silans T, Maurin I, Chaves de Souza Segundo P, Saltiel S, Gorza M P, Ducloy M, Bloch D, Meneses D S and Patrick Echegut P 2009 Temperature dependence of the dielectric permittivity of CaF₂, BaF₂ and Al₂O₃: application to the prediction of a temperature-dependent van der Waals surface interaction exerted onto a neighbouring Cs(8P_{3/2}) atom *J. Phys.: Condens. Matter* **21** 255902
- [27] Hinds E A and Sandoghdar V 1991 Cavity QED level shifts of simple atoms *Phys. Rev. A* **43** 398–403
- [28] Dutier G, Yarovitski A, Saltiel S, Papoyan A, Sarkisyan D, Bloch D and Ducloy M 2003 Collapse and revival of a Dicke-type coherent narrowing in a sub-micron thick vapor cell transmission spectroscopy *Europhys. Lett.* **63** 35
- [29] Briaudeau S, Saltiel S, Nienhuis G, Bloch D and Ducloy M 1998 Coherent Doppler narrowing in a thin vapor cell: observation of the Dicke regime in the optical domain *Phys. Rev. A* **57** R3169
- [30] Bloch D and Ducloy M 2005 Atom–wall interaction *Advances in Atomic, Molecular and Optical Physics* vol 50, ed B Bederson and H Walther (New York: Academic) pp 91–156
- [31] Ducloy M and Fichet M 1991 General theory of frequency modulated selective reflection: influence of atom surface interactions *J. Physique II* **1** 1429–46
- [32] Oria M, Chevrollier M, Bloch D, Fichet M and Ducloy M 1991 Spectral observation of surface induced van der Waals attraction on atomic vapour *Europhys. Lett.* **14** 527–32
- [33] Chevrollier M, Fichet M, Oria M, Rahmat G, Bloch D and Ducloy M 1992 High resolution selective reflection spectroscopy as a probe of long-range surface interaction: measurement of the surface van der Waals attraction exerted on excited Cs atoms *J. Physique II* **2** 631–57
- [34] Chevrollier M, Bloch D, Rahmat G and Ducloy M 1991 Van der Waals induced spectral distortions in selective reflection spectroscopy: the strong surface interaction regime *Opt. Lett.* **16** 1879–81
- [35] Laloties A, Maurin I, Fichet M, Bloch D, Ducloy M, Balasanyan N, Sarkisyan A and Sarkisyan D 2008 Selective reflection spectroscopy at the interface between a calcium fluoride window and Cs vapour *Appl. Phys. B* **90** 415–20
- [36] Passerat de Silans T 2009 *PhD Thesis* Université Paris Nord—Paris XIII
- [37] Chaves de Souza Segundo P, Hamdi I, Fichet M, Bloch D and Ducloy M 2007 Selective reflection spectroscopy on the UV-resonance line of Cs: simultaneous probing of the van der Waals atom–surface interaction sensitive to far IR couplings and interatomic collisions *Laser Phys.* **17** 983–92
- [38] Passerat de Silans T, Maurin I, Laloties A, Chaves de Souza Segundo P and Bloch D 2011 Extra sub-Doppler lines in the vicinity of the third resonance 6S–8P transition of atom Cs attributed to optically induced Cs dimers *Phys. Rev. A* **83** 043402
- [39] Sarkisyan D 2009 Private communication
- [40] Obrecht J M, Wild R J and Cornell E A 2007 Measuring electric fields from surface contaminants with neutral atoms *Phys. Rev. A* **75** 062903
- [41] McGuirk J M, Harber D M, Obrecht J M and Cornell E A 2004 Alkali-metal adsorbate polarization on conducting and insulating surfaces probed with Bose–Einstein condensates *Phys. Rev. A* **69** 062905
- [42] Jahier E, Guena J, Jacquier P, Lintz M and Bouchiat M A 2001 Implementation of a sapphire cell with external electrodes for laser excitation of a forbidden atomic transition in a pulsed E-field *Eur. Phys. J. D* **13** 221–9
- [43] Sarkisyan D and Melkonyan A 1989 T-shaped leucosapphire cell for vapours of alkali-metal atoms *Instrum. Exp. Tech.* **32** 485
- [44] Laloties A, Passerat de Silans T, Maurin I, Gorza M P, Ducloy M and Bloch D 2014 arXiv:1403.3898 to be published

ARTICLE

Received 27 Mar 2014 | Accepted 10 Jun 2014 | Published 9 Jul 2014

DOI: 10.1038/ncomms5364

Casimir–Polder interactions in the presence of thermally excited surface modes

Athanasios Laliotis^{1,2}, Thierry Passerat de Silans^{1,2,3}, Isabelle Maurin^{1,2}, Martial Ducloy^{1,2} & Daniel Bloch^{1,2}

The temperature dependence of the Casimir–Polder interaction addresses fundamental issues for understanding vacuum and thermal fluctuations. It is highly sensitive to surface waves, which, in the near field, govern the thermal emission of a hot surface. Here we use optical reflection spectroscopy to monitor the atom–surface interaction potential between a $\text{Cs}^*(7D_{3/2})$ atom and a hot sapphire surface at distances of ~ 100 nm. In our experiments, that explore a large range of temperatures (500–1,000 K), the surface is at thermal equilibrium with the vacuum. The observed increase of the interaction with temperature, by up to 50%, relies on the coupling between atomic virtual transitions in the infrared range and thermally excited surface-polariton modes. We extrapolate our findings to a broad distance range, from the isolated atom to the short distances relevant to physical chemistry. Our work also opens the prospect of controlling atom–surface interactions by engineering thermal fields.

¹Laboratoire de Physique des Lasers, Université Paris 13, Sorbonne Paris-Cité, F-93430, Villetaneuse, France. ²CNRS, UMR 7538, LPL, 99 Avenue J.-B. Clément, F-93430 Villetaneuse, France. ³Laboratório de Superfície, DF-CCEN, Cx. Postal 5086 Universidade Federal de Paraíba, 58051-900 João Pessoa, Paraíba, Brazil. Correspondence and requests for materials should be addressed to A.L. (email: laliotis@univ-paris13.fr).

At the onset of the twentieth century, the spectral behaviour of black-body radiation (BBR), although a prototype of an incoherent source, has inspired the quantization of the electromagnetic field. It also inevitably led to the recognition of the existence of zero-point energy, the so-called vacuum fluctuations. Vacuum fluctuations are ultimately responsible for the finite lifetime (spontaneous emission) and a displacement of the energy states of an isolated atom (Lamb shift). In a 'hot' vacuum (vacuum and thermal fluctuations), both lifetime and Lamb shift exhibit a temperature dependence^{1,2} whose influence becomes increasingly important for ultimate optical clocks³.

Vacuum fluctuations are also responsible for the Casimir force, an attraction between two neutral bodies such as two metallic surfaces, currently considered to be of utmost fundamental importance, while also playing a considerable role in Micro and Nano-Electro-Mechanical Systems⁴. For Casimir effect studies, an exact evaluation of the temperature corrections is still required for a comparison between theory and high-precision experiments^{5–8}, which until now have always been performed at room temperature^{9,10}.

Closely related is the long-range atom–surface interaction, now generically described as the Casimir–Polder (CP) effect^{11,12}. It is of practical relevance for devices that trap atoms or molecules close to a surface, such as chips or nanofibres, intended for quantum information processing experiments^{13,14}. Again, temperature corrections may play a key role, as exemplified by measurements embarked on the search of exotic non-Newtonian gravity force¹⁵. Until now, the only measurement demonstrating a temperature dependence of the CP attraction was performed at distances 7–11 μm , where the interaction is extremely small¹⁶. Critical to experimental success was an enhancement due to an out-of-equilibrium effect¹⁷, where the surface is held at a higher temperature than the surrounding vacuum.

In the near-field regime, thermal emission exhibits properties radically different from those of the (far-field) BBR¹⁸, including spatial coherence¹⁹ and a spectrum intimately related to the resonances of the material through surface modes²⁰. For distances smaller than 100 nm, the CP interaction is in the van der Waals (vW) regime¹¹, which resembles the interaction between a fluctuating dipole and its electrostatic image in front of the surface. It is characterized by a $-C_3z^{-3}$ potential, where z is the atom–surface distance and C_3 is the vW coefficient²¹. In contrast to the far-field regime analysed in refs 16,17, the near-field CP interaction strongly depends on the dielectric properties of the surface, especially when surface modes coincide with atomic resonances²². The coupling between atoms (in the vacuum side) and surface polaritons can lead to exotic effects such as atom–surface giant attraction ($C_3 > 0$), or even repulsion ($C_3 < 0$). A negative C_3 was experimentally demonstrated in the past^{23,24} for $\text{Cs}^*(6D_{3/2})$ against a sapphire surface. Further extension to a Förster-like real energy transfer of the atomic excitation into a surface mode was also observed²⁵.

This resonant atom–surface enhanced process was intrinsically restricted to excited atoms at zero temperature ($T = 0$). Conversely, when surface polariton modes are thermally populated^{23,26,27}, the atom surface coupling is not limited to an atomic virtual emission, but can be reversed, and the vicinity with the surface can induce a virtual or real atomic excitation. With respect to the mean occupation number of photons of energy $\hbar\omega$, $n(\omega, T) = \left[e^{\frac{\hbar\omega}{k_B T}} - 1 \right]^{-1}$, only low-energy atomic transitions should contribute to this type of thermal effects: at room temperature, only modes of wavelength $> 50 \mu\text{m}$ are significantly populated. This suggests that only excited high-lying state atoms or even molecules could be sensitive to temperature effects in the near-field regime, while ground state atoms are typically excluded.

Here we report on spectroscopic measurements of the vW coefficient between a $\text{Cs}^*(7D_{3/2})$ atom and a sapphire surface as a function of temperature. We briefly discuss the theoretical predictions that justify the particular choice of the atom–surface system and present experimental observations of a sensitive temperature dependence of the CP interaction at distances on the order of 100 nm. We extrapolate our findings to a broad distance range and discuss applications that could stem from our work.

Results

Before discussing our experimental findings, we first describe the theoretical reasoning behind the choice of the specific atom–surface system. The vW coefficient for a given $|i\rangle$ level sums up the contributions of all allowed dipole couplings $|i\rangle \rightarrow |j\rangle$ of frequency ω_{ij} , considered negative in the case of virtual emission. For our experiment a schematic diagram of the Cs energy levels and the relevant couplings is shown in Fig. 1a. For an ideal conductor, one obtains simply $C_3 = \frac{1}{12} \sum_j |\langle i | \mathbf{D} | j \rangle|^2$, with $\langle i | \mathbf{D} | j \rangle$

the dipole moment matrix elements. In the case of a real dielectric, each contribution is individually weighed by an image coefficient $r(\omega_{ij}, T)$, given below²⁷:

$$r(\omega_{ij}, T) = \int_0^\infty S(iu) f(\omega_{ij}, T, u) du - 2\text{Re}[S(\omega_{ij})] n(\omega_{ij}, T) \quad (1)$$

In equation (1), the first term, sometimes called 'non-resonant', resembles a distance-dependent Lamb shift due to vacuum and thermal fluctuations covering the entire frequency spectrum. Here, u is the integration variable, $S(\omega) = [\varepsilon(\omega) - 1]/[\varepsilon(\omega) + 1]$ is the surface response (see Fig. 1b for sapphire), with $\varepsilon(\omega)$ the complex bulk permittivity of the window, and $f(\omega_{ij}, T, u)$ is a generic function that groups all other contributions and turns the integral into a discreet sum over the Matsubara frequencies, when $T \neq 0$. The second term, often called 'resonant', is reminiscent of the interaction between a classical oscillating dipole and its own reflected field^{28,29}. For virtual absorption ($\omega_{ij} > 0$), it is simply proportional to the surface response at the atomic frequency and the mean photon occupation number $n(\omega_{ij} > 0, T)$, hence null at $T = 0$ (ref. 22). For a virtual emission ($\omega_{ij} < 0$) the sign is inverted and one has to account for one additional photon due to spontaneous emission, so that $n(\omega_{ij} < 0, T) = -[1 + n(|\omega_{ij}|, T)]$. In Fig. 1c, we show the image coefficient of sapphire for a virtual absorption at different temperatures. A large temperature dependence is observed for virtual transitions whose frequency is in the vicinity of the surface polariton at 12.1 μm (830 cm^{-1}). For smaller frequencies, the two terms of equation (1) tend to compensate (inset of Fig. 1c) and temperature effects are smaller. This compensation is perfect only in the case of a dispersion-less ideal conductor³⁰. Interestingly, in the high-frequency side of the spectrum, a small but non-negligible temperature dependence is observed, despite the small number of average photons present. This can be traced back to sapphire dispersion as well³¹. In the case of virtual emission, the temperature dependence of the image coefficient is analogous and adds to the resonant behaviour at $T = 0$ mentioned above. Table 1 shows the contributions of each dipole coupling relevant for $\text{Cs}^*(7D_{3/2})$. Remarkably, the $7D_{3/2} \rightarrow 5F_{5/2}$ virtual absorption at 10.8 μm , responsible for only half of the C_3 value at low temperature, carries nearly all of the C_3 temperature dependence. Conversely, the two important virtual atomic emissions $7D_{3/2} \rightarrow 8P_{1/2}$ at 29 μm and $7D_{3/2} \rightarrow 8P_{3/2}$ at 39 μm , exhibit only small temperature dependence despite their small energy.

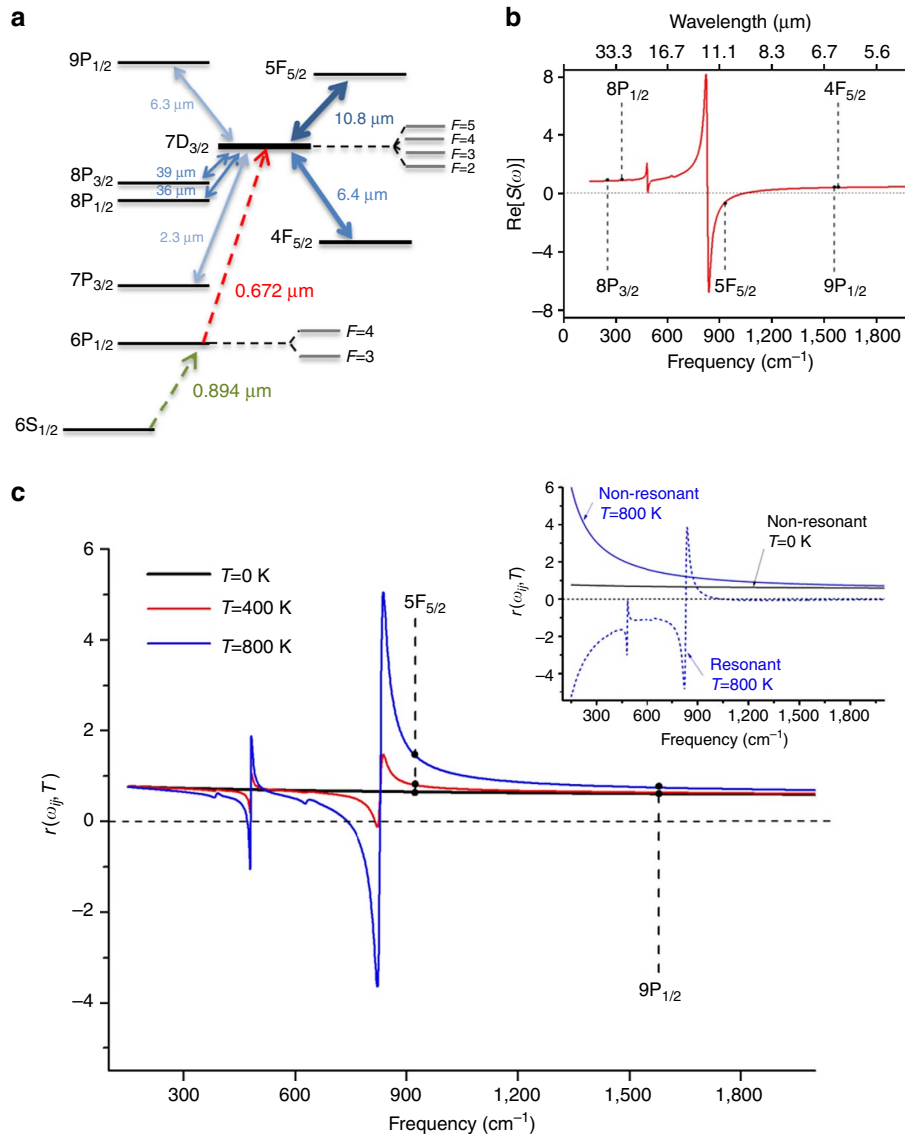


Figure 1 | Atom-surface system. (a) The Cs energy levels and the dipole transitions relevant to our experiment. The dashed arrows represent the optical excitation scheme, with pumping from the ground $6S_{1/2}$ and probing from the $6P_{1/2}$ level. (b) The real part of the sapphire surface response, $\text{Re}[S(\omega)]$. We use experimental measurements performed at room temperature given in ref. 39. The solid points show the positions of the relevant dipole coupling from $7D_{3/2}$. (c) The image coefficient of a sapphire surface for a virtual atomic absorption ($\omega_{ij} > 0$) as a function of the transition frequency for $T = 0$ K, $T = 400$ K and $T = 800$ K. The inset shows separate plots of resonant (dashed) and non-resonant (solid) contributions for $T = 800$ K and for $T = 0$ (resonant term is zero). One notes that the monotone behaviour predicted at $T = 0$ disappears at finite temperatures.

Table 1 | Contributions of individual atomic transitions.

Cs ($7D_{3/2}$)	ω (cm^{-1})	λ (μm)	C_3 (ideal conductor)	C_3 ($T = 0$ K)	C_3 ($T = 200$ K)	C_3 ($T = 400$ K)	C_3 ($T = 600$ K)	C_3 ($T = 800$ K)	C_3 ($T = 1,000$ K)
$7P_{1/2}$	-4,282.2	-2.33	0.89	0.39	0.39	0.38	0.37	0.35	0.34
$4F_{5/2}$	-1,575.4	-6.35	3.37	0.61	0.6	0.52	0.4	0.21	0
$8P_{1/2}$	-338.7	-29.52	11.49	12.09	12.09	12.42	12.89	13.53	14.17
$8P_{3/2}$	-256.1	-39.05	5.32	5.07	5.06	5.14	5.27	5.44	5.61
$5F_{5/2}$	923.7	10.83	36	23.2	23.52	28.54	37.64	48.91	61.5
$9P_{1/2}$	1,589.4	6.29	1.41	0.86	0.86	0.89	0.96	1.04	1.13
Total			59.6	42.8	43.1	48.5	58.2	70.2	83.4

The values of the global C_3 coefficient, in $\text{kHz}\mu\text{m}^3$, as well as the individual contributions of the most important dipole couplings for different temperatures. The C_3 values for an ideal conductor are also given. Here we use the values of the dielectric constant as measured at $T = 300$ K, ignoring the effects of temperature on the dielectric properties of sapphire. These are analysed in detail in ref. 39, but in our case they are negligible.

For our experimental demonstration, we use selective reflection (SR) spectroscopy on the $6P_{1/2} \rightarrow 7D_{3/2}$ line ($\lambda = 672$ nm), with a prior pumping step $6S_{1/2} \rightarrow 6P_{1/2}$ ($\lambda_p = 894$ nm). Linear SR spectroscopy on the interface between a dielectric and an atomic vapour is a long established spectroscopic method, in which the changes of the reflectivity coefficient near the atomic resonance yield information on the vapour spectrum close to the surface, typically probing a $\lambda/2\pi$ depth (~ 100 nm) largely compatible with the vW regime. SR spectroscopy, in its frequency-modulated version, has been rendered suitable for an accurate evaluation of the vW distance-dependent transition shift through numerous successive developments^{21,23,24,32–35}. Here we use an intense beam at 894 nm, resonant with the $6S_{1/2} \rightarrow 6P_{1/2}$ transition, which creates an almost uniform population of $Cs^*(6P_{1/2})$ atoms. SR spectroscopy is then performed on the $6P_{1/2} \rightarrow 7D_{3/2}$ line with a weak probe beam at 672 nm. Our experimental set-up (Fig. 2a) is similar to the one previously described in refs 23,24. Our experiment essentially measures the temperature dependence of the interaction between sapphire and $Cs^*(7D_{3/2})$, as the attraction exerted on $Cs^*(6P_{1/2})$ is negligible (< 2 kHz μm^3)³⁵.

Our measurements are conducted in an all-sapphire Cs vapour cell, shown in Fig. 2b. Sapphire has the benefit of being a robust material, reliable enough to allow the construction of a high-temperature cell³⁶ that operates at temperatures exceeding 1,000 K. The window, on which the SR experiment is performed, is ‘super-polished’ and post annealed with an average roughness of ~ 0.3 nm, measured by atomic force microscopy. A differential heating system allows an independent control of the Cs vapour density, which is governed by a low-temperature reservoir usually operated in the range of ~ 400 –450 K. A separate oven controls the

temperature of the window, which is in equilibrium with its surrounding environment. This temperature T , varied between 500 and 1,000 K, is the one relevant for the atom-surface interaction. Experimentally, we scan the frequency of the 672-nm laser, sent under a near-normal incidence on the hot sapphire window, around one of the ensemble of resolved hyperfine components, that is, either the $6P_{1/2} (F=4) \rightarrow 7D_{3/2} \{F'=3,4,5\}$, or the $6P_{1/2} (F=3) \rightarrow 7D_{3/2} \{F'=2,3,4\}$ transitions (see Fig. 1a). An auxiliary saturated absorption (SA) experiment is implemented (Fig. 2a) to provide frequency markers of the free-atom spectrum. As in refs 23,24,33–35, and thanks to the linearity of SR spectroscopy, a universal theoretical model³², taking into account the spatially inhomogeneous vW shift of the transition, the transient regime of optical interaction for moving atoms and the atomic velocity distribution, is used to fit the recorded spectra. The adjustable parameters are the vW coefficient (C_3) and the linewidth of the atomic transition (Γ).

In Fig. 3a, we present experimental spectra measured at the lowest ($T=490$ K) and the highest ($T=1,000$ K) window temperature. One notes the tremendous influence of the atom-surface interaction (see inset for $C_3=0$) and important differences in the spectra when changing temperature. The theoretical fits are in very good agreement and the difference with the experimental curves is hardly visible at this scale. The linewidth of the atomic transition is kept constant in both experiments so that the changes in the shape of the spectra can be traced directly back to the change of the C_3 coefficient. Figure 3b presents several other spectra for three indicative values of the window temperature ($T=520$ K, $T=750$ K and $T=1,000$ K). Excellent fittings are observed in all cases and the evolution of the fitting parameters demonstrates a clear increase of the strength of the atom-surface interaction with temperature. We have performed various independent tests to check the consistency of our measurements, in the same way as in ref. 23. For a given window temperature, we notably vary the Cs vapour pressure by changing the reservoir temperature, therefore changing the value of Γ due to collision broadening. These changes, although affecting the amplitude and shape of our spectra, do not modify the fitted C_3 values. In addition, when comparing the two different hyperfine manifolds, one observes strong differences in the overall shape of the curves owing to the different relative weight of each hyperfine transition, but identical values for C_3 and Γ are extracted for both spectra (Fig. 3c). Our measurements were also performed for many different spots on the sapphire window, with no significant changes. This is a crucial point because local structure variations (for example, roughness) or impurities (defects or ions) may severely affect atom-surface interaction and bias our measurements^{37,38}. Consistent measurements were even found for a set of preliminary measurements performed in a sapphire cell with a lower surface quality. These precautions also assure us that no chemical degradation of the surface occurs with continuous exposure on chemically aggressive alkali vapour at elevated temperatures. Previous efforts to look for strong thermal effects predicted to occur at moderate temperatures for $Cs^*(8P)$ ^{34,35,39} close to fluoride windows whose surface resonances fall in the 30–40 μm range had turned out to be unsuccessful⁴⁰ due to the extreme mechanical and thermal fragility of fluoride windows. On the contrary, sapphire has been remarkably stable under these extreme conditions.

Our experimental results are summarized in Fig. 4. The experimental error bar for C_3 is on the order of 15% when fitting a single spectrum (see Fig. 7 of ref. 40), but reduces down to 5–10% after using all our independent measurements. One observes a significant increase of the vW coefficient with temperature ($\sim 50\%$ from 500 to 1,000 K), which is in excellent

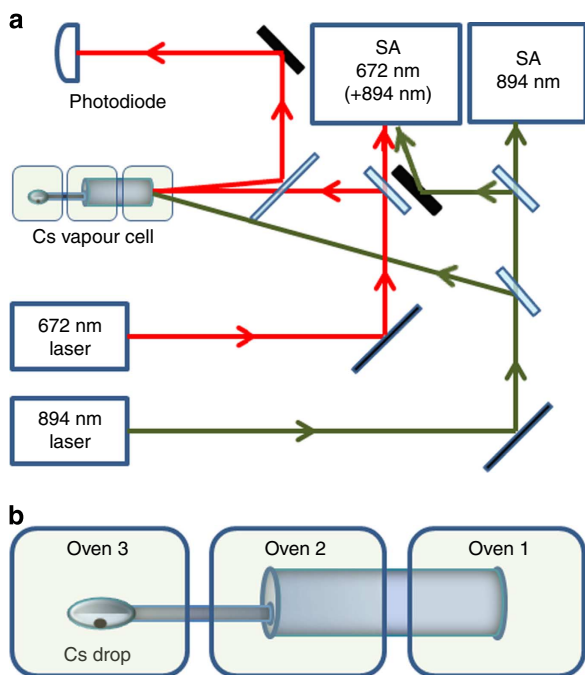


Figure 2 | Experimental set-up and Cs vapour cell. (a) Schematic of the experimental set-up. The essential experiment is a frequency-modulated (FM) SR at normal incidence at 672 nm, the oblique irradiation at 894 nm beam pumps the atoms to the intermediate $6P_{1/2}$ level; the two SA experiments, at 894 nm ($6S_{1/2} \rightarrow 6P_{1/2}$), and at 672 nm ($6P_{1/2} \rightarrow 7D_{3/2}$), are respectively used for the locking and monitoring of the laser frequencies. (b) Schematic of the heated Cs cell with sapphire windows showing the differential heating, allowing separate control of the atomic vapour density, and of the window temperature.

agreement with the theoretical prediction, unambiguously demonstrating the fundamental thermal effects on the CP interaction. Our prediction requires the knowledge of the transition probabilities⁴¹ and of the dielectric constant of sapphire on the entire spectrum. This introduces some small uncertainty in the theoretical values. The major contributing factor comes from the transition probabilities, which are not accurately known for all dipole couplings. We use theoretical estimates given in ref. 41 to which we moderately assign a 5% uncertainty. In Fig. 4, we also show theoretical predictions using two different sets of experimental measurements^{39,42} of the sapphire dielectric constant. The former³⁹ analyses in detail the effects of temperature (up to 800 K) on the dielectric constant of sapphire. The latter⁴² also provides data for the sapphire

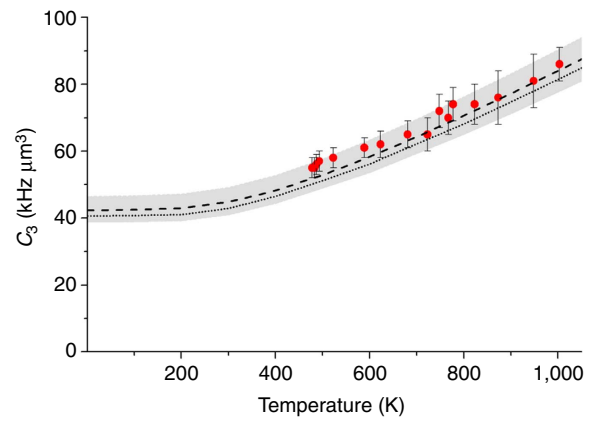


Figure 4 | Experiment versus theory. The C_3 (van der Waals) coefficient as a function of temperature: red points represent experimental measurements. The dotted and dashed lines, respectively, represent theoretical predictions using the dielectric constant of sapphire reported in refs 39,42. The grey shaded area of 5% plotted around the theoretical curves represents the uncertainty assigned to the transition probabilities.

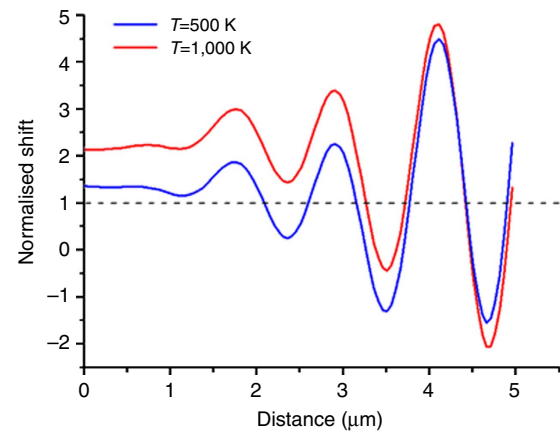
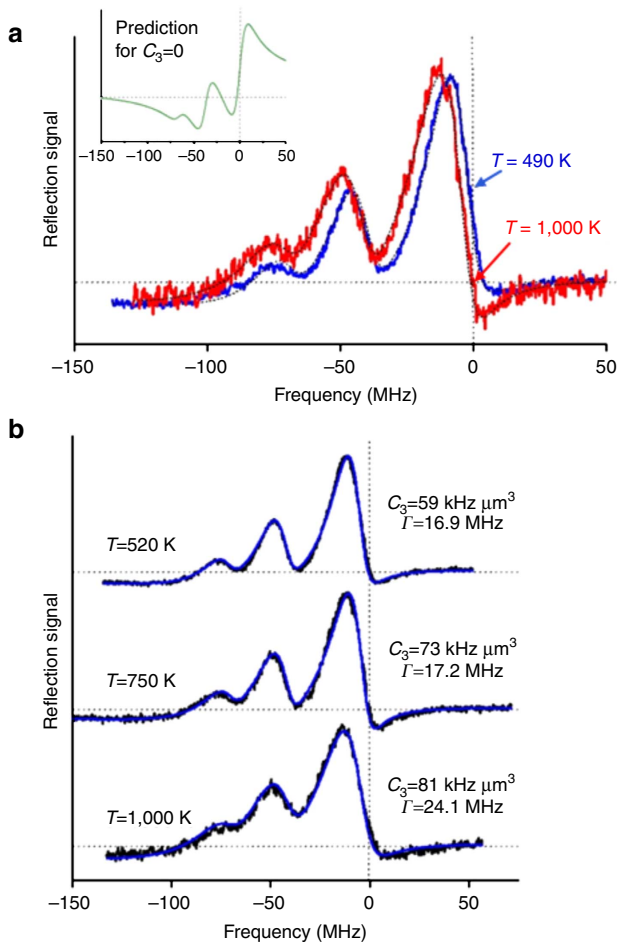


Figure 5 | Distance dependence of the CP interaction. Spatial dependence of the free energy shift of the Cs($7D_{3/2}$) atom in front of a sapphire surface, for $T=500$ K (blue) and $1,000$ K (red), normalized to the spatially varying van der Waals electrostatic limit, $-C_3(T=0)/z^3$ (dashed black line).

Figure 3 | Experimental spectra and theoretical fits. (a) Normalised frequency modulated (FM) SR spectra on the $6P_{1/2} (F=4) \rightarrow 7D_{3/2} (F=3, 4, 5)$ transition (672 nm) for a window temperature at $T=490$ K (blue) and at $T=1,000$ K (red). The frequency axis is referenced to the hyperfine component of the $6P_{1/2} (F=4) \rightarrow 7D_{3/2} (F=5)$ transition as determined by the auxiliary SA. In the inset, we show the predicted FM SR spectrum in the absence of atom-surface interaction, that is, $C_3=0$. The observed shift and lineshape distortion of the experimental curves are a clear evidence of the atom-surface interaction. The lower signal/noise ratio for $1,000$ K window is further discussed in the Methods section. The dashed black lines are the respective theoretical fits, demonstrating the same linewidth for both temperatures $\Gamma=19$ MHz and an increase of C_3 with temperature from 55 to 86 $\text{kHz } \mu\text{m}^3$ (b) Experimental spectra (black) for FM SR at the $F=4 \rightarrow F=\{3,4,5\}$ hyperfine manifold for various window temperatures along with the corresponding theoretical fits (blue). The parameters used to fit the spectra are also indicated. (c) Experimental measurements (black) with their respective theoretical fits for $F=4 \rightarrow F=\{3,4,5\}$ (blue) and $F=3 \rightarrow F=\{2,3,4\}$ (red) manifold at identical conditions for both window temperature and vapour pressure/density. Despite the difference in the shape of the curves, the fit gives identical values for both $C_3=64$ $\text{kHz } \mu\text{m}^3$ and $\Gamma=16$ MHz. The window temperature is $T=630$ K.

dielectric constant on the extraordinary axis, which, in our experiment, is perpendicular to the window. Taking sapphire birefringence into account⁴³ has a small effect on our theoretical predictions. Further calculations show that the atom–surface interaction is independent of the actual axis orientation of sapphire to within 1%. Note that the uncertainties of the dielectric constant of sapphire may have a significant impact if a virtual transition coincides with surface polariton frequency.

Discussion

To extrapolate our findings to a larger scope and a variety of regimes, we also considered the effects of propagation for our Cs*(7D_{3/2})/sapphire system. Figure 5 shows for various temperatures the spatial evolution of the atom–surface interaction potential, as determined through a full quantum electrodynamics calculation. It confirms the validity of the $-C_3z^{-3}$ vW limit at any temperature for distances up to 100–200 nm, typically probed by SR spectroscopy. The typical evolution of the shift of a ground state atom, from z^{-3} (vW) to z^{-4} (CP asymptotic limit), and then after distances greater than the ‘thermal length’ back to z^{-3} (Lifshitz regime)^{16,17}, is unnoticeable. Rather, the major correction to the vW limit is an oscillating behaviour from attraction to repulsion with an envelope decreasing slower than z^{-3} , typical of an excited atom due to the reflection of spontaneous emission²⁸. In particular, the major contribution to oscillations comes from the 7D_{3/2} → 7P_{3/2} transition at 2.33 μm for which propagation effects ‘switch on’ much closer to the surface. Temperature dependence is small in this distance regime due to the absence of thermal photons at this wavelength. Thermal effects are the strongest in the near field as a consequence of the surface polariton. We point out here that our calculations give the free energy shift (see ref. 27 and references therein) due to the presence of the hot surface, ignoring the effects of BBR on an isolated atom. Taking into account this effect, discussed in detail in ref. 1, the thermal contribution to the CP shift is dominant only when the atom is < 1 μm away from the surface.

The distance limit that our experiments explore extends down to the nanometric range (~ 1 nm). This distance is already in the asymptotic ‘long-distance’ limit for various physical chemistry processes, of interest for *a priori* calculations^{44,45}. Our result demonstrating that the CP attraction increases with temperature contradicts the generally accepted behaviour of thermal desorption. This should, nonetheless, be taken with a grain of salt, as the vW potential measured here is for an atomic excited state. However, our fundamental studies can provide new insights for the microscopic understanding of physico-chemical processes. As an example, in a temperature-dependent desorption process the thermally excited surface modes may selectively enhance a channel of energy transfer⁴⁶, thus favouring a particular energy state for the desorbed atom or molecule.

In conclusion, we have established that the interaction between a Cs*(7D_{3/2}) atom close to a hot sapphire surface, in thermal equilibrium with the environment, increases with temperature. This effect relies on the coupling of atomic excitations to surface polariton modes, which is critical in the vW regime of distances. A very good quantitative agreement with theory is observed. The influence of temperature reveals the quantum electrodynamics nature of the van der Waals interaction and may provide a useful knob to control forces between neutral atoms and surfaces up to their complete cancellation or change of sign. It is in particular possible to extend, with temperature as an extra parameter, the current studies on the Casimir interaction with specially designed nano- or microstructured surfaces, where the shaping allows tailoring the thermal field and possibly the interaction (repulsion

and torque). Atoms may also be used as sensitive quantum probes of coherent thermal fields¹⁹ or even of the correlated properties of thermal emission^{47,48}. An alternative geometry would be a thin vapour cell^{38,49}, which is a simple realization of a dielectric cavity, and an example of a situation where the temperature-dependence of surface interaction should depend on the surface geometry⁵⁰.

Methods

Thermal equilibrium in the vapour cell. A schematic of the specially designed Cs cell, prepared by the group of D. Sarkisyan (Ashtarak, Armenia), is shown in Fig. 2b. It consists of a 10-cm-long cylindrical sapphire tube onto which two sapphire windows are glued. The primary window is ‘super-polished’ with the *c* axis perpendicular to the surface. It has a small wedge allowing us to select the reflection from the vapour interface. The mineral gluing is capable to resist temperatures up to 1,200 K. The secondary window is of a lower surface quality. The 7-cm-long sidearm, parallel to the cell’s main body, is glued on a small hole drilled on the secondary window.

For this sidearm Cs cell, we have implemented a multiple section oven around the whole cell. Oven 1, ~ 5 cm long, controls the temperature of primary window region. It keeps the sapphire window in thermal equilibrium with the surrounding BBR. The temperature inside oven 1 can be chosen in the 500–1,000 K range. For such temperatures, the Cs vapour pressure would be considerable, and pressure broadening too high for any meaningful SR measurements. Ovens 2 and 3, also ~ 5 cm long each, impose a large temperature gradient on the entire cell and keep the sidearm as a ‘cold spot’ of the cell, where Cs condenses in liquid form. Oven 3 controls the temperature of the sidearm and, therefore, the Cs vapour pressure inside the cell. It is typically kept at temperatures around 400–450 K corresponding to a Cs equilibrium atom density ~ 10¹⁴–10¹⁵ cm⁻³.

The temperature of each oven is measured with thermocouples, whose location can be moved, to evaluate the temperature homogeneity of the oven. Our readings inside oven 1 confirm that temperature is homogeneous to within 10–20 K. It is important to notice that the implementation of the differential heating in the Cs cell generates a temperature gradient on a length scale (~ 10 cm), which does not impact the temperature relevant for the atom–surface interaction. In addition, our measurements probe an atom–surface interaction at the level of a single atom, making the ‘temperature’ of the atomic vapour, as an ensemble of moving atoms, irrelevant for our investigation.

Atomic vapour and optical pumping. For our SR measurements, Cs atoms are first pumped to the 6P_{1/2} level, by an 894 nm pump laser. The role of this pump laser is to provide a quasi-thermal velocity distribution of Cs*(6P_{1/2}) atoms at the Cs vapour interface. This was already achieved in previous experiments^{23,24}. We benefit from collisions, which redistribute the 6P_{1/2} excitation to all velocities of both hyperfine components. To avoid any velocity-selective pumping, the pump laser frequency is resonant to the 6P_{1/2} hyperfine level, which is not directly probed by the 672-m SR laser (for example, pump reaching the 6P_{1/2} (*F* = 4) level and probe starting from the 6P_{1/2} (*F* = 3) level, or vice versa). The penetration depth of the pumping beam is usually several tens of microns (depending on the exact beam intensity and Cs vapour density).

The cell structure and multiple oven design means that the atomic gas is not in equilibrium. Because of collisions, one expects a uniform pressure throughout the cell and a Cs velocity distribution that depends primarily on the local surface temperature. This implies that the Cs density is locally smaller in the hottest areas of the cell, while simultaneously the atomic velocity distribution gets broader. As a result, the SR signal reduces when increasing the temperature of the primary window. This is clearly observed in our measurements (Fig. 3a).

Optical set-up. A distributed bragg reflector laser at 894 nm is used to pump the atoms to the 6P_{1/2} intermediate level. The pumping beam is relatively of high power, ~ 10 mW, with a waist of ~ 800 μm, and can be sent to the cell on an oblique incidence, practically limited by the geometry of oven 1. An extra on/off amplitude modulation is applied to the pump beam with an acousto-optic modulator, at a frequency of 10 kHz, to improve detection sensitivity. The pump frequency is locked through an auxiliary set-up of SA at 894 nm.

The SR probe is an extended cavity laser at 672 nm. The probe beam is slightly smaller, ~ 500 μm waist, to ensure a complete overlap with the pump, and less powerful, ~ 50 μW, to avoid saturating the atoms. It is sent to the sapphire window under nearly-normal incidence (on the order of 10 mrad). The laser frequency is scanned by applying a voltage on the piezoelectric element attached to the external grating. The laser is frequency modulated at 1 kHz, with ~ 5 MHz amplitude. An auxiliary SA experiment and a low finesse Fabry–Perot cavity provide us with frequency markers. An improved method of controlling the frequency scan by beating the probe with a frequency-locked reference laser was also used without any observable improvement in the quality of our SR spectra fits. The reflection of the probe beam is measured with a low-noise photodiode and then demodulated with two cascaded lock-in amplifiers. The atomic signal is typically between four and five orders of magnitude smaller than the reflection from the sapphire/vapour interface.

Fitting method. C_3 measurements are extracted by fitting experimental spectra to a library of theoretical curves depending on a dimensionless parameter ($A = 2C_3 \Gamma^{-1} (2\pi/\lambda)^3$, with Γ the optical linewidth). Linearity of SR spectroscopy imposes the relative amplitudes and the frequency spacing of the hyperfine components of a given manifold to their theoretical values. The experimental spectrum is compared with a theoretical curve, of a given A , by dilating the frequency axis, to obtain $\Gamma^{23,24,32-35}$. We also allow for an overall offset of the spectrum and adjustment of the global amplitude of the theoretical curve to reflect experimental instabilities. We then change the dimensionless A value and repeat the process until the best fit is identified. This provides a measurement of the C_3 coefficient and the transition linewidth $\Gamma^{23,24,32-35}$. We also allow for a global pressure shift (the same for all hyperfine components). When the above rigid constraints are used, the small differences between the fits and the experimental spectra are probably not entirely of statistical nature. In previous works (see pages 247–248 of ref. 24), we have used the frequency spacings and the relative amplitudes between the hyperfine components as free parameters. This slightly improves the fit quality but has negligible effects on the measured values of C_3 and Γ . In the experiment described here, we have restricted the number of free parameters to a minimum. The error bars are conservatively chosen by identifying the values of C_3 and Γ , for which the fit curve falls clearly outside the bounds defined by the noise of the experimental curve⁴⁰. We can also account for a finite Doppler width correction²⁴, as the theoretical modelling is essentially developed in the infinite Doppler width approximation. This correction mostly modifies the wings of the SR spectrum. Here, we can safely ignore this correction (attempted for some fittings with no significant changes). This is probably because the width of the hyperfine manifold, which determines the overall lineshape, is much smaller than the Doppler width.

References

- Farley, J. W. & Wing, W. H. Accurate calculation of dynamic Stark shifts and depopulation rates of Rydberg energy levels induced by blackbody radiation. Hydrogen, helium and alkali-metal atoms. *Phys. Rev. A* **23**, 2397–2424 (1981).
- Hollberg, J. & Hall, J. L. Measurement of the Shift of Rydberg energy levels induced by blackbody radiation. *Phys. Rev. Lett.* **53**, 230–233 (1984).
- Bloom, B. J. *et al.* An optical lattice clock with accuracy and stability at the 10^{-18} level. *Nature* **506**, 71–75 (2014).
- Chan, H. B., Aksyuk, V. A., Kleiman, R. N., Bishop, D. J. & Capasso, F. Quantum mechanical actuation of microelectromechanical systems by the Casimir force. *Science* **291**, 1941–1944 (2001).
- Mohideen, U. & Roy, A. Precision measurement of the Casimir force from 0.1 to 0.9 μm . *Phys. Rev. Lett.* **81**, 4549–4552 (1998).
- Boström, M. & Sernelius, B. E. Thermal effects on the Casimir force in the 0.1–5 μm range. *Phys. Rev. Lett.* **84**, 4757–4760 (2000).
- Genet, C., Lambrecht, A. & Reynaud, S. Temperature dependence of the Casimir effect between metallic mirrors. *Phys. Rev. A* **62**, 012110 (2000).
- Sushkov, A. O., Kim, W. J., Dalvit, D. A. R. & Lamoreaux, S. K. Observation of the thermal Casimir force. *Nat. Phys.* **7**, 230–233 (2010).
- Laurent, J., Sellier, H., Mosset, A., Huan, S. & Chevrier, J. Casimir force measurements in Au-Au and Au-Si cavities at low temperature. *Phys. Rev. B* **85**, 035426 (2012).
- Castillo-Garza, R. & Mohideen, U. Variable-temperature device for precision Casimir-force-gradient measurement. *Rev. Sci. Instrum.* **84**, 025110 (2013).
- Casimir, H. B. G. & Polder, D. The influence of retardation on the London-van der Waals forces. *Phys. Rev.* **73**, 360–372 (1948).
- Sukenik, C. I., Boshier, M. G., Cho, D., Sandoghdar, V. & Hinds, E. A. Measurement of the Casimir-Polder force. *Phys. Rev. Lett.* **70**, 560–563 (1993).
- Sagué, C., Vetsch, E., Alt, W., Meschede, D. & Rauschenbeutel, A. Cold-atom physics using ultrathin optical fibers: light-induced dipole forces and surface interactions. *Phys. Rev. Lett.* **99**, 163602 (2007).
- Chang, D. E., Sinha, K., Taylor, J. M. & Kimble, H. J. Trapping atoms using nanoscale quantum vacuum forces. Preprint at <http://arxiv.org/abs/1310.5970> (2013).
- Harber, D. M., Obrecht, J. M., McGuirk, J. M. & Cornell, E. A. Measurement of the Casimir-Polder force through center-of-mass oscillations of a Bose-Einstein condensate. *Phys. Rev. A* **72**, 033610 (2005).
- Obrecht, J. M. *et al.* Measurement of the temperature dependence of the Casimir-Polder force. *Phys. Rev. Lett.* **98**, 063201 (2007).
- Antezza, M., Pitaevskii, L. P. & Stringari, S. New asymptotic behavior of the surface-atom force out of thermal equilibrium. *Phys. Rev. Lett.* **95**, 113202 (2005).
- Babut, A., Joulain, K., Chapuis, P. O., Greffet, J. J. & De Wilde, Y. Blackbody spectrum revisited in the near field. *Phys. Rev. Lett.* **110**, 146103 (2013).
- Greffet, J. J. *et al.* Coherent emission of light by thermal sources. *Nature* **416**, 61–64 (2002).
- Shchegrov, A. V., Joulain, K., Carminati, R. & Greffet, J. J. Near-field spectral effects due to electromagnetic surface excitations. *Phys. Rev. Lett.* **85**, 1548–1551 (2000).
- Bloch, D. & Ducloy, M. In: *Advances in Atomic, Molecular and Optical Physics* vol. 50 (eds Bederson, B. & Walther, H.) (Elsevier Academic 91–156, 2005).
- Fichet, M., Schuller, F., Bloch, D. & Ducloy, M. van der Waals interactions between excited-state atoms and dispersive dielectric surfaces. *Phys. Rev. A* **51**, 1553–1564 (1995).
- Failache, H., Saltiel, S., Fichet, M., Bloch, D. & Ducloy, M. Resonant van der Waals repulsion between excited Cs atoms and sapphire surface. *Phys. Rev. Lett.* **83**, 5467–5470 (1999).
- Failache, H., Saltiel, S., Fichet, M., Bloch, D. & Ducloy, M. Resonant coupling in the van der Waals interaction between an excited alkali atom and a dielectric surface an experimental study via stepwise spectroscopy. *Eur. Phys. J. D* **23**, 237–255 (2003).
- Failache, H., Saltiel, S., Fischer, A., Bloch, D. & Ducloy, M. Resonant quenching of gas-phase Cs atoms induced by surface polaritons. *Phys. Rev. Lett.* **88**, 243603 (2002).
- Barton, G. van der Waals shifts in an atom near absorptive dielectric mirrors. *Proc. R. Soc. (London) A* **453**, 2461–2495 (1997).
- Gorza, M. P. & Ducloy, M. Van der Waals interactions between atoms and dispersive surfaces at finite temperature. *Eur. Phys. J. D* **40**, 343–356 (2006).
- Hinds, E. A. & Sandoghdar, V. Cavity QED level shifts of simple atoms. *Phys. Rev. A* **43**, 398–403 (1991).
- Wylie, J. M. & Sipe, J. E. Quantum electrodynamics near an interface. II. *Phys. Rev. A* **32**, 2030–2043 (1985).
- Ellingsen, S., Buhmann, S. Y. & Scheel, S. Temperature-independent casimir-polder forces despite large thermal photon numbers. *Phys. Rev. Lett.* **104**, 223003 (2010).
- Saltiel, S., Bloch, D. & Ducloy, M. A tabulation and critical analysis of the wavelength dependent dielectric image coefficient for the interaction exerted by the surface onto a neighbouring excited atom. *Optics Commun.* **265**, 220–233 (2006).
- Ducloy, M. & Fichet, M. General theory of frequency modulated selective reflection: Influence of atom surface interactions. *J. Phys. II France* **1**, 1429–1446 (1991).
- Chevrollier, M. *et al.* High resolution selective reflection spectroscopy as a probe of long-range surface interaction: measurement of the surface van der Waals attraction exerted on excited Cs atoms. *J. Phys. II France* **2**, 631–657 (1992).
- Chaves de Souza Segundo, P., Hamdi, I., Fichet, M., Bloch, D. & Ducloy, M. Selective reflection spectroscopy on the UV-resonance line of Cs: simultaneous probing of the van der Waals atom-surface interaction sensitive to far IR couplings and interatomic collisions. *Laser Phys.* **17**, 938–992 (2007).
- Lalot, A. *et al.* Selective reflection spectroscopy at the interface between a calcium fluoride window and Cs vapour. *Appl. Phys. B* **90**, 415–420 (2008).
- Sarkisyan, D., Hinze, U., Meyer, L. & Wellegenhausen, B. Efficient cw sodium Raman laser operation in a high temperature sapphire cell. *Appl. Phys. B* **70**, 351–354 (2000).
- Obrecht, J. M., Wild, R. J. & Cornell, E. A. Measuring electric fields from surface contaminants with neutral atoms. *Phys. Rev. A* **75**, 062903 (2007).
- Fichet, M. *et al.* Exploring the van der Waals Atom-Surface attraction in the nanometric range. *Europhys. Lett.* **77**, 54001 (2007).
- Passerat de Silans, T. *et al.* Temperature dependence of the dielectric permittivity of CaF_2 , BaF_2 and Al_2O_3 : application to the prediction of a temperature-dependent van der Waals surface interaction exerted onto a neighbouring $\text{Cs}(8P_{3/2})$ atom. *J. Phys. Condens. Matter* **21**, 255902 (2009).
- Passerat de Silans, T. *et al.* Experimental observations of temperature effects in the near-field regime of the Casimir-Polder interaction. *Laser Phys.* **24**, 074009 (2014).
- Lindgard, A. & Nielsen, S. E. Transition probabilities for the alkali isoelectronic sequences Li, Na, K, Rb, Cs, Fr. *Atomic Data Nuclear Tables* **19**, 533–633 (1977).
- Barker, A. S. Infrared lattice vibrations and dielectric dispersion in corundum. *Phys. Rev.* **132**, 1474–1481 (1963).
- Gorza, M. P., Saltiel, S., Failache, H. & Ducloy, M. Quantum theory of van der Waals interactions between atoms excited state atoms and birefringent dielectric surfaces. *Eur. Phys. J. D* **15**, 113–126 (2001).
- Tao, J., Perdew, J. P. & Ruzsinszky, A. Accurate van der Waals coefficients from density functional theory. *Proc. Natl Acad. Sci. USA* **109**, 18–21 (2012).
- Gobre, V. V. & Tkatchenko, A. Scaling laws for van der Waals interactions in nanostructured materials. *Nat. Commun.* **4**, 2341 (2013).
- Buhmann, S. Y., Tarbutt, M. R., Scheel, S. & Hinds, E. A. Surface-induced heating of cold polar molecules. *Phys. Rev. A* **78**, 052901 (2008).
- Klaers, J., Schmitt, J., Vewinger, F. & Weitz, M. Bose-Einstein condensation of photons in an optical microcavity. *Nature* **468**, 545–548 (2010).
- Carusotto, I. & Ciuti, C. Quantum fluids of light. *Rev. Mod. Phys.* **85**, 299–366 (2013).
- Kubler, H., Shaffer, J. P., Baluktian, T., Löw, R. & Pfau, T. Coherent excitation of Rydberg atoms in micrometre-sized atomic vapour cells. *Nat. Photon* **4**, 230–233 (2010).
- Lai, K. S. & Hinds, E. A. Blackbody excitation of an atom controlled by a tunable cavity. *Phys. Rev. Lett.* **81**, 2671–2674 (1998).

Acknowledgements

It is a pleasure to thank J.R. Rios Leite for fruitful and fascinating discussions, as well as for his long-standing interest in our work, M.-P. Gorza, P. Chaves de Souza Segundo and H. Failache for early contributions to this work and numerous discussions, D. Sarkisyan for the fabrication of high-temperature cells and G. Pichler for kindly lending us a sapphire vapour cell. The France–Brazil co-operation has been supported by CAPES-COFECUB Ph 740/12 and 456-04.

Author contributions

The experiment was built by A.L. with the participation of T.P. The oven system was built by I.M. with the participation of A.L. Data collection was performed by A.L., T.P. and I.M. Fitting the spectra was done by A.L. and I.M. The numerical calculation of the C3 coefficient was done by A.L. and I.M. The evaluation of the CP interaction as a function of distance were done by A.L. and M.D. Physical interpretation of temperature

effects was done mainly by A.L. and D.B., with the participation of I.M., T.P. and M.D. The manuscript was written by A.L. and D.B.

Additional information

Supplementary Information accompanies this paper at <http://www.nature.com/naturecommunications>

Competing financial interests: The authors declare no competing financial interests.

Reprints and permission information is available online at <http://npg.nature.com/reprintsandpermissions/>

How to cite this article: Laliotis, A. *et al.* Casimir-Polder interactions in the presence of thermally excited surface modes. *Nat. Commun.* 5:4364 doi: 10.1038/ncomms5364 (2014).

Three-dimensional confinement of vapor in nanostructures for sub-Doppler optical resolution

Philippe Ballin, Elias Moufarej, Isabelle Maurin, Athanasios Laliotis, and Daniel Bloch

Citation: *Appl. Phys. Lett.* **102**, 231115 (2013); doi: 10.1063/1.4809668

View online: <http://dx.doi.org/10.1063/1.4809668>

View Table of Contents: <http://apl.aip.org/resource/1/APPLAB/v102/i23>

Published by the [American Institute of Physics](#).

Additional information on *Appl. Phys. Lett.*



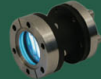



Journal Homepage: <http://apl.aip.org/>

Journal Information: http://apl.aip.org/about/about_the_journal

Top downloads: http://apl.aip.org/features/most_downloaded

Information for Authors: <http://apl.aip.org/authors>

ADVERTISEMENT

<p>a sampling of our products</p>		<p>for surface and materials science</p>	<p>www. rbdinstruments .com</p>	<p>celebrating over 20 years of innovation</p>
				
<p>deposition tools</p>	<p>desorption systems</p>	<p>sputter ion sources</p>	<p>viewports</p>	<p>usb picoammeters</p>

Three-dimensional confinement of vapor in nanostructures for sub-Doppler optical resolution

Philippe Ballin, Elias Moufarej, Isabelle Maurin, Athanasios Laliotis, and Daniel Bloch^{a)}

Laboratoire de Physique des Lasers, Université Paris 13, Sorbonne Paris-Cité, France and CNRS, UMR 7538, 99 Avenue J.-B. Clément, F-93430 Villetaneuse, France

(Received 22 March 2013; accepted 4 May 2013; published online 11 June 2013)

We confine a Cs thermal vapor in the interstitial regions of a glass opal. We perform linear reflection spectroscopy on a cell whose window is covered with a thin film (10 or 20 layers) of ~ 1000 nm (or 400 nm) diameter glass spheres and observe sub-Doppler structures in the optical spectrum for a large range of oblique incidences. This original feature associated with the inner (3-dimensional) confinement of the vapor in the interstitial regions of the opal evokes a Dicke narrowing. We finally consider possible micron-size references for optical frequency clocks based on weak, hard to saturate, molecular lines. © 2013 AIP Publishing LLC. [<http://dx.doi.org/10.1063/1.4809668>]

Free atom and molecules are the elementary components providing universal frequency references, in the radiofrequency (*r.f.*) and optical domains as well, but the size of the corresponding devices (clocks) is large. The ultimate performances allowed by laser-cooled atoms or ions require huge cooling and trapping volumes. Simpler systems, based upon a thermal vapor, still remain bulky because a low gas density is required to minimize collisions, and also because the free molecules must be kept far away from the surface. For many applications, including communication technologies, there is an urgent need to develop compact frequency references of various levels of accuracy. Pushing conventional vapor technologies up to their minimal size limits, an integrated optical (*r.f.*) clock device as small as a “grain of rice” was demonstrated,¹ relying on known macroscopic techniques.

Recently, vapor phase spectroscopy has started to be combined with the realm of micro- and nanostructures.^{2–13} Meter-long holey or photonic fibers, sealed with a vapor inside,^{2–5} have allowed “all-fibered cell” with a two-dimensional (2-D) confinement; aside from the size reduction, a benefit is the possibility of enhanced nonlinear optical effects.^{2,3} The pores of a glassy medium have been used as an atomic vapor container, but only the free alkali-metal atoms having escaped outside the porous glass were observed for a 7–30 nm pore size.⁶ An interest of such a system is that a specific desorption process allows controlling the atomic density independently of the thermodynamic equilibrium (light-induced atomic desorption “LIAD” atomic dispenser). Spectroscopy inside the interstitial regions⁷ could be performed for larger pores. Multiple photon scattering increases the effective absorption length, but broad resonances are imposed by the high-density of the molecular gas and by transit time. Until now, the major Doppler broadening, associated to thermal molecular motion, could not be eliminated for these 2-D or 3-D confined vapors, except with a holey fiber, when using a nonlinear scheme of saturated absorption (SA) spectroscopy and a rather large confinement.^{4,5} Moreover, tightening the confinement (e.g., from a 20 μm diameter core to 10 μm)⁴ causes a broadening owing

to transit time, in spite of a possible enhancement of the contribution of slow atoms.⁵

In the work of our group,^{8–11} notable spectroscopic advantages, including Doppler-free resonances in nonlinear⁸ and linear spectroscopy,^{9,10} and sensitivity to atom-surface interaction,¹¹ were demonstrated for 1-D confinement (possibly down to <100 nm). This 1-D confinement proves now useful for noticeable demonstrations of collective effects such as Rydberg blockade¹² and cooperative Lamb shift,¹³ but it uses a bulky technology.

Here, we probe Cs atoms confined in the sub-micronic interstitial regions of an opal made of glass spheres of diameter $d \sim 1 \mu\text{m}$ or (alternatively) $d \sim 400$ nm. Working on the D_1 and D_2 resonance line doublet of Cs ($\lambda_1 = 894$ nm and $\lambda_2 = 852$ nm), we demonstrate sub-Doppler structures in the linear regime induced by the 3-D confinement of the vapor.

To construct our sealed Cs vapor cells (cylindrical glass tube with a reservoir and two windows, length ~ 4 cm, diameter ~ 4 cm, see Fig. 1), one of the window is partially coated with a thin opal, self-organized layer-by-layer through a soft chemistry technique of Langmuir-Blodgett deposition.¹⁴ The cohesion of the opal, only resulting from the weak van der Waals contact forces, is further enhanced through annealing. Dispersion in the size of the glass spheres make the opal polycrystalline. An approximate compact arrangement combining *f.c.c.* and *h.c.* structures is expected, with compacity defects increasing with successively deposited layers.¹⁴ Once filled with Cs, the opals become greenish or even dark, a signature of the generation of alkali clusters favored by the trapping of Cs atoms in the interstitial regions of the opal. This effect jeopardized our initial attempts to work with massive opals of small spheres.¹⁵ For thin opals, extra-heating of the window (typically, $T_{\text{window}} \sim 180\text{--}200$ °C for $T_{\text{reservoir}} \leq 110$ °C) returns the opals (10 or 20 layers) with $d \sim 1 \mu\text{m}$ spheres to its initial light milky appearance. For a 10 layers opal cell with $d \sim 400$ nm spheres, a slight coloring always remains, but consistent results are still obtained. The vapor density, measured by independent spectroscopic experiments, appears unaffected by residual trapping of Cs inside the opal.

Optically, a thin opal is a transparent scattering medium. The transmission for 10 layers is less than 1% when the sphere size ($d \sim 1 \mu\text{m}$) compares with the (near IR)

^{a)}E-mail: daniel.bloch@univ-paris13.fr

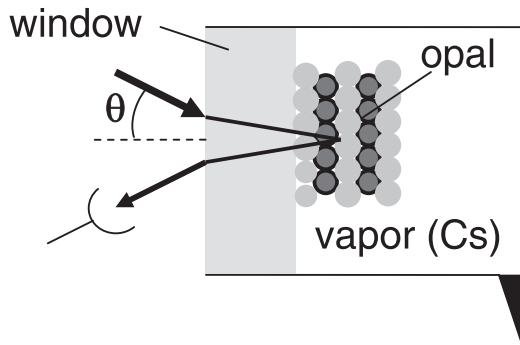


FIG. 1. Schematic of the experiment, with 5 layers of (enlarged) nanospheres. The second and fourth layers are darker to show the compact arrangement.

wavelength of Cs (for the opal with $d \sim 400$ nm spheres, the initial 30%–50% transmission decreases due to the Cs coloring). Remarkably, the “corrugated” nature of the window/opal interface (Fig. 1) does not prevent the observation of specular reflection from the opal-covered window. Under normal incidence, the reflectivity on this side is comparable to the one (4%) at the flat air/window (input) interface; for oblique incidences, reflectivity becomes polarization-dependent, with a Brewster-like (quasi-null) minimum for TM reflection.¹⁶ The monitoring of reflectivity (“reflection spectroscopy”) is the basis of our spectroscopic analysis.

The origin of this reflection is a complex nano-optics problem because scattering occurs here on a dimension comparable to the wavelength. We have developed two approaches, considering either a stratified medium with an effective index governed by the (planar) filling factor of the opal¹⁷ or a rigorous finite element method,¹⁸ restricted however to a small (2 or 3) number of layers for numerical convenience. In essence, the “window + opal” system combines the $[(2/3)^{1/2}d]$ periodicity of the opal (assumed to be compact), with a nearly empty gap (thickness $d/2$) at the window/opal interface (Fig. 1). The reflectivity, apparently large for a “glass/glass” interface, relates to the size of the gap allowed by the nearly empty contact region between the window and the opal first layer.^{17,18} This reflectivity is predicted to depend upon the incidence angle, exhibiting oscillations in its wavelength dependence, and Bragg peaks. These features were experimentally demonstrated with a white source and a spectrum analyzer.¹⁷

To enhance the visibility of narrow spectroscopic contributions, we apply a frequency modulation (FM) to the laser

(typically at $f \sim 10$ kHz, with an amplitude 5–20 MHz), and process the reflected light with a lock-in detector in order to frequency-derive the spectrum.^{8–11,19} For $d \sim 1 \mu\text{m}$ opals, our findings summarize as follows:

- (i) Near normal incidence, (FM) reflection on the opal exhibits a nearly antisymmetric lineshape (Fig. 2), whose width (~ 30 MHz) is clearly below the ~ 200 MHz half-Doppler width, although broader than the (5 MHz) natural width of the transition.
- (ii) Increasing the incidence angle, the lineshape largely broadens-up.
- (iii) For large incidence angles ($\theta \sim 30$ – 60° , as measured at the external air/window interface), a sub-Doppler structure (≤ 30 MHz) appears, superimposed to the broad Doppler-broadened structure and better seen in TM polarization (Fig. 3). This narrow structure, whose shape evolves rapidly with the incidence angle, is located at the Doppler-free resonance (determined in an auxiliary SA experiment). The amplitude of this narrow structure remains a fraction of the broad signal after FM detection: in a direct detection, it would hence correspond to a few% of the broad signal. With $2f$ detection, the broad background nearly vanishes, yielding only the narrow structure (Fig. 4).
- (iv) This sub-Doppler structure appears in the linear regime of incident intensity. We have carefully checked that it does not originate in a residual nonlinear signal (as easily occurring with optical pumping, see, e.g., Ref. 6), nor in a stray signal as induced by scattering in the opal. Our sensitivity allows us to reach $\sim 10 \mu\text{W}/\text{cm}^2$ incident intensity, well below the few mW/cm^2 Cs saturation intensity in volume.²⁰

These results are unchanged for cells with 10 and 20 layers, or when investigating various regions of the opal (i.e., they are not associated to local defects or orientation in the opal). The Cs density in the interstitial regions appears similar to the one of the free volume, as shown when comparing—after due FM width normalization—the amplitude of the signal with the one at the flat interface (uncoated region of the opal). For the $d \sim 400$ nm opal, analogous results are obtained in spite of the remaining Cs clusters.

Until now, only two techniques had generated sub-Doppler and linear spectroscopic signals with a vapor, namely: selective reflection (SR) spectroscopy at a flat window/vapor interface,^{19,21} and thin cell spectroscopy.^{9–11} In both techniques, corresponding to a kind of 1-D confinement

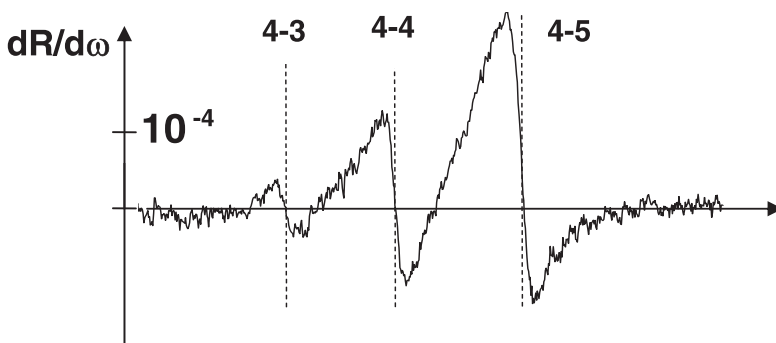


FIG. 2. Frequency spectrum of the FM reflectivity ($dR/d\omega$ with R the reflectivity, and ω the frequency) at an opal interface ($d = 1 \mu\text{m}$, 20 layers) under near normal incidence, for the $F=4 \rightarrow F' = \{3, 4, 5\}$ manifold of the Cs line D_2 line. The dashed lines are markers for the respective frequencies of the same manifold, as obtained in the reference saturated absorption spectrum. The vertical scale is normalized to the non resonant reflectivity. FM excursion: 20 MHz; Cs temperature: 90°C .

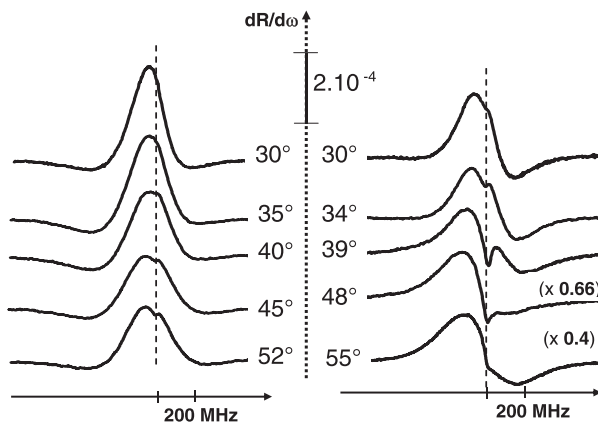


FIG. 3. Same as Fig. 2, for the D_1 resonance line, with the dashed line for the center of the equivalent saturated absorption spectrum. External incidence angle θ (see Fig. 1) as indicated; FM excursion: 15 MHz, Cs temperature: $\sim 110^\circ\text{C}$. (left): TE polarization; (right): TM polarization.

(either optical, or mechanical), the Doppler broadening is suppressed only under normal incidence: the dominant contribution comes from atoms flying nearly parallel to the walls, less sensitive to relaxation or transient effects imposed by wall collisions. Here, the sub-Doppler contribution observed at oblique incidences is a feature with no equivalent, which we attribute to the 3-D confinement in the interstitial regions of the opal.

For such an interpretation, we first rule out the contribution of the free vapor/opal interface, analogous to SR at a corrugated interface (after propagation through the entire opal thickness). Indeed, the results are similar for the 20 and 10 layers opal, while the transmission is much weaker for the 20 layers opal. Second, the response of the empty region surrounding the first (half)-layer of glass spheres may evoke a quasi 1-D confinement, instead of a genuine 3-D confinement. This confined region can yield a behavior resembling the one of a vapor nanocell,¹⁰ characterized by a sub-Doppler lineshape under normal incidence and a broadening-up with the incidence angle; because of this, we attribute an essential part of the signal observed under small incidence angles to this region. The corrugated interface, like a

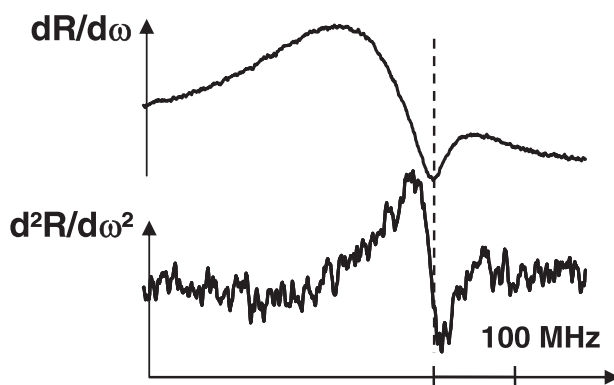


FIG. 4. Comparison between the first ($dR/d\omega$) and second ($d^2R/d\omega^2$) harmonic detection for the frequency spectrum of reflection on the 20 layers $d = 1 \mu\text{m}$ opal (D_1 line). TM polarization; $\theta = 40^\circ$, FM excursion: 20 MHz; Cs temperature: 120°C ; intensity $\sim 50 \mu\text{W}/\text{cm}^2$.

distribution of incidence angles, may induce a residual broadening, justifying the ~ 30 MHz width. Conversely, even if some peculiar incidences on the corrugated first half-layer may produce a guided wave (e.g., like in plasmonics), one cannot justify that the narrow linear signal originates from this region for oblique incidences spanning on a large range.

Rather, we associate the sub-Doppler contribution at oblique incidences to a probing of atoms confined *inside* the interstices of the opal. Indeed, in reflection spectroscopy, the atomic back-action is as a summing of the local atomic responses (i.e., absorption and dispersion), modulated by a complex propagation factor. At a planar interface, the reflected field²¹ is governed by a contribution $\propto \int_0^{+\infty} p(z) \exp(i\beta kz) dz$, with $\exp(i\beta kz)$ the (oblique) backward propagation factor, and with $p(z)$ the complex atomic response at a z distance to the surface: $p(z)$ includes the spectral dependence over the various atomic velocities and the non local transient response of the moving atoms; here, the phase factor for the incident propagation is included too. For an interface with an opal, an analogous treatment is possible, although more complex. The strong and periodical variations of the number of atoms, governed by the local emptiness factor between spheres, must be included in $p(z)$, as well as the distribution of atomic trajectories in the interstices. Propagation is also more complex: the backward propagation, yielding the reflection, sums up the light coherently *scattered* by the emitters from the periodical interstices; the field driving the atomic polarization $p(z)$ is not simply the propagating transmitted field but may have to include the scattered light.¹⁸ Changing the incidence, the wavelength, or even the polarization modifies the spatial distribution of the complex atomic emission, possibly turning a good matching with the periodicity of the opal into a mismatch. A Bragg-type derivation provides a crude estimate²² of the incidence that yields a constructive contribution from the atoms located in inner interstices. It must be tempered by the initial dephasing associated to the first half-layer of interstices, by the attenuation of the exciting field towards the inner region and by the complex nature of the atomic response (absorption/dispersion). Also, the defects in the opal periodicity¹⁴ strongly affect the visibility of the deepest interstices.

Experimentally, the major argument for the contribution of the inner regions in the narrow spectral contribution is the high sensitivity of the lineshapes to polarization and incidence angle (Fig. 3). The field propagation being very sensitive to polarization and incidence, a minor change in propagation makes the summing of the atomic response favoring either absorption, or dispersion, and induce sensible changes in the lineshape.²³ A comparison between the D_1 and D_2 lines confirms this influence of the propagation. In our linear regime, the spectrum of the D_2 line, with its hyperfine structure, can be simply predicted from the D_1 spectrum with its isolated hyperfine component. A good agreement is indeed found up to those oblique incidences for which a sub-Doppler response appears. Thence, the lineshapes profoundly differ, notably in the mixture of broad and narrow structures. In spite of the tiny difference in wavelengths, propagation has changed critically with the λ/d ratio.¹⁷

The inner contribution that we have discussed above is spectroscopically sub-Doppler, and a full interpretation of this point is still pending. Our research was inspired by the Dicke idea^{24,25} that the Doppler broadening disappears when the atomic motion remains confined within a fraction of the wavelength. The Dicke narrowing is found in a variety of situations: for 3-D confinement, it is classically a confinement imposed by buffer gas collisions, which was early observed for thermal gases in *r.f.* transitions,²⁴ and it assumes collisions changing only velocity, with no loss of coherence; conversely, in the Dicke narrowing for a 1D-confined system,^{9,10,25} collisions to the surface induce a complete de-excitation, with all atoms evolving in a transient regime of interaction, and the line-narrowing originates in the (logarithmically) enhanced contribution of (1-D) slow atoms. None of these situations seems to apply clearly to our opal-confined gas. Here, the narrow contribution does not seem to be limited by wall-collisions like in Ref. 7, perhaps because of an enhanced contribution of slow atoms.⁵ The (3-D) Dicke narrowing with a buffer gas has remained elusive in the optical domain,²⁶ and this was our initial reason to choose opals with $d \sim \lambda$ ($\sim 1 \mu\text{m}$) spheres.²⁷ At optical energies, a notable difference between buffer-gas confinement and wall-confinement is that a collision with a perturber atom (buffer gas) induces only a “dephasing” collision because the kinetic energy is too weak to allow inelastic collision; conversely, a genuine energy quenching occurs when an atom collides a hard medium like a glass sphere.

In conclusion, aside from our success in confining the alkali-metal vapor in a way compatible with spectroscopy, our major result is the observation of a sub-Doppler signal in linear spectroscopy, originating from the inner regions of the opal. For applications, a sensitive issue that requires further experimental studies is the stability of the shape of the narrow structure, whose symmetry presently varies with the incidence angle. Alternate to the reflection measurements reported here, a detection of the scattered light could be considered,²⁸ allowing complex or irregular frontiers of the confining nanostructured medium. From our results and as a benefit of the intrinsic linearity of the method combined with the presence of narrow spectral features, one may envision very compact sub-Doppler references based on weak (hardly saturable) molecular lines, possibly applicable to no-drift gas sensors. The probed volume yielding a sub-Doppler response can be conceptually as small as several spheres (i.e., several λ^3), and the irradiation extremely focused. An efficient multiple scattering could also increase the effective optical path inside the resonant vapor, as in Ref. 7. Another extension of our experiments would be to look for an equivalent sub-Doppler contribution in a porous medium, when the average pore size is $< \lambda$. All these self-organized or random confinement systems combine a simpler realization and similar advantages than the macroscopic array of sub-wavelength cells proposed in Ref. 29. Note that as long as the confinement length remains above $\sim 100 \text{ nm}$, the atom-surface interaction (Ref. 11, and references therein) perturbs only marginally the atomic resonances. Conversely, in a situation far from a gas at thermal equilibrium,³⁰ a Dicke narrowing is reported associated to confinement in small pores, at the expense of an important frequency shift. In the same manner,

the atomic motion tends to wash out the photonic crystal nature of an opal, with its local succession of field enhancement/inhibition. Finally, let us add that in complementary experiments to be reported elsewhere, we observed for long time scales, a LIAD³¹ inside the opal, that we attribute to the quasi-porous intimate nature of the glass spheres.³² This increases the versatility of experiments combining resonant gases and opals.

Work performed in the frame of the ANR Project Mesoscopic gas 08-BLAN-0031, and ECOS-Sud U08-E01 (France-Uruguay Program). We acknowledge discussions with M. Ducloy and M.-P. Gorza, contributions to early steps of the experimental work by M.-P. Gorza, and to opal measurements by H. Failache (ECOS-SUD U08-E01), discussions on the Dicke narrowing with J. R. Rios Leite (CAPES-COFECUB 740/12), and discussions on the field propagation in the opal with I. Zabkov (PICS#5813 CNRS-Russian Foundation for Basic Physics). The opal was deposited at CRPP-Bordeaux in the S. Ravaine team, and the opal cell built-up by F. Thibout (LKB ENS,) with advices for optical quality by T. Billeton (LPL).

¹S. Knappe, V. Shah, P. D. D. Schwindt, L. Hollberg, J. Kitching, L. A. Liew, and J. Moreland, *Appl. Phys. Lett.* **85**, 1460 (2004).

²F. Benabid, F. Couny, J. C. Knight, T. A. Birks, and P. S. J. Russell, *Nature* **434**, 488 (2005).

³S. Ghosh, A. R. Bhagwat, C. K. Renshaw, S. Goh, and A. L. Gaeta, *Phys. Rev. Lett.* **97**, 023603 (2006).

⁴R. Thapa, K. Knabe, M. Faheem, A. Naweed, O. L. Weaver, and K. L. Corwin, *Opt. Lett.* **31**, 2489 (2006).

⁵J. Hald, J. C. Petersen, and J. Henningsen, *Phys. Rev. Lett.* **98**, 213902 (2007).

⁶A. Burchianti, A. Bogi, C. Marinelli, C. Maibohm, E. Mariotti, and L. Moi, *Phys. Rev. Lett.* **97**, 157404 (2006).

⁷T. Svensson, E. Adolffson, M. Lewander, C. T. Xu, and S. Svanberg, *Phys. Rev. Lett.* **107**, 143901 (2011).

⁸S. Briaudeau, D. Bloch, and M. Ducloy, *Europhys. Lett.* **35**, 337 (1996).

⁹S. Briaudeau, S. Saliel, G. Nienhuis, D. Bloch, and M. Ducloy, *Phys. Rev. A* **57**, R3169 (1998).

¹⁰G. Dutier, A. Yarovitski, S. Saliel, A. Papoyan, D. Sarkisyan, D. Bloch, and M. Ducloy, *Europhys. Lett.* **63**, 35 (2003).

¹¹M. Fichet, G. Dutier, A. Yarovitsky, P. Todorov, I. Hamdi, I. Maurin, S. Saliel, D. Sarkisyan, M.-P. Gorza, D. Bloch, and M. Ducloy, *EPL* **77**, 54001 (2007).

¹²H. Kübler, J. P. Shaffer, T. Baluktian, R. Löw, and T. Pfau, *Nature Photon.* **4**, 112–116 (2010).

¹³J. Keaveney, A. Sargsyan, U. Krohn, I. G. Hughes, D. Sarkisyan, and C. S. Adams, *Phys. Rev. Lett.* **108**, 173601 (2012).

¹⁴P. Massé, Ph.D. dissertation, University of Bordeaux1, 2007; P. Massé, R. A. L. Vallée, J.-F. Dechézelles, J. Rosselgong, E. Cloutet, H. Cramail, X. S. Zhao, and S. Ravaine, *J. Phys. Chem. C* **113**, 14487–14492 (2009).

¹⁵P. Ballin, Ph.D. dissertation, University of Paris13, 2012.

¹⁶A. V. Baryshev, A. B. Khanikaev, H. Uchida, M. Inoue, and M. F. Limonov, *Phys. Rev. B* **73**, 033103 (2006).

¹⁷I. Maurin, E. Moufarej, A. Laliotis, and D. Bloch, “A stratified effective index modelling for the optics of an opal deposited on a window” (unpublished).

¹⁸I. Zabkov, V. Klimov, A. Laliotis, E. Moufarej, I. Maurin, and D. Bloch, “Field structure and optical properties of an ultra-thin opal” (unpublished).

¹⁹A. M. Akul’shin, V. L. Velichanskii, A. S. Zibrov, V. V. Nikitin, V. V. Sautenkov, E. K. Yurkin, and N. V. Senkov, *ZHETF Pis’ma v Redaktsiiu* **36**, 247–250 (1982) [*JETP Letters* **36**, 303–307 (1982)].

²⁰Saturation for the reflection on the opal requires an even higher intensity ($\sim 25 \text{ mW/cm}^2$).

²¹G. Nienhuis, F. Schuller, and M. Ducloy, *Phys. Rev. A* **38**, 5197–5205 (1988).

²²Bragg diffraction yields $\theta_{D1} \sim 49^\circ$ and $\theta_{D2} \sim 56^\circ$ for $d = 1 \mu\text{m}$ from (second-order) equation $\lambda/n_{\text{op}} = (2/3)^{1/2} d \cos\theta_{\text{in}}$, with θ_{in} the (internal) incidence angle in the window, n_{op} the effective index in the opal (~ 1.3 according to Ref. 14), and considering a 1.4 index for the window.

- ²³See the Appendix of M. Chevrollier, M. Fichet, M. Oria, G. Rahmat, D. Bloch, and M. Ducloy, *J. Phys. II* **2**, 631 (1992).
- ²⁴R. H. Dicke, *Phys. Rev.* **89**, 472 (1953); J. P. Wittcke and R. H. Dicke, *ibid.* **103**, 620 (1956).
- ²⁵R. H. Romer and R. H. Dicke, *Phys. Rev.* **99**, 532 (1955).
- ²⁶In optics, the Dicke narrowing only appears as a minute correction in a detailed lineshape analysis (see, e.g., J. Wang, P. Ehlers, I. Silander, and O. Axner, *J. Opt. Soc. Am. B* **28**, 2390 (2011) and references therein).
- ²⁷The interstices have roughly a size $\sim d/2$. They differ for *f.c.c.* or *h.c.* structure—see Ref. 15—are actually interconnected and may include some kinds of long tubes.
- ²⁸S. Villalba, H. Failache, A. Laliotis, L. Lenci, S. Barreiro, and A. Lezama, *Opt. Lett.* **38**, 193 (2013).
- ²⁹A. N. Naumov, A. A. Podshivalov, K. N. Drabovich, R. B. Miles, and A. M. Zheltikov, *Phys. Lett. A* **289**, 207 (2001). Note that in this work, a λ -thickness is considered rather than the required $\lambda/2$ value (see Refs. 9 and 10).
- ³⁰D. B. Cassidy, M. W. J. Bromley, L. C. Cota, T. H. Hisakado, H. W. K. Tom, and A. P. Mills, Jr., *Phys. Rev. Lett.* **106**, 023401 (2011); See also comment by D. G. Green and G. F. Gribakin.
- ³¹M. Meucci, E. Mariotti, P. Bicchi, C. Marinelli, and L. Moi, *Europhys. Lett.* **25**, 639 (1994).
- ³²I. A. Karpov, E. N. Samarov, V. M. Masalov, S. I. Bozhko, and G. A. Emel'chenko, *Phys. Solid State* **47**, 347 (2005).



A LETTERS JOURNAL EXPLORING
THE FRONTIERS OF PHYSICS

OFFPRINT

**Infiltrating a thin or single-layer opal with an
atomic vapour: Sub-Doppler signals and crystal
optics**

ELIAS MOUFAREJ, ISABELLE MAURIN, ILYA ZABKOV, ATHANASIOS
LALLOTIS, PHILIPPE BALLIN, VASILY KLIMOV and DANIEL BLOCH

EPL, **108** (2014) 17008

Please visit the website
www.epljournal.org

Note that the author(s) has the following rights:

- immediately after publication, to use all or part of the article without revision or modification, **including the EPLA-formatted version**, for personal compilations and use only;
- no sooner than 12 months from the date of first publication, to include the accepted manuscript (all or part), **but not the EPLA-formatted version**, on institute repositories or third-party websites provided a link to the online EPL abstract or EPL homepage is included.

For complete copyright details see: <https://authors.eplletters.net/documents/copyright.pdf>.



A LETTERS JOURNAL EXPLORING
THE FRONTIERS OF PHYSICS

**AN INVITATION TO
SUBMIT YOUR WORK**

www.epjournal.org

The Editorial Board invites you to submit your letters to EPL

EPL is a leading international journal publishing original, innovative Letters in all areas of physics, ranging from condensed matter topics and interdisciplinary research to astrophysics, geophysics, plasma and fusion sciences, including those with application potential.

The high profile of the journal combined with the excellent scientific quality of the articles ensures that EPL is an essential resource for its worldwide audience. EPL offers authors global visibility and a great opportunity to share their work with others across the whole of the physics community.

Run by active scientists, for scientists

EPL is reviewed by scientists for scientists, to serve and support the international scientific community. The Editorial Board is a team of active research scientists with an expert understanding of the needs of both authors and researchers.



www.epjournal.org



OVER
560,000
full text downloads in 2013

24 DAYS
average accept to online
publication in 2013

10,755
citations in 2013

*"We greatly appreciate
the efficient, professional
and rapid processing of
our paper by your team."*

Cong Lin
Shanghai University

Six good reasons to publish with EPL

We want to work with you to gain recognition for your research through worldwide visibility and high citations. As an EPL author, you will benefit from:

- 1 Quality** – The 50+ Co-editors, who are experts in their field, oversee the entire peer-review process, from selection of the referees to making all final acceptance decisions.
- 2 Convenience** – Easy to access compilations of recent articles in specific narrow fields available on the website.
- 3 Speed of processing** – We aim to provide you with a quick and efficient service; the median time from submission to online publication is under 100 days.
- 4 High visibility** – Strong promotion and visibility through material available at over 300 events annually, distributed via e-mail, and targeted mailshot newsletters.
- 5 International reach** – Over 2600 institutions have access to EPL, enabling your work to be read by your peers in 90 countries.
- 6 Open access** – Articles are offered open access for a one-off author payment; green open access on all others with a 12-month embargo.

Details on preparing, submitting and tracking the progress of your manuscript from submission to acceptance are available on the EPL submission website www.epletters.net.

If you would like further information about our author service or EPL in general, please visit www.epjournal.org or e-mail us at info@epjournal.org.

EPL is published in partnership with:



European Physical Society



Società Italiana di Fisica

edp sciences IOP Publishing

EDP Sciences

IOP Publishing

Infiltrating a thin or single-layer opal with an atomic vapour: Sub-Doppler signals and crystal optics

ELIAS MOUFAREJ^{1,2}, ISABELLE MAURIN^{1,2}, ILYA ZABKOV³, ATHANASIOS LALLOTIS^{1,2}, PHILIPPE BALLIN^{1,2},
VASILY KLIMOV⁴ and DANIEL BLOCH^{2,1(a)}

¹ *Laboratoire de Physique des Lasers, Université Paris13 - Sorbonne-Paris-Cité - 99 Av. JB Clément, 93430 Villetaneuse, France*

² *UMR 7538 du CNRS - 99 Av. JB Clément, 93430 Villetaneuse, France*

³ *Moscow Institute of Physics and Technology (State University) - Institutskiy Pereulok 9, 141700 Dolgoprudny, Russia*

⁴ *P.N. Lebedev Physics Institute - 53 Leninskii prospekt, 119991 Moscow, Russia*

received 19 June 2014; accepted in final form 15 September 2014
published online 1 October 2014

PACS 78.67.-n – Optical properties of low-dimensional, mesoscopic, and nanoscale materials and structures

PACS 42.82.Fv – Hybrid systems

PACS 34.35.+a – Interactions of atoms and molecules with surfaces

Abstract – Artificial thin glass opals can be infiltrated with a resonant alkali-metal vapour, providing novel types of hybrid systems. The reflection at the interface between the substrate and the opal yields a resonant signal, which exhibits sub-Doppler structures in linear spectroscopy for a range of oblique incidences. This result is suspected to originate in an effect of the three-dimensional confinement of the vapour in the opal interstices. It is here extended to a situation where the opal is limited to a few- or even a single-layer opal film, which is a kind of bidimensional grating. We have developed a flexible one-dimensional layered optical model, well suited for a Langmuir-Blodgett opal. Once extended to the case of a resonant infiltration, the model reproduces quick variations of the lineshape with incidence angle or polarization. Alternately, for an opal limited to a single layer of identical spheres, a three-dimensional numerical calculation was developed. It predicts crystalline anisotropy, which is demonstrated through diffraction on an empty opal made of a single layer of polystyrene spheres.

Copyright © EPLA, 2014

Sub-Doppler atomic spectroscopy and confinement. – The development of meta-materials and artificial materials, at a scale comparable to or smaller than optical wavelengths, opens large prospects to manipulate optical fields with unprecedented possibilities. Only few connections have been established with atomic physics until now, even though atomic transitions provide universal filters or references for light frequency. It is only very recently that cold atoms can be manipulated in the vicinity of artificial materials [1]. Rather, confined atoms or molecules are usually in a thermal gas state and undergo the spectroscopic Doppler broadening when they are confined close to artificial materials such as porous materials [2,3] and holey or photonic fibres [4,5]. Sub-Doppler resolution was demonstrated only through *nonlinear* schemes derived from the saturated absorption technique (well known for

large volume) for a vapour undergoing a loose confinement (not better than $10\ \mu\text{m}$), either with a counterpropagating beam [5] in a holey fibre, either [3] through the nearly counterpropagating effect of the scattered light in a porous medium.

For a one-dimensional (“1-d”) confinement with nanocells of dilute vapour, a sub-Doppler contribution appears in *linear* spectroscopy, restricted to nearly normal incidence [6]. This is because of a transient regime of absorption, which enhances the relative contribution of the slow atoms, and which can be traced back to a special type of Dicke narrowing. Looking for a three-dimensional (“3-d”) extension of these observations, we eventually observed sub-Doppler structures for the reflection from a gas confined in the interstitial regions of an opal of glass nanospheres [7].

In the present work, we extend our previous experimental investigations [7] by improving the range of

^(a)E-mail: daniel.bloch@univ-paris13.fr (corresponding author)

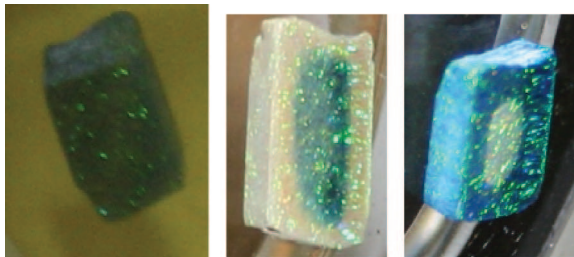


Fig. 1: (Colour on-line) The 1 mm thick opal, totally opaque after filling up the cell with Cs (left), becomes (centre) inhomogeneous and greenish—in the course of evaporation obtained by selective heating of the opal region; it returns (right) to a darker colour when the heating-up of the window is stopped, with colouring occurring first on the outer part.

experimental conditions yielding sub-Doppler structures. In particular, we reduce the opal thickness of the confining opal. Unexpectedly, we still observe narrow sub-Doppler spectra with an opal made of a single-layer arrangement of nanospheres opal.

The detailed physics of the atomic response leading to these narrow sub-Doppler line remains elusive: it combines i) the nano-optics problem of light propagation inside the opal, ii) the light-atom interaction in opal voids (of a complex shape) whose response is transient and non-local because of the atomic motion, and finally iii) the summing-up of atom radiation onto the direction of the reflected field. To improve our understanding of the optics which governs the excitation brought to the atoms, and the summing-up of the atomic response, we have implemented two kinds of optical models. The first one takes into account the intrinsic imperfections of our typical opals (prepared by a Langmuir-Blodgett deposition) and can be extended to the case of a resonant infiltration; the other one deals with the special case of a single-layer opal, and predicts a crystalline anisotropy, that we eventually observed for a well-organized single-layer opal.

Infiltrating an opal with caesium vapour. – An opal consists of a crystalline arrangement of mono-disperse micro- or nano-spheres, usually made of glass (silica) or polystyrene. Various schemes of soft chemistry allow producing a self-organized photonic crystal [8], whose local defects are numerous because of the self-organization.

Filling up the interstitial regions of such a photonic crystal with spectroscopically convenient vapours of alkali metal—Cs in our case—is not easy as the infiltration induces cluster formation in the small interstices. This problem is exemplified in fig. 1, where we show successive pictures of a thick opal (1 mm thickness, sphere diameter $D \sim 200$ nm) after the filling-up of an evacuated sealed glass cell where the opal was introduced. When filling up the cell, the Cs vapour condenses within the interstices of the opal. The opal looks almost black, and does not even exhibit a metallic aspect. Because the interstices are numerous, and are of a small size, it is much more difficult to

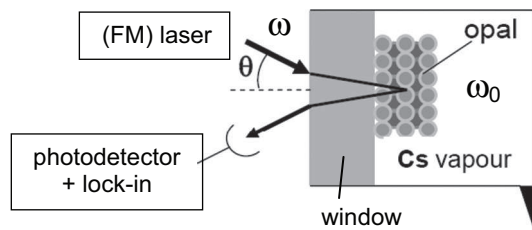


Fig. 2: Scheme of reflection spectroscopy at the interface between a Cs cell window, and a LB opal deposited on it. For convenience, the size of the thin opal (made here of 5 layers in a compact arrangement) is strongly exaggerated. The frequency of the incident beam ω is scanned across the Cs resonance ω_0 . θ is the incidence angle in air before the window.

evaporate the dense Cs than for a usual planar interface. Evaporated atoms are easily re-adsorbed, or interact with neighbouring atoms to generate clusters, whose signature is the greenish colouring of the opal. Moreover, when heating up the opal to evaporate the dense Cs, thermal inhomogeneities and the dynamics of evaporation and read-sorption mostly result in the displacement of the coloured regions bearing the clusters. A possible explanation of the considerable trapping of the Cs atoms in the opal interstices could be that silica nanospheres are far from being perfectly spherical as revealed by electron microscopy [9] (rather, glass spheres are structured as a quasi-spherical cluster of smaller spheres).

A successful operation occurred when replacing the macroscopic opal by a thin opal prepared through a Langmuir-Blodgett (LB) layer-by-layer deposition technique [10]. LB deposition allows controlling the number of layers (presently between 1 and 20) deposited on a glass window, at the expense of the crystal quality (a LB opal is usually organized only in a random hexagonal close-packed—rhcp—structure). The window is further inserted into a cell (see fig. 2), finally sealed after filling-up with Cs. Until now, the cell thickness remains macroscopic (typically 4 cm), although it would be advantageous to fabricate a cell thin enough for the opal to be just a “spacer” for the two windows [11]. This project has been delayed until now because of residual inhomogeneities in the opal thickness on the one hand, and because of technological problems for the gluing of highly parallel windows on the other hand. Practically, a sufficient overheating of the opal-covered window resulted in a stable operation for the opal, which remains with its milky appearance (*i.e.* it does not absorb, but scatters light in spheres of a size comparable to the wavelength).

Sub-Doppler reflection from the opal interface. – The design of the cell containing the opal infiltrated with Cs vapour does not allow using transmission spectroscopy to probe the infiltrated opal (see fig. 2) because nearly all of the active (optically resonant) volume is filled with free vapour, rather than with the opal. A detection of the scattered light may be implemented, but should view

only the region of the opal, and requires a high sensitivity. Rather, our detection relies on the spectroscopic monitoring of the light reflected at the interface between the window and the opal (see fig. 2), *i.e.* we look for the resonant changes $\Delta R(\omega - \omega_0)$ of the reflectivity R when the irradiation frequency is tuned across the atomic vapour resonance. The spatial origin of the signal that we monitor is a problem mostly addressed in the next section. Note that the resonances for a dilute gas are considerably narrower than any wavelength-dependent behaviour associated to the photonic-crystal nature of the opal. In order to relatively enhance the narrowest contributions in the spectrum, we adopt a frequency modulation (FM) technique, where a lock-in detector yields the frequency derivative of the reflection spectrum.

Our initial experiments [7,12] were performed with frequency-tunable narrow linewidth laser diodes on the doublet of resonance lines of Cs ($\lambda_1 = 0.894 \mu\text{m}$ and $\lambda_2 = 0.852 \mu\text{m}$) with cells containing deposited opals made of 10 or 20 layers of $1 \mu\text{m}$ diameter spheres. Observations were similar for these two opals, and no significant difference is found between the Cs density in the opal region and in the gas region (Cs density 10^{13} – 10^{14} at/cm³). Sub-Doppler spectra were observed under near normal incidence, whose width was ~ 30 – 40 MHz, as opposed to the ~ 400 MHz full Doppler width (the natural width for Cs resonance is ~ 5 MHz, and the collision self-broadening is comparable to this width). In spite of a considerable broadening when increasing the incidence angle θ , the major result is that narrow sub-Doppler structures, superimposed to a broad spectrum, appear for a limited range of (large) oblique incidences ($\theta \sim 40$ – 50°). The contrast is higher for TM polarization, and for a given incidence, the shape of this structure strongly differs for TE or TM polarizations. Also, for a given polarization, the shape and amplitude evolve quickly with the incidence angle. In addition, major differences appear when comparing neighbouring wavelengths such as λ_1 and λ_2 . All these original observations were made in the pure *linear* regime of resonant interaction. Our simple interpretation was that close to normal incidence, the narrow spectra are rather analogous to the ones of a thin cell [6] because of the large voids between the window and the first half-layer of spheres, while the sub-Doppler structures observed for a range of oblique incidences were a genuine consequence of the 3-d confinement of the atomic vapour.

We have recently carried out complementary experiments with new cells and different sphere diameters ($D \sim 400$ nm). To study the weak Cs line at $\lambda = 455$ nm (see fig. 3(a)), the sensitivity has been enhanced by compensating for a residual amplitude modulation induced by the FM laser. In addition to well-resolved hyperfine components close to normal incidence (*e.g.* 3°), we find ranges of oblique incidences (see, *e.g.*, 36°) where relatively narrow structures mix up with broader features associated to a full Doppler width (~ 800 MHz). Their shape varies quickly with the incidence angle. Polarization

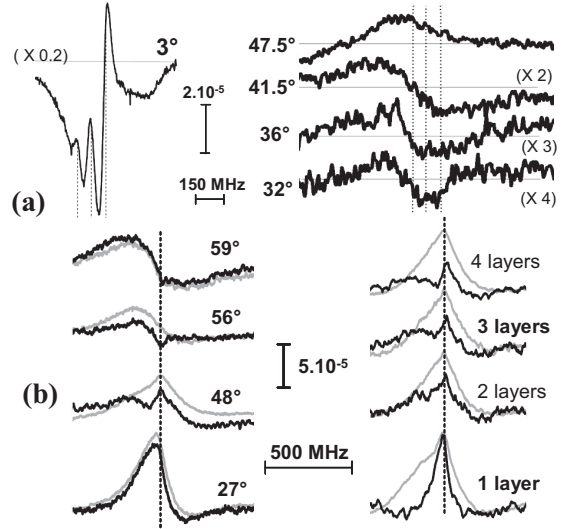


Fig. 3: FM reflection spectra on Cs at an opal interface. For all spectra, the vertical (dashed) lines mark atomic resonances (provided by auxiliary saturated absorption spectra). The vertical scale provides $\Delta R/R$ for a 16 MHz amplitude of the FM. (a) Experiments on the $\lambda = 455$ nm line at $T = 140^\circ\text{C}$ ($\sim 1.5 \cdot 10^{14}$ at/cm³) for an opal made of 10 layers of $D = 400$ nm; incidence angles as indicated, TM polarization; (b) experiments at $\lambda_1 = 894$ nm at $T = 100^\circ\text{C}$ ($\sim 2 \cdot 10^{13}$ at/cm³) on a multizone opal ($D = 1030$ nm) and TE (grey) or TM (black) polarizations. Spectra on the left are for a 3-layers zone, incidence as indicated and on the right for a 45° incidence, and number of layers as indicated.

dependence is always strong, with TM polarization generally more favourable, perhaps because nonresonant reflection is weaker in the vicinity of the Brewster angle. For larger spheres ($D \sim 1 \mu\text{m}$) and $\lambda = 455$ nm, rather broad structures, however well below the full Doppler width, have been also observed for a limited range of incidence angles.

We have also acquired sealed Cs vapour cells bearing a multi-zone window (covered by stripes of opals made with, *e.g.*, 1, 2, 3 and 4 layers). With these few-layer opals, narrow structures are still observed on the Cs D_1 line far away from normal incidence (fig. 3(b)). Their amplitude is relatively larger than for a many-layer opal and can hinder the Doppler-broadened structure. Remarkably, in the limiting case of a single layer of glass spheres, a sub-Doppler lineshape remains observable in TM polarization. This novel and polarization-dependent result is unexpected as it cannot be traced back to a 3-d confinement.

In all these experiments, the lineshapes are highly sensitive to light polarization. For experiments as ours which are performed in the linear regime (with respect to intensity), only the complex propagation inside the opal (and not the atom excitation) can be affected by the light polarization. This is why we have addressed the problem of the optical propagation in the opal through modelling, and performed complementary experiments on noninfiltrated opals. We report below on two different types of

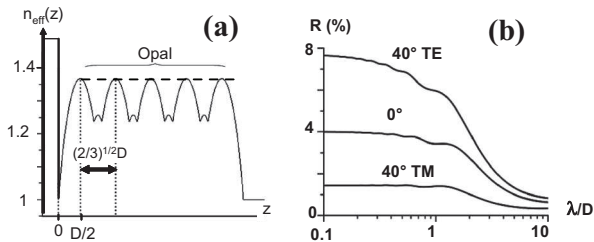


Fig. 4: (a) Effective index model used to describe the opal as a layered medium; the horizontal dashed line is for a “fused” opal model. (b) Calculated reflection at the window/“fused” opal interface as a function of λ/D for normal incidence or for $\theta = 40^\circ$ and TE or TM polarization as indicated. The index for the glass nanospheres is 1.4, and 1.5 for the ($z < 0$) window.

optical approaches: one, well suited to a LB opal of several layers, allows considering a resonant infiltration; the other one, specific to a single layer, makes the geometrical orientation an important parameter.

Layered model of the opal and resonant infiltration. – Many models were developed to understand the optics of photonic crystal. They are often based upon heavy numerical bandgap calculations, and do not take into account the many defects and partial disorder of a LB opal. They are not well suited to include a perturbative change of parameters, such as the λ/D ratio, or the sphere or substrate index. To overcome these difficulties, we have developed [13] a 1-d model, based upon a transfer matrix calculation analogous to a multi-layer thin film, with the layered effective index $n_{\text{eff}}(z)$ described by

$$n_{\text{eff}}(z) = \{(f(z)n_{\text{sphere}}^2 + [1 - f(z)]\}^{1/2}. \quad (1)$$

In eq. (1), z is the distance to the window, and $f(z)$ the filling factor of the opal in the plane at height z . The structure of $n_{\text{eff}}(z)$ is shown in fig. 4(a). To simulate the scattering in the transparent opal, an additional extinction parameter is added. This flexible model easily allows *quantitative* predictions, notably of the width and amplitude of the Bragg rejection peak, and even of high-order Bragg peaks. Dedicated tests with a variety of opals deposited on a window have shown a reasonable success against experimental data, which was acquired with a white source and a spectrometer [13]. The intrinsic disorder of the rhcp arrangement of a LB opal, and dispersion in the glass sphere sizes justifies the success of this crude 1-d model replacing a complex 3-d photonic crystal.

This model also helps to interpret the physics underlying the predicted behaviours. In particular, it includes quite naturally the break of the compact arrangement for the first and last half-layers. This exemplifies a very general problem encountered with photonic crystals: optical measurements require a coupling to the outside regions —*e.g.* by transmission or reflection—, which breaks the periodicity (on a λ scale) at the interface. In fig. 4(b), a calculation is performed for a “fused” opal in order to enhance the “gap” effect between the substrate and

the first layer. It shows that the reflectivity from the interface is very close to the one for a substrate/vacuum interface when the irradiation wavelength remains comparable to the opal size (*i.e.* for $\lambda/D \leq 1$, reflectivity is the same as for $\lambda/D \rightarrow 0$, which is the prediction for an elementary planar interface). This is in agreement with experiments [7,13].

This model, based upon a linear matrix formalism, can be extended [14] to describe an opal infiltrated by a low-density resonant medium (*e.g.* a gas of motionless atoms or a liquid containing a resonant doping). For this purpose, one simply assumes the resonant infiltrated medium to be characterized by an index $n_{\text{infiltr}} = 1 + \delta n$, and extrapolates the layered model to a first-order expansion in δn . The density of the resonant dilute medium is assumed to evolve periodically, following the density of voids in the opal $[1 - f(z)]$. Calculating the effect of an infinitesimal slice of resonant medium, one finds that the resonant change in the reflectivity oscillates with the spatial position of the slice. The period of this oscillation depends on the wavelength and on the incidence angle. Its phase differs for the contributions originating in $\text{Re}(\delta n)$ or in $\text{Im}(\delta n)$ (respectively dispersive and absorptive contribution); it also varies with light polarization (for large incidences). Hence, when integrating the elementary responses over the distribution of the infiltrated material, it is only for specific incidence angles that this spatially oscillating response matches the periodical emptiness factor $[1 - f(z)]$, governed by the opal geometry. In this case, a large resonant signal is predicted, owing to a constructive contribution of the response of the whole infiltrated material. This shows that the origin of the resonant reflection extends over several wavelengths, *i.e.* over the deep layers of the opal. For a resonant infiltrated material characterized by a complex dependence $\text{Re}[\delta n(\omega - \omega_0)]$ and $\text{Im}[\delta n(\omega - \omega_0)]$, it is the overall lineshape of the resonant reflectivity which varies quickly with the incidence angle and with the incident polarization. This is observed in fig. 5, where a complex Lorentzian resonance is assumed. Such a modelling provides a simple analogy with the quick variations, experimentally observed in a gas, with the incidence angle and polarization. It is however too limited to deal with the complexity of a transient velocity-dependent atomic resonance, and to justify sub-Doppler widths.

Figure 5 shows relative resonant changes $\Delta R/R$, because it allows an easier comparison between TE and TM polarizations. Despite the limited range of incidence angles, the variations of the nonresonant reflectivity R for a given polarization are non-negligible in fig. 5. This is because of a simultaneous second-order Bragg peak of reflectivity. This coincidence, surprising only at first sight, is due to the fact that the condition for a matched contribution of the resonant slices is analogous to the conditions yielding a Bragg-type resonance [14]. This does not mean that the resonant variations which are predicted are just an effect of this (weak) photonic-crystal mode. Indeed, the lineshapes predicted in fig. 5 are highly sensitive to

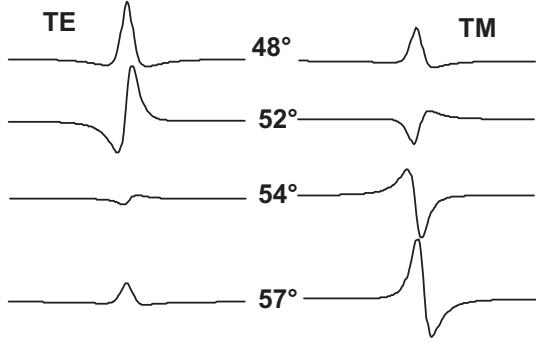


Fig. 5: Calculated FM frequency lineshapes for $\Delta R/R$ around resonance for an infiltrated opal. The complex index δn of the infiltrated material is assumed to be governed by a Lorentzian resonance. Calculation for a 20-layers opal, $\lambda/D = 0.852$, and a scattering analogous to an absorption $0.2D^{-1}$. Polarization and incidence angles as indicated, all curves represented with the same scale. For 48° , 52° , 54° , 57° , and respectively (TE, TM) polarizations, one finds $R = (5.9\%, 0.45\%), (10.3\%, 0.29\%), (7.3\%, 0.14\%), (5.9\%, 0.08\%)$.

the assumptions chosen to evaluate the resonant response. In particular, we have ignored the optical excitation induced by the resonant scattered light, which should affect the phase of excitation in the infiltrated medium.

Single-layer opal and crystal optics. – The layered effective index model is not well suited for a single- or double-layer opal. Conversely, a rigorous numerical calculation by finite elements, taking into account the periodicity associated to a perfect crystal, has been developed by Zabkov *et al.* [15]. By truly taking into consideration the shape and periodicity of the contacting spheres, the calculation should provide a quantitative evaluation of the reflection and transmission coefficients, and of the scattering as well, with no need for an *ad hoc* extinction coefficient. In this nano-optics approach, the crystal orientation φ , defined relatively to the plane of incidence (see fig. 6), is a key parameter of the calculation

The model predicts rapid variations of reflectivity with the opal orientation for some wavelengths (see fig. 6). However, general trends (*e.g.* a minimum around 530 nm and 700 nm) are easily found. They are probably associated to a kind of resonance between the wavelength and the optical size of the sphere. We have performed experiments on a single layer of glass spheres ($D = 0.73 \mu\text{m}$) deposited on a microscope slide, using fibered “white laser” source and a spectrometer, as described in [13]. Experimentally, opals made of glass spheres are highly poly-domain because of dispersion in sphere diameter. This implies the inclusion in the model of a numerical averaging over the orientation angles. Very good agreement with experiments is hence found with this averaging, for reflection and transmission as well (fig. 6). Note that transmission appears less sensitive to the opal orientation.

Until now, our opals made of glass spheres through a LB technique have not been able to exhibit the diffractive

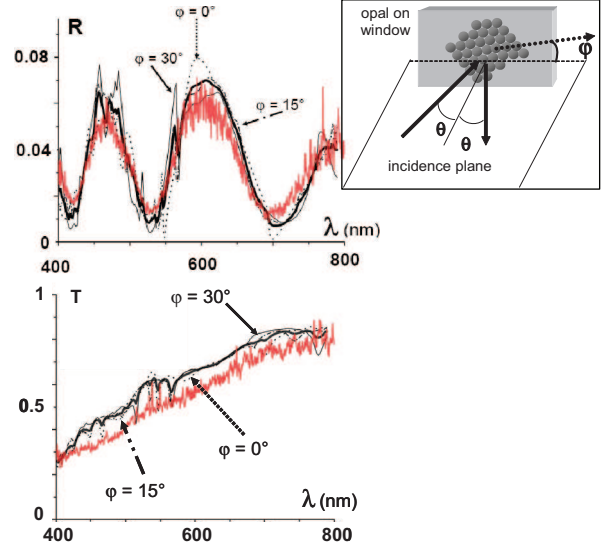


Fig. 6: (Colour on-line): Reflection (R) and transmission (T) spectra of a single layer of glass opal. The inset defines the irradiation incidence angle (θ) and the opal orientation (φ) angle. The experiment (red), where noise is apparent, is performed with $D = 0.73 \mu\text{m}$ glass spheres, $\theta = 15^\circ$, and the polarization is TM. The calculations (black) are for a dimensionless parameter λ/D and adjusted to the effective D value. Various orientations of the opal are considered (as indicated), and the thick black line is for a randomized orientation.

behaviour [11,16] associated to the hexagonal distribution of spheres in an elementary opal layer. This is because of a high dispersion in sphere diameter (up to $\sim 5\%$) for glass spheres. Conversely, for polystyrene spheres, single domains are found on large areas owing to a much smaller dispersion ($\sim 10^{-3}$). The hexagonal diffraction structure, usually turned into a circle for a highly poly-domain opal, has been easily observed with visible light when focusing our blue laser at 455 nm onto an opal with $D = 0.28 \mu\text{m}$ spheres. High-order diffraction spots could even be observed. Under normal incidence, there is no TE or TM polarization relatively to the incidence plane, but a preferential polarization direction can be expected relatively to the opal orientation. In other words, the intrinsic anisotropy of the opal makes it optically a crystal. As shown in fig. 7, the diffraction efficiency for $\lambda = 455 \text{ nm}$ varies by $\sim 30\%$ under normal incidence when changing polarization. Smaller variations ($\sim 10\%$) are found for a longer wavelength (green He-Ne laser at $\lambda = 543 \text{ nm}$).

The numerical model has the ability to predict the diffraction efficiency and its anisotropy. A comparison with our results would provide a sensitive test of the presence of opal defects, affecting the mesoscopic organization of the spheres, or the microscopic geometry of individual spheres [9].

As previously discussed, *transmission*, used here to monitor diffraction, cannot be presently applied to an opal infiltrated with vapour. Meanwhile, we have also

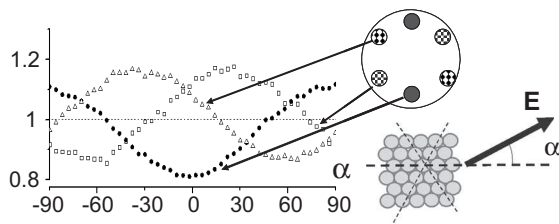


Fig. 7: Relative intensity of a pair of diffracted spots as a function of the orientation of the linear polarization for an irradiation under normal incidence. The direction of polarization α (in degrees) is defined by the opal orientation (see bottom right). This relative intensity is normalized by the average hexagonal diffraction efficiency. The circular inset (top right) shows different pairs of equivalent spots for an opal oriented as shown. The experiment is performed on a single layer of polystyrene spheres ($D = 0.28 \mu\text{m}$, $\lambda = 455 \text{ nm}$).

observed, hexagonal diffraction *in reflection* on a single-layer polystyrene opal, although with a weaker efficiency. Hence, extension to a single-layer infiltrated opal essentially requires the feasible preparation of a single-domain *glass opal* [11].

Conclusion. – Artificial glass opals prepared in thin layers can be used to confine atomic vapours. They offer a simple example of a hybrid system interfacing atoms with artificially structured materials. Sub-Doppler spectroscopic signals are found for a gas-infiltrated opal. A generalization of these results has even been found for a single-layer opal, which can be viewed as a kind of 2-dimensional grating deposited on the window. A major step for the full understanding of these signals would be to obtain a detailed description of the optical propagation inside the opal, which is usually a partially disordered photonic crystal. A simplified layered model has allowed to understand the strong influence of the gap region between the substrate and the contact region of an opal or more generally of a photonic crystal, and the possibility to observe the response of an in-depth infiltration. A detailed three-dimensional treatment for a single-layer opal has revealed crystal-optics properties, experimentally observed through polarization-sensitive diffraction. This may allow versatile detection schemes based upon the simultaneous detection of diffracted and reflected beams, opening prospects of new insights to analyze the origin of the sub-Doppler contributions in infiltrated opals.

* * *

Work supported by ANR (08-BLAN-0031 “Mesoscopic gas”), and partly by CNRS-PICS 5813. We thank A. MAÎTRE (INSP-Paris) for providing us with the thick opal,

S. RAVAINÉ (CNRS Bordeaux) for the LB opals, and F. THIBOUT (LKB-Paris) for fabricating the vapour cells.

This article has been submitted by participants at the META’14 event in Singapore in May 2014. EPL supports the META series by providing annual sponsorship. The scientific content has been peer reviewed under the same guidelines and criteria as all other EPL letters.

REFERENCES

- [1] OKABA S., TAKANO T., BENABID F., BRADLEY T., VINCETTI L., MAIZELIS Z., YAMPOL’SIIH V., NORI F. and KATORI H., *Nat. Commun.*, **5** (2014) 4096 (DOI:10.1038/ncomms5096).
- [2] SVENSSON T., ADOLFSSON E., LEWANDER M., XU C. T. and SVANBERG S., *Phys. Rev. Lett.*, **107** (2011) 143901.
- [3] VILLALBA S., LALLOTIS A., LENCI L., BLOCH D., LEZAMA A. and FAILACHE H., *Phys. Rev. A*, **89** (2014) 023422.
- [4] BENABID F., COUNY F., KNIGHT J. C., BIRKS T. A. and RUSSELL P. S. J., *Nature*, **434** (2005) 488.
- [5] COUNY F., LIGHT P. S., BENABID F. and RUSSELL P. S. T. J., *Opt. Commun.*, **263** (2006) 28; SLEPKOV A. D., BHAGWAT A. R., VENKATARAMAN V., LONDERO P. and GAETA A. L., *Phys. Rev. A*, **81** (2010) 053825.
- [6] DUTIER G., YAROVITSKI A., SALTIEL S., PAPOYAN A., SARKISYAN D., BLOCH D. and DUCLOY M., *Europhys. Lett.*, **63** (2003) 35.
- [7] BALLIN P., MOUFAREJ E., MAURIN I., LALLOTIS A. and BLOCH D., *Appl. Phys. Lett.*, **102** (2013) 231115.
- [8] BLANCO A., CHOMSKI E., GRABTCHAK S., IBISATE M., JOHN S., LEONARD S. W., LOPEZ C., MESEGUER F., MIGUEZ H., MONDIA J. P., OZIN G. A., TOADER O. and VAN DRIEL H. M., *Nature*, **405** (2000) 437.
- [9] KARPOV I. A., SAMAROV E. N., MASALOV V. M., BOZHKO S. I. and EMEL’CHENKO G. A., *Phys. Solid State*, **47** (2005) 347.
- [10] MASSÉ P., VALLÉE R. A. L., DECHÉZELLES J.-F., ROSSELGONG J., CLOUTET E., CRAMAIL H., ZHAO X. S. and RAVAINÉ S., *J. Phys. Chem. C*, **113** (2009) 14487.
- [11] ROMANELLI M., MAURIN I., TODOROV P., CHAN C. H. and BLOCH D., *Ann. Phys. (Paris)*, **32** (2007) 127.
- [12] BALLIN P., MOUFAREJ E., MAURIN I., LALLOTIS A. and BLOCH D., *Proc. SPIE*, **8770** (2013) 87700J.
- [13] MAURIN I., MOUFAREJ E., LALLOTIS A. and BLOCH D., *The optical interface of a photonic crystal: modelling an opal with a stratified effective index*, arXiv:1407.5777 (2014).
- [14] MAURIN I. and BLOCH D., *Opal infiltrated with a resonant medium: Spectral lineshape and in-depth contribution*, in preparation.
- [15] ZABKOV I. *et al.*, unpublished.
- [16] WOSTYN K., ZHAO Y., YEE B., CLAYS K., PERSOONS A., DE SCHAETZEN G. and HELLEMANS L., *J. Chem. Phys.*, **118** (2003) 10752.

Optics of an opal modeled with a stratified effective index and the effect of the interface

ISABELLE MAURIN,^{1,2,*} ELIAS MOUFAREJ,^{1,2} ATHANASIOS LALITIS,^{1,2} AND DANIEL BLOCH^{2,1}

¹Laboratoire de Physique des Lasers, Université Paris 13, Sorbonne Paris-Cité, F-93430 Villetaneuse, France

²CNRS, UMR 7538, 99 Avenue J.-B. Clément, F-93430 Villetaneuse, France

*Corresponding author: isabelle.maurin@univ-paris13.fr

Received 27 May 2015; revised 2 July 2015; accepted 2 July 2015; posted 6 July 2015 (Doc. ID 241459); published 31 July 2015

Reflection and transmission for an artificial opal are described through a model of stratified medium based upon a 1D variation of an effective index. The model is notably applicable to a Langmuir–Blodgett-type disordered opal. Light scattering is accounted for by a phenomenological absorption. The interface region between the opal and the substrate, or the vacuum, induces a periodicity break in the photonic crystal arrangement, which exhibits prominent influence on the reflection, notably away from the Bragg reflection peak. Experimental results are compared with our model. The model is extendable to inverse opals, stacked cylinders, or irradiation by evanescent waves. © 2015 Optical Society of America

OCIS codes: (050.5298) Photonic crystals; (050.6624) Subwavelength structures; (130.5296) Photonic crystal waveguides; (050.2065) Effective medium theory; (310.5448) Polarization, other optical properties.

<http://dx.doi.org/10.1364/JOSAB.32.001761>

1. INTRODUCTION

Structures with a refractive index periodically varying on a scale comparable with an optical wavelength are described as “photonic crystals” [1–6], and photonic energy bands can be predicted. The interest in photonic crystals is usually connected to their “bulk” optical properties, with the expectation of specific propagation rules *inside* the periodic arrangement of the crystal. Apart from the band structure, the photonic crystal periodicity (on a wavelength scale), and their possible self-organization, make them interesting in themselves. In nearly all cases, the optical information of interest requires detection *outside* the photonic crystal. This makes the effect of the interface critical: (1) as a principle, this boundary region tends to break the periodicity typical of the photonic crystal; (2) optical reflection at the interface usually probes the optical response on a dimension related to the optical wavelength λ . For these reasons, experimental tests of the quality of a photonic crystal are at a risk to explore mostly the quality of the first layers only, notably when the tests are conducted in reflection (see, e.g., [7,8]).

Many techniques were developed to solve the difficulty of fabricating 3D or 2D photonic crystals [9]. Soft chemistry methods [10–15] are convenient in spite of a limited choice of geometry and materials. In particular, artificial opals can be obtained through the self-organization of a mono-disperse distribution of submicrometric spheres (in polystyrene, silica, or even TiO₂). In a process of sedimentation or convection involving evaporation of a solvent [10–13] and deposition of the spheres onto a substrate, the microscopic description of

the evaporation of the solvent justifies that artificial opals, produced as a bulk material, tend to organize as a compact face-centered cubic (FCC) crystalline arrangement [13] of dielectric spheres. The three-dimensional organization can be observed for good quality opals [16–20], through specific signatures associated to the simultaneous organization along the (111) and (200) crystalline planes. An alternate fabrication technique is the Langmuir–Blodgett (LB) method, which consists of a successive layer-by-layer deposition of spheres and allows control of the number of layers [14,15]. In such a technique, the photonic crystal, whose quality is affected by the sphere size dispersion, is usually highly polycrystalline, notably in the direction normal to the LB deposition plane: the crystalline arrangement usually exhibits a random hexagonal close-packed (RHCP) structure (i.e., a mix of FCC and HCP hexagonal close-packed lattices rather than a true FCC arrangement). In all cases, the opal is not self-supported but has grown from a (planar) substrate, with the (111) plane parallel to the substrate. The present work is devoted to a simple description of the optics of an artificial and rather disordered (LB-like) opal and focuses on the influence of the interface region between the opal and its substrate.

Bandgap calculations solely based upon the opal periodicity (and indices, sphere diameter...) are not sufficient because the interface breaks the periodicity. Rather, various *ad hoc* models were developed in the literature. Numerical calculations based upon finite element methods (see [21,22]) can predict reflection, transmission, and scattering, including speckle

and coherent multiple diffraction. They are nonetheless heavy and of a limited versatility under a small change in the parameters of the opal or to deal with the random defects of a self-organized material. Alternately, simplified models based upon the scalar wave approximation (SWA) were also considered, relying on the periodicity of the photonic crystal (normally to the deposition plane); they are often restricted to normal incidence [23–26].

A fully homogeneous “effective index” model has also been popular in the photonic crystal literature [27] (and for opals since [11]), which restricts to a “zero-dimension” the crystal periodicity. In this approach, the concept of “effective index,” initially developed in optics to take into account inclusion of “small-size” crystallites (i.e., small relatively to the relevant optical wavelength), is extended to glass spheres whose size is of the same order of magnitude as the wavelength. This crude model has even been used to describe antireflection properties of a single layer opal [28,29]. It is actually often combined with the geometrical periodicity of the opal crystalline arrangement [11,16–18,30,31] in order to predict a peak of reflectivity in analogy with a Bragg diffraction peak, so that the “effective index” allows us to determine the optical periodicity inside the opal. By adjusting the model to experiments performed under various incidences, a refined estimate of the sphere diameter and/or of the sphere index (i.e., an indication of porosity) is sometimes obtained [18,32]. However, such an approach cannot predict quantitatively transmission or reflection (nor scattering).

In the present work, we consider a stratified 1D version of an effective index model. This stratified description of the opal layers allows a much better description of the interfacial regions between the opal and the substrate (or the vacuum), notably for these extreme regions where the glass spheres are not in a compact arrangement. Such a model, although mentioned in some occurrences in the literature [33,34], has not been fully developed until now [35]. Among several advantages, including rather simple and versatile 1D calculations, it appears well suited to a thin LB opal with its already mentioned RHCP structure. The purpose of such a 1D index model is intrinsically restricted to a fair description of reflection and transmission behaviors, while light scattering and diffraction are out of reach. Rather, an *ad hoc* loss [34] has to be added to the model to avoid the sum of the reflection and transmission coefficients to be unity for a transparent-material-like glass. The major original result of our model is that it demonstrates the strong influence of the opal “interface,” which is defined, depending on the experimental conditions, as the contact region including the substrate on which the opal is deposited, or as the nonplanar interface between vacuum and the opal. This single interface is at the origin of most of the reflection properties, notably for all incidences falling far away from the specific condition of Bragg reflection. We show also that the model, which intrinsically includes the complex interferences between all thin slices of opal, applies satisfactorily to understand the buildup of a quasi-“Bragg diffraction” and the residual Fabry–Perot-like oscillations [10,16,17,20,36] or the effect of an imperfect opal periodicity [16,36]. The extension of our results to the specific resonant properties of a material infiltrated in the void regions of an opal [37] has also been considered and is the topic of a

specific paper [38]. Finally, results derived from some of our previous experiments [39,40], which were mostly devoted to the analysis of the infiltration of a resonant gas into an opal, and from complementary dedicated experiments on some smaller diameter opals, are shown to be compatible with our predictions once the extinction parameter is adjusted.

The paper is organized as follows: in Section 2, we describe the opal as a stratified medium and introduce the treatment through a transfer matrix approach. Although the transfer matrix is a classical method, we provide in Appendix A some details to validate the introduction of an absorption coefficient replacing scattering. In Section 3, we discriminate the contribution of the different regions of the opal, through simplified distributions of the stratified index (e.g., “fused opal” model) and notably discuss the specific influence on reflection of the interface between substrate (or vacuum) and the opal. The coherent construction of a Bragg reflection associated to the (bulk) periodicity of the opal and the effect of a single layer defect introduced on purpose, or as a fabrication defect, are also considered. Section 4 first summarizes our previous experimental findings concerning the reflection at an opal interface at specific λ/D values (λ the optical wavelength, D the diameter of the opal spheres) and reports on dedicated experiments performed with a white laser on small size opals (with numerous defects) in a regime making the Bragg reflection observable. Section 5 summarizes the results and briefly considers some possible extensions.

2. OPTICAL MODEL OF THE OPAL AND FORMALISM

A. Stratified Effective Index

The “effective index” model has been generally applied to average, through a single parameter, the optical properties of a medium that includes voids or impurities, whose size is much smaller than the optical wavelength (λ) (see, e.g., [41] and references therein). The effective index n_{eff} is deduced from an “averaged” permittivity. For a dielectric medium with small size (vacuum) voids, it is hence defined as

$$n_{\text{eff}} = [f \cdot \varepsilon + (1 - f)]^{1/2}, \quad (1)$$

with ε the dielectric constant of the filling material ($\varepsilon = n^2$ with n the dielectric index of the filling material), and f the (volume) filling factor of the dielectric medium.

To extend an “effective index” description to a “stratified effective index” model for the opal, one has to “slice” the opal in successive layers parallel to the (111) plane. In the case of an LB opal, many defects may occur for each deposited layer, but the overall structure of successive deposited layers is respected as long as a cumulative disorder has not totally washed out the crystalline structure. This is the reason to apply a model for which the “effective index” $n_{\text{eff}}(z)$ is stratified along the direction z perpendicular to the substrate, with the density measured only over a plane of an opal layer, parallel to the substrate. Although slicing is essentially a discrete operation, there is no inconvenience in going to a continuous description, with infinitely thin slices. This requires us to consider a spatially dependent (along z) filling factor $f(z)$ in the plane of the dielectric material (circles for opal). The stratified effective index distribution is, hence, given by

$$n_{\text{eff}}(z) = [f(z) \cdot \varepsilon + (1 - f(z))]^{1/2}, \quad (2)$$

as long as the medium surrounding the sphere is assumed to be vacuum, and $f(z)$ is discussed below.

B. Sphere Packing in an Ideal Opal and Periodicity Index

We consider here the case of an ideal opal in order to use the resulting $f(z)$ in Eq. (2). The ideal opal is a close-packed arrangement of identical spheres, which can be described as successive layers of bidimensional sections of close-packed spheres (a single layer of spheres). The successive layers themselves are arranged in a compact manner, so that the distance between two successive layers is $(2/3)^{1/2} \cdot D$, with D the sphere diameter.

For the first layer above the substrate (which we locate in the $z \leq 0$ region), the filling factor, which corresponds to a closed-packed distribution of circles in hexagonal cells in the equatorial plane ($z = D/2$), is given by

$$f_1(z) = 2\pi z \cdot (D - z)H(z)/(3^{1/2}D^2), \quad (3)$$

with $H(z) = 1$ for $0 \leq z \leq D$ and $H(z) = 0$ elsewhere.

For an opal made of N layers arranged in a compact manner, the filling factor $f(z)$ has to take into account the interpenetration between layers and is the sum of the filling factor of the individual layers:

$$f(z) = \sum_{i=1}^N f_1[z - (i - 1) \cdot D \cdot (2/3)^{1/2}]. \quad (4)$$

In Fig. 1, we show the filling factor for an opal of glass spheres [Fig. 1(a)], along with the corresponding effective index, in a discretized slice version [see Fig. 1(b)]. The two structures are very similar, with the $(2/3)^{1/2} \cdot D$ periodicity between the first equatorial plane (at $D/2$) and the last one. Figure 1 clearly shows that the “opal and substrate” system combines an internal region with periodicity [here $(2/3)^{1/2} \cdot D$ because we have assumed a compact opal], and nearly empty regions (of a thickness $D/2$) close to the substrate. The consequences of this periodicity break, occurring in the interfacial regions (for the first and last half-layers as well), are discussed in Section 3.

C. Propagation in a Stratified Medium

1. Matrix Formalism and Reflection/Transmission Coefficients

The matrix formalism [42,43] for a stratified medium made of successive parallel transparent layers allows calculating the reflection and transmission coefficients. The elementary matrix allows going from one layer to a neighboring one, with the limiting boundary conditions provided by the continuity of the tangential components of the total (electric and magnetic) field at an interface, and Snell’s law for transmission and reflection has to be satisfied at the successive interfaces. In this formalism, the two principal polarizations, TE and TM, do not mix and have to be dealt with separately. For a real opal, this implies that we assume that principal polarizations do not mix through propagation, although such a mixing can be predicted when taking into account all the symmetries of an FCC opal [44].

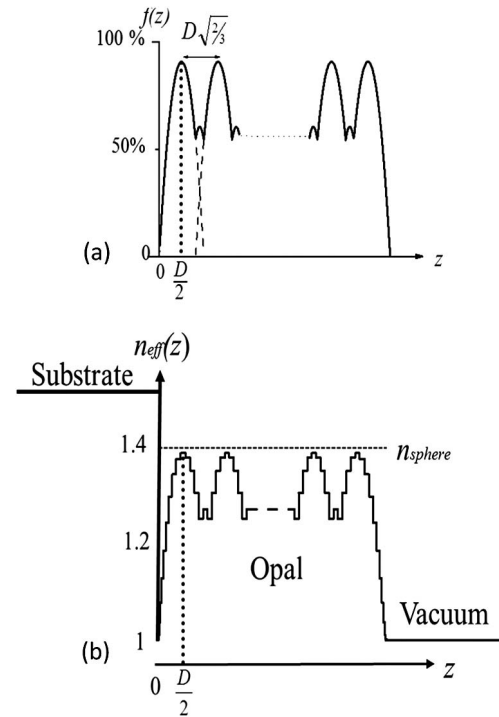


Fig. 1. (a) Full line: the filling factor $f(z)$ in the z -height plane for an opal made of N layers. The dashed lines below $f(z)$ represent the individual filling factors for the first and second layers. (b) The 1D effective index $n_{\text{eff}}(z)$ of the opal, for $n_{\text{sphere}} = 1.4$, shown here in discrete version (stratified medium made of finite thickness layers).

The matrix formalism can also apply in the presence of absorption losses [see Appendix A, notably Eq. (A18)]. As mentioned in Section 1, we introduce such a phenomenological loss in lieu of scattering. Let us note that the absorption integrated over a single layer must remain small for the stratified model to be a useful description of the opal structure; indeed, if the scattering on a single layer of spheres becomes too strong, it would be difficult to identify an effect of the crystalline organization of the opal along z . Note also that, according to Snell’s law, the incidence angle to be considered for a given layer exhibits a complex value, which no longer represents a direction of propagation [45,46]. However, as long as the input and output media (vacuum or glass) are assumed to be transparent, there is no difficulty in defining the incidence, reflection, and emergence (real) angles. Moreover, the change in the propagation direction is negligible when the loss term in the complex refractive index remains small. The corresponding details are provided in Appendix A.

2. Input and Output Media for an Opal Deposited on a Substrate

We consider an opal that is deposited on a transparent substrate, like a glass (parallel) window. Two situations of interest can be discriminated: light entering from the substrate side (as in our experimental work [39,40] with a resonant gas), or from vacuum (or air). In all cases, the media outside the opal are transparent, and they are considered to be infinite in the matrix formalism. Actually, in an experiment, the transparent substrate has a finite size, and light first propagates in the vacuum before

entering into the window. For a thick enough window, a minor wedge angle, which does not affect the direction of light propagation inside the opal, is sufficient to make negligible all internal interferences inside the window, and the specific transfer matrix associated to the (thick) window can be ignored. The effect of this slab is equivalent to that of an “incoherent” layer [45]. For convenience, to help compare the cases when light enters from the substrate or from the vacuum region, we use in all the following the “external” incidence angle, labeled θ . This “external angle” is defined as the angle in vacuum; this assumes that when light goes from the substrate (index n_0) to the opal (with an incidence θ_0 in the substrate), the substrate itself is illuminated from the vacuum, under an “external” incidence angle $\theta = \sin^{-1}(n_0 \sin \theta_0)$.

Note that our assumption that the substrate on which the opal is deposited is a nearly parallel slab (index n_0) implies that $n_0 \sin \theta_0 \leq 1$. A larger range of effective incidence angles, not restricted to $\sin \theta_0 \leq 1/n_0$, can be considered by our formalism and would be very interesting to probe. Experimentally, such a situation could be addressed in a total reflection geometry for an opal deposited on a prism-shaped substrate, allowing the probing of the attenuated reflection as induced by the transmission to the opal.

3. Loss Coefficient Equivalent to the Scattering Effect

It is a known and remarkable point that, for a slab (or layer in a stratified medium) of a given thickness, the dephasing associated to propagation decreases when the incidence angle increases. Conversely, as recalled in Appendix A, the field attenuation increases with the incident angle proportionally to the length traveled inside the medium. This says that the loss coefficient to be introduced may have to depend on the incidence angle. This phenomenological absorption should also depend on the wavelength, through the sphere size/wavelength ratio D/λ (or $Dn_{\text{sphere}}/\lambda$) and possibly on the polarization (TE or TM).

In most cases, we neglect the incidence angle dependence mentioned above, which is in rough agreement with experimental behaviors that we report on in Section 4. We have mostly performed our numerical simulations with a loss coefficient independent of the wavelength or sometimes following a kind of Rayleigh law in λ^{-4} .

The formal calculation of a stratified medium easily allows for a spatial distribution of the loss $\alpha(z)$ distribution. In various occurrences, we have compared a spatially constant loss model [$\alpha(z) = \alpha$], with a model where losses occur only inside the sphere [$\alpha(z) = \alpha f(z)$], or in the voids [$\alpha(z) = \alpha(1 - f(z))$], or where the losses depend on the contact surface [i.e., on the sphere perimeter in the considered layer $\alpha(z) = \alpha f(z)^{1/2}$]. As long as the average (small) loss per layer remains unchanged, there are no significant changes to be predicted when varying the model, taking into account the scattering losses. It is, hence, just simpler to consider a constant loss model.

3. MAJOR RESULTS OF THE MODEL

A. General Behavior of the Model and Typical Numerical Values

To predict the optical behavior of an opal deposited on a substrate, we apply the stratified model (Section 2 and

Appendix A) with numerical values chosen according to the experimental conditions, polarization (TE, TM, or linear combination), the side of incidence (opal or substrate side), incidence (“external”) angle θ , and irradiation wavelength λ . For the opal, the relevant figures are the number of layers (N) (typically up to 10 or 20, as scattering tends to hinder the role of the deepest layers), the sphere index n_{sphere} (in all the following, we take numerically $n_{\text{sphere}} = 1.4$) from which $n_{\text{eff}}(z)$ is deduced, the substrate index $n_{\text{substrate}}$, the sphere diameter D (or only the reduced parameter D/λ), and the absorption α , possibly dependent on λ or on θ .

Numerically, the calculations for a given opal are performed for a finite number of slices and converge when this number is increased. Practically, it is efficient to divide the opal in a given number (N_{step}) of layers of equal thickness per period in the periodic region, and in N_b steps to describe the sharper variations of $n(z)$ on the first and last half-layers. For faster convergence, these latter “slices” in half-layer regions have unequal thicknesses in order to ensure a regular growth for $n(z)$. In these conditions, when D and λ are comparable, we avoid any convergence problems by taking $N_b \sim 50$, and $N_{\text{step}} \sim 20\text{--}40$, meaning that a total of less than 10^3 steps is needed for a rather thick opal made of 20 layers.

To illustrate several of the typical behaviors that we will detail in further subsections, we present in Fig. 2(a) a reflection spectrum calculated using the model described in Section 2, covering a considerable range of wavelength (or λ/D value). We assume an opal made of a large number of layers ($N = 20$) of glass spheres (with $n_{\text{sphere}} = 1.4$ as usual), deposited on a similar glass substrate ($n_{\text{substrate}} = 1.4$). Either we ignore the scattering losses [Fig. 2(a)] or we replace scattering by an absorption independent of λ , which remains small enough for a single layer but is nonnegligible for the whole opal [Fig. 2(b)] [47]. Differences are only quantitative between these two reflection spectra. Major similarities are found, showing that the detailed description of the scattering loss is not essential. Note that the equivalent transmission spectra would be strongly affected by the choice of the loss model, which is why all discussions in the present section will be restricted to reflection.

Figure 2 permits us to distinguish several important features. First, one recognizes a sharp reflection “Bragg peak” for $\lambda/D \sim 2.06$. As is well known, this strong peak of reflection may mean that light cannot enter into the opal, as this situation corresponds to a bandgap region of a photonic crystal, even if the opal is not a fully periodical system. When absorption is taken into account [Fig. 2(b)], light is only partly reflected

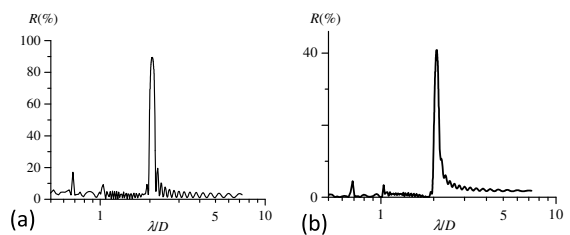


Fig. 2. Reflection spectrum calculated for $N = 20$ layers. Irradiation on the vacuum side, TE polarization, $\theta = 20^\circ$, $n_{\text{substrate}} = 1.4 = n_{\text{sphere}}$. The absorption coefficient is (a) $\alpha D = 0$ and (b) $\alpha D = 0.1$.

and partly lost inside the opal: the system of destructive interferences that prohibits propagation has become imperfect. The detailed features of this reflection peak (width, asymmetry, line shape, ...) are essentially determined by the numerical values and shape modeling chosen for the opal. This is to be compared with numerous studies in the literature where the line shape of the Bragg peak is just described by a quantity such as a FWHM (see, e.g., [16]), ignoring the asymmetry of a real line shape.

Two other peaks of smaller amplitude can also be identified ($\lambda/D \sim 1.04$ and $\lambda/D \sim 0.7$), which are known to be associated with high-order Bragg diffraction. Apart from these peaks, reflection remains rather weak and exhibits recognizable oscillations. All these features, from small oscillations to the Bragg peaks' asymmetry, originate in interference effects.

In the next subsections, we address the major features of Fig. 2, replacing when possible the stratified opal by even simpler models, to focus on a specific effect. In particular, we discriminate the essential effect of the periodicity break in the vicinity of the interface region, from various effects of periodicity (Bragg peak and Fabry–Perot-like effects), which are already well identified in the literature. We also include a local defect inside the opal [48–50]. For simplicity, we choose the loss coefficient α to be wavelength independent in Section 3.

B. Effect of the Interface between the Opal First Half-Layer and Substrate or Vacuum on Reflectivity

It has been recognized that reflectivity of a photonic crystal is not always proof of its good organization and even that the reflectance of a “photonic glass” [7], which is an intrinsically disordered medium made of identical spheres, may resemble the reflectance of the equivalent photonic crystal.

Here, to outline the symmetry break imposed by the interface region, rather than the effect of opal periodicity, we consider a specific stratified system of a “fused opal,” whose index varies according to the local effective index [Eq. (2)] for the first half-layer of spheres ($0 \leq z \leq D/2$), and where the periodic region of the opal is replaced by a “fused” region of constant index n_{\max} [on an infinite length or, at least, on a length largely exceeding the extinction length; see Fig. 3(a)]. For continuity reasons, we assume $n_{\max} = n(z = D/2)$, so that we choose numerically $n_{\max} = 1.36$ (for $n_{\text{sphere}} = 1.4$). We take a moderate absorption coefficient $\alpha D = 0.1$ (see Fig. 3) to allow a finite size of the “fused opal.”

The reflection coefficient is expected to depend on the ratio λ/D , which governs the ratio between the wavelength and the extension ($\sim D/2$) of the “gap” region. Two limits can be predicted: for $\lambda/D \gg 1$, the “gap” region becomes so thin that it can be ignored, and the reflectivity can be simply estimated (through Fresnel formulas) from the interface between the substrate (or vacuum) and the constant index of the “opal” with constant index; conversely, for short wavelengths $\lambda/D \ll 1$, light mostly feels the contrast between the substrate and vacuum at the contact plane with the spheres (or a null contrast for an irradiation from the vacuum region) and further accommodates with the slowly varying index. Here, we provide insight to the predicted evolution between these two extreme behaviors, covering a large range of λ/D ratios. Figures 3 and 4 summarize the results for the two principal polarizations and various incidence angles.

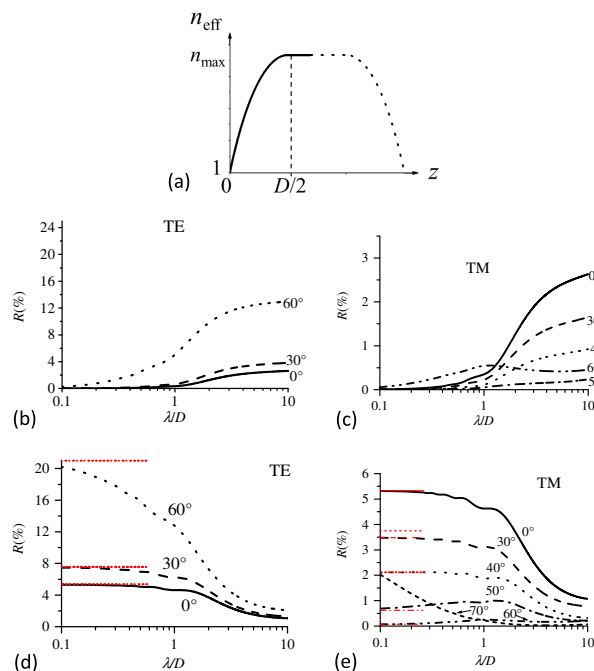


Fig. 3. Reflectivity for the “fused opal” model. (a) Effective index of the “fused opal.” (b), (c), (d), and (e) Normalized wavelength (λ/D) dependence of the reflectivity for the indicated external incidence angle θ . The irradiation is (b) and (c) from the vacuum side and (d) and (e) from the substrate side. Polarization is TE for (b) and (d) and TM for (c) and (e). In (d) and (e), the dotted or dashed lines (red on line) for the smaller values of λ/D indicate the Fresnel reflection coefficient for a planar substrate/vacuum interface. Calculations for $\alpha D = 0.1$ and for (d) and (e), $n_{\text{substrate}} = 1.6$.

In Figs. 3(b) and 3(c), reflectivity on the vacuum side (i.e., $n_{\text{substrate}} = 1$) in the short wavelength limit is extremely small, as expected, and increases in a nearly monotone manner with increasing λ/D ratio. For $\lambda/D \rightarrow \infty$, it typically approaches the Fresnel reflection coefficients (which are incidence and polarization dependent) at a vacuum/ n_{\max} interface.

For reflection on the substrate side, we choose a high value $n_{\text{substrate}} = 1.6$ in Figs. 3(d) and 3(e) to show how one goes from a Fresnel reflection limit from “ $n_{\text{substrate}}/\text{vacuum}$ ” to a “ $n_{\text{substrate}}/n_{\max}$ ” interface when going from the short wavelength limit (i.e., long “gap” region) to the long wavelength limit (i.e., short “gap” region). The same kind of nearly monotone evolution appears in Fig. 4 showing the influence of the substrate index (calculated for the normal incidence). In TM polarization [see Figs. 3(c) and 3(e)], the reflection coefficient remains very small around 50° – 60° incidence, a behavior reminiscent of a Brewster angle at a single flat interface. In spite of these simple trends, one also observes, when looking more in detail at Figs 3 and 4, tiny wavy behaviors. These behaviors are a signature of the multiple interferences intrinsic to a stratified index medium, which is here restricted to a “smooth” and monotone half-layer interface.

In Figs. 3 and 4, one sees that the behavior for an irradiation on the substrate side [Figs. 3 and 4] remains close to the asymptotic regime of small λ/D values, where the dominant effect is the “gap” between the substrate and the thin empty region, as

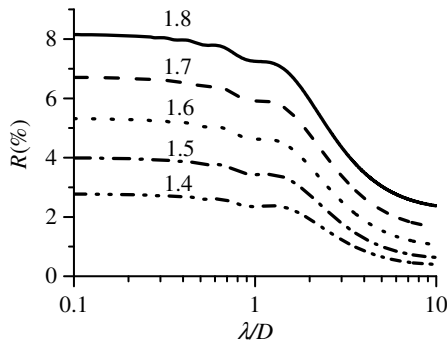


Fig. 4. Normalized wavelength (λ/D) dependence of the reflectivity for the “fused opal” model, for normal incidence irradiation from the substrate side. Values of $n_{\text{substrate}}$ as indicated. Calculations are for $\alpha D = 0.1$.

long as $\lambda \leq D$. It is rather for very long wavelengths, when the effect of dephasing (~ 1 rad, i.e., propagation over $\lambda/2\pi$) cannot occur on a distance comparable with the interface thickness ($D/2$), that the gap region can be neglected. It is worth noting that, around the “Bragg reflection peak” evidenced in Fig. 2, which is found for $\lambda/D \sim 2$, the effect of the interface region is not yet negligible and must be fully taken into account for a quantitative description of the amplitude or shape of the Bragg peak.

C. Bragg Reflection and Fabry–Perot Oscillations

In Fig. 2, the sharp peak for $\lambda/D \approx 2.06$ in the reflectivity spectrum is a well-known feature of an opal [11,14,16–18]. It is associated with a “forbidden band” in a photonic crystal approach and corresponds to a nearly prohibited transmission. Describing this strong reflectivity as a “Bragg reflection” is actually a way to underline an analogy with the X-ray diffraction on the periodically located point-like nuclei in the structure of an atomic or molecular crystal. Note that the extremely small size of nuclei, and their precise arrangement relatively to the distance between successive planes, leads to a definition of the Bragg angle, which is incommensurately sharper than the one encountered with opals. For an opal, the periodic 3D grating actually relies on an ensemble of contacted spheres, but the principle of a geometric condition governing the direction of a Bragg diffraction still applies. The standard Bragg condition $k\lambda = 2a \cos(\theta)$, with k an integer, a the distance between successive planes, and θ the incidence angle, should, however, include the effect of propagation in the opal as a heterogeneous medium, so that a modified equation [11] is often applied to find the wavelength λ_{max} for an opal [17,18,30]:

$$k\lambda_{\text{max}}/D = 2 \cdot (2/3)^{1/2} (n_{\text{eff}}^2 - \sin^2 \theta)^{1/2}. \quad (5)$$

Equation (5) takes into account the $(2/3)^{1/2} \cdot D$ geometrical periodicity of the opal, and the Bragg condition is satisfied in a fictitious medium whose index is the averaged effective index n_{eff} (usually estimated with the compact filling factor 74%), and for which the effective incidence deduces by the Snell’s law from the external incidence angle θ (i.e., in vacuum). The peak at $\lambda/D \approx 2.06$ in Fig. 2 is, hence, compatible with a first-order ($k = 1$) Bragg diffraction peak.

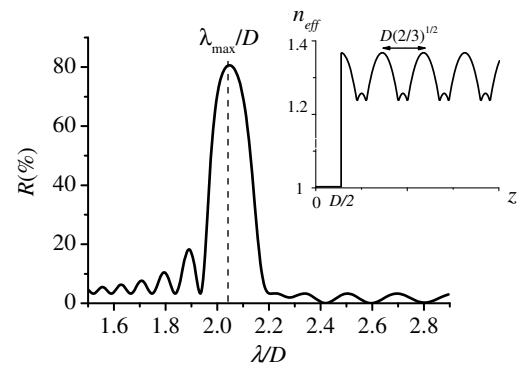


Fig. 5. Reflectivity spectrum for a periodic distribution of the effective index $n_{\text{eff}}(z)$, as shown in the inset. Calculations are for $N = 18$, $\theta = 20^\circ$, $n_{\text{substrate}} = 1.4$, $\alpha D = 0.193$, and TM polarization.

The sensitivity of the Bragg peak region to the details of the opal shape is illustrated in Fig. 5. Figure 5 is the result of a calculation for a simplified opal, in which the smooth “gap” regions (first and last half-layers) are replaced by a single arbitrary step ($N_b = 1$). The behavior is analogous to the one shown in Fig. 2 around the Bragg peak. However, the residual line shape asymmetry around the Bragg peak differs from the one appearing in Fig. 2. The line shape is again modified, even with minor changes in the shape of the periodic structure or when keeping a detailed description ($N_b = 50$) of the interface region, as is the case in Fig. 6 (see, e.g., for $N_{\text{layer}} = 10$ or for $N_{\text{layer}} = 30$).

Also, it is when increasing the number of layers that the contribution of the periodic region can be recognized. One typically needs at least three layers (see Fig. 6) to recognize a Bragg diffraction peak in reflection. The peak gets sharper (maximized amplitude and minimized width) when increasing the number of layers, while the position of the peak moves to an asymptotic value, obtained for ~ 10 – 20 layers with our realistic choice of parameters. The number of layers needed to reach the asymptotic behavior of a thick opal depends on the scattering/extinction parameter.

Our model also provides line shape and amplitude predictions for the already mentioned higher-order Bragg reflectivity

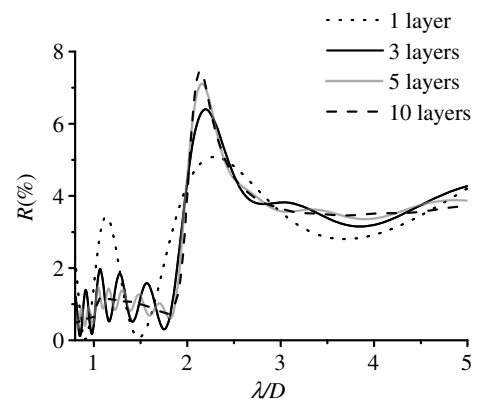


Fig. 6. Reflectivity spectra (vacuum side), as a function of the number of layers N (as indicated). TE polarization, $n_{\text{substrate}} = 1.4$, $\alpha D = 0.0552$, $\theta = 20^\circ$. The curve for $N = 30$ (not shown) is just superimposed to the one for $N = 10$.

peaks, as can be revealed by some differences between Figs. 2(a) and 2(b). However, a practical limitation for the validity of these predictions is due to the absorption coefficient replacing the effect of scattering. This effect can indeed undergo considerable variations over an octave of wavelength.

Apart from the first- and high-order Bragg reflection peaks, tiny quasi-periodic oscillations are seen in Figs. 2, 5, and 6. One can note in Fig. 6 that their periodicity and amplitude decrease when increasing the number of layers. These oscillations, which disappear in a too simple model when the exit layer is not reached, are associated with a Fabry–Perot-like effect between the two extreme regions of the opal. As can be verified in Fig. 6, they tend to cancel for a thick opal because of the extinction by scattering. These oscillations are often mentioned in the literature [16,17] and are sometimes used to evaluate the opal thickness or to assess the parallelism of the deposited layers.

D. Effects of a Defective Layer in the Opal

The quality of a real opal arrangement strongly depends on the uniformity of sphere size, which can be good for polystyrene spheres, while dispersion is higher for glass spheres. Also, the opal quality tends to degrade layer after layer due to dispersion in sphere size, clustering of spheres, sphere porosity, arrangement defaults, etc. This is a major limitation for all theories relying on the periodicity of the opal.

To illustrate the flexibility of our model and to approach a realistic situation [26,49] on the road to a disordered opal, we introduce an on-purpose defect in the i th layer of the opal, assuming for the index a sudden change to a constant value, which locally breaks the periodicity. Figure 7 illustrates how the shape of the reflectivity spectrum changes with the position of the defect. Whatever the position of the defect layer, the peak reflectivity decreases, while the position of the Bragg peak is marginally modified. The change is stronger when the defect is located among the first layers. This had to be expected because the first layer's contribution is critical for the buildup of the Bragg peak, while absorption (or optical scattering) makes the contribution of the remote layers less important, as already seen in Fig. 7.

4. EXPERIMENTAL OBSERVATIONS

A. Initial Observations

Our initial interest for the optics of opals started with spectroscopic experiments dedicated to the analysis of the resonant

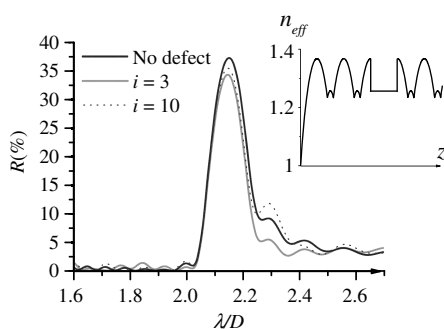


Fig. 7. Reflectivity spectra (vacuum side) under normal incidence for various positions of the i th layer carrying a defect (see inset); $n_{\text{substrate}} = 1.4$, $aD = 0.09$.

behavior of a gas infiltrated in an opal. These experiments, initially conducted at $\lambda = 852$ nm and $\lambda = 894$ nm on opals made of 10 or 20 layers of glass spheres with $D = 1.0$ μm deposited on a standard glass ($n_{\text{substrate}} \approx 1.5$) [39], were enriched by experiments with $\lambda = 455$ nm, and with opals $D \sim 400$ nm [40]. In addition to the scattering of the incident light, whose residual coherence occasionally leads to specific diffraction figures, such as a hexagonal diffraction for a single opal layer [51], or to more complex structures for a perfect multilayer arrangement [16,45], we had noted that a fraction of the beam undergoes a specular reflection at the substrate/opal interface, while another part of the beam is transmitted. The presence of such reflected beams, although well documented even far away from the Bragg reflected peak [39,52], is partly unexpected because the opal/substrate and opal/vacuum interfaces are strongly nonplanar (at a microscopic/wavelength scale). Also, the incident beam polarization (assuming a principal polarization for the irradiation) is mostly conserved [53–55] for these reflected or transmitted beams. A major result is that reflectivity at the substrate/opal interface (for 10 or 20 layers as well) is extremely close to the one measured on the bare substrate ($\sim 4\%$ under normal incidence). This is true independently of the incidence angle or polarization, as long as the reflection remains rather small (practically, this regime breaks only for TE polarization above 30° – 40°). For large incidence angles and TM polarization, reflection on the opal becomes very small, a situation analogous to the Brewster incidence on a flat surface. All these behaviors appear fully compatible with the results of our 1D stratified model, when we show (Section 3.B) that reflectivity at the interface remains close to the value predicted for a simple planar interface, as long as λ does not largely exceed the “gap” size.

B. Dedicated Experiments

In this section, we report on dedicated experiments performed on an opal where we used a white light irradiation, in order to test some of our predictions related to the Bragg-type reflectivity peak. Also, we measure transmission and reflection in order to explore how a simple conversion of the scattering effect into a “loss” term can be acceptable.

1. Experimental Setup

Our experiments with white light were restricted to a single sample made of 20 layers of silica spheres smaller than in previous section ($D = 280$ nm $\pm 5\%$). The Langmuir–Blodgett deposition technique was used to fabricate this opal, which has many structural defects owing to the dispersion in sphere size, resulting in a polycrystalline opal. The substrate of the opal is a microscope slide (glass), whose index is close to the one of the SiO_2 microspheres; the parallelism of the microscope slide is poor enough to make internal interferences negligible.

The sample was illuminated with a collimated white light from a fibered-type supercontinuum source (LEUKOS SM 20, for 400–1700 nm, pulses < 1 ns, repetition rate: 20 Hz, average power > 40 mW). The beam diameter was around 2 mm, corresponding to an averaging on many spheres (at this scale, each layer of the opal is already polycrystalline). The beams of interest (the reflected one and the transmitted one) are collected by a second optical fiber connected to a fibered spectrometer

(Ocean Optics USB 2000+, detection for $\lambda = 200\text{--}1100$ nm, resolution $\Delta\lambda \sim 0.4$ nm). The orientation of this detection fiber must be carefully optimized to ensure that the collection efficiency is the same all over the spectrum. This is an important source of uncertainty for a multimode fiber and for an analysis over a rather broad spectra range, and this sets limits to our experimental sensitivity. Despite these limitations, our goal is to compare effective measurements with predictions and not just line shapes in arbitrary units. Reflection and transmission spectra of the opal are obtained once normalized against the spectral content of the white source (temporal fluctuations are notable, requiring frequent analyses of the spectrum content of the white source). For sensitivity reasons, reliable spectra are obtained mostly in the 400–800 nm region, covering for our opal a 1.5–3 range of λ/D values, complementary to our initial experiments.

The reflection and transmission spectra were recorded for various incident angles θ , both for an irradiation on the vacuum side and on the substrate side. The incident polarization was controlled by an external polarizer. In our experiments, the polarization of the beam after reflection or transmission in the opal appears unchanged despite the 3D scattering [53–55].

2. Transmission Measurements and the Evaluation of Scattering Losses

In the previous section (Section 3), we used our model only for the opal reflectivity, rather than for transmission, because some important features of reflectivity are rather insensitive to the scattering losses. Transmission, intrinsically sensitive to the absorption term, is also provided by the matrix formalism (Section 2).

Experiments (see Fig. 8) clearly show wavelength dependence for transmission, which drops down in the short wavelength region, although glass remains transparent. One also notes a strong dip in the transmission (around 550 nm), for a wavelength range corresponding to the Bragg reflection peak,

when propagation through the opal is (nearly) forbidden [11]. To be able to model the decrease in transmission for the shorter wavelengths, we have investigated various power laws for the wavelength dependence of the absorption coefficient. We find a reasonable agreement for the transmission spectrum for an absorption coefficient resembling a Rayleigh-like scattering, $\alpha(\lambda) = \beta/\lambda^4$ with β a constant. In all of the following, we take $\beta = 1.5 \cdot 10^{-20} \text{ m}^3$, with the assumption that this coefficient is independent of the incidence angle. Remarkably, the Bragg transmission dip is satisfactorily reproduced by our calculation [Figs. 8(a) and 8(b)], relatively to its amplitude and width. This agreement persists when changing the side of irradiation for this transmission measurement (i.e., propagation through the substrate and the opal, or propagation through the opal and the substrate), or the polarization. When increasing the incidence angle [Figs. 8(c) and 8(d)], there is still reasonable agreement between the experiment and the prediction, although we have not adjusted any parameter in the model, keeping the same parameter for the absorption (in the stratified model, this corresponds to a constant absorption per unit of “light traveled length” [see Appendix A]).

3. Fitting Reflectivity Measurements

Figure 9 presents the reflectivity spectra for a large range of incidence angles, TE and TM polarizations, and irradiation on the opal and substrate sides. The predictions of the model, in which the same set of parameters is used for all these experiments, are also provided. The choice of the explored λ/D range implies the presence of a Bragg reflection peak, whose exact position should vary with the incidence angle. We observe indeed a good agreement between the experimental and theoretical positions of these peaks, whose wavelength becomes smaller when increasing the incidence angle. In Fig. 10, we have plotted the experimental peak wavelength for reflection as a function of the incidence angle. It is compared, on the one hand,

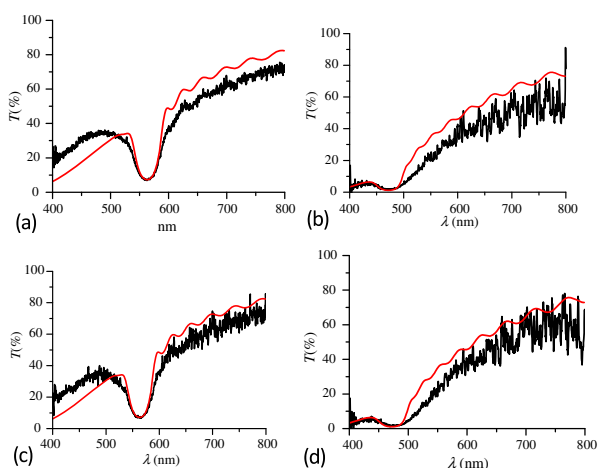


Fig. 8. Transmission spectra (TE polarization) on an opal made with 20 layers of $D = 276$ nm glass spheres. (a) and (b) Vacuum side. (c) and (d) Substrate side. For (a) and (c), $\theta = 20^\circ$. For (b) and (d), $\theta = 50^\circ$. Experimental curves (in black) are compared with the calculated values (red on line), for which one has taken $\alpha = \beta/\lambda^4$, with $\beta = 1.5 \cdot 10^{-20} \text{ m}^3$.

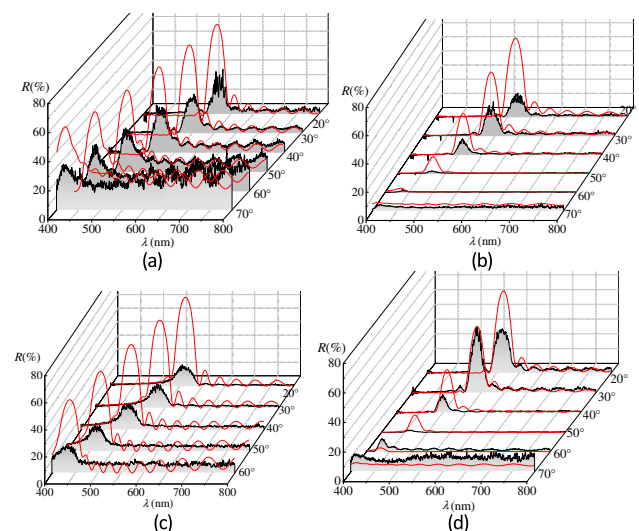


Fig. 9. Reflectivity spectra for various incidence angles θ (as indicated) for the same experimental sample (black) and related calculations (red on line) as in Fig. 8. (a) and (b) On vacuum side. (c) and (d) On substrate side. Polarization (a) and (c) TE and (b) and (d) TM.

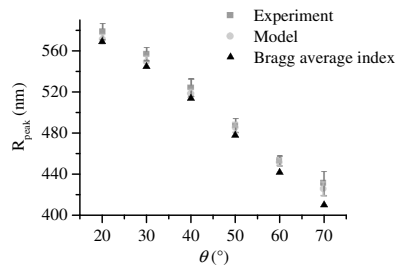


Fig. 10. Position of the peak of the reflectivity spectrum (R_{peak}) as a function of the incidence angle (substrate side). Comparison between the experiment, our calculations, and the simplified Bragg equation (sample and calculations are similar to Fig. 9, TE polarization).

with the predictions of our model, which includes the periodic regions of the opal and the peripheral half-layers, and, on the other hand, with the simplified Bragg model, taking into account a global effective index [Eq. (5)]. Although the differences remain marginal, our model seems more precise than the one with a global effective index.

A specific added value of our model is that it predicts the width and amplitude of this Bragg peak, as it already did satisfactorily for transmission. Here, the estimates for the width appear in an acceptable agreement with the experiment. Our model is even able to produce sometimes an excellent fitting (e.g., 30° and 20° in TM) with the experiment, including a satisfactory agreement for the small oscillations, shown to be Fabry–Perot type (see Section 3.C). Note that the exact thickness of our sample and, hence, the phase of these oscillations remains unknown because of the defects in the opal fabrication. These defects may also explain the observed quantitative discrepancies in the reflection amplitude. In particular, when the Bragg peaks appear smaller than predicted, it is natural to consider that the opal, with its successive layer-by-layer deposition, is not as periodical as in the ideal calculation. We also observe a satisfactory trend for the overall reflectivity (away from the Bragg peak) when varying the incidence angle, with differing behaviors for TE and TM polarizations. In particular, in TM polarization [Figs. 9(b) and 9(d)], the overall reflectivity decreases close to zero for large angles especially for irradiation from substrate side (i.e., large contrast between the input medium (substrate) and the first half-layer “gap”). This is expected [35,53–55] and is analogous to a near Brewster incidence angle, when the reflectivity undergoes a strong influence of the first half-layer.

Finally, a more intriguing observation is on Fig. 9(d) for $\theta = 50^\circ$, where the residual experimental Bragg peak has a higher amplitude than predicted. This could originate in a residual depolarization of the reflected (or “backscattered”) light or, simply, in an imperfect polarization of the light-reaching opal. A marginal mixture of TE and TM polarizations inside the opal [44] would, hence, explain the observation of a Bragg peak when calculations rigorously limited to TM are not able to justify such an effect.

5. CONCLUSION AND PERSPECTIVES

To summarize, our simple model based on a stratified effective index in a direction z perpendicular to the opal permits us to

evaluate the main features of reflection and transmission for an opal deposited on a substrate and allows for quantitative predictions. A major strength of such a 1D model is that is well-suited to include the partial disorder of a real opal, which is particularly notable when fabricated by LB methods; oppositely, it cannot include the details of the crystalline structure of the opal with its various symmetry planes [e.g., the reflection on a (200) plane]. The need to introduce an *ad hoc* extinction coefficient to describe scattering may limit the range of validity of the quantitative predictions because this coefficient is susceptible to vary strongly with the wavelength or to a lesser extent with the incidence angle. Our experiments, despite their limited scope, show that these variations may be not so dramatic.

Our model, based upon a system of interferences between all the thin layers of the opal, makes it easy to discriminate between various physical effects, including interferences (Bragg peak at first and high order and Fabry–Perot-type oscillations) with their wavy behaviors in reflection/transmission spectra and their sensitivity to a small change in the internal structure as well as reflection from the interface region.

The demonstration of the influence of the first half-layer, which intrinsically breaks the periodicity because of an interface with a substrate of an arbitrary index (or with vacuum), is an important result easily evidenced by our model. The size of the “gap” region, relatively to the wavelength, is an essential parameter. It must be emphasized that this corresponds to a general situation, often unduly ignored when evaluating the optics of a photonic crystal. This “interface” coupling, occurring on a wavelength scale, easily hinders internal (in-depth) features such as defects of the opal or of a photonic crystal.

The model we have developed is highly flexible. It is easy to introduce a defective layer in the opal, and it would be also possible to introduce some dispersion in the average layer thickness, or to introduce an extra layer, noncompactly arranged as can be imposed by the purposeful [50] introduction of a special layer. Our 1D model is intrinsically applicable to a compact arrangement of stacked parallel cylinders [27], provided that $f(z)$ is properly redefined in Eq. (3). It also can be applied to an inverse opal. It is worth noting that, although the effective medium theory is applicable when the inhomogeneities are much smaller than the wavelength, our quantitative approach uses very thin slices, or steps in the calculation, thus making our improved “effective index” model more applicable. Also, the orientation of the opal parallel to the substrate is an intrinsic source of structural anisotropy for polarization (see [39]; note also the differing TE/TM wavelength dependence in Fig. 3), although all media are microscopically isotropic. These points have been discussed in the literature [56]. In the same spirit, our formalism is applicable to an opal deposited on a prism, leading to the intriguing situation where propagation in the interface region (when $\lambda \leq D$) is mostly due to an evanescent wave.

Finally, it is possible to consider the situation of an opal infiltrated by some material (liquid, gas, dopants), as if the infiltration is an added defect to the layer structure. This is done in another work [38], where we calculate the optical response of a resonant material infiltrated in a photonic crystal and demonstrate that, under specific conditions, rather remote regions

of the opal contribute to the reflectivity for well-chosen incidences.

APPENDIX A: MATRIX TRANSFER TREATMENT

We consider an incident light irradiation in the $z \leq 0$ region of index n_0 defined by its electric field:

$$\mathbf{E} = E_0 \cdot \exp j(\omega t - \mathbf{k} \cdot \mathbf{r})\mathbf{u}, \quad (\text{A1})$$

with ω the (circular) frequency (corresponding to a wavelength in vacuum λ). In Eq. (A1), \mathbf{k} is the wave vector and \mathbf{u} the unit vector, giving the direction of the polarization. As shown in Fig. 11, the beam is incident under an incidence θ_0 on a medium composed of N finite parallel layers (perpendicular to z , in the $z \geq 0$ region), and ended by a region of index n_{N+1} .

The matrix formalism takes into account the propagation in each layer for the forward and backward field components resulting from successive transmission and reflection and which propagate under an angle satisfying the Snell's law at the successive interfaces.

Following the notations of Fig. 11, one defines the tangential component of the electric (respectively, magnetic) field at the generic boundary between the $(i-1)$ th and i th layers as $E_{i-1,i}$ (respectively, $H_{i-1,i}$). We first consider a transparent stratified medium. For the i th layer, the index is defined as n_i , the thickness as d_i , and the propagation angle as θ_i with

$$n_0 \sin \theta_0 = n_i \sin(\theta_i). \quad (\text{A2})$$

The transfer matrix M_i then appears when comparing the $(i-1)$ th and i th layers boundary, with the i th and $(i+1)$ th layers boundary. One finds

$$\begin{pmatrix} E_{i-1,i} \\ H_{i-1,i} \end{pmatrix} = M_i \begin{pmatrix} E_{i,i+1} \\ H_{i,i+1} \end{pmatrix}, \quad (\text{A3})$$

with

$$M_i = \begin{pmatrix} \cos(\delta_i) & j \sin(\delta_i)/Y_i \\ jY_i \sin(\delta_i) & \cos(\delta_i) \end{pmatrix}. \quad (\text{A4})$$

In Eqs. (A3) and (A4), one has defined

$$\delta_i = (2\pi/\lambda)n_i d_i \cos(\theta_i), \quad (\text{A5})$$

and Y_i depends on the polarization.

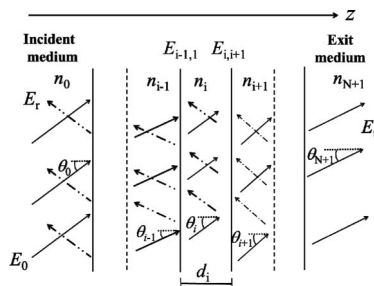


Fig. 11. Schematics of the propagation in the stratified description. $E_{i,i+1}$ is the tangential component of the electric field at the interface between the i th layer and the $(i+1)$ th layer. The direction of the plane waves (forward and backward) propagating in the i th layer is governed by the angle $\sin \theta_i = (n_0/n_i) \sin \theta_0$.

For TE polarization,

$$Y_i = n_i \cos(\theta_i). \quad (\text{A6})$$

For TM polarization,

$$Y_i = n_i / \cos(\theta_i). \quad (\text{A7})$$

For N layers, the total matrix M is the product of individual transfer matrices M_i , so that the input and output tangential fields can be calculated by multiplying the different transfer matrices together:

$$\begin{pmatrix} E_{0,1} \\ H_{0,1} \end{pmatrix} = M \begin{pmatrix} E_{N,N+1} \\ H_{N,N+1} \end{pmatrix}, \quad (\text{A8})$$

with

$$M = \begin{pmatrix} A & B \\ C & D \end{pmatrix} = M_1 M_2 \dots M_N. \quad (\text{A9})$$

The tangential components of the field at the input and output boundaries can be rewritten:

$$E_{0,1} = E_0(1+r), \quad (\text{A10})$$

$$E_{N,N+1} = t \cdot E_0, \quad (\text{A11})$$

$$H_{0,1} = E_0(1-r)Y_0, \quad (\text{A12})$$

$$H_{N,N+1} = E_0 t Y_{N+1}, \quad (\text{A13})$$

with r and t the standard reflection and transmitted amplitude coefficients $r = E_r/E_0$ and $t = E_t/E_0$ and E_r and E_t defined in Fig. 11.

Hence, one deduces

$$r = \frac{Y_0 A + Y_0 Y_{N+1} B - C - Y_{N+1} D}{Y_0 A + Y_0 Y_{N+1} B + C + Y_{N+1} D}, \quad (\text{A14})$$

$$t = \frac{2Y_0}{Y_0 A + Y_0 Y_{N+1} B + C + Y_{N+1} D}, \quad (\text{A15})$$

from which the reflection and transmission intensity coefficients are simply calculated:

$$R = r \cdot r^*, \quad (\text{A16})$$

$$T = [n_{N+1} \cos(\theta_{N+1})/n_0 \cos(\theta_0)] \cdot t \cdot t^*. \quad (\text{A17})$$

Phenomenological losses are introduced by an absorption coefficient for each slice (α_i for the i th slice) of the stratified index model, appearing in a complex index N_i :

$$N_i = n_i - j\kappa_i = n_i - j\alpha_i \lambda / 4\pi. \quad (\text{A18})$$

Note that it is only when the absorption integrated over a single layer of spheres remains small that the stratified model can be useful to describe the opal structure; indeed, a too strong scattering would make it difficult to recognize an effect of the crystalline organization of the opal along z .

The previous matrix formalism still applies for media stratified with a complex index. The real angle θ_i is replaced by a complex value, noted θ'_i , which no longer represents a direction of propagation [44,46]. However, this complex incidence θ'_i still obeys the Snell's law [see Eq. (A2)], and, significantly, the quantity $N_i \sin(\theta'_i) = n_0 \sin \theta_0$ remains real because the input and output media (vacuum or glass) are transparent (n_0, n_{N+1} are real). Moreover, the propagation direction

remains unchanged if the absorption is weak ($\kappa_i \ll 1$). Indeed, the phase-term δ_i appearing in the matrices of Eqs. (A3) and (A4), given without absorption by

$$\delta_i = (2\pi/\lambda)n_i d_i \cos \theta_i = (2\pi/\lambda)d_i(n_i^2 - n_0^2 \sin^2 \theta_0)^{1/2}, \quad (\text{A19})$$

becomes complex with absorption

$$\begin{aligned} \delta'_i &= (2\pi/\lambda)N_i d_i \cos \theta'_i \\ &= (2\pi/\lambda)d_i[(n_i - j\kappa_i)^2 - n_0^2 \sin^2 \theta_0]^{1/2}, \end{aligned} \quad (\text{A20})$$

so that, with the $\kappa_i \ll 1$ approximation, one has

$$\begin{aligned} \delta'_i &\approx (2\pi/\lambda)d_i(n_i^2 - n_0^2 \sin^2 \theta_0)^{1/2} \\ &\quad - j(2\pi/\lambda)d_i\kappa_i n_i(n_i^2 - n_0^2 \sin^2 \theta_0)^{-1/2}, \end{aligned} \quad (\text{A21})$$

which can be rewritten as

$$\begin{aligned} \delta'_i &\approx (2\pi/\lambda)d_i n_i \cos \theta_i - j(2\pi/\lambda)d_i \kappa_i n_i / \cos \theta_i \\ &= \delta_i - j(2\pi/\lambda)d_i \kappa_i n_i / \cos \theta_i. \end{aligned} \quad (\text{A22})$$

Funding. Agence Nationale de la Recherche (ANR) (08-BLAN-0031 Mesoscopic gas).

Acknowledgment. The opal was deposited at CRPP-Bordeaux in the Serge Ravaine group. We acknowledge discussions with the Agnès Maitre group.

REFERENCES AND NOTES

- E. Yablonovitch, "Inhibited spontaneous emission in solid-state physics and electronics," *Phys. Rev. Lett.* **58**, 2059–2062 (1987).
- S. John, "Strong localization of photons in certain disordered dielectric superlattices," *Phys. Rev. Lett.* **58**, 2486–2489 (1987).
- V. P. Bykov, "Spontaneous emission in a periodic structure," *Sov. Phys. J. Exp. Theor. Phys.* **35**, 269–273 (1972).
- C. M. Soukoulis, ed., *Photonic Band Gaps and Localization*, Vol. **38** of NATO Advanced Study Institute, Series B: Physics (Plenum, 1993).
- E. N. Economou, ed., *Photonic Band Gap Materials*, Vol. **315** of NATO Advanced Study Institute, Series E: Applied Sciences (Plenum, 1996).
- C. M. Bowden, J. P. Dowling, and H. O. Everitt, eds., "Development and applications of materials exhibiting photonic band gaps," *J. Opt. Soc. Am. B* **10**, 280 (1993).
- P. D. García, R. Sapienza, and C. López, "Photonic glasses: a step beyond white paint," *Adv. Mater.* **22**, 12–19 (2010).
- K. W.-K. Shung and Y. C. Tsai, "Surface effects and band measurements in photonic crystals," *Phys. Rev. B* **48**, 11265–11269 (1993).
- C. López, "Materials aspects of photonic crystals," *Adv. Mater.* **15**, 1679–1704 (2003).
- P. Jiang, J. F. Bertone, K. S. Hwang, and V. L. Colvin, "Single-crystal colloidal multilayers of controlled thickness," *Chem. Mater.* **11**, 2132–2140 (1999).
- H. Míguez, C. López, F. Meseguer, A. Blanco, L. Vázquez, R. Mayoral, M. Ocaña, V. Fornés, and A. Mifsud, "Photonic crystal properties of packed submicrometric SiO₂ spheres," *Appl. Phys. Lett.* **71**, 1148–1150 (1997).
- D. Norris, E. Arlinghaus, L. Meng, R. Heiny, and L. Scriven, "Opaline photonic crystals: how does self-assembly work?" *Adv. Mater.* **16**, 1393–1399 (2004).
- D. Gasperino, L. Meng, D. J. Norris, and J. J. Derby, "The role of fluid flow and convective steering during the assembly of colloidal crystal," *J. Cryst. Growth* **310**, 131–139 (2008).
- S. Reculosa and S. Ravaine, "Synthesis of colloidal crystal of controllable thickness through the Langmuir-Blodgett technique," *Chem. Mater.* **15**, 598–605 (2003).
- M. Bardosova, M. E. Pemble, I. M. Povey, and R. H. Tredgold, "The Langmuir-Blodgett approach to making colloidal photonic crystals from silica spheres," *Adv. Mater.* **22**, 3104–3124 (2010).
- J. F. Galisteo-López, E. Palacios-Lidón, E. Castillo-Martínez, and C. López, "Optical study of the pseudogap in the thickness and orientation controlled artificial opals," *Phys. Rev. B* **68**, 115109 (2003).
- T. Maka, D. N. Chigrin, S. G. Romanov, and C. M. Sotomayor Torres, "Three dimensional photonic crystals in the visible regime," *PIER* **41**, 307–335 (2003).
- A. Avoine, P. N. Hong, H. Frederich, J.-M. Frigerio, L. Coolen, C. Schwob, P. T. Nga, B. Gallas, and A. Maître, "Measurement and modelization of silica opal reflection properties: Optical determination of the silica index," *Phys. Rev. B* **86**, 165432 (2012).
- E. Pavarini, L. C. Andreani, C. Soci, M. Galli, F. Marabelli, and D. Comoretto, "Band structure and optical properties of opal photonic crystals," *Phys. Rev. B* **72**, 045102 (2005).
- V. G. Fedotov and A. V. Sel'kin, "Interference of additional modes in spectra of opal-like photonic crystals in the multiple diffraction regime," *Phys. Solid State* **53**, 1140–1144 (2011).
- J. B. Pendry and A. MacKinnon, "Calculation of photon dispersion relations," *Phys. Rev. Lett.* **69**, 2772–2775 (1992).
- P. M. Bell, J. B. Pendry, L. Martín Morenó, and A. J. Ward, "A program for calculating photonic band structures and transmission coefficients of complex structures," *Comput. Phys. Commun.* **85**, 306–322 (1995).
- J. F. Bertone, P. Jiang, K. S. Hwang, D. M. Mittleman, and V. L. Colvin, "Thickness dependence of the optical properties of ordered silica-air and air-polymer photonic crystals," *Phys. Rev. Lett.* **83**, 300–303 (1999).
- D. M. Mittleman, J. F. Bertone, P. Jiang, K. S. Hwang, and V. L. Colvin, "Optical properties of planar colloidal crystals: Dynamical diffraction and the scalar wave approximation," *J. Chem. Phys.* **111**, 345–354 (1999).
- S. Satpathy, Z. Zhang, and M. R. Salehpour, "Theory of photon bands in three-dimensional periodic dielectric structures," *Phys. Rev. Lett.* **64**, 1239–1242 (1990).
- J. Wang, L. Yang, D. Lin, Y. Luo, D. Li, and Q. Meng, "Optical studies of random disorder of colloidal photonic crystals and its evolution in evaporation induced self-assembly," *J. Chem. Phys.* **137**, 234111 (2012).
- P. Lalanne, "Effective medium theory applied to photonic crystals composed of cubic or square cylinders," *Appl. Opt.* **35**, 5369–5380 (1996).
- C.-H. Chan, A. Fischer, A. Martínez-Gil, P. Taillepierre, C.-C. Lee, S.-L. Yang, C.-H. Hou, H.-T. Chien, D.-P. Cai, K.-C. Hsu, and C.-C. Chen, "Anti-reflection layer formed by monolayer of microspheres," *App. Phys. B* **100**, 547–551 (2010).
- W. Zhou, M. Tao, L. Chen, and H. Yang, "Microstructured surface design for omnidirectional antireflection coatings on solar cells," *J. Appl. Phys.* **102**, 103105 (2007).
- M. Romanelli, C. Vion, C. Barthou, P. Benalloul, J. M. Frigerio, A. Maitre, P. T. Nga, T. Cuong, A. Gruzintsev, and A. Redkin, "Angle-resolved reflectivity and self-activated luminescence of 3D photonic crystal," *J. Korean Phys. Soc.* **52**, 1589–1593 (2008).
- W. L. Vos, R. Sprik, A. van Blaaderen, A. Imhof, A. Lagendijk, and G. H. Wegdam, "Strong effects of photonic band structures on the diffraction of colloidal crystals," *Phys. Rev. B* **53**, 16231–16235 (1996).
- F. García-Santamaría and P. V. Braun, "Are artificial opals non-close-packed fcc structures?" *Appl. Phys. Lett.* **90**, 241905 (2007).
- Y. A. Vlasov, M. A. Kaliteevski, and V. V. Nikolaev, "Different regimes of light localization in a disordered photonic crystal," *Phys. Rev. B* **60**, 1555–1562 (1999).
- Note that in [33], the calculation provided in the appendix considers an averaging over the index, rather than over the permittivity. There is also a misprint in the height of the successive layers.
- A. G. Bazhenova, A. V. Sel'kin, A. Y. Men'shikova, and N. N. Shevchenko, "Polarization-dependent suppression of bragg reflections in light reflection from photonic crystals," *Phys. Solid State* **49**, 2109–2120 (2007).
- S. G. Romanov, T. Maka, C. M. Sotomayor Torres, M. Miller, R. Zentel, D. Cassagne, J. Manzaneres-Martínez, and C. Jouanin,

- "Diffraction of light from thin-film polymethylmethacrylate opaline photonic crystals," *Phys. Rev. E* **63**, 056603 (2001).
37. Y. A. Vlasov, V. N. Astratov, O. Z. Karimov, A. A. Kaplyanskii, V. N. Bogomolov, and A. V. Prokofiev, "Existence of a photonic pseudogap for visible light in synthetic opals," *Phys. Rev. B* **55**, R13357 (1997).
 38. I. Maurin and D. Bloch, "Resonant infiltration of an opal: reflection line shape and contribution from in-depth regions," *J. Chem. Phys.* **142**, 234706 (2015).
 39. P. Ballin, E. Moufaret, I. Maurin, A. Laliotis, and D. Bloch, "Three-dimensional confinement of vapor in nanostructures for sub-Doppler optical resolution," *Appl. Phys. Lett.* **102**, 231115 (2013).
 40. E. Moufaret, I. Maurin, I. Zabkov, A. Laliotis, P. Ballin, V. Klimov, and D. Bloch, "Infiltrating a thin or single layer opal with an atomic vapour: sub-Doppler signals and crystal optics," *Europhys. Lett.* **108**, 17008 (2014).
 41. S. Datta, C. T. Chan, K. M. Ho, and C. M. Soukoulis, "Effective dielectric constant of periodic composite structures," *Phys. Rev. B* **48**, 14936–14943 (1993).
 42. E. Hecht, *Optics*, 4th ed. (Pearson Education, 2002), p. 428, Chap. 9.
 43. P. Yeh, *Optical Waves in Layered Media* (Edition Lavoisier, 2005).
 44. A. Balestreri, L. C. Andreani, and M. Agio, "Optical properties and diffraction effects in opal photonic crystal," *Phys. Rev. E* **74**, 036603 (2006).
 45. C. C. Katsidis and D. I. Siapkas, "General transfer-matrix method for optical multilayer systems with coherent, partially coherent, and incoherent interference," *Appl. Opt.* **41**, 3978–3987 (2002).
 46. J. E. Davis, "Multilayer reflectivity," <http://space.mit.edu/~davis/memos/multilayer.pdf>.
 47. For a given material, transparency over the broad spectral range that we consider is highly hypothetical; rather, the model can be used to describe a measurement at a fixed wavelength, and, for various opal diameters, the loss rate is then proportional to the inverse of the sphere size.
 48. V. G. Solov'ev, C. M. Sotomayor Torres, and S. G. Romanov, "Reflection, transmission, and Scattering of light by Photonic crystals based on opal films," *Russ. Phys. J.* **47**, 286–292 (2004).
 49. V. N. Astratov, A. M. Adawi, S. Fricker, M. S. Skolnick, D. M. Whittaker, and P. N. Pusey, "Interplay of order and disorder in the optical properties of opal photonic crystals," *Phys. Rev. B* **66**, 165215 (2002).
 50. P. Massé, R. A. L. Vallée, J.-F. Dechézelles, J. Rosselgong, E. Cloutet, H. Cramail, X. S. Zhao, and S. Ravaine, "Effects of the position of a chemically or size-induced planar defect on the optical properties of colloidal crystals," *J. Phys. Chem. C* **113**, 14487–14492 (2009).
 51. M. Romanelli, I. Maurin, P. Todorov, C. H. Chan, and D. Bloch, "A 2D nanosphere array for atomic spectroscopy," *Ann. Phys.* **32**, 127–130 (2007).
 52. J. F. Galisteo-López and C. López, "High-energy optical response of artificial opals," *Phys. Rev. B* **70**, 035108 (2004).
 53. J. F. Galisteo-Lopez, F. López-Tejiera, S. Rubio, C. López, and J. Sánchez-Dehesa, "Experimental evidence of polarization dependence in the optical response of opal based photonic crystals," *Appl. Phys. Lett.* **82**, 4068–4070 (2003).
 54. A. V. Baryshev, A. B. Khanikaev, H. Uchida, M. Inoue, and M. F. Limonov, "Interaction of polarized light with three-dimensional opal-based photonic crystals," *Phys. Rev. B* **73**, 033103 (2006).
 55. A. V. Baryshev, A. B. Khanikaev, R. Fujikawa, H. Uchida, and M. Inoue, "Polarized light coupling to thin silica-air opal films grown by vertical deposition," *Phys. Rev. B* **76**, 014305 (2007).
 56. B. Wood, J. B. Pendry, and D. P. Tsai, "Directed subwavelength imaging using a layered metal-dielectric system," *Phys. Rev. B* **74**, 115116 (2006).

Resonant infiltration of an opal: Reflection line shape and contribution from in-depth regions

Isabelle Maurin and Daniel Bloch

Citation: *The Journal of Chemical Physics* **142**, 234706 (2015); doi: 10.1063/1.4922614

View online: <http://dx.doi.org/10.1063/1.4922614>

View Table of Contents: <http://scitation.aip.org/content/aip/journal/jcp/142/23?ver=pdfcov>

Published by the [AIP Publishing](#)

Articles you may be interested in

[Photonic surfaces for designable nonlinear power shaping](#)

Appl. Phys. Lett. **106**, 061110 (2015); 10.1063/1.4907946

[Numerical investigation of optical Tamm states in two-dimensional hybrid plasmonic-photonic crystal nanobeams](#)

J. Appl. Phys. **116**, 043106 (2014); 10.1063/1.4891222

[Omnidirectional reflection from nanocolumnar TiO₂ films](#)

J. Appl. Phys. **112**, 084317 (2012); 10.1063/1.4759138

[Depth-profiling of elastic and optical inhomogeneities in transparent materials by picosecond ultrasonic interferometry: Theory](#)

J. Appl. Phys. **110**, 124908 (2011); 10.1063/1.3665646

[Broadband omnidirectional reflection from negative index materials](#)

Appl. Phys. Lett. **87**, 261921 (2005); 10.1063/1.2151251

A promotional banner for AIP APL Photonics. The background is a vibrant orange and red gradient with a bright sunburst effect on the right. On the left, there is a small image of the journal cover for APL Photonics, which features a blue and white abstract design. A yellow starburst graphic with the words 'OPEN ACCESS' in red is overlaid on the journal cover. To the right of the journal cover, the text 'Launching in 2016!' is written in a large, white, sans-serif font, followed by 'The future of applied photonics research is here' in a smaller, white, sans-serif font. In the bottom right corner, the AIP APL Photonics logo is displayed in white.

Resonant infiltration of an opal: Reflection line shape and contribution from in-depth regions

Isabelle Maurin^{1,2,a)} and Daniel Bloch^{2,1,b)}

¹Laboratoire de Physique des Lasers, Université Paris 13, Sorbonne Paris-Cité, Villetaneuse, France

²CNRS, UMR 7538, 99 Avenue J.-B. Clément, F-93430 Villetaneuse, France

(Received 6 March 2015; accepted 3 June 2015; published online 19 June 2015)

We analyze the resonant variation of the optical reflection on an infiltrated artificial opal made of transparent nanospheres. The resonant infiltration is considered as a perturbation in the frame of a previously described one-dimensional model based upon a stratified effective index. We show that for a thin slice of resonant medium, the resonant response oscillates with the position of this slice. We derive that for adequate conditions of incidence angle, this spatially oscillating behavior matches the geometrical periodicity of the opal and hence the related density of resonant infiltration. Close to these matching conditions, the resonant response of the global infiltration varies sharply in amplitude and shape with the incidence angle and polarization. The corresponding resonant reflection originates from a rather deep infiltration, up to several wavelengths or layers of spheres. Finally, we discuss the relationship between the present predictions and our previous observations on an opal infiltrated with a resonant vapor. © 2015 AIP Publishing LLC. [<http://dx.doi.org/10.1063/1.4922614>]

I. INTRODUCTION

Photonic crystals offer the possibility to modify the distribution of optical modes, hence changing the properties of embedded absorbers or of resonant emitters. Conversely, a distribution of resonant particles inside the photonic crystal¹ may allow a fine tuning of the optical properties of the material or can be of interest for a variety of sensors. An artificial opal, which is a (quasi-) crystalline arrangement of identical transparent nanospheres like glass nanospheres, is an approximate realization of a photonic crystal,² obtained through soft chemistry. The opal voids easily allow for an infiltration by a resonant fluid (liquid or gas). When an opal is prepared layer-by-layer in a Langmuir-Blodgett (LB) technique,³ the number of layers of nanospheres is kept under control, but a random hexagonal closed packed (*r.h.c.p.*) structure is generated, without a genuine crystalline order along the normal to the surface. Also, the optical properties of a photonic crystal, often analyzed through a reflection detection, strongly depend on the interface between the crystal itself and the external medium where detection is operated.⁴

Here, we extend a calculation previously developed for the optics of an opal,⁴ to estimate on reflection the resonant effects of an infiltration. This is a type of “selective reflection” spectroscopy for a resonant medium embedded in the voids of the opal, where the optical reflection is monitored when the irradiation frequency is tuned around the resonance. In Ref. 4, the calculation, which applies to a broad range of wavelengths (λ) and sphere diameters (D), uses a one-dimensional stratified effective index defined through a height-dependent mix of the index of the glass spheres and of the voids. It has revealed convenient to emphasize the role of the first

half-layer of spheres—“gap” region between the substrate and the compact opal—or of the last half layer, notably in reflection, as the “effective index” of this “gap” region is smaller than in the regions where the spheres are compactly arranged. The calculation is simple in its principle because it replaces the effect of a three-dimensional scattering by an *ad hoc* one-dimensional extinction coefficient. Nevertheless, it describes the reflection signal as interferences between the reflection from stratified layers, so that one recovers various standard predictions, notably Fabry-Perot type oscillations between the peripheral regions of the opal, and Bragg reflection peaks for well-chosen sets of wavelength λ and incidence angle θ . Technically, the continuous variations of the effective index are discretized to make the calculations tractable.

The stratified effective index model⁴ relies on a linear formalism through a product of propagation matrices. This notably allows introducing a defect layer (see Sec. III-4 of Ref. 4). In the present work, the infiltrated material is assumed to exhibit simple resonances, as for a homogeneously broadened gas (neglecting all effects of an internal motion) or a (weakly) absorbing liquid, and is considered as a perturbation in the effective index description of the opal.⁵ In Sec. II, we consider the effect of adding a single thin “slice” of a resonant material, which is a kind of a “defect layer.” We show that, for a given location of the slice, the resonant change in reflection can single out the absorptive part of the resonant response, or the dispersive one, and generally yield a mix of these features. For simplicity, we always neglect the smooth wavelength dependence of the optical response of the bare opal itself.⁴ Indeed, we always assume the resonance of the material to be sharper than the wavelength dependence of the opal, even around a Bragg reflection peak of the opal.

In a second step (Sec. III), the resonant material is considered to be spatially distributed in the voids (interstices) of the opal, and we calculate the resonant effect by the coherent

^{a)}isabelle.maurin@univ-paris13.fr

^{b)}daniel.bloch@univ-paris13.fr

addition of the effect of the various resonant slices, assumed to be weighted by the density of the voids. We hence show (Sec. IV) that for a matching condition between the optical periodicity of the propagating wave (depending on the incidence angle) and the geometrical distribution of the opal, one can be sensitive in reflection to the contribution of relatively deep resonant layers. In Sec. V, we finally compare these predictions of quick evolutions of the line shape with experimental situations previously encountered with an infiltration of a Doppler-broadened gas of atoms undergoing thermal motion.^{6,7}

II. EFFECT OF A SINGLE SLICE OF A RESONANT MATERIAL

The layered effective index model⁴ deals with the optics of the opal assuming that the opal is stratified parallel to the substrate, as governed by a (discretized) index $N_{eff}(z)$. An extinction coefficient $\alpha(z)$ is introduced in $N_{eff}(z)$, despite the transparency of the opal spheres, in order to take into account the scattering, so that

$$\begin{aligned} N_{eff}(z) &= n_{eff}(z) - j \alpha(z)\lambda/4\pi \\ &= \Re[N_{eff}(z)] + j \Im[N_{eff}(z)], \end{aligned} \quad (1)$$

with $n_{eff}(z)$ a real index connected to the spatial variation—integrated over a plane parallel to the substrate—of the opal density (see Fig. 1(a)); for simplicity, $\alpha(z)$ is assumed to be constant with z (see discussion in Ref. 4) and independent of the propagation direction of the beam. Here, because we assume the presence of a slice of resonant infiltrated material, of a thickness Δz , located between z_0 and $z_0 + \Delta z$, we introduce an extra resonant (complex) contribution to the local optical index,

$$\Delta N(\omega) = \Re[\Delta N(\omega)] + j \Im[\Delta N(\omega)] \quad (2)$$

which has to be added in Eq. (1) (for $z_0 \leq z \leq z_0 + \Delta z$). The value of $\Delta N(\omega)$ depends on the (nearly resonant) excitation frequency ω . In Eq. (2), $\Re[\Delta N(\omega)]$ corresponds to the dispersive part of the resonance, and $\Im[\Delta N(\omega)]$ to the absorption of the infiltrated material (assuming $\Im[\Delta N(\omega)] < 0$).

To calculate the effect of the resonant infiltrated slice, a perturbation expansion is applied to the calculation of the reflection coefficient.⁸ Note that in a perturbative approach, the reflection coefficient in amplitude, and in intensity, behaves similarly. Hence, the resonant change in reflectivity solely depends on the product $\Delta N(\omega) \cdot \Delta z$ because of linearity. Moreover, this linearity applies separately to $\Re[\Delta N(\omega)] \cdot \Delta z$ and to $\Im[\Delta N(\omega)] \cdot \Delta z$, so that the frequency line shape of the reflective response of this resonant slice is simply deduced from the knowledge of the complex resonance $\Delta N(\omega)$.

Figure 2 shows a variety of situations, where calculations are for realistic parameters corresponding for D and λ_1 values to experimental situations that we have analyzed^{6,7} and to a realistic extinction coefficient, see Ref. 4. As a general result, the predicted change $\Delta R(z_0, \omega)$ in the reflection coefficient R oscillates with the position z_0 of the resonant slice. The spatial period of this oscillation is determined by the optical propagation, showing a dependence on the wavelength of the excitation λ (Fig. 2(b)) and on the incidence angle (Fig. 2(c)). Naturally,

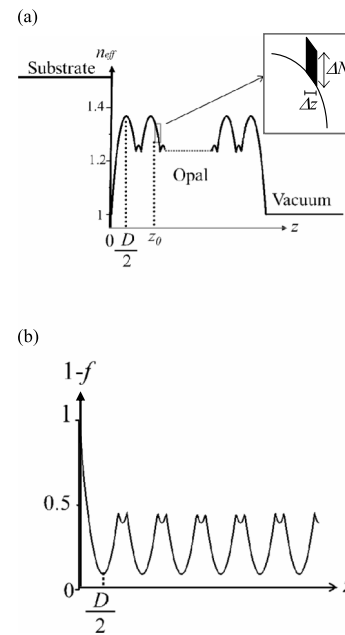


FIG. 1. (a) Stratified layered effective index for an opal, including an additional perturbative slice $\Delta N \cdot \Delta z$ located in z_0 ; (b) spatial distribution $[1 - f(z)]$ of the voids and of the infiltrated material.

this spatial period depends not only on the vacuum wavelength λ but also depends on the (averaged) value of $n_{eff}(z)$, defining the “effective” wavelength in the opal. The oscillation with the position of the resonant slice embedded in a layered material generalizes a well-known behavior for the reflective contribution of an additional slice in a homogeneous medium (see, e.g., Ref. 9). In addition to this oscillating behavior, the response is spatially damped, as a consequence of the phenomenological attenuation coefficient $\alpha(z)$ introduced to take into account the effect of light scattering.

A closer look on this oscillation reveals a (spatial) phase shift when turning the resonance from dispersive to absorptive (Fig. 2(d)). This phase-shift can be traced back to the well-known fact that, relatively to the incident driving field, the resonant (field) response of the driven material itself exhibits a phase-shift when the response goes from dispersion to absorption. An analogous but weaker phase-shift is also found when switching the incident polarization from one to the other principal polarization, i.e., from transverse-electric (TE) to transverse-magnetic (TM) (see Fig. 2(e)). This phase-shift associated to polarization would not be predicted for a resonant slice in a homogeneous isotropic medium: it is a genuine signature of the stratified medium in which the resonant layer is embedded.^{4,6,7} It is indeed the propagation to this resonant layer, and from it, which differs for a TE- or TM-polarized beam, owing to a polarization-dependent combination of transmission and reflection coefficients through the successive layers. This justifies that the polarization dependence of these oscillations is small for weak incidence angles and becomes possibly sizeable for large incidence angles, notably in the vicinity of the opal “Brewster” angle (see Ref. 4). This kind of birefringence can be viewed as the result of the anisotropy introduced by the organization of the rather thick opal parallel to the window.

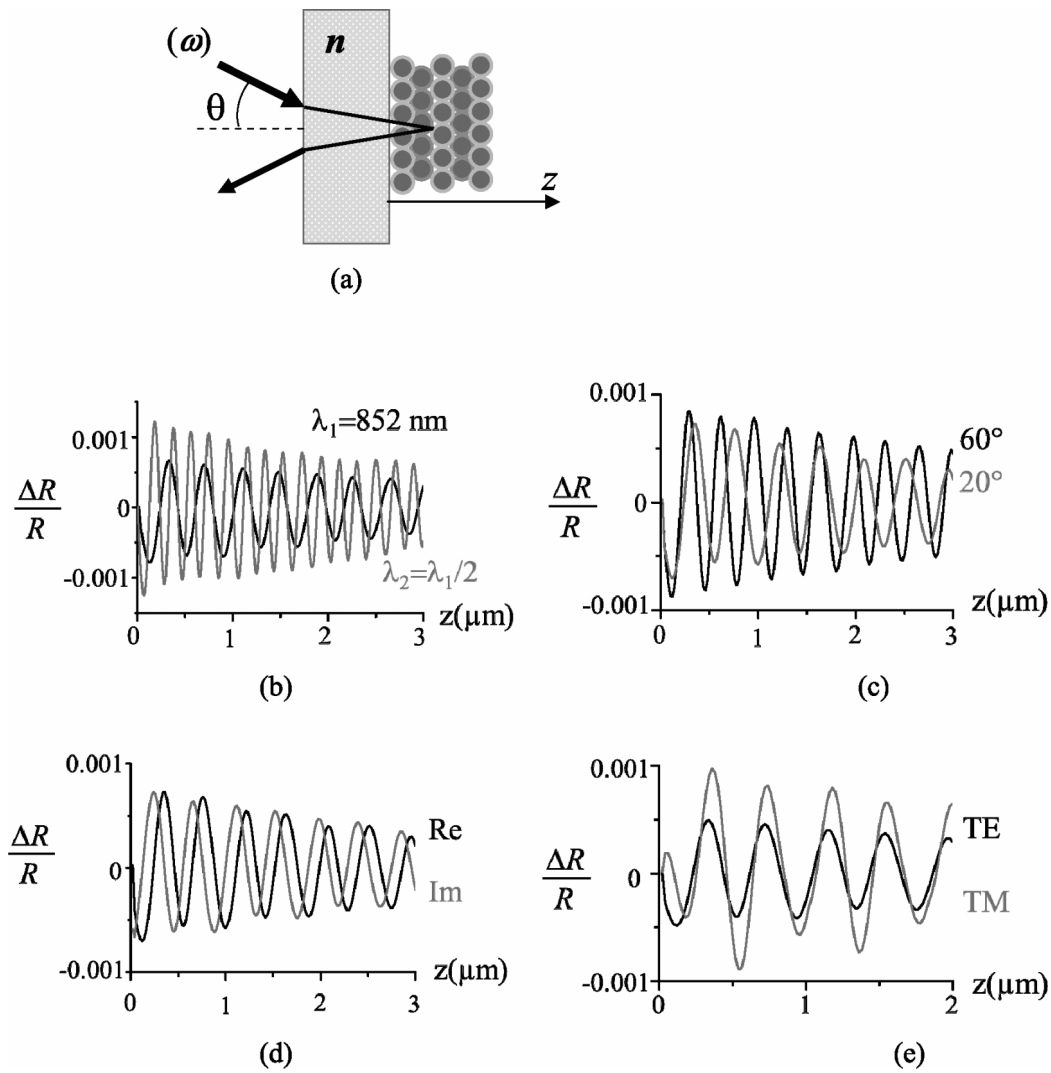


FIG. 2. Relative change in the opal reflectivity as a function of the position z of an elementary additional slice and of the external incidence angle θ . (a) Scheme of the set-up; (b) comparison between $\lambda_1 = 852$ nm and $\lambda_2 = 426$ nm, with $\theta = 45^\circ$ and TE polarization; (c) comparison between $\theta = 20^\circ$ and $\theta = 60^\circ$, with $\lambda = 852$ nm and TE polarization; (d) comparison between a dispersive contribution (labelled Re) for $\Delta N(\omega) \cdot \Delta z$ real and the equivalent absorptive one for $\Delta N(\omega) \cdot \Delta z$ imaginary (labelled Im), for $\lambda = 852$ nm, $\theta = 60^\circ$, and TE polarization; (e) comparison between TE polarization and TM polarization, with $\lambda = 852$ nm and $\theta = 45^\circ$ ($R = 4.7\%$ for TE, $R = 0.56\%$ for TM). The opal is assumed to be made of $1 \mu\text{m}$ diameter glass spheres, with a glass index $n = 1.4$ identical to the index of the substrate. The extinction coefficient replacing the scattering is chosen to be $\alpha = 2 \times 10^5 \text{ m}^{-1}$, and the LB opal is made of 20 layers (or more) of glass spheres, in order to get a result independent of the opal thickness. One has taken $\Delta N(\omega) \cdot \Delta z = 10^{-11}$ nm for (b), (c), (e), and (d) when $\Delta N(\omega)$ is real and $\Delta N(\omega) \cdot \Delta z = -j \times 10^{-11}$ nm for (d) when $\Delta N(\omega)$ is imaginary.

III. SPATIALLY DISTRIBUTED INFILTRATION, MATCHING, AND DEEP LAYERS CONTRIBUTION

The linearity of our calculation also allows evaluating the global effect of a resonant infiltration by summing the contribution of elementary slices. Only the density of the resonant material must remain weak enough to justify a perturbation expansion on the reflection coefficient. The change of reflectivity becomes

$$\Delta R(\omega) = \int_0^\infty \frac{\Delta R(z, \omega)}{\Delta z} dz, \quad (3)$$

with $\Delta R(z, \omega)$ the change of reflectivity for an elementary slice, located in z and of a Δz thickness, as calculated in Sec. II.

At this step, the spatial distribution of the infiltrated material must be considered. Indeed, if one simply assumes a constant density for the infiltrated material, the oscillations of

the response $\Delta R(z, \omega)$ for an elementary slice (Sec. II and Fig. 2) just lead to a coherence length limited to the (reduced) period of the oscillation. Above a ~ 1 rd shift, distant slices no longer interfere constructively. Practically, it is more natural to assume that the resonant material fills up only the voids of the opals, so that its density must follow the $[1 - f(z)]$ spatial distribution (see Fig. 1(b)). This density, which also governs the corresponding (sliced) optical index $\Delta N(\omega)$, is periodical after the first half layer of spheres.

A match between the optical periodicity of the response (for an elementary slice) and the geometrical periodicity of the infiltration occurs for specific sets of wavelength and incidence angle. Interesting situations then appear, as can be seen with a plot of the partial integration,

$$\Delta R_z(\omega) = \int_0^z \frac{\Delta R(z, \omega)}{\Delta z} dz. \quad (4)$$

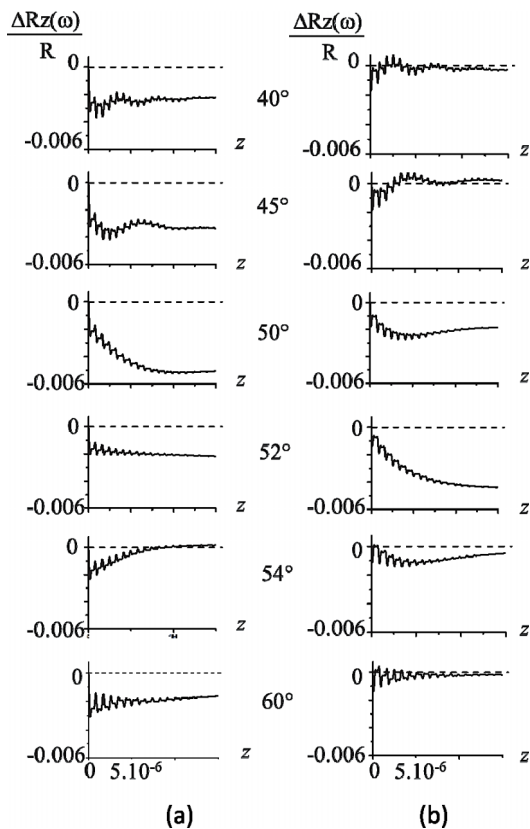


FIG. 3. Relative change in the reflectivity $\Delta R_z(\omega)/R$ as a function of the limit z of the infiltrated region for the indicated incidence angles: (a) dispersive resonance $\Delta N(\omega) = 5 \times 10^{-4}$; (b) absorptive resonance $\Delta N(\omega) = -5 \times 10^{-4} \cdot j$. The opal features are the same as in Fig. 2, polarization is TE, $\lambda = 852$ nm.

In Fig. 3, this partial integration from the interface is shown for a variety of incidence angles, with $\Delta N(\omega)$ proportional to the $[1 - f(z)]$ distribution and purely real (Fig. 3(a)) or purely imaginary (Fig. 3(b)). These partial integrations always exhibit a fast oscillating behavior with the boundary of the integration. This had to be expected from Fig. 2. Interestingly, and despite these oscillations, the partial integration increases with the distance over several optical wavelengths for some incidences [notably in Fig. 3(a) for $\theta = 50^\circ$ and dispersive response $\Delta N(\omega) = \Re[\Delta N(\omega)]$ or for $\theta = 52^\circ$ and absorptive response $\Delta N(\omega) = j \Im[\Delta N(\omega)]$ in Fig. 3(b)]. In some sense, the coherence length is now governed by a kind of “supergrating,” involving the geometrical periodicity of the material density and the optical periodicity of the response. The already-mentioned phase shift between dispersive-type and absorptive-type resonance justifies that the most sizeable responses for each kind of resonance are not obtained for the same incidence. Analogous changes of the optimal incidence angle to get these long “coherence lengths” can also be found when comparing TE and TM polarizations, as a result of the phase shift between TE and TM elementary responses. The essence of this regime of “long coherence length” is that a notable contribution to the resonant signal originates in deep layers of the opal.

Additionally, one notes that for the optimal incidence (e.g., $\theta = 52^\circ$ for absorptive response), the partial integral sticks to a long-distance asymptotic value (Fig. 3(b)), instead

of growing continuously when increasing the domain of integration. This is an effect of the attenuation coefficient. Conversely, even for a small mismatching (e.g., $\theta = 50^\circ$ for absorptive response), the overall integration exhibits a small decrease for long distances after having reached an extreme. In some cases, like for 40° or 52° (dispersive response), the integral apparently sticks to a given value, already determined by the first layer. Indeed, the first half-layer, mostly made of voids and allowing a high density of the infiltrated material, can have a predominant influence. This behavior can appear as an offset, which may be discriminated in some cases (see, e.g., the case of gas of “moving” atoms⁶). In the same manner, the $[1 - f(z)]$ distribution includes a residual non-modulated infiltration (for a perfect opal, this floor represents a $\sim 9\%$ density): its effect is equivalent to a tiny (resonant) change of the sphere index.

IV. RESONANT LINE SHAPES

The linearity of the treatment, applied in Sec. III separately to a purely real or purely imaginary resonant change $\Delta N(\omega)$, is the basis to predict, from the integrated value $\Delta R(\omega)$ (Eq. (3), which is the long distance limit of the partial integration discussed in Sec. III and Fig. 3) the reflection line shape for the infiltrated opal. The marked sensitivity of the amplitude $\Delta R(\omega)$ to the incidence angle is illustrated in Fig. 4, where $\Delta R(\omega)$ is plotted as a function of θ , when the resonant response is either purely dispersive ($\Im[\Delta N(\omega)] = 0$) or absorptive ($\Re[\Delta N(\omega)] = 0$). The sensitivity to the resonant medium is the highest around the angle satisfying a matching between the opal periodicity and the optical propagation, but marked differences can be seen between absorptive and dispersive responses. This implies that for a given line shape of the intrinsic optical resonance of the infiltrated material, the reflection signal exhibits considerable variations of the line shape under a small change of the incidence angle. Similar strong variations arise when changing polarization from TE to TM.

These quick variations are illustrated in Fig. 5, where for simplicity, we assume for the infiltrated material a (complex) Lorentzian response,

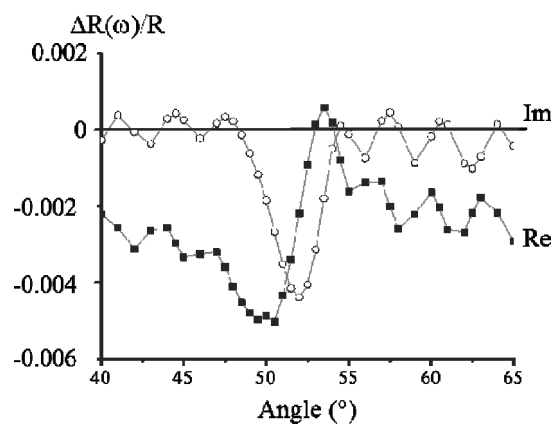


FIG. 4. Relative change in the reflectivity $\Delta R(\omega)/R$ for a wholly filled opal as a function of the incidence angle, for a dispersive resonance (labelled Re) $\Delta N(\omega) = 5 \times 10^{-4}$, and for an equivalent absorptive resonance (labelled Im) $\Delta N(\omega) = -5 \times 10^{-4} \cdot j$. The opal features are the same as in Fig. 2, polarization is TE, $\lambda = 852$ nm.

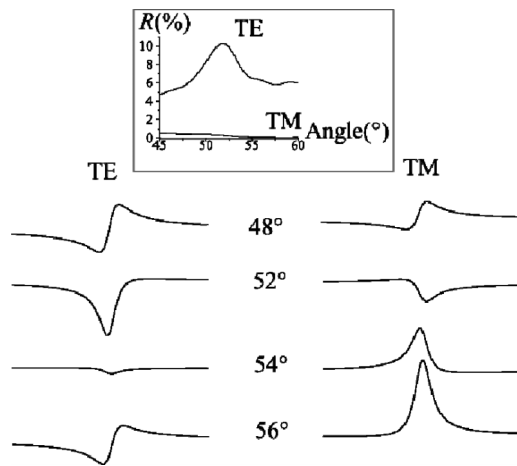


FIG. 5. Calculated frequency line shapes of the relative change in the reflection signal for an infiltration exhibiting a (complex) Lorentzian response and for incidence angles as indicated. Polarization is (a) TE and (b) TM. The scale of relative amplitude is the same for all curves, and one has, respectively, $R = 5.93\%$, 10.32% , 7.33% , 6.32% for 48° , 52° , 54° , 56° in TE polarization and $R = 0.45\%$, 0.29% , 0.14% , 0.08% in TM polarization. The inset shows the nonresonant behaviour of the reflection with the incidence angle, notably illustrating a second-order Bragg diffraction for TE, and a Brewster-like incidence in TM (same 852 nm wavelength and opal sphere diameter as in Fig. 2).

$$\Delta N(\omega) \propto -[1 - f(z)][(\omega - \omega_0) - j\gamma]^{-1}, \quad (5)$$

with ω_0 the center of the resonance and γ the width of the Lorentzian response of the infiltrated material.

It is worth noting that, in order to compare the resonant changes in the reflection signal, we have plotted in Fig. 5 the *relative* change of reflectivity $\Delta R(\omega)/R$. In particular, for TM polarization (see inset of Fig. 5), the non resonant reflection is pretty weak, but exhibits notable variations: this is because we are in the region of a Brewster-like incidence.⁴ In TE polarization, R exhibits a maximum around 52° , which can be actually traced back to a second-order “Bragg peak,” as shown to exist in Ref. 4. The resonant variation predicted for the reflectivity line shape $\Delta R(\omega)/R$ with the incidence angle is much larger and essentially different in shape, than the one governed by high-order Bragg reflection, whose shape may eventually become a dip through complex interferences in reflection which do not all satisfy the Bragg-matching condition. Anyhow, as long as the density of the resonant medium mimics the opal geometry, the coincidence is intrinsic between the incidence yielding spatial coherence of the response of the infiltrated material and the one of Bragg reflection, as corresponding to a coherent summing of the successive reflection over the opal layers. This can be verified when calculations are performed for a different set of (λ, D) values.

V. DISCUSSION AND CONNECTION WITH POSSIBLE EXPERIMENTS

The above approach was initially developed to help interpreting experiments with an infiltration of a low-density atomic gas, sensitive to the thermal atomic motion, inside the interstitial regions of a LB opal.⁶ In addition to the expected Doppler-broadened structures resulting from the thermal atomic

motion, we had observed sub-Doppler contributions, but only for a range of oblique incidences and with rapid variations of these narrow line shapes when varying the incidence angle. The profound physical origin of this sub-Doppler contribution, probably connected to a velocity-selective transient behaviour in the confined interstitial responses, has remained elusive until now.^{6,7} Various optical considerations had led us to attribute⁶ the narrow signal to a resonant response of atoms three-dimensionally confined inside the opal. In spite of the physical differences between our present local index approach, applicable only for a motionless resonant medium, and the Doppler-broadened gas, it is interesting to note that the sets of line shapes calculated in Fig. 5 exhibit some similarities¹⁰ with the narrow sub-Doppler structures appearing in Ref. 6. This can appear as an additional indication that these narrow structures are truly related to an in-depth resonant response inside the opal. Our model notably predicts the possibility of dramatic changes in the line shape for a given incidence and for a modest change in the wavelength. This resembles our observations,⁶ when comparing results on the Cs doublet resonance lines, with the D_1 line at $\lambda_1 = 894$ nm and the D_2 line at $\lambda_2 = 852$ nm. A sensitivity to polarization is here predicted, analogous to what was dramatically observed in experiments. Also, for a more radical change in the wavelength, like when turning to the second resonance line of Cs at $\lambda = 455$ nm, one predicts here a faster variation of the line shape with the incidence angle, as has been recently observed.⁷

Anyhow, the present modeling cannot have the ambition to deal with the Doppler effect associated to atomic thermal motion, and it is restricted to homogeneously broadened simple resonant fluid materials. Aside from the intrinsic limitations of our one-dimensional stratified medium, several limitations may apply to the quantitative findings of our model. First, the linearity argument applies in principle only for a low signal or density of resonant particles. Here, careful checks may be needed as the calculation for an opal is practically sliced in up to $\sim 10^3$ slices (see, e.g., the estimation for numerical calculation in Ref. 4). Second, a glass opal prepared by a LB method tends to exhibit numerous structural defects, which increase with the distance to the surface as corresponding to successive steps of deposition. Such defects should impact the periodicity of the $[1 - f(z)]$ density function and reduce the possibility to generate a coherent resonant response from the most remote layers. The observation of a non resonant high-order Bragg peak may provide an indication of the quality of the opal, sustaining the predicted sharp variations with the incidence. Note that, with polystyrene spheres, highly ordered LB opals can be produced. They could be compatible with various infiltrating materials, although not relevant for experiments with alkali metal vapors.

Finally, an important limitation of the model is that in its essence, the one-dimensional stratified medium ignores the light scattered by the opal, considered only through phenomenological losses. This scattered resonant light also contributes to the excitation of the infiltrated material, and the phase of the corresponding excitation (not necessarily random) usually differs from the one resulting from the excitation by the propagating field. As an alternate asymptotic regime, one may consider that the resonant excitation is only induced by a

purely incoherent scattering. This leads again to a periodical spatial distribution of field emission by the infiltrated material, but with modified quantitative predictions. The general behavior, with its sharp dependence on the incidence angle and on polarization, would nevertheless remain similar, while the coincidence with a high-order Bragg peak should disappear. This says that even if it makes it difficult to assess the ordering quality of the opal by an analysis of the variations of the resonant signal, the general type of behavior that we describe is robust relatively to the specific hypotheses of the model.

VI. CONCLUSION

The above simplified one-dimensional method has allowed considering the coupling of a resonant material with an opal, up to the possible predictions of line shapes, a task which would be formidable for a purely three-dimensional numeric approach. By rather general arguments, we have shown that infiltration of relatively deep regions of a photonic crystal can be observed for a well-chosen narrow range of experimental considerations. Our numerical evaluations were performed in view of already performed experiments, in a regime far away from the main bandgap of the opal. Nevertheless, the enhanced sensitivity to the resonant material tends to occur close to a (high-order) Bragg condition, because the constructive interferences needed for a spatially coherent resonant excitation of the medium are driven by the same incident field allowing the interferences leading to the Bragg condition. This may naturally change if the exciting field is induced by the scattered light. For longer wavelengths (and unchanged sphere size), in the vicinity of the first-order Bragg reflection peak, our model could help understanding to which extent a nearly forbidden propagation becomes partially allowed with the resonant infiltration.¹¹ Because the depth of the observed resonant response remains however confined at maximum to few wavelengths, our predictions of a sharp sensitivity to incidence angle and polarization should apply as well to a thick opal prepared by sedimentation. Finally, our conclusions can be straightforwardly extended to the situation of an inverse opal or to the detection of resonant transmission in a sufficiently thin LB opal. An extension of this method to the spectroscopy of an infiltrated photonic fiber may even be considered on the basis of a scalar approach such as proposed in Ref. 12.

ACKNOWLEDGMENTS

Work supported by the ANR project “Mesoscopic gas” 08-BLAN-0031. We thank the referee for drawing us our attention to Refs. 5 and 12.

- ¹Yu. A. Vlasov, V. N. Astratov, O. Z. Karimov, A. A. Kaplyanskii, V. N. Bogomolov, and A. V. Prokofiev, “Existence of a photonic pseudogap for visible light in synthetic opals,” *Phys. Rev. B* **55**, R13357 (1997).
- ²C. López, “Materials aspects of photonic crystals,” *Adv. Mater.* **15**, 1679–1704 (2003).
- ³S. Reculosa and S. Ravaine, “Synthesis of colloidal crystal of controllable thickness through the Langmuir–Blodgett technique,” *Chem. Mater.* **23**, 598 (2003).
- ⁴I. Maurin, E. Moufaret, A. Laliotis, and D. Bloch, “The optical interface of a photonic crystal: Modelling an opal with a stratified effective index,” e-print [arXiv:1407.5777](https://arxiv.org/abs/1407.5777); “Optics of an opal modeled with a stratified effective index and the effect of the interface,” *J. Opt. Soc. Amer. B* (submitted).
- ⁵Such a perturbative approach has already been used, but not for a spectroscopic resonance, in a more general context of a layered medium, see P. Bertrand, C. Hermann, G. Lampel, J. Peretti, and V. I. Safarov, “General analytical treatment of optics in layered structures: Application to magneto-optics,” *Phys. Rev. B* **64**, 235421 (2001).
- ⁶P. Ballin, E. Moufaret, I. Maurin, A. Laliotis, and D. Bloch, “Three-dimensional confinement of vapor in nanostructures for sub-Doppler optical resolution,” *Appl. Phys. Lett.* **102**, 231115 (2013).
- ⁷E. Moufaret, I. Maurin, I. Zabkov, A. Laliotis, P. Ballin, V. Klimov, and D. Bloch, “Infiltrating a thin or single layer opal with an atomic vapour: Sub-doppler signals and crystal optics,” *EPL* **108**, 17008 (2014).
- ⁸In all the following—see discussion in Sec. V—we assume that the elementary resonant slice has a thickness Δz much smaller than the sphere size and than the wavelength. Also, the resonant change of reflectivity is assumed to be small relatively to the non resonant reflectivity. Of course, this assumes that this non resonant reflectivity has not dropped down to zero, as it may occur accidentally, e.g., in specific Brewster-like situations assuming the opal to be ideal. The non perturbative regime for an opal would extend the findings for a flat interface described in A. M. Akulshin, V. L. Velichansky, A. I. Zherdev, A. S. Zibrov, V. I. Malakhova, V. V. Nikitin, V. A. Sautenkov, and G. G. Kharisov, “Selective reflection from a glass–gas interface at high angles of incidence of light,” *Sov. J. Quantum Electron.* **19**, 416 (1989).
- ⁹G. Nienhuis, F. Schuller, and M. Ducloy, “Nonlinear selective reflection from an atomic vapor at arbitrary incidence angle,” *Phys. Rev. A* **38**, 5197 (1988); see also the appendix of M. Chevrollier, M. Fichet, M. Oriá, G. Rahmat, D. Bloch, and M. Ducloy, “High resolution selective reflection spectroscopy as a probe of long-range surface interaction: Measurement of the surface van der Waals attraction exerted on excited Cs atoms,” *J. Phys. II* **2**, 631 (1992).
- ¹⁰Note that in Ref. 6 frequency-modulation (FM) technique is used, which actually yields $\Delta R(\omega)/d\omega$.
- ¹¹P. J. Harding, P. W. H. Pinkse, A. P. Mosk, and W. L. Vos, “Nanophotonic hybridization of narrow atomic cesium resonances and photonic stop gaps of opaline nanostructures,” *Phys. Rev. B* **91**, 045123 (2015).
- ¹²T. M. Monro, D. J. Richardson, N. G. R. Broderick, and P. J. Bennett, “Holey optical fibers: An efficient modal model,” *J. Lightwave Technol.* **17**, 1093 (1999).

